This document was prepared for the ETI by third parties under contract to the ETI. The ETI is making these documents and data available to the public to inform the debate on low carbon energy innovation and deployment.

Programme Area: Marine

Project: PerAWAT

Title: Implementation Report: Time-Domain Model

Abstract:

This deliverable describes the current implementation status of the wave energy converter (WEC) numerical modelling software being developed by Gerald Hassan and Partners Ltd under the PerAWAT project. The report contains details for implementing the derived methodology in the time domain to analyse arrays in regular and irregular waves, such that it could be replicated by a 3rd Party. Initial results related to the influence of several design variables are presented. A detailed description and assessment of the performance of different fundamental device concepts and power take-offs is included. Implications for the further model development are discussed.

Context:

The Performance Assessment of Wave and Tidal Array Systems (PerAWaT) project, launched in October 2009 with £8m of ETI investment. The project delivered validated, commercial software tools capable of significantly reducing the levels of uncertainty associated with predicting the energy yield of major wave and tidal stream energy arrays. It also produced information that will help reduce commercial risk of future large scale wave and tidal array developments.

GL Garrad Hassan

ETI MARINE PROGRAMME PROJECT
PerAWaT MA1003
WG1 WP1 D3
IMPLEMENTATION REPORT: TIME-DOMAIN MODEL

Client	Energy Technologies Institute
Contact	Geraldine Newton-Cross
Document No	104327/BR/05
Issue	1.0
Classification	Not to be disclosed other than in line with the terms of the Technology Contract
Date	6 May 2011

Author:

M Livingstone, E Mackay,
B Child, J Lucas, J Cruz

Checked by:

J Cruz

Approved by:

R I Rawlinson-Smith

IMPORTANT NOTICE AND DISCLAIMER

1. This report is intended for the use of the Client on whose instructions it has been prepared, and who has entered into a written agreement directly with Garrad Hassan and Partners Limited ("GH"). GH's liability to the Client is set out in that agreement. GH shall have no liability to third parties for any use whatsoever without the express written authority of GH. The report may only be reproduced and circulated in accordance with the Document Classification and associated conditions stipulated in this report, and may not be disclosed in any public offering memorandum without the express written consent of GH.

2. This report has been produced from information relating to dates and periods referred to in this report. The report does not imply that any information is not subject to change.

KEY TO DOCUMENT CLASSIFICATION

Strictly Confidential	:	Recipients only
Private and Confidential	:	For disclosure to individuals directly concerned within the recipient's organisation
Commercial in Confidence	:	Not to be disclosed outside the recipient's organisation
GH only	:	Not to be disclosed to non GH staff
Client's Discretion	:	Distribution at the discretion of the client subject to contractual agreement
Published	:	Available to the general public

REVISION HISTORY

Issue	Issue date	Summary
1.0	06.05.2011	D3 Implementation Report: Time-Domain Analysis - Original issue (electronic version only)

CONTENTS

LIST OF TABLES

LIST OF FIGURES

EXECUTIVE SUMMARY

The present report (WG1 WP1 D3) describes the current implementation status of the wave energy converter (WEC) numerical modelling software being developed by Garrad Hassan and Partners Ltd. (GH) under the PerAWaT project. The report builds on previous deliverables, namely the Methodology Report (WG1 WP1 D1B) and the frequency-domain implementation report (WG1 WP1 D2), and details the core aspects and key functionalities of the developed code, with emphasis to the performance variables related to time-domain simulations.

The report is organised in nine sections which give a detailed overview of:

- The scope of the documents and its key objectives – Section 1;
- The architecture of the developed code, the core aspects of a multi-body dynamic solver and key time-domain implementation details – Section 2;
- The hydrodynamics module – Section 3;
- The wave analysis module and its functionality – Section 4;
- The moorings module and its functionality (exemplified via a case study) – Section 5;
- The power take-off (PTO) and control modules and their functionality – Section 6;
- The optimiser module and its functionality – Section 7;
- Case studies that outline initial results – Section 8;
- A summary of the key features implemented to date and planned extensions – Section 9.

As an overall summary, this report present the capabilities of the baseline software in a time-domain formulation, which were implemented following the 'Next steps' guidelines presented in previous PerAWaT deliverables. Using the frequency-domain implementation report (WG1 WP1 D2) as a starting point, this report begins by presenting background information regarding the GH multi-body code (Bladed) which is used as the kernel unit to describe the dynamics of the WECs. Under PerAWaT GH has developed a series of software routines that plug into the Bladed code, to allow the definition of a wide range of WECs. This new package (code named WaveDyn) can be considered a loads calculation tool which allows the reduction of the uncertainty in the estimation of the relevant (single WEC) performance variables and the definition of the parameterisation of the WEC behaviour in order to use this in the optimiser module (code named WaveFarmer).

Although the core structure is shared between the frequency- and time-domain formulations, and thus was originally presented in WG1 WP1 D2, it is important to recall the baseline structure in any summary attempt. The modules originally envisaged for the WaveFarmer code structure in the Methodology Report (WG1 WP1 D1B, Section 1) are now covered in the WaveDyn multi-body modelling approach, namely the 'FD', 'TD', 'Basic Controller', 'External forces code' and the 'Wave data loader'. The 'Basic Controller' and 'External forces code' blocks operate as the series of parallel multi-body Calculation Modules shown in the figure on the next page, whilst the FD and TD blocks are represented in the higher level WVStructure co-ordinating code. The wave data loader is one of the I/O routines in the Hydrodynamics Calculation Module. It is envisaged (although not implemented at this stage) that the Calculation Modules may be developed to give the user the option of replacing the core functionality of each with a DLL interface. WaveFarmer as a software package now refers purely to the array design code (and includes the Optimiser and Mapping blocks shown in WG1 WP1 D1B). WaveFarmer's ability to interact with WaveDyn is described in Section 7.

The multi-body dynamic solver provides a means of mathematically describing the structural forces within the WEC structure. All of the non-structural forces applied to the WEC, resulting from the hydrodynamics, PTO or moorings must be calculated separately in code modules parallel to the core code (MBCore). If the flexible nature of the multi-body structural approach, which allows a range of WECs to be defined and simulated, is to be maintained then a multi-body theme must be propagated throughout these applied force calculations. The hydrodynamic and mooring forces need to be calculated on a body-by-body basis and PTO calculations are associated with a particular joint in the multi-body structure. Furthermore, the separation between the structural and the non-structural code modules facilitates future updates to be developed and implemented on a case-by-case basis.

To summarise the above description, the complete software formulation for the WEC modelling code may be seen as a collection of parallel multi-body Calculation Modules, including MBCore (see the figure below):

- The geometrical/structural definition formulated using the MBCore code.
- A hydrodynamic definition containing the hydrodynamic information and force calculation functions for the wave activated bodies in the system (any wave activated structural body having a parallel hydrodynamic body containing its particular hydrodynamic properties).
- A moorings system built up from multiple mooring line 'bodies', each containing information on the line properties and attachment location on the geometrical structure.
- A PTO system containing information on the PTO properties and force calculation functions for any joint contributing to the energy capture of the device.
- A control system containing the control algorithm used to control / operate the PTO.

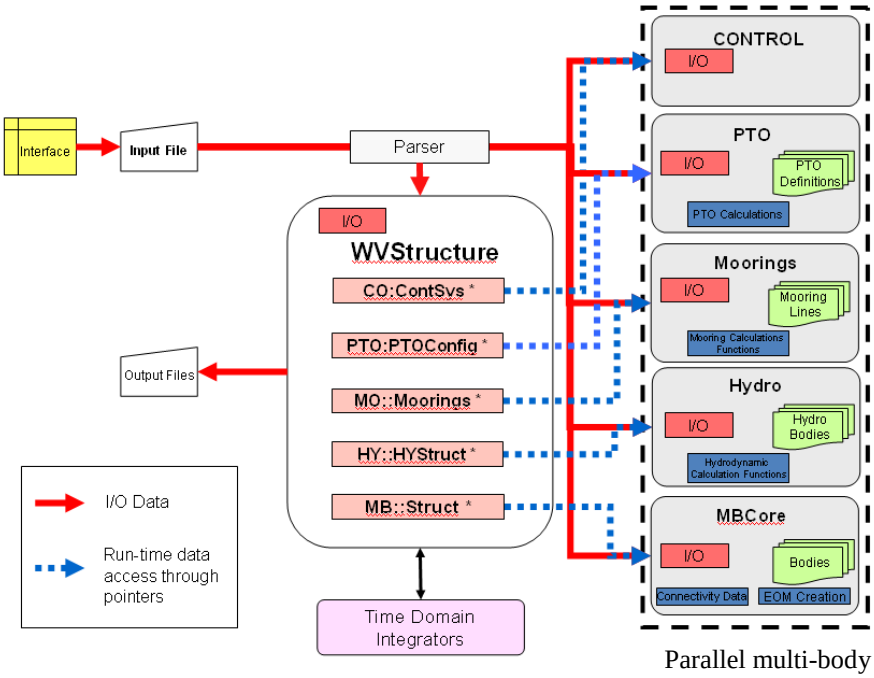

Parallel multi-body Calculation Modules.

The modular WaveDyn architecture

Each of these modules (apart from the MB core) was specifically developed (and will continue to be developed) under PerAWaT. The functionalities of each module are discussed in greater detail in the corresponding sections of this report. This includes also the optimiser module and the wave analysis module, which are not represented in the previous figure as these are outside the WaveDyn structure (the former is effectively the core WaveFarmer code and the latter is shared between WaveDyn and WaveFarmer).

The time-domain formulation allows a detailed characterisation of a WEC and / or an array of WECs. The description of the external forces (e.g. mooring force; PTO force), can be highly nonlinear, unlike the frequency-domain approach where these must remain linear (or be linearised) for the model to be valid. This more accurate description of the main subsystems results in a more computationally intensive model, which may lead to limitations regarding the number of WECs if restrictive computational times are applied. Nevertheless it is possible to consider such time-domain formulation as the target in terms of numerical accuracy.

It must be stressed that the current software structure is common to the frequency and time-domain models, and also suitable for coupling with the spectral-domain models developed under WG1 WP2. Synergies with the methodology developed in WG1 WP2 will also allow a spectral-domain representation of the fundamental device concepts (FDCs) via the core modules presented in this report. It is envisaged that such spectral-domain representation will allow the optimisation of large (100+ WECs) arrays of FDCs. The first direct consequence of sharing the core structure is that there are considerable synergies between this report (WG1 WP1 D3) and its frequency-domain equivalent (WG1 WP1 D2 Implementation Report: Frequency-Domain Model).

This has resulted in the use of some sections of WG1 WP1 D2 in this report, with the suitable adaptations and updates. The major differences are associated with the development and implementation of:

- The wave analysis module, namely the method for spectral fitting, accuracy of fitted spectra and the effect of the parameterisation on the energy yield);
- The moorings module, for which the baseline implementation now allows nonlinear applied loads to be considered (results for a case study using one of the FDCs are presented);
- The PTO and control modules, as in the time-domain the description of the external forces can be nonlinear (leading, e.g., to the first PTO template);
- The optimiser module, namely the integration with the time-domain solver (WaveDyn) and detailed investigation regarding aspects that affect the computational efficiency and both the layout and PTO optimisation.

When compared with the formulation presented in WG1 WP1 D2, it is in the above listed modules that most of the time-domain implementation effort is immediately clear, although changes to other modules (core and structural) were made. Such additional effort should not be neglected as it ultimately ensures that the user of the PerAWaT tools will be able to have a single interface irrespective of the formulation and details that his / her WEC (or array of WECs) model requires.

The initial results presented in this report show the baseline functionality of the code while exploring the potential of a time-domain formulation, namely the ability to apply nonlinear mechanically applied force profiles (e.g. PTO, moorings). In Section 8 the following aspects are covered in the case studies:

- The ability to define different FDCs with different characteristics;
- The influence of different wave input conditions in the response of the WEC;
- The influence of the array layout in the power absorption characteristics;

- The influence of the control of the PTO of each array element in the power absorption characteristics (by treating the array as a power plant).

Even though the results in Section 8 are preliminary, such case studies allowed the test of the functionality of each module and an effort was made to align these with the verification scenarios listed in WG0 D1. Furthermore, the core functionality and case studies here presented are also well suited for the configurations to be modelled experimentally under WG2. It is expected that this will ensure that comparisons related to initial results from different project partners (GH, UoOx and QUB) can be more easily made. However, and as listed in WG1 WP1 D1B, these cases should not be confused with a set of representative scenarios for which results will form part of the Beta testing specification and will be presented in WG1 WP1 D4 and D15 (versions A and B). Finally, the report is concluded with the presentation of immediate next steps that constitute the last series of implementation steps prior to the first Beta release (Section 9.2).

1 INTRODUCTION

1.1 Scope of this document

This document describes the implementation of the core modules of the wave energy converter (WEC) and wave farm modelling package in the time-domain. The primary objective of the numerical models developed under WG1 is to predict the performance of an array of WECs under different input conditions, multiple design constraints and for several objective functions. The core modules described in this report allow the design and optimisation of arrays of fundamental device concepts (FDCs) previously identified in WG0 D1. The time-domain model builds from the frequency-domain approach and allows more accurate descriptions of several core components, such as nonlinear description of the applied (external forces) associated with the moorings system and / or the power take-off (PTO).

As mentioned in WG1 WP1 D2, it should be emphasised that work on the core modules will occur throughout the course of the PerAWaT project. As a consequence the results presented in the implementation reports and those derived from all versions except Beta 2 should be seen as indicative of the model functionalities and not as verified or validated outputs. It is likely that the verification and validation exercises will assist the consortium (and GH in particular) in debugging the code and in identifying potential caveats of the actual formulation.

This report shares a common structure and some key sections with WG1 WP1 D2. It begins by presenting background information regarding the GH multi-body code (MBCore), which is used to describe the geometry and structural forces within WEC designs, in sufficiently flexible manner in order to model the different FDCs (Section 2). As described in WG1 WP1 D2, and given the necessity to develop a tool that is able to analyse any FDC in isolation including the loading environment and also a tool that is able to accurately predict the energy yield for a given array layout, two complementary software packages are now envisaged: WaveDyn, which can be considered a loads calculation tool and is designed to simulate the performance of a single WEC; and WaveFarmer, an optimiser module that evaluates the performance of a WEC in any given array position. The parameterisation of the WEC model and its individual environmental conditions allows WaveFarmer to use WaveDyn as an equation of motion solver. In WG1 WP1 D2 that parameterisation was limited to a frequency-domain model of each WEC; via the implementation described in this report a time-domain model of each WEC can be made. Further work will explore the potential of spectral-domain representation of WECs (WG1 WP2). The optimiser module (WaveFarmer) is fundamentally capable of using any of these models, i.e. it is agnostic regarding the solver.

An update of the specific software routines that have been developed and their interaction with the MBCore code is given in Section 2, and further detailed in the subsequent sections. In particular, and as in WG1 WP1 D2, the following modules are described in the sections mentioned below:

- Hydrodynamics – Section 3;
- Wave climate – Section 4;
- Moorings – Section 5;
- PTO and control – Section 6;
- Optimiser – Section 7.

In all these sections, the starting point is Section 9.2 (‘Next steps’) of WG1 WP1 D2, where the immediate extensions when considering the time-domain formulation were identified. Each individual

section is then further developed by presenting details related to the implementation of such extensions.

The report is concluded with two further sections. Firstly, in Section 8 the functionalities of the time-domain implementation are illustrated by presenting results for a series of cases studies. These refer to simulations where single FDCs and arrays of FDCs are analysed and their response to representative input conditions is quantified. Finally, in Section 9 the key functionalities of the software (at this stage) are summarised and the potential extensions detailed, for each individual modules.

1.2 Purpose of the time-domain model

The key objectives of the time-domain model described in this report are to allow:

1. the modelling of various FDCs (in isolation or in an array) under a wide range of input conditions;
2. the modelling of the external forces, namely the PTO and moorings forces, to a greater level of detail than that associated with a frequency-domain approach;
3. the completion of a core software structure, common to the frequency and time-domain models, and also suitable for coupling with the spectral-domain models developed under WG1 WP2.

The time-domain model allows a detailed characterisation of a WEC and / or an array of WECs. Unlike the frequency-domain approach, the description of the external forces (e.g. mooring force; PTO force), and the structural geometry (dictating the kinematics in response to these), can be nonlinear. Typically this leads to a more computationally intensive model, suitable for the detailed assessment of the performance of a WEC or an array of WECs. Some fundamental hydrodynamic properties obtained in the frequency-domain are still necessary, as the solution of the radiation and diffraction problems are still dependent (for an explicit model) on the use of a flow solver as described in WG1 WP1 D2. The core code and functionalities are shared between both the frequency and time-domain formulations (e.g. the optimiser module has the same key functionalities). Synergies with the methodology developed in WG1 WP2 will also allow a spectral-domain representation of the FDCs via the core modules presented in this report. It is envisaged that such spectral-domain representation will allow the optimisation of large (100+ WECs) arrays of FDCs.

As a direct consequence of objective 3 (listed above) there is considerable cross-over between this report (WG1 WP1 D3) and its frequency-domain equivalent (WG1 WP1 D2 Implementation Report: Frequency-Domain Model). This has resulted in the use of some sections of WG1 WP1 D2 in this report, with the suitable adaptations and updates. The key differences are associated with the description of the applied forces, and with the further development of the PTO, control and moorings modules.

Finally, it must be recognised that the implementation reports (frequency and time-domain) should not be confused with a theory or a user manual. Although there are more resemblances with regard to the draft theory manuals (WG1 WP1 D4a and D15a), both implementation reports are documents subject to further updates prior to the compilation of the Beta releases, as part of the ongoing verification and validation effort.

1.3 Specific tasks associated with WG1 WP1 D3

The tasks addressed in this report are:

1. Development of a time-domain numerical model aligned with the methodology and objectives defined in WG1 WP1 D1b.

2. Definition of a common software structure to be shared between the frequency and time-domain versions of the wave farm modelling package, including all the associated modules.

3. Compilation of a first series of representative results, to illustrate the core functionalities and typical outputs (allowing end-user feedback to be incorporated in the software releases).

1.4 WG1 WP1 D3 acceptance criteria

The acceptance criteria as listed in the Technology Contract and the sections of this report that demonstrate that they have been met are:

1. The report contains details of the model implementation of the previously defined methodology (WG1 WP1 D1b) in the time-domain to analyse arrays of FDCs in regular and irregular waves (such that it could be replicated by a third-party) - Sections 2 through 7.
2. Initial results related to the influence of several design variables (FDC, wave climate, array layout, control of the PTO for each array element, …) are presented - Section 8.
3. A detailed description and assessment of the performance of different FDCs and PTOs will be included – Sections 6 and 8.
4. Implication for the further model development activities are discussed - Section 9.

2 WAVEDYN CODE ARCHITECTURE

2.1 Overview of the implementation: the need for multi-body modelling

As highlighted in WG1 WP1 D2, the wave energy industry is currently at an infant stage, and no standard WEC type or design has yet emerged. This means that a variety of geometrical and internal system formats are currently under development. It is unclear whether the WEC designs will converge. As multiple WECs are now approaching a late pre-commercial development stage, a WEC performance and loading simulation tool designed to service the industry as a whole must operate to some extent in a multi-body format, as this is the only viable approach to model WECs with different configurations (type of FDC, number of bodies, etc).

A multi-body simulation concept allows a wide range of engineering systems to be modelled, using a single simulation tool, as a generalised collection of interacting components, or bodies. In a multi-body system each body only contains information about its own physical properties (and potentially also the nature of external forces applied directly to it) and serves as a building block for the generation of a complete multi-body structure using a generalised technique. A record of the connectivity between adjacent bodies allows forces or prescribed deflections, or any change that affects the system states – the minimum set of variables that wholly describe the system at a given instant in time – to be applied at one body and transmitted through the structure (in a structural sense, the states are the displacements and velocities of all the degrees-of-freedom, DOFs).

The key aspects of the formulation of the GH multi-body structural code are outlined in the following subsections. Some of these aspects are common in both the frequency and time-domain implementations, and as a results the multi-body software concept was initially introduced in WG1 WP1 D2.

2.2 WaveDyn calculation modules: MBCore and the applied force calculations

Developments in GH's wind turbine performance and loading software, Bladed, have in recent years stimulated the creation of an in-house structural multi-body formulation. The code, "MBCore", has experienced an extensive internal verification and validation procedure and has been developed as a stand-alone library that is discrete from the wind turbine specific Bladed modelling software, making it ideally suited to an expanded role as the geometrical and internal structural forces formulation in the WaveDyn WEC design tool. The application of the MBCore rigid body modelling capabilities, including structural connectivity and nomenclature, and coordinate system conventions, was described in detail WG1 WP1 D2. A summary of the structural coordinate system conventions has been included in Appendix A for reference. WaveDyn uses MBCore as a means to define a mechanical equation of motion for the system which may then be solved in the time-domain by a central WaveDyn integrator. At the start of each simulation, the WEC structure is built up by the WaveDyn parsing code as it reads in the structural information provided by the user. A validity check is carried out (ensuring the structure is not indeterminate or physically broken) before the structural equations of motion are formulated and information regarding the number of structural system states to be integrated is returned to the integrator code.

During simulation, the MBCore structure operates in parallel with a set of applied force calculation modules as shown in Figure 2.1. These include a hydrodynamic, moorings and PTO and Control modules. The modules each contain parallel multi-body structures, incorporating 'bodies' within which all of the information required to evaluate applied forces on their structural, MBCore counterparts are stored. At each integrator timestep, the applied force calculation modules may request kinematic structural information from MBCore and return loads to be applied to the structure so that the complete set of parallel multi-body structures may be solved over time by the central integrator.

The kinematic, loading and system integrator states information is transferred through a coordinating level of code, marked in Figure 2.1 as 'WVStructure', which also handles the transfer of the returned loads to the MBCore system.

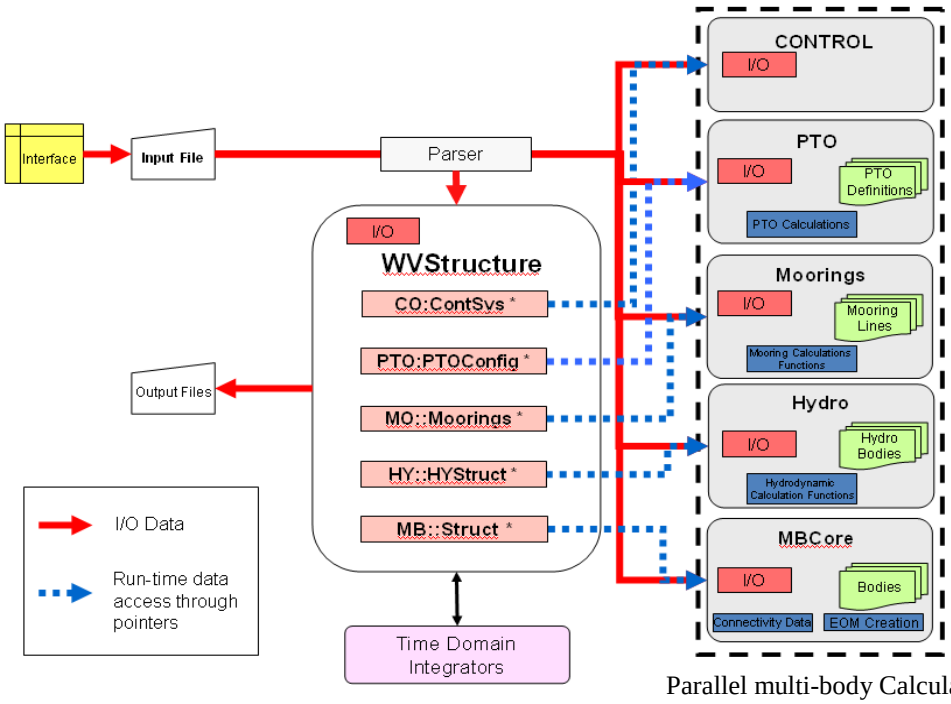

Figure 2.1. The modular WaveDyn architecture.

2.3 The time-domain numerical integration process

The WaveDyn code structure is designed for time-domain simulation, although the results may be later processed, in the case of linear models, to obtain frequency-domain results. Indeed, the time-domain integration process is the driving functionality behind the WaveDyn code architecture. The code operates with explicit integrators, which require the system to return the state derivatives as a function of a supplied set of state values. Some integrator algorithms require multiple state derivative calculations to be completed at each simulation timestep, passing the system a different set of *intermediate* state values in each call and using the state derivative values returned by the system to calculate a *final* set of state values for the timestep; these are the values that are saved as the simulation results before the simulation advances to the next step. Other, multi-step integrators may rely on state values for multiple past timesteps for the calculation of future timestep states. Variable timestep integrator algorithms adjust the timestep size dynamically based on the magnitude of the state derivative values, so that periods where the system dynamics are fast can be more accurately captured. The WaveDyn code has been designed to support a range of integrators, potentially requiring intermediate state calls and variable timestep functionality. Implicit integration algorithms are not currently supported, however later developments to WaveDyn requiring the solution of numerically stiff systems could result in their inclusion in the future. The calculation modules would not need to be modified significantly for this to occur, but the integration algorithm would need to incorporate an

iterative numerical root-finding algorithm (such as a Newton-Raphson implementation) to allow the integrator to rapidly converge on a consistent set of next timestep system states.

The integrator is designed so that it may operate on states used in the calculations completed by any one of the calculation modules. These may be the freedom displacements and velocities in the case of MBCore, or internal PTO states, such as accumulator charge, to potentially states describing the mooring dynamics or hydrodynamics. At the start of the simulation, the integrator makes an initialisation call, which queries all of the active calculation modules for states. The calculation module structures analyse their systems and return the initial state values as well as any integration process tolerances to the integrator, receiving a reference index for the state positions in the complete integrator state list. On subsequent timesteps, the integrator code calls a function in each of the calculation modules that returns the indices of the states that module requires. The appropriate state values are then passed to the calculation module so that it may evaluate loads or motions (using the CalcStateDevs functions in the case of the applied force modules) and return the state derivatives to be used in the integration algorithm. The applied force calculation modules require additional, kinematic data from MBCore to complete the load calculations and so this is provided alongside the necessary integrator state values. The overall process was described briefly in WG1 WP1 D2 and is illustrated by Figure 2.2. Note that the control module acts on the system through the PTO and so has not been included in the diagram. It is possible for internal control states to exist in the control calculation, in which case these would be processed directly by the integrator as well.

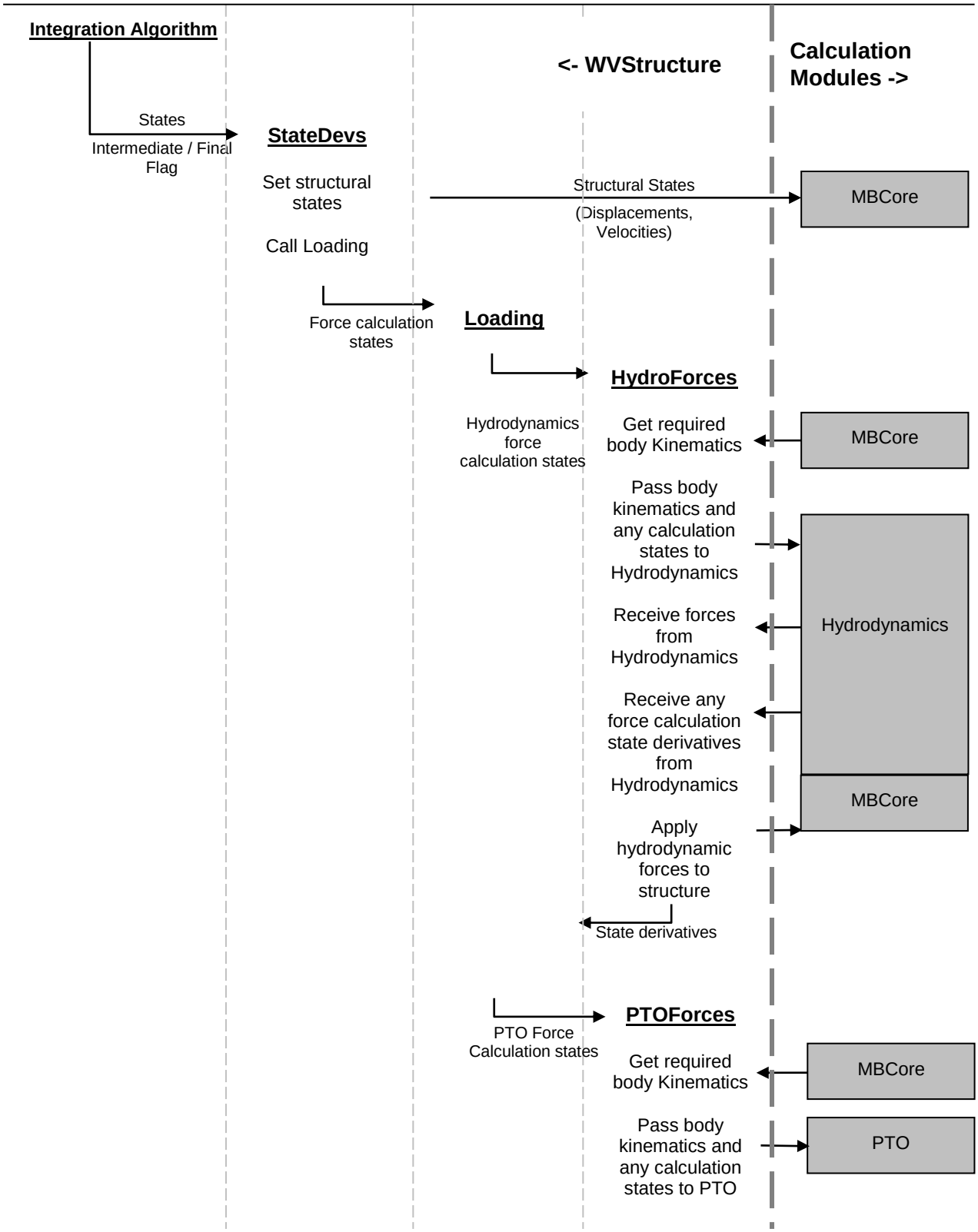

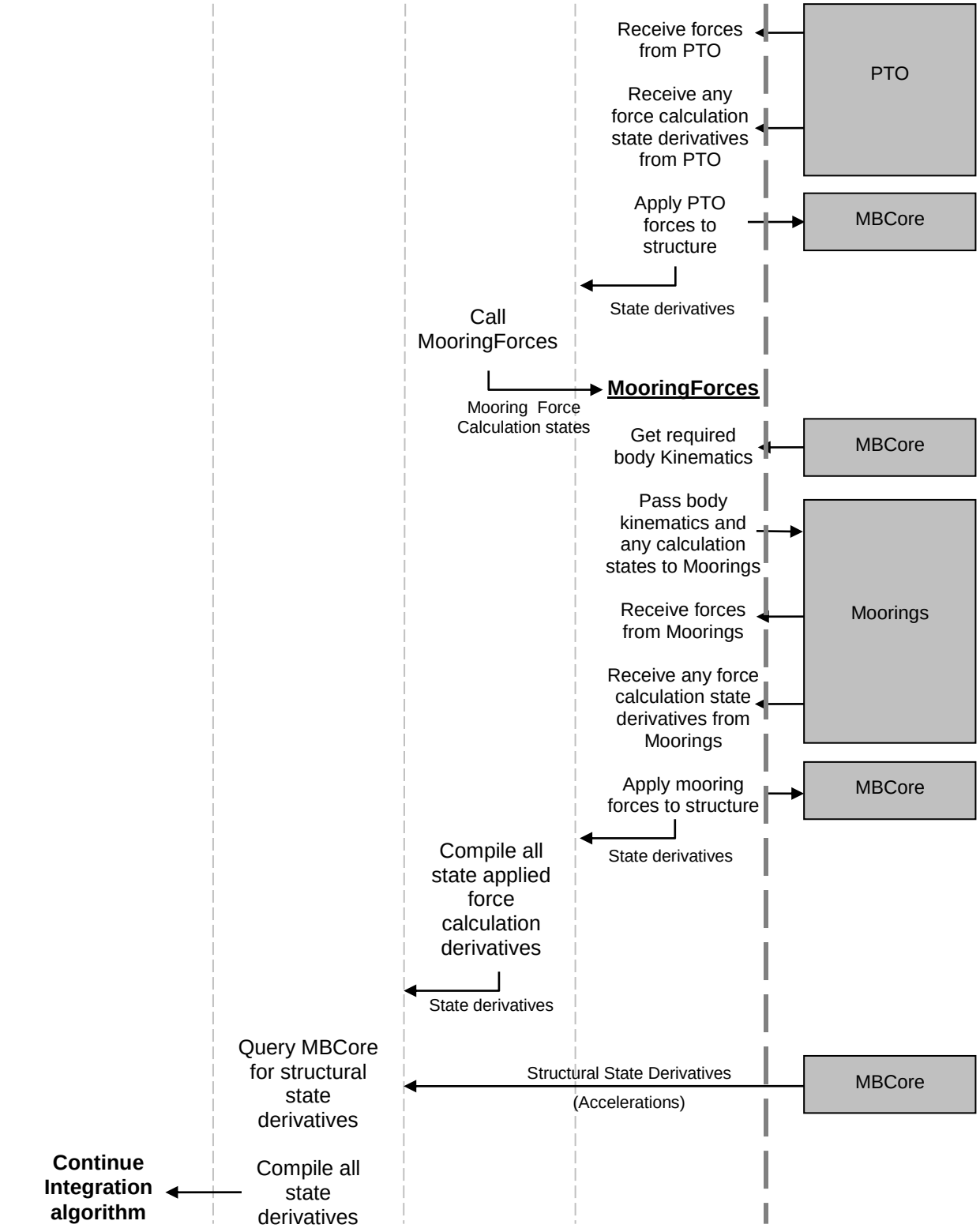

Figure 2.2. The State Derivatives Calculation Process in WVStructure.

2.4 Input data handling

Apart from the 'Interface' and 'Input' file blocks, the code illustrated in Figure 2.1 collectively constitutes what may be referred to as the WaveDyn *engineering code* executable. The engineering code is responsible for completing a user-specified simulation and writing the simulation outputs but is reliant on receiving a description of the WEC as an input file. The WaveDyn input file may take one of two alternative forms; the first of these is the '.IN' text file format that was described in detail in Section 2.7 of WG1 WP1 D2 and consists of blocks of body parameters marked by {BODY and }BODY tags as well as wave environment and simulation control information. The second input file type has been developed with recent work, performed outside PerAwaT, on a prototype WaveDyn graphical user interface (GUI), which writes a .xml format input file for the engineering code to parse.

The applied force calculation module input parameter data formats for the .IN file input option are described in Sections 3 and 6 and also in WG1 WP1 D2 as, without GUI support, this format is the more demanding for the user compile. The information contained in both .IN and xml input file formats is consistent however and a thorough description of the user input process using the WaveDyn GUI will be provided in the draft WaveDyn user manual under WG1 WP1 D4a / D4b.

A preliminary screenshot of the developmental WaveDyn GUI is presented in Figure 2.3 below.

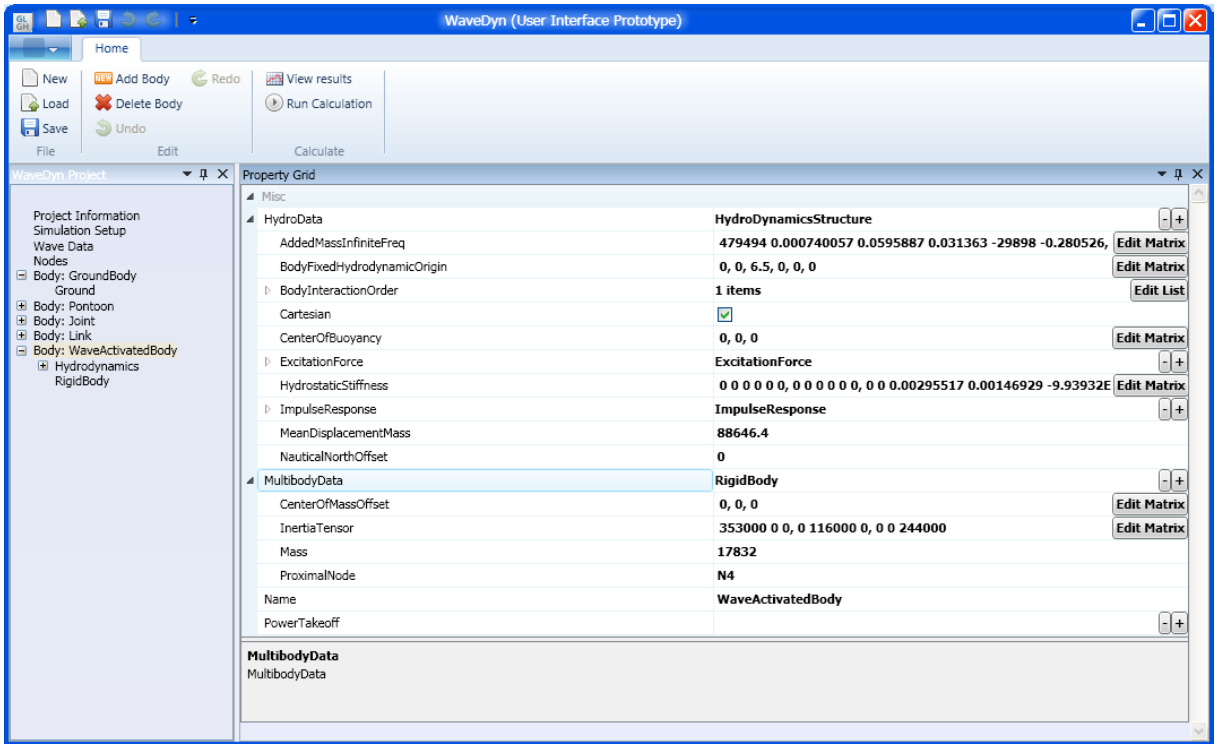

Figure 2.3. Screen-shot of the prototype WaveDyn GUI.

The GUI prompts the user to supply the compulsory set of simulation setup and wave data parameters and also supports the construction of the multi-body system structure through the addition of new bodies (notice the 'Add Body' and 'Delete Body' buttons on the ribbon bar) and connecting nodes. Hydrodynamic and PTO properties may be added to the bodies (the equivalent to incorporating <hy >hy and <pto >pto blocks in the .IN file) using specifically designed interface screens that support matrix and vector entry in the .IN file text format or in a graphical grid where data may be copied and

pasted from a spreadsheet or other cell-based interface (such as the MATLAB variable editor). A screen-shot of the matrix editing window is shown in Figure 2.4.

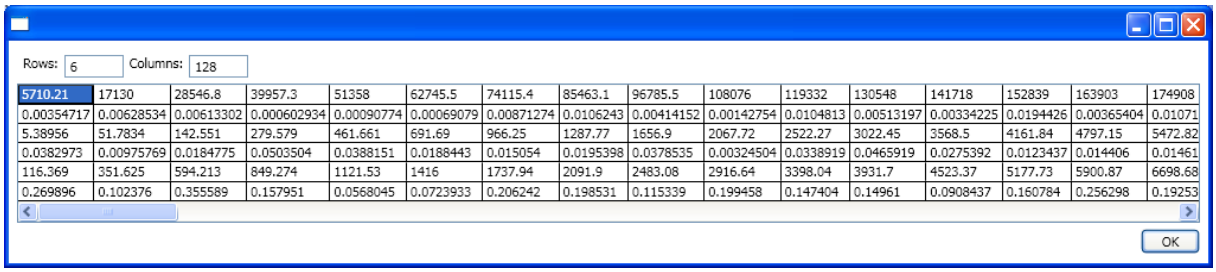

5710.21	17130	28546.8	39957.3	51358	62745.5	74115.4	85463.1	96785.5	108076	119332	130548	141718	152839	163903	174908
0.00354717	0.00628534	0.00613302	0.000602934	0.00090774	0.00069079	0.00871274	0.0106243	0.00414152	0.00142754	0.0104813	0.00513197	0.00334225	0.0194426	0.00365404	0.01071
5.38956	51.7834	142.551	279.579	461.661	691.69	966.25	1287.77	1656.9	2067.72	2522.27	3022.45	3568.5	4161.84	4797.15	5472.82
0.0382973	0.00975769	0.0184775	0.0503504	0.0388151	0.0188443	0.015054	0.0195398	0.0378535	0.00324504	0.0338919	0.0465919	0.0275392	0.0123437	0.014406	0.01461
116.369	351.625	594.213	849.274	1121.53	1416	1737.94	2091.9	2483.08	2916.64	3398.04	3931.7	4523.37	5177.73	5900.87	6698.68
0.269896	0.102376	0.355589	0.157951	0.0568045	0.0723933	0.206242	0.198531	0.115339	0.199458	0.147404	0.14961	0.0908437	0.160784	0.256298	0.19253

Figure 2.4. Matrix editing window in the WaveDyn GUI.

A user may use the GUI to save and load model definitions and call the engineering code executable to run the defined simulation by clicking on the 'Run Calculation' button; it is at this point that a .xml input file is written for the engineering code parser to read in as shown in Figure 2.1, although the .xml format is also used for the save and load operations.

2.5 Output data handling

2.5.1 Data collection and storage in the code

The WaveDyn simulation results are required to incorporate data calculated throughout the modular, multi-body code structure. Scope limitations inside the software mean that it is extremely useful to be able to save output data at the location where it is calculated, however it is equally the case that all output variables need to be tabulated in a consistent format and written in a coordinated manner. Repeatedly opening and closing output files to write small amounts of data is computationally expensive, advocating the argument for an output buffer approach and grouping of multiple output variables in a single output file. The format of the data written to disk must lend itself to graph plotting or post-processing codes and must accommodate the variability in the output data types, which may, in the case of vector and matrix data, have multiple dimensions.

GH have previously developed an output file format for wind industry applications, which is supported by existing graph plotting and statistical post-processing functionality for multi-dimensional data. The format is human readable, as long as the numerical data is printed in ASCII rather than binary format and also lends itself to use in post-processing tools based on e.g. MATLAB. The output file generation code embedded in the other software products is not easy to extract however, so whilst a final, well developed results file format is available for WaveDyn to use, all of the code required to generate the output has been developed separately under PerAWaT and is documented in full below. The code is much more flexible than the original pre-PerAWaT GH output generation code, embracing the modular, multi-body WaveDyn formulation so that additional outputs may be easily added as new features are developed.

WaveDyn simulations produce multiple output files, each containing data with a consistent set of dimensions. The data itself is stored alone (without headers or axes) in a file with an .$XX file extension on the simulation output path, where the "XX" is a two digit reference number. The output stream headings and axes for the data dimensions, as well as a general description of the data in the output group are provided a 'header file', which has a .%XX extension (the reference number matching the data file). The format of both file types is described below.

Each .$XX file may be considered a single, multi-dimensional group of data. The first dimension of the data group is always a list of variable names (such as 'Radiation Force', 'Excitation Force',

'Hydrostatic Force'), these are the data series streams available to view, whilst the subsequent dimensions describe the data (so the second might be 'Surge', 'Sway', 'Heave', 'Roll', 'Pitch', 'Yaw' and the third might be time or frequency). The first group dimension (the variable names) represent the columns in the .$XX data file, whereas the data dimensions must each be assigned an 'axis', which is defined by a self-contained block of parameters in the header file (see Section 2.5.2) containing ordinate values and unit type. The output data order within the columns in the .$XX files is subject to the size of the data dimension axes, but in the hydrodynamic forces example given previously, each time or frequency value is made up of six rows, one for each freedom. The subsequent six rows represent the next time or frequency. The data dimensions (and their axes) are defined once in the header (.%XX) file for all variables in the data group, so variables may only be grouped together in an output file/header combination if they have the same dimensions.

The multi-body nature of the simulation code means that the number of outputs produced by the simulation is not explicitly known at the code development stage (it is heavily dependent on the number of bodies in each of the multi-body calculation modules). Equally a user may wish to specify that some outputs are logged in the simulation but not others. If the output generation code is to accommodate this, it is convenient to once again adopt an object orientated approach. A set of data handling classes operating on four levels have been defined for the purpose in a dedicated output data project. The details of each are described in Table 2.1 below: The C++ project containing these files is visible to each of the Calculation Modules.

Class Name	**Functionality**	**Derived Classes**
GHIOAxis	Contains the axis information for a single data dimension. Each axis can be one of three types. Type 1 allows the axis to contain a list of tick-mark labels (such as Surge, Sway, Heave, Roll, Pitch,Yaw). Type 2 is an equally spaced numerical ordinate defined by a start value and a step size (the time ordinate for a fixed timestep simulation may fall into this category). Type 3 contains a list of numerical values that are not necessarily equally spaced (a variable timestep integrator simulation could more easily use this format, as can may a frequency spectrum ordinate where a finer resolution might be advantageous over a particular frequency range). The class contains member functions for adding data to Type 1 and Type 3 axes (called by GHIOSeries objects) and also for writing the axis properties data to a output header (.%XX) file.	None
GHIOSeries	Contains the recorded data buffer for a single output variable as well as pointers to the GHIOAxis objects describing the data dimensions. Member functions support the recording of new data values (which must be provided in conjunction with new axis data to ensure the axis and series dimensions match) and clearance of the recorded data so that memory is made available once the values have been written to disk. The data buffers can have a pre-allocated size in memory to speed up the recording of data as long as the data flushing (write to disk) interval is known (so that the size of buffer required can be calculated). The pre-allocation size is passed down from GHIOControl and updated if necessary every time a call is made to add a new value to the series. Memory pre-allocation is important for simulation speed as it prevents constant movement of the potentially large data buffers to new memory locations.	Three derived classes support recording of scalar, vector and matrix data.

GHIOGroup	Class to contain multiple GHIOSeries objects. The data from each GHIOGroup is written to disk on a single data (.$XX) file, with a corresponding header (.%00). Member functions provide functionality to flush all the GHIOSeries object data buffers, writing data to disk, and to write the header lines in the .% file. A call is made to the GHIOAxis objects through one of the GHIOSeries objects to write the axis header lines.	Three derived classes support scalar, vector and matrix GHIOSeries objects
GHIOControl	The top level class accommodates multiple GHIOGroup objects. Member functions support the addition of new GHIOGroups and allow an external code to instruct all GHIOGroup objects to flush their GHIOSeries data, or to write their header (.%XX) files. Memory pre-allocation for all GHIOSeries objects in the simulation may also be updated.	None. Accommodates a mixture of GHIOGroup types.

Table 2.1. Data output classes functionality.

Each calculation module contains a pointer to a GHIOControl object, to which it adds GHIOGroup objects as the bodies in its multi-body system are constructed (during the .IN file parse process). The GHIOGroup objects contain sets of GHIOSeries objects, one for each body variable being reported. The GHIOGroup object ensures that all of the GHIOSeries objects it contains point to the same GHIOAxis objects describing their data dimensions. Both the GHIOSeries and GHIOAxis objects designed to report data from a body are created by the body constructor functions, which are called before the new body GHIOSeries are compiled to form a GHIOGroup in the GHIOControl object.

In the WaveDyn formulation, the GHIOControl pointers in each calculation module are set to a single GHIOControl object on the memory heap (the only object of this type). This allows the WVStructure co-ordinating code to control how the output files for all of the GHIOGroups are written, by calling the GHIOControl object member function. At the lower end of the formulation, the GHIOSeries objects are directly accessible by the mathematical functions in the bodies in the Calculation Modules, making it easy to add new values as they are calculated.

2.5.2 Output format: the output header (.%XX) file

The GH output format header files contain a series of parameter – value sets in the order described in Table 2.2.

Variable Name	Type	Valid Range	Description	Notes
FILE	String	-	Corresponding .$XX data file path and name.	
ACCESS	String	D or S	Data in the .$XX file is in: D = Binary format S = ASCII format	Always ASCII in WaveDyn.
FORM	String	F or U	Formatted/ Unformatted	Not used by WaveDyn.
RECL	Integer	2,4,8	Record length for binary files	Not used by

				WaveDyn.
FORMAT	String	I*2, I*4, R*4, R*8	Variable type for binary files. The * may be omitted.	Not used by WaveDyn.
MISSING	String		Value denoting missing data	Not used by WaveDyn.
HEADREC	Integer	>=0	No. of bytes at start of binary file, or no. of lines at start of ASCII file, which are used to store header information rather than numerical data.	Not used by WaveDyn – no header names are stored in the .$XX file.
CONTENT	String		Description/source of data	
CONFIG	String	type of data	e.g. STATIONARY, TRANSIENT, TABLE, etc.	All WaveDyn data is STATIONARY.
NDIMENS	Integer	1 - 5	The number of dimensions of the data file. The first dimension is used for defining the number of distinct variables within the data file (the number of GHIOSeries objects in the group).	
DIMENS	NDIMENS integers (whitespace separated)	>0	The number of elements in each dimension. Potentially, each element of the first dimension can have different units and a different description. The last dimension is used for the independent variable	
GENLAB	String	-	Label that describes the whole of DIMENS[1]	Just as additional information.
VARIAB	DIMENS[1] Strings (whitespace separated),	-	List of variable names for each variable represented in DIMENS[1]. Separated by spaces, names containing spaces to be enclosed in single quotes.	
VARUNIT	DIMENS[1] Strings (whitespace separated),	See list in Table 2.3 below	List of units for each variable represented in DIMENS[1].	
VAROFFSET	Double precision, floating point.	-	Recorded data value (in SI units) = VARSCALE*(V - VAROFFSET)	Optional, default = 0
VARSCALE	Double precision, floating	-	where V = Value in file	Optional, default = 1

	point.			

FOR d = 2 to NDIMENS (For each data dimension axis. These lines are written by GHIOAxis)

AXISLAB	String	-	Label for the variable represented by DIMENS[2] (in single quotes if it contains spaces)	
AXIUNIT	String	See Table 2.3.	Units for the variable represented by DIMENS[2] as in table below.	
AXIMETH	Integer	1,2,3	Axis Type as described in Table 2.1: 1 = list of labels 2 = Start value and step (for regularly spaced values) 3 = list of values	

IF AXIMETH = 1 (Axis Type 1 – as described in Table 2.1)

AXITICK	List of strings, DIMENS[d] long.	-	List of axis tick mark labels	

ELSE IF AXIMETH = 2 (Axis Type 2 – as described in Table 2.1)

MIN	Double	-	Start value	
STEP	Double	-	Step size	

ELSE IF AXIMETH = 3 (Axis Type 3 – as described in Table 2.1)

AXIVAL	List of Doubles, DIMENS[d] long. Whitespace separated.	-	List of values	

END IF

END FOR

Table 2.2. Output header file parameter-value combinations.

The ‘unit’ parameters described in Table 2.2 can be set to any one of the parameter strings described in Table 2.3 below.

Label	Meaning	Label	Meaning	Label	Meaning
L	Length (m)	FLL		-	No units
L/T	Speed (m/s)	FLTT/AA		N	No units

A	Angle (rad)	T	Time (s)	FL/L	
A/T		1/T		LLL	
M	Mass (Kg)	P	Power (W)	F/LL	
M/L		PT		LLL/A	
MLL		A/P		Q	Reactive power (VA)
F	Force (N)	A/PT		I	Current (A)
FL	Torque (Nm)	A/PTT		V	Voltage (V)
F/L		M/LLL		VI	
FL/A		M/LT			
FLT/A		L/TT			

Table 2.3. GH Output file unit strings.

An example output file header produced by WaveDyn is given in below

```
FILE      TestPowprod.$04
ACCESS    S
FORM U
RECL 4
FORMAT    R*4
CONTENT   Float-MB
CONFIG    STATIONARY
NDIMENS   3
DIMENS    2    6    4000
GENLAB    Float-MB
VARIAB    'Global Position'  'Global Velocity'
VARUNIT   L    L/T
AXISLAB   'Freedom'
AXIUNIT   -
AXIMETH   1
AXITICK   'Surge'   'Sway'    'Heave'   'Pitch'   'Roll'    'Yaw'
AXISLAB   'Time'
AXIUNIT   T
AXIMETH   2
MIN       0.0
STEP      0.01
```

Figure 2.5. An example WaveDyn output file header (.%XX) file.

2.5.3 Output format: the output data file (.$XX)

Data is written to the output data file (.$XX) as columns. There are DIMENS[1] columns, one for each GHIOSeries in the group. The data in the rows is then written in sequential order, one dimension at a time, so for a frequency spectrum of vector data, where the DIMENS[2] dimension is the vector size and DIMENS[3] is the frequency ordinate, the first DIMENS[2] rows will be together represent the first frequency value and the next DIMENS[2] rows will represent the next frequency value, and so on until the end of the data is reached. This arrangement is illustrated by the examples below:

Example 1:

Header lines:
```
NDIMENS = 3
DIMENS  = 4, 3, 2
```

The data has the form (where "A312" represents the value at the third position in the first dimension, the first position in the second dimension and the second position in the third dimension):
```
A111 A211 A311 A411
A121 A221 A321 A421
A131 A231 A331 A431
A112 A212 A312 A412
A122 A222 A322 A422
A132 A232 A332 A432
```

Example 2:

Header lines:
```
NDIMENS = 2
DIMENS  = 2, 3
```

The data has the form:
```
A11 A21
A12 A22
A13 A23
```

When the first dimension only has a size of 1 (there is only one output variable in the group – so only one GHIOSeries object in the GHIOGroup object for which the outputs are being generated), then the format takes an alternative form to make better use of the space available in the output file. If the header file lists three dimensions (the GHIOSeries are storing vector values over perhaps a time history or frequency spectrum), then the second dimension is typically small (the number of vector elements) and is denoted by the separate columns in the data file; whilst the third dimension (which is typically large – the time or frequency ordinate) is represented by the rows, as shown in Example 3 (in this case the third dimension is not large, having a size of 3 only):

Example 3:

Header lines:
```
NDIMENS = 3
DIMENS  = 1,5,3
```
- Note the 1 as the size of the first dimension

The data has the form:
```
A111 A121 A131 A141 A151
A112 A122 A132 A142 A152
A113 A123 A133 A143 A153
```

If the first dimension only has a size of 1 and the header file lists just two dimensions (so the GHIOGroup contains a single GHIOSeries of scalar data recorded over, perhaps time or frequency), then the second dimension is typically large and so the data is stored as a single column as shown in Example 4 (where once again, the second dimension is not actually large, having a size of 6 only).

Example 4:

Header lines:

```
NDIMENS = 2
DIMENS  = 1,6                 - Note the 1 as the size of the first dimension
```

The data has the form:

```
A11
A12
A13
A14
A15
A16
```

This format is designed to ensure that the data files contain many rows rather than many columns.

All data is written to the output data files in standard index form with six decimal places (seven significant figures) and an exponent.

2.5.4 Post-processing functions

The GUI incorporates the GH 'Data View' results plotting and tabulation tool, which allows a user to browse for a completed WaveDyn simulation and view the output data, either in graphical format (many of the plots shown in Sections 6, 7 and 8 have been produced in Data View) or in tables displayed on screen or exported to an text or Microsoft Excel file. The Data View facility reads the WaveDyn output header and data files and is shared with the Bladed wind turbine modelling software, which has lead to the development of more advanced features allowing the user to switch between multiple unit types (such as radians or degrees) and to rapidly produce multiple plots or compute a set of basic statistics on a simulation time-series. A screen-shot of the Data View window is shown in Figure 2.6.

Use of the existing GH output file format means that an additional, statistical data processing code, DTSignal can complete a number of more advanced statistical analysis operations on the output data. This may form a template for WaveDyn's more advanced, future post-processing tools; however the WaveDyn version will contain more wave specific processing operations.

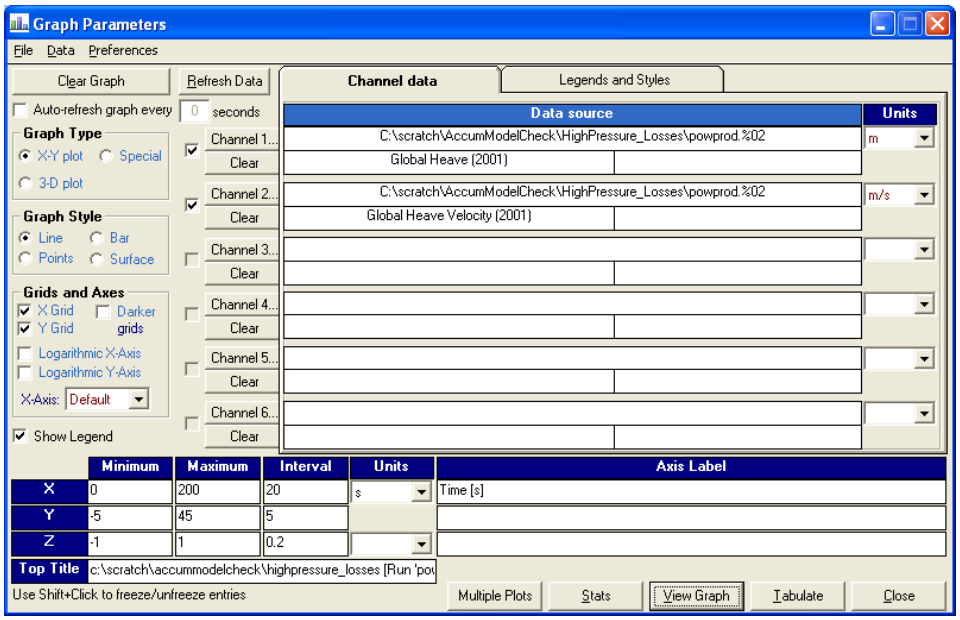

Figure 2.6. The Data View Graphical User Interface Window.

3 HYDRODYNAMICS MODULE

3.1 Overview of the development strategy: key theoretical aspects

In the time-domain, the hydrodynamics module is required to evaluate the excitation, radiation and hydrostatic forces acting on each wave activated body in the system and return a set of resultant forces to be applied at particular locations in the WEC structure. It is useful to refer to the time-domain equation of motion for a single body under wave loading in the form described in detail in WG1 WP1 D1b, reproduced below for convenience.

$$\left(m_m + m_r(\infty)\right)\ddot{x} + f_{hs}(x) + \int_{-\infty}^{t} k(t-\tau)\dot{x}(\tau)\, d\tau = f_e(t) + f_{ext}(x, \dot{x}, ..., t) \qquad [3.1]$$

The structural elements of the equation of motion are compiled by the MBCore Calculation Module, so that in reality the equation of motion is solved by WaveDyn for the complete system in an expanded, more generalise form; however on an individual body basis, the hydrodynamic forces in terms of a constant, infinite frequency added-mass, a hydrostatic stiffness, a radiation force convolution and a wave excitation force are applied in the format indicated. The constant added-mass at infinity values for the wave activated bodies, $m_r(\infty)$, may be added directly to the MBCore structure at the beginning of the simulation and so the task in the Hydrodynamics Calculation module is to evaluate:

- the excitation force, $f_e(t)$;
- the radiation convolution term, $\int_{-\infty}^{t} k(t-\tau)\dot{x}(\tau)\, d\tau$, and
- the hydrostatic force, $f_{hs}(x)$ which is a linear stiffness term if a water-plane area is assumed constant (for the case for a linear formulation),

for each wave activated body in the system. Note that interactions between adjacent bodies means that the velocities vector, $\dot{x}(\tau)$ is comprised not just of the velocity components for the body in question, but also those of all of the surrounding bodies and the impulse response functions matrix, k contains cross-terms for these accordingly.

3.2 Data formats and co-ordinate systems

The user is responsible for supplying the hydrodynamic data for the wave activated bodies. The WaveDyn engineering code executable is designed to read input data from both a .IN text file, the format introduced in WG1 WP1 D2, and an .xml input format written by the graphical user interface (GUI), under development for the first Beta 1 release – see Figure 3.1. The actual input parameters and numerical quantities themselves are the same regardless of the format and a complete, updated list of the hydrodynamic inputs required by WaveDyn is given in Table 3.1 below. A complete set of data must be provided for each wave activated body in the system.

Table 3.1. Hydrodynamics Force Calculation Data .IN File Parameters.

WaveDyn Hydrodynamic Input Parameters			
Input Parameter Name (as presented in the .IN file)	**Data Format**	**Parser Dependencies**	**Description**
`-Morrison 0+BEM`	Integer Value. ≥ 0 : Boundary Element Method Body <0 : Morrison Element Body (not currently supported)	None Parameter is compulsory, even though it is currently redundant.	Simple Flag. Morrison element data is not currently supported; all bodies must be modelled using a Boundary Element Method (BEM) flow solver data.
Radiation Force Data			
`BodyInteractOrder`	Vector of N strings. N is the total number of wave activated bodies in the system.	None Compulsory	Describes the order in which the inter-body cross-terms appear in the `AddMassInf` and `IRFData` matrices
`AddMassInf`	6x6N Matrix – Added mass and moments of inertia about the body centre of mass. Includes inter-body cross-terms.	None, Compulsory	Added masses and moments of inertia at infinity
`ImpResAvailable`	Integer Value >0 – Impulse response function data provided ≤ 0 – Impulse response function not provided	None, Compulsory	If the impulse response function is not provided it may be calculated from the radiation damping data, however this is not currently supported.
`NumRDampFreq`	Integer	None, Compulsory	Number of frequencies at which radiation damping data will be provided.
`RDampFreq`	Vector of `NumRDampFreq` elements. Each element is a double precision, floating point number.	Read if `NumRDampFreq` > 0 Otherwise parameter should be omitted.	Frequency ordinate of radiation damping data.
`RDampMat`	`NumRDampFreq` 6x6 Matrices. Each new matrix must start on a new line. New lines	Read if `NumRDampFreq` > 0 Otherwise parameter should be omitted.	Radiation damping data. Matrix format is Surge, Sway, Heave, Roll, Pitch, Yaw.

	mid-matrix may still be used instead of a "," to mark a new row.		
IRFEqualTimeSpace	Double precision floating point number. Impulse response function time ordinate is equally spaced, by this amount if >0. <0 – Spacing is uneven.	Read if ImpResAvailable > 0 Otherwise parameter should be omitted.	Equal spacing of the time ordinate speeds up interpolation of the data during evaluation of the radiation forces convolution integral at run-time.
NumImpResTimes	Integer	Read if ImpResAvailable > 0 Otherwise parameter should be omitted.	Number of time values in the impulse response function time ordinate.
IRFTimes	Vector of NumImpResTimes elements. Each element is a double precision, floating point number.	Read if ImpResAvailable > 0 Otherwise parameter should be omitted.	Impulse response function time ordinate.
IRFData	NumImpResTimes 6x6N matrices. Each new matrix must start on a new line. New lines mid-matrix may still be used instead of a "," to mark a new row.	Read if ImpResAvailable > 0 Otherwise parameter should be omitted.	Impulse response function data. Includes local body and inter-body cross-terms in column-wise the order specified by BodyInteractOrder.
IRFCutTime	Double precision floating point number.	Read if ImpResAvailable > 0 Otherwise parameter should be omitted.	Length of time-history used in the evaluation of the radiation force convolution for the body in question. Short time will speed up the simulation but will result in loss of accuracy.
MinConvInterval	Double precision floating point number.	Read if ImpResAvailable > 0 Otherwise parameter should be omitted.	The minimum time spacing between values stored in the convolution time history buffers. A short time reduces simulation speed, but improves accuracy.
Excitation Force Data			
NumExciteFreq	Integer	None, Compulsory	Number of frequency values in the excitation force frequency ordinate.
ExciteFreqEqSpace	Double precision	None,	Equal spacing of the

	floating point number. Impulse response function frequency ordinate is equally spaced, by this amount if >0. <0 – Spacing is uneven.	Compulsory	frequency ordinate speeds up interpolation of the data during evaluation of the wave excitation forces at run-time.
`NumExciteDirs`	Integer	None, Compulsory	Number of direction values in the excitation force direction ordinate.
`ExciteDirEqSpace`	Double precision floating point number. Impulse response function direction ordinate is equally spaced, by this amount if >0. <0 – Spacing is uneven.	None, Compulsory	Equal spacing of the direction ordinate speeds up interpolation of the data during evaluation of the wave excitation forces at run-time.
`-Naut 0+Cart`	Integer ≥ 0 : Direction ordinate provided in global cartesian angles. <0 : Direction ordinate provided in nautical angles.	None, Compulsory	Incident wave direction ordinate for the excitation force data. In WaveDyn, the positive global x-axis points South
`NorthACFromBodyX`	Double precision floating point number.	Only read if `-Naut 0+Cart < 0` (Nautical) Otherwise parameter should be omitted.	Cartesian angle of excitation force direction ordinate North axis, measured anti-clockwise from global X direction.
`ExciteFreqs`	Vector of `NumExciteFreq` elements. Each element is a double precision, floating point number.	None, Compulsory	Excitation force data frequency ordinate.
`ExciteDirs`	Vector of `NumExciteDirs` elements. Each element is a double precision, floating point number.	None, Compulsory	Excitation force data directions ordinate.
`Amp`	6 x `NumExciteFreq` Matrix. Each element is a double precision, floating point number.	`Amp` and `Phase` pair provided `ExciteDirs` number of times. `Amp =`	Excitation force amplitude data in Surge, Sway, Heave, Roll, Pitch, Yaw for a single direction, over

		Phase = Amp = Phase = … At least one set is compulsory.	the complete frequency range.
Phase	6 x NumExciteFreq Matrix. Each element is a double precision, floating point number.		Excitation force phase data in Surge, Sway, Heave, Roll, Pitch, Yaw for a single direction, over the complete frequency range.
PhaseOrigin	3 element vector. Each element is a double precision, floating point number.	None	The phase origin for the excitation data, $d_{g\phi}$. The third element should always be set to the water depth.
Hydrostatic Force Data			
MeanDispMass	Double precision floating point number.	None	The mass of water displaced by the body at its starting, equilibrium position.
HydStaticStiff	6x6 Matrix. Each element is a double precision, floating point number	None, Compulsory	Hydrostatic stiffness matrix for Surge, Sway, Heave, Roll, Pitch, Yaw.
CentreBuoyBodyFix	3 element (x,y,z) vector of double precision floating point numbers.	None	The position of the body centre of buoyancy relative to the hydrodynamic coordinates reference location defined by BodyFixedHyOrigin.
BodyFixedHyOrigin	6 Element vector of double precision, floating point numbers	None, Compulsory	Global position of hydrodynamic co-ordinates reference location.

A screen-shot of the hydrodynamic input parameters as they appear in the developmental WaveDyn GUI is shown in Figure 3.1 below. Note that at present the parameters are simply displayed on the interface screen in alphabetical order. When the user opts to run a calculation from the GUI, a .xml file containing the parameter names and values is written to disk so that it may be read in by the engineering code executable. The .xml input file is also copied to the simulation output location so that it may be referred to at a later date.

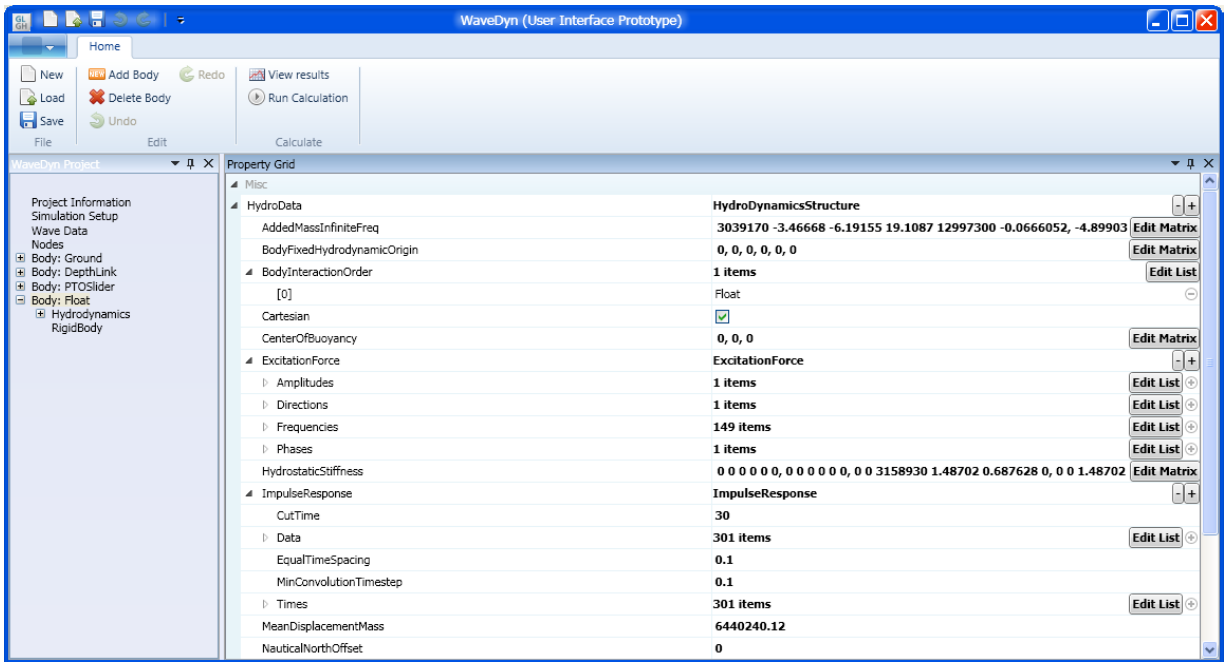

Figure 3.1. WaveDyn hydrodynamic input parameters, as displayed in the developmental GUI.

The hydrodynamic input parameters listed above must be calculated using a commercially available potential flow solver for all but the simplest of body shapes. A selection of these was reviewed in the methodology report (WG1 WP1 D1b, Section 3.4). GH have developed a set of MATLAB based processing scripts which convert outputs from the WAMIT flow solver to the WaveDyn input format. Similar scripts may be developed for other flow solvers by WaveDyn users or GH as necessary; the task consists of reformatting or reordering the data, so that it may be quickly entered into the WaveDyn user interface, and to dimensionalise the values where appropriate.

It is typical for potential flow solvers to provide hydrodynamic data for a body in a form that refers to the motion about a fixed reference position in global space. This is usually the body's static equilibrium position (in the absence of waves) and is provided in global coordinates as a user input to both the flow solver and to WaveDyn as the `BodyFixedHyOrigin` parameter. `BodyFixedHyOrigin` marks the position of the hydrodynamic coordinate system origin for the hydrodynamic force calculations and as such, incorporates a translational (X,Y,Z) location and a pitch, roll, yaw orientation for the hydrodynamic coordinate system axes. WaveDyn hydrodynamic force calculations for each body are completed relative to this equilibrium reference frame and so a set of coordinate system transformations must be applied to both the instantaneous MBCore kinematic data used as inputs to the calculations and the resulting force vectors that are returned. The transformations are described in detail in WG1 WP1 D2 and may also be found in Appendix B for convenience.

3.3 The multi-body hydrodynamics approach

The user may choose to define hydrodynamic properties for any rigid body component in the WaveDyn model and so the hydrodynamic force calculations need to be completed on a body-by-body basis. The hydrodynamics module is built on two levels to accommodate this, as shown in Figure 3.2. The lowest 'body' level contains multiple instances of a hydrodynamic body class, 'HYNodalBody'. Each of the HYNodalBody objects contains the hydrodynamic data for one of the bodies in the system and is constructed directly as the WaveDyn input files are parsed. The HYNodalBody objects are enclosed within a container object of 'HYStruct' class, the higher code level in the hydrodynamics calculation module. The HYStruct object operates as the interface for communication with the WVStructure coordinating code and incorporates a number of member functions designed to manipulate the HYNodalBodies list: ReadWaves and ReadHYData are the hydrodynamics module parsing functions for reading the user supplied flow solver coefficients and wave data and AddHYNodalBody adds a new HYNodalBody to the HYStruct, calling the HYNodalBody constructor.

On each simulation time-step, a HYNodalBody member function 'CalStateDevApprove' is called for each HYNodalBody in the system. This process is coordinated by a higher level HYStruct function, which ensures that loads are obtained for the entire system. CalStateDevApprove converts the global kinematic data for the body to hydrodynamics co-ordinate system referenced values and completes the excitation, radiation and hydrostatic forces calculations described in Section 3.4; a resultant force vector is then generated from the combined calculation results and converted back to global coordinates before being returned to the caller. The proximal node name of the body to which the hydrodynamic data is related is stored in the HYNodalBody object and also returned so that the forces may be identified by the coordinating WVStructure code and applied at the correct location on the MBCore structural model. The CalStateDevApprove function is common across the applied force Calculation Module 'body' level classes (see the PTO Module structural diagram, Figure 6.1) and may also return state derivative values for any internal calculation module states that need to be solved by the WaveDyn integrator. There are no such states in the case of the hydrodynamics module.

A specially designed return type class (not shown in Figure 3.2) has been defined to accommodate the force-proximal node combinations of data that are produced by the CalStateDevApprove functions in all of the applied force Calculation Modules, including Hydrodynamics, allowing the information to be returned to the HydroForces function in WVStructure in a coordinated manner.

Both HYStruct and HYNodalBody classes also include an 'InitialiseStates' function called at the start of the simulation. As previously mentioned, the hydrodynamics module contains no internal states to set up (unlike the PTO module – see Section 6), but may at this time complete any pre-simulation checks.

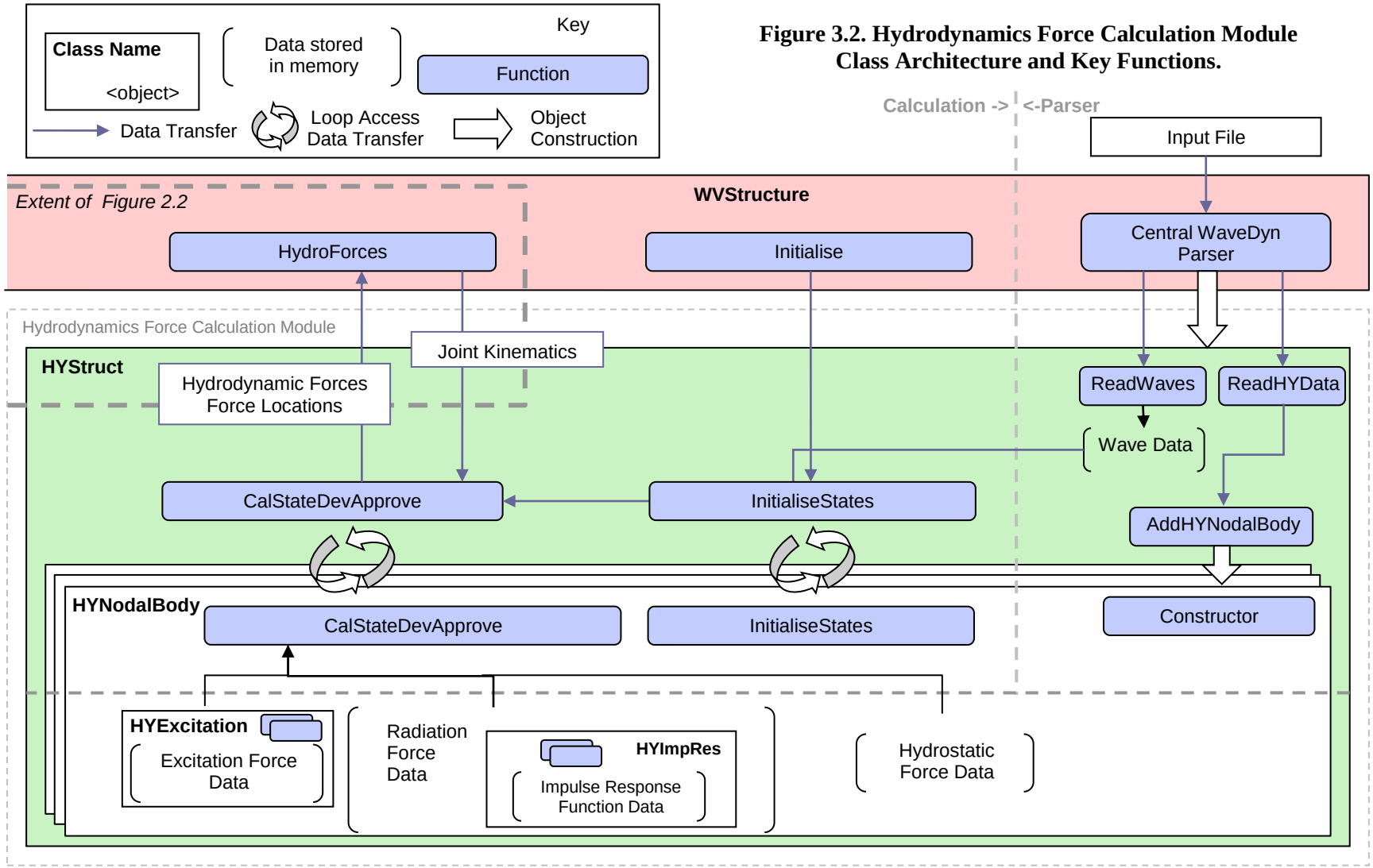

Figure 3.2. Hydrodynamics Force Calculation Module Class Architecture and Key Functions.

3.4 Force calculation algorithms

The HYNodalBody CalStateDevApprove function calculation process for each of the three main hydrodynamic force components is described in the sub-sections below.

3.4.1 Excitation force

The excitation force data read by the parser (see Table 3.1) is stored directly in an instance of a bespoke class built specifically to support the calculation process, HYExcitation. HYExcitation contains three-dimensional amplitude and phase information storage variables and the matching frequency and direction ordinates (the third dimension distinguishing between surge, sway, heave, pitch, roll and yaw data). HYExcitation object construction in constrained so that the calling code must first supply the frequency ordinate, before subsequently adding on 6 x Number of frequencies, amplitude and phase matrices in combination with a direction value. This arrangement allows the amplitude and phase matrix sizes to be checked to ensure values have been provided for the complete range of frequencies. The primary role of HYExcitation is embodied in a member function that may be called at any time to return two 6x1 vectors, representing the excitation force amplitude coefficient and phase data for a requested frequency and direction. This is useful in allowing the simulation code to loop through each of the wave frequency-direction components in the sea-state description, computing the excitation force contribution from each. Following linear wave theory, the component results are then summed to form an overall excitation force at time t as follows:

$$f_e = \sum_n f_{e,n} = \sum_n \Re\left(F_{e,n} e^{j(\omega t + \phi_n)}\right) \qquad [3.2]$$

where the complex excitation force amplitude, $F_{e,n}$ for wave frequency and directional component n has an amplitude that is equal to the product of the wave amplitude, A and the amplitude coefficient value determined by the flow solver, Γ (this is the value that is obtained from the `Amp` matrices). The complex amplitude phase, ϕ_e, is given directly by the phase data in the `Phase` matrices. ϕ_n is also a phase term, but is the wave component phase provided by the sea-state definition., so that for each wave component, the excitation force is calculated as:

$$f_{e,n} = \Gamma_n A_n \sin\left(\omega_n t + \phi_{e,n} + \phi_n\right) \qquad [3.3]$$

The calculation is completed simultaneously for each of the surge, sway, heave, pitch, roll and yaw direction contributions.

It may be that the wave frequencies and directions in the sea-state description do not match the values in the frequency and direction ordinates for the stored coefficient data (the user may choose to define a sea-state for the WaveDyn simulation with different frequency components than those used in the initial flow solver calculations); in this case, the HYExcitation class will need to complete a two-dimensional interpolation of the data (as an interpolation in frequency and direction may be necessary). The interpolation process may be thought of as consisting of two key parts:

1 A search to find the data values either side of the interpolation point;

2 The interpolation calculation itself.

As noted in WG1 WP1 D2, if a linear interpolation strategy is used then the calculation (point 2) is quick and simple, however the search process (point 1) can take potentially take large amounts of time

and it is important to employ a quick search algorithm as the sea-state definition may contain a large number of component frequencies and directions for which amplitude and phase data is required. A search can be avoided altogether if the user supplies the data with equally spaced direction and frequency ordinates, as specified by the ExciteFreqEqSpace and ExciteDirEqSpace parameters described in Table 3.1 (in which case the indices of the data values either side of the interpolation point can be calculated directly). If this is not the case, then, rather than simply looking through the frequency and direction ordinates sequentially, WaveDyn has been designed to search using a mid-point bisection method, where the required value is reached by sequentially halving the search range using a single comparison with the middle data value, as shown in Figure 3.3. The code has been written so that data may be supplied by the user with the frequency and direction ordinates in either ascending or descending order.

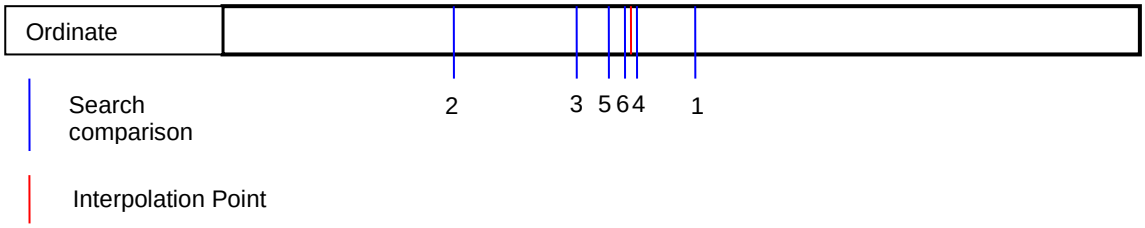

Figure 3.3. Mid-point bisection interpolation method. The first 6 search comparisons have been numbered.

Additional care must be taken in the excitation force phase interpolation process as it is likely that the user will supply the excitation force phase data in a 'wrapped' form, where the phase angles have been reduced down to a 2 π range. In this case, there may be a sudden jump in phase numerically as the angle switches from $+\pi$ to $-\pi$ or 2π to 0, as shown in the example set of data in Figure 3.4. Interpolation between these two points can lead to an erroneous phase value.

Two potential options are available to prevent this from happening:

1. Pass the data through an algorithm designed to 'unwrap' the data, adding or subtracting 2π to points when a jump is detected so that a smooth, continuous curve is created for interpolation.

2. Convert the amplitude-phase values for each frequency and direction into a complex amplitude term, with real and imaginary parts. Interpolate for both the real and imaginary components and then re-extract the amplitude and phase information.

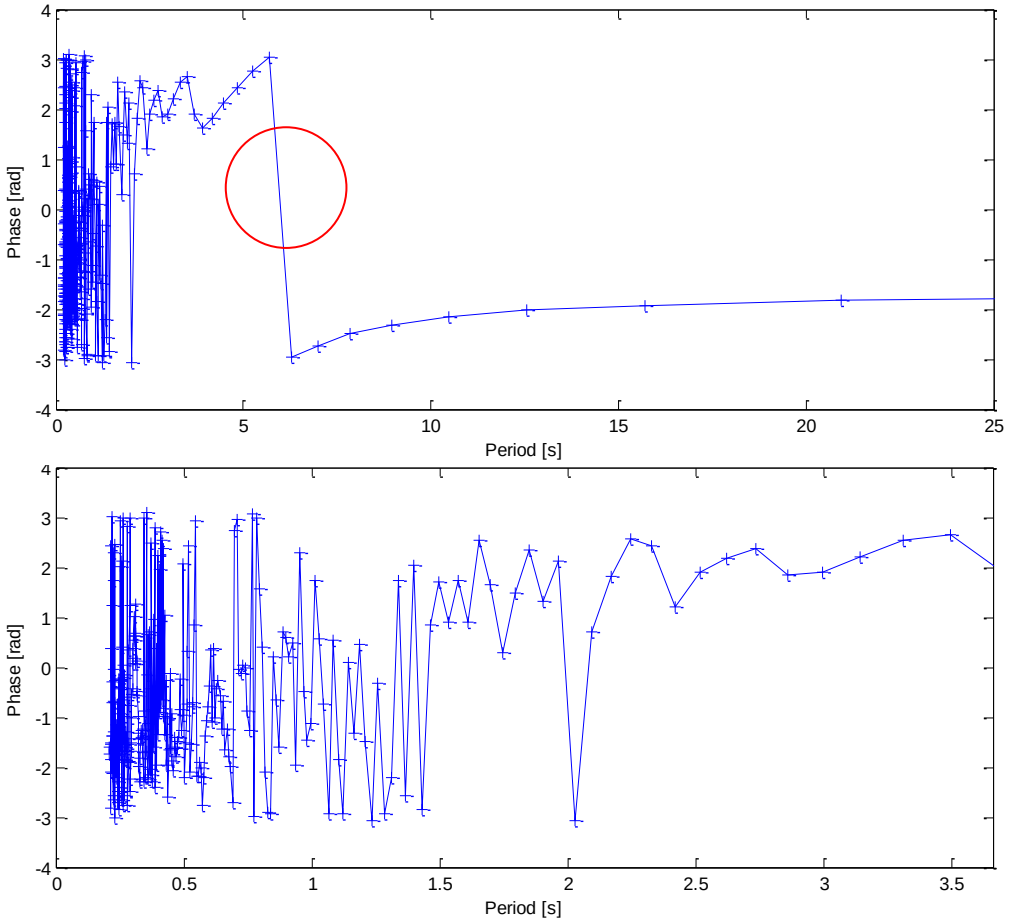

Figure 3.4. Typical excitation phase input data variation with wave period. The phase angle wrapping to ±π has created 'jumps' in the data, as highlighted by the red circle in the upper plot at a period of 6s. The lower plot focuses on the high frequency end of this data, where the phase jumps are more difficult to identify without a very fine frequency resolution because the phase changes very rapidly and the jump points are not resolved.

The first of the two options would produce the ideal platform for an accurate phase interpolation, however generating an effective unwrapping algorithm becomes difficult if the phase differences between points at consecutive frequency or direction values is large so that the step between values may encompass the jump and a large actual phase change either side of the jump, masking the presence of the jump itself. Even if the user enters data with a comparatively fine resolution, this is invariably the case at high wave frequencies, where the phase changes quickly (notice that at the low period end of Figure 3.4, the jumps in phase are not at all discernable).

The second method avoids the need to identify phase jumps, but still suffers from the periodic nature of the phase data at high frequencies, where the phases change quickly, as it reduces the interpolation to a process that may be compared with drawing a straight line between two points on a polar plot. As the phase change between two points approaches π radians, the interpolated result becomes increasingly misleading, as shown in Figure 3.5.

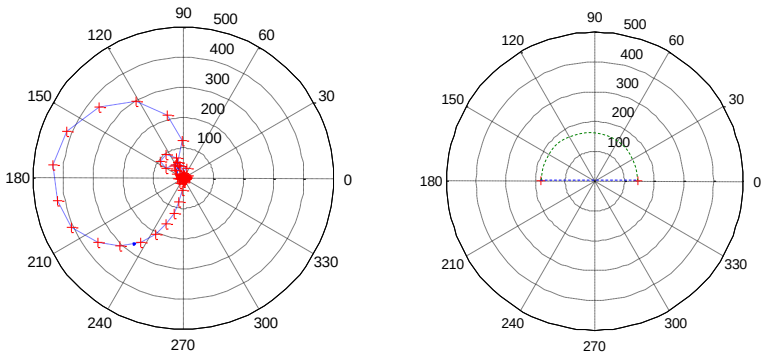

Figure 3.5. The real and imaginary part linear interpolation of the excitation force complex amplitude values is equivalent to drawing straight lines between points on a polar plot. This process is illustrated by the blue dashed line. This works well for points closely spaced in phase as is generally the case (shown on the left plot), but much less well if the phase difference between consecutive points is large, as illustrated by the two points in the right hand plot. In the large phase difference case, direct interpolation of the phase alone would produce a much more accurate result as indicated by the green dashed line. Unfortunately this method required the phase angle data to be correctly 'unwrapped' first.

Fortunately, most real wave climates contain little energy at very high frequencies where the interpolation accuracy breaks down and WECs are typically designed to be too heavy to respond significantly to such waves. Tests with an initial implementation using complex number interpolation appear reliable, even for coarse frequency and directions resolutions, for the wave components that are critical to the WEC response. Complex number interpolation was selected for the implementation over the phase unwrapping approach as it negates any need to determine an appropriate threshold level with which to identify phase wrapping jumps..

Rapid excitation phase change with wave frequency can also occur for bodies in the flow solver calculation that are placed a long way from the global origin, as a small frequency change leads to the propagation of an increasingly large phase difference with distance from the in-phase location (or origin). This can mean that even at frequencies as low as 0.1Hz, if the frequency step between excitation phase points is not very small and some of the bodies in the system are far from the origin, then excitation force data interpolation may become inaccurate. This additional, position related effect can be removed by subtracting a term quantifying the position related phase change contribution from the data points either side of the interpolation point, completing the interpolation process and then subsequently adding on the appropriate term to the interpolated result. The position related contribution is physically the wave phase lag at the body hydrodynamic coordinate system location (as defined by `BodyFixedHyOrigin`, d_{gHY}) relative to the origin for which wave phases are defined, $d_{g\phi}$ and may be calculated for any wave frequency and direction component as:

$$\phi_p = k\left(d_{gHY} - d_{g\phi}\right)^T \begin{pmatrix} \cos\theta \\ \sin\theta \\ 0 \end{pmatrix}, \qquad [3.4]$$

where θ is the wave direction and k is the wave number k, which may be calculated from the dispersion relationship (Tucker and Pitt, 2001), accounting for the water depth h:

$$\omega^2 = gk\tanh(kh) \qquad [3.5]$$

using a Newton-Raphson type root finding algorithm (this tends to converge very quickly as in practice the hyperbolic term is often very close to 1).

The remaining phase value in the excitation force data (once the position component has been removed) represents the phase difference between the waves acting on the body at the body location and the excitation force applied.

A user wishing to mitigate all of the potential phase interpolation inaccuracies described above may simply run the flow solver for exactly the wave frequency and direction components to which the device will be exposed, thereby bypassing the interpolation stage altogether. This may require a new flow solver calculation every time the simulation length (and hence surface-elevation repeat time) is changed for an irregular sea-state investigation (assuming the simulation is to maintain statistically representative), unless an initial flow solver run is completed with the finest frequency step size and the user limits themselves to repeat times that rely on integer multiples of this.

3.4.2 Radiation force

The radiation force calculation process involves a numerical evaluation of the radiation forces convolution integral, as discussed in Section 3.1:

$$f_r' = \int_{-\infty}^{t} k(t-\tau)\dot{x}(\tau)\, d\tau \qquad [3.6]$$

It is envisaged that the user may choose to either enter radiation damping matrices for a number of wave frequencies, in which case the Hydrodynamics calculation module will need to compute the impulse response function from these, or to provide impulse response function data directly. The latter option alone has been implemented in the core WaveDyn code at this stage, however impulse response function calculation code has been implemented in the WAMIT data processing MATLAB algorithms. Before this code is moved to WaveDyn it is important to add logic designed to check that the radiation damping data provided by the flow solver meets two criteria necessary to ensure that the impulse response function integral,

$$k(t) = \frac{2}{\pi}\int_0^{\infty} B_r(\omega)\cos(\omega t)\, d\omega \qquad [3.7]$$

is evaluated correctly (Equation 3.7 was derived in WG1 WP1 D1b, Section 3.3):

- The flow solver must be run for the full frequency range over which the radiation damping, $B_r(\omega)$ has significant non-zero amplitude; it is possible that this will be wider than the range of frequencies for which the device is actually responsive and so this requirement is not immediately obvious (particularly at the high frequency end). The integral in Equation 3.7 covers the full frequency range from 0 to ∞ so the radiation damping values at 1s still affect the time-domain device response to waves with a 10s or any other period.

- The frequency resolution requested for the flow solver outputs must be sufficiently high to prevent aliasing at the highest impulse response function time required (the impulse response function cut-off time). At large time values, t, the cosine term, $\cos(\omega t)$, varies rapidly with ω (the variation occurs with an 'frequency' of t rad/s/s) and so if the integral in Equation 3.7 is evaluated using these frequency points only then aliasing (and indeed even just a very coarse frequency resolution) can have a large affect on the integral value. The Nyquist criterion for the process is met if the frequency resolution, $\Delta\omega < \pi / t_{cutoff}$, where t_{cutoff} is the greatest time for which the impulse response function should be evaluated (and is passed to WaveDyn via the parameter `IRFCutTime` in Table 3.1). A greater resolution may still be advisable for improved accuracy, although at the high t values, approaching t_{cutoff}, where this is most important, the integral result is typically relatively small. Running the flow solver with such a frequency resolution can be time consuming but it is possible to fit a curve to the radiation damping distribution which can then be interpolated with a sufficiently fine range of frequencies.

Once the impulse response functions have been evaluated, they are passed to the core WaveDyn C++ code for use in the simulation calculations. As described in WG1 WP1 D2, a specifically designed data handling class has been created in WaveDyn to assist with the radiation force calculation process described by Equation 3.6. The HYImpRes class contains variables used to store the impulse response function data and member functions designed to read and write values to these variables during the input file parsing process (ensuring data is stored in ascending time order) and interpolate the impulse response function for a given time. The interpolation algorithm is analogous to that described for the excitation force coefficients in Section 3.4.1 above, with the IRFEqualTimeSpace parameter being used to determine whether or not the data is equally spaced. The data is interpolated in one direction only (time), returning a 6x6 surge, sway, heave, roll, pitch, yaw matrix of the approximate impulse response function values at the time requested.

Another member function in HYImpRes incorporates the convolution calculation itself. This final function requires a velocity time history (two vector containers, one storing past time-step velocity values, the other storing the times at which they were calculated) as its input and completes the convolution, in a matrix format (handling surge, sway, heave, roll, pitch and yaw values simultaneously), using a trapezium rule approximation. The current body velocity kinematic data is pushed on to the velocity time history at the start of the calculation so that the final time value stored in the time history vector is the current time, t. The convolution time parameter τ runs from the furthest point back in the time history (towards $-\infty$) to the current time, so a vector representing impulse response function kernel, $k(t-\tau)$, can be compiled by interpolating the impulse response function data at each $t-\tau$ combination provided by the discrete set of τ values. The $\dot{x}(\tau)$ vector is simply the velocity history, so a vector c containing the element-by-element products of the *N* values stored in each of the velocity and kernel vectors (where *N* is six times the number of wave activated bodies in the complete system, as described in Table 3.1) can now be compiled to contain the values to be used for the Equation 3.6 integration:

$$c[1] = k[1] * \dot{x}[1] \;\; ; \quad c[2] = k[2] * \dot{x}[2] ; \;\; \ldots ; \;\; c[N] = k[N] * \dot{x}[N] \qquad [3.8]$$

which is coded as the summation:

$$f_r{}' = \sum_{i=0}^{N-1} \left(0.5 * \left(T[i+1] - T[i]\right) * \left(c[i] + c[i+1]\right)\right) \qquad [3.9]$$

where T represents the vector of velocity history times and [ ] is used to denote access to a particular vector value.

The algorithm described above accommodates the use of variable time-step integrators which may mean that the velocity time history is not stored with equally spaced time intervals. Once the integration has been completed, a check is made to assess if the calculation is part of an intermediate integrator call, or a complete time-step result evaluation. If the call is intermediate, then the current velocity value, which is added to the velocity time history at the beginning of the hydrodynamic forces calculation, is removed again. This ensures that only complete time-step values have an effect on the force calculation in future time-steps.

3.4.3 Hydrostatic force

The time-domain calculations require a complete evaluation of all the hydrostatic and gravitational loads acting on each wave activated body in the system. The MBCore code is responsible for applying the gravitational loading, which for the rigid, homogenous bodies in WaveDyn is essentially a weight vector acting through the centre of mass, but all buoyancy related effects are embodied in the hydrodynamics applied force calculation module.

The total buoyancy force and moment on each submerged or semi-submerged body at its proximal node can be expressed as the surface integrals (Newman, 1977):

$$\underline{f}_b = -\rho g \iint_{S_B} \begin{bmatrix} \underline{n} z \\ \left(\left[\underline{d}_{HY} - \underline{d}_{HY\ BF}\right] \times \underline{n}\right)\ z \end{bmatrix} dS \qquad [3.10]$$

where the coordinate z represents the vertical offset from the body hydrodynamic coordinate system, $\underline{n}$ is the unit vector normal to the body surface, $\underline{d}_{HY}$ is the global position a point on the surface in the hydrodynamic coordinate system, and $\underline{d}_{HY\ BF}$ is the instantaneous position of the body proximal node in hydrodynamic coordinates. Note that $\underline{f}_b$ is a 6x1 element vector containing both force and moment terms.

Applying Gauss's theorem to Equation 3.10 yields the volume integral form:

$$\underline{f}_{b\_Surge,Sway,Heave} = \rho g \begin{bmatrix} 0 \\ 0 \\ \iiint_V dV \end{bmatrix} \qquad [3.11]$$

$$\underline{f}_{b\_Roll,Pitch,Yaw} = -\rho g \iiint_{V} \left[\nabla \times z\left(\underline{d}_{HY} - \underline{d}_{HY\ BF}\right)\right]\, dV \qquad [3.12]$$

where v is the instantaneous submerged volume.

Neglecting the second-order variation of the volume integrals as the submerged volume changes due to the instantaneous free-surface displacement from the $z = 0$ plane and maintaining the assumption of small body motions about the hydrodynamic origin, Equations 3.11 and 3.12 can be linearised to give (Newman 1977):

$$\underline{f}_b = \rho g \begin{bmatrix} 0 \\ 0 \\ V_0 - \underline{d}_{HY\ BF\,3} S + \underline{d}_{HY\ BF\,4} S_2 - \underline{d}_{HY\ BF\,5} S_1 \\ -\left(V_0\left(y_B + \underline{\theta}_{HY\ BF\,4} z_B - \underline{\theta}_{HY\ BF\,6} x_B\right) - \underline{d}_{HY\ BF\,3} S_2 + \underline{\theta}_{HY\ BF\,4} S_{22} - \underline{\theta}_{HY\ BF\,5} S_{12}\right) \\ V_0\left(x_B + \underline{\theta}_{HY\ BF\,6} y_B - \underline{\theta}_{HY\ BF\,5} z_B\right) - \underline{d}_{HY\ BF\,3} S_1 + \underline{\theta}_{HY\ BF\,4} S_{12} - \underline{\theta}_{HY\ BF\,5} S_{11} \\ 0 \end{bmatrix} \qquad [3.13]$$

where $\underline{\theta}_{HY\ BF}$ is the vector of roll, pitch and yaw rotations describing the instantaneous position of the body in the hydrodynamic coordinate system, V_0 is the mean displaced volume of the body and the vector $\left[x_B, y_B, z_B\right]$ is the position of the centre of buoyancy for the body, in the hydrodynamic coordinate system. Additionally, S is the body waterplane area in its static position and the waterplane moments are defined in hydrodynamic coordinates, $\left[x, y, z\right]$, as the following integrals over the static wetted profile:

$$S_j = \iint_{S_0} x_j\, dS \qquad j = 1,2 \qquad [3.14]$$

$$S_{ij} = \iint_{S_0} x_i x_j\, dS$$

In practice, the terms in Equation 3.13 that do not include the waterplane area and moments may be evaluated in a more general sense in WaveDyn simply as a constant buoyancy force in the case of $\underline{f}_{b3}$ and the cross-product of this value and the instantaneous position vector describing the position of the centre of buoyancy, relative to the proximal node in the hydrodynamic coordinate system for the moment values. The value of this position vector is found by rotating `CentreBuoyBodyFix` using the instantaneous body position. The value of `CentreBuoyBodyFix` and the waterplane area and moment terms are extracted from the flow solver output. In the waterplane area and moments cases these are typically provided as stiffness values which may then be applied to the instantaneous body displacement in the hydrodynamic coordinate system, $\underline{d}_{HY\ BF}$, $\underline{\theta}_{HY\ BF}$. The precise format of the hydrostatic stiffness matrix produced by the flow solver must be known in order to do this as frequently some of the additional linearised terms given in Equation 3.13 and some weight-related components (which are handled by MBCore in WaveDyn) must be removed to ensure that they are not accounted for twice in the simulation.

4 WAVE ANALYSIS MODULE

4.1 Overview of the development strategy

The target specifications for the wave base module to be developed in PerAWaT were defined in WG1 WP1 D1b. In summary, the base module was to have the following capabilities:

- Generate standard shape frequency spectra and directional spreading functions for a given sea state parameter vector;
- Load directional spectra from measured data;
- Output a list of wave components corresponding to a given spectrum to the FD and TD simulations;
- Create a probabilistic parametric description of a site-specific wave climate from measured spectra.

The implementation of the first three of the above bullet points was described in WG1 WP1 D2, together with a description of the progress to date regarding the fourth point. The method for describing a wave climate consisted of fitting the spectrum with models formed as sums of standard spectral shapes (either JONSWAP, Ochi or Gamma) and quantifying the goodness-of-fit of the spectrum. At the time of writing WG1 WP1 D2 only the fit of models formed as sums of JONSWAP spectra had been considered. In the subsequent sections, the fit of spectra formed as sums of either JONSWAP, Ochi or Gamma spectra is compared using long datasets for three locations.

First, the models used to describe wave spectra are described in Section 4.2. A new method for parameterising spectral shapes is introduced in Section 4.3 which enables the range of spectral shapes for a given H_s and T_e to be reduced to a 2-parameter space and for theoretical bounds to be placed on the range of valid parameters. An updated method for spectral fitting is presented in Section 4.4 and the data used is described in Section 4.5. The accuracy of the fitted spectra is discussed in Section 4.6 and an analysis of the observed range of shapes is presented in Section 4.7. Initial results concerning the effect of parameterisation on the accuracy of energy yield estimation are given in Section 4.8. Finally, conclusions and further work are listed in Section 4.9.

4.2 Models for frequency spectra

In this section a recap of the definitions of the forms of fitted spectra is presented. These were originally discussed in D2.

There are several commonly used forms for unimodal spectra which result from a combination of theoretical considerations and empirical evidence. In deep-water the shape of the spectrum is controlled by the balance between the wind input, dissipation from white-capping and nonlinear quadruplet wave-wave interactions. During active wave growth, when the waves are relatively steep, nonlinear quadruplet interactions play a central role in controlling the shape of the spectrum, forcing it towards ‘standard’ unimodal shapes and smoothing local deviations (Young and Van Vledder, 1993). If the wind input varies sufficiently slowly (as is normally the case in a storm) then nonlinear quadruplet interactions dominate and a JONSWAP type spectrum will evolve. However, if the wind drops or the waves leave their generation area then the steepness of the waves will decrease (due to frequency- and direction-dispersion) and the quadruplet interactions will decrease accordingly. In this case the spectral shape will depend upon the history of the individual wave components and a ‘standard’ shape cannot be expected. This can result in spectra with multiple peaks, from one or more

swells possibly together with a local wind sea. In these cases parametric descriptions of the frequency spectrum can be formed as a sum of two or more standard unimodal spectra.

A useful review of models for spectral shapes is presented by Michel (1999).The author notes that the most commonly used forms of unimodal spectra belong to the family given by:

$$E(f) = \alpha f^{-r} \exp(-\beta f^{-s}) \gamma^{\delta(f)}, \text{ for } \alpha, \beta, r, s > 0, \gamma > 1, \quad [4.1]$$

where

$$\delta(f) = \exp\left(-\frac{1}{2}\left(\frac{f-f_p}{\sigma f_p}\right)^2\right), \quad [4.2]$$

and it is usually assumed that

$$\sigma = \begin{cases} 0.07 \text{ for } f \geq f_p \\ 0.09 \text{ for } f \geq f_p \end{cases} \quad [4.3]$$

The parameters r and s control the shape of the spectrum, α is the scale parameter, β is the location parameter (in terms of frequency) and γ is known as the peak enhancement factor. The peak frequency of the spectrum is given by

$$f_p = \left(\frac{s\beta}{r}\right)^{\frac{1}{s}} \quad [4.4]$$

The high frequency tail of spectrum is proportional to f^{-r}. There is some debate on whether the spectral tail follows an f^{-4} shape or an f^{-5} shape. Most recent theoretical and empirical evidence suggests that an f^{-4} shape is more appropriate (see Holthuijsen, 2007, for a review). However, the most commonly used spectra in ocean engineering have an f^{-5} tail. For practical purposes though the difference appears to be negligible.

The family of spectra given by Eq. 4.1 have five free parameters. To describe the sea state with fewer variables, some of these parameters can be fixed whilst the others are left free. The most commonly used families of spectra with one, two and three free parameters are summarised in Table 4.1. Fixing $r = 5$, $s = 4$ and $\gamma = 1$, gives the commonly used form proposed by Bretschneider (1959). A special form of the Bretschneider spectrum for 'fully developed' seas was proposed by Pierson and Moskowitz (1964), where α is fixed and the energy in the spectrum depends on the value of β only (equivalently H_s is in fixed ratio to T_p). The JONSWAP form (Hasselmann et al., 1973) was a further generalisation of Bretschneider spectra which accounted for the more peaked spectral shapes observed in fetch-limited wind seas. The term 'Ochi spectra' has been used here for the case where $s = 4$, $\gamma = 1$ and r is a free parameter, after the use of this type of spectrum by Ochi and Hubble (1976). Finally, the term 'Gamma spectra' is used by some authors (e.g. Boukhanovsky and Guedes Soares, 2009) to describe the form where $\gamma = 1$, r is a free parameter and $s = r - 1$, and will be used here. Obviously, for this type of spectrum it could have been written equivalently that s is free and r is fixed as $s + 1$.

Formulations for spectra in shallow water such as the TMA spectrum (Bouws et al, 1985) or the form proposed by Young and Babanin (2006) have not been implemented at present as only deep-water WECs are considered in PerAWaT.

Free parameters	**Name**	α	β	r	s	γ
1	Pierson-Moskowitz	5.0×10^{-4}	free	5	4	1
2	Bretschneider	free	free	5	4	1
3	JONSWAP	free	free	5	4	free
3	Ochi	free	free	free	4	1
3	Gamma	free	free	free	r - 1	1

Table 4.1. Free and fixed parameters for families of unimodal spectra given by Eq. 4.1.

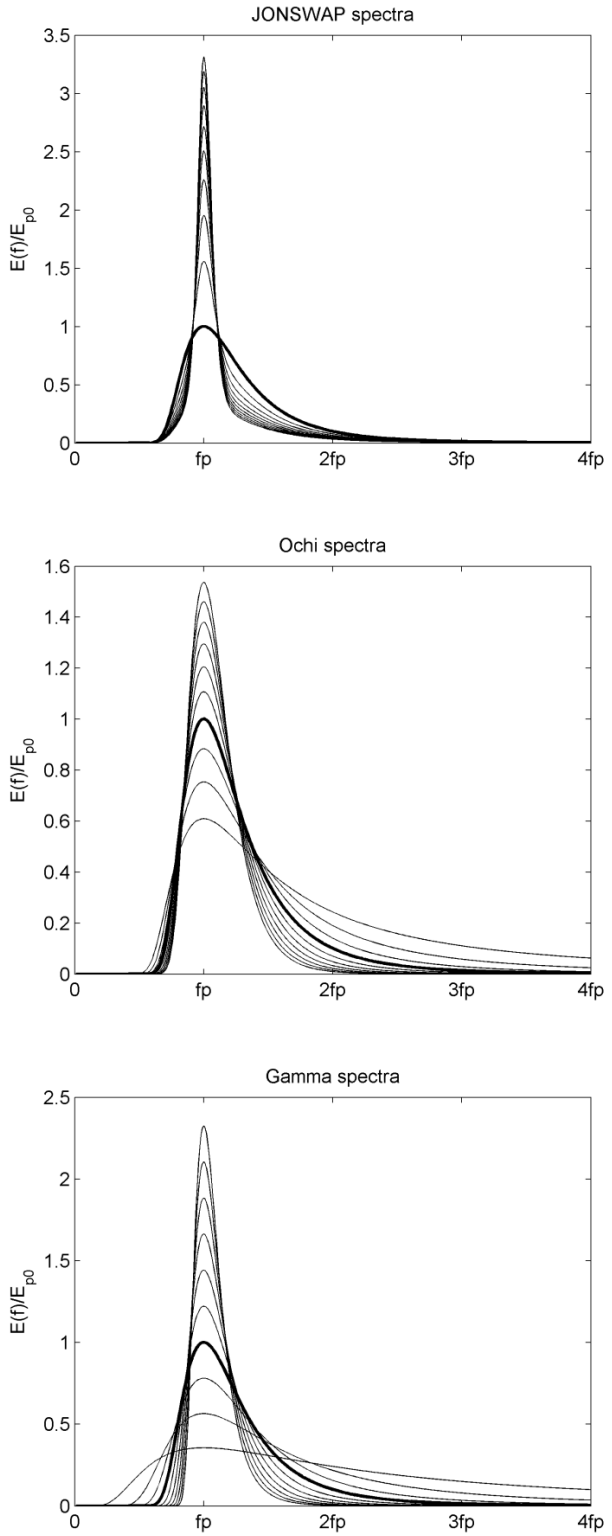

Figure 4.1. JONSWAP spectra for γ = 1-10 and Ochi and Gamma spectra for r = 2-11. Spectral densities have been normalised so that m_0 = 1. In each plot the Bretschneider spectrum is shown in bold.

Examples of the JONSWAP, Ochi and Gamma families are shown in Figure 4.1 for fixed H_s and f_p and a range of the third free parameter. In each case the Bretschneider spectrum is a special case and is

indicated with a bold line. For the JONSWAP family the Bretschneider spectrum is the limiting form, corresponding to the most broad-banded member. As the peak enhancement factor, γ, increases the spectra become more peaked, but a spread of energy remains between about $0.6f_p$ and $2f_p$. Gamma and Ochi spectra can take more broad-banded forms than JONSWAP spectra, albeit with the possibility of a physically unrealistic amount of energy in the tail for low values of r. For Ochi spectra there is little variation in the shape for frequencies less than f_p, whereas for Gamma spectra the proportion of energy below f_p increases as r decreases. For higher values of r, both Gamma and Ochi spectra can have an arbitrarily narrow concentration of energy about the peak frequency.

The moments of the spectrum are defined as

$$m_n = \int_0^\infty f^n E(f)\,\mathrm{d}f \qquad [4.5]$$

For spectra defined by Eq. 4.1 with γ =1 the moments of the spectrum can be expressed as explicit functions of α, β, r and s:

$$m_n = \frac{\alpha}{s}\beta^{\frac{n-r+1}{s}}\Gamma\left(\frac{r-n-1}{s}\right) \text{ for } n < r-1 \qquad [4.6]$$

If $\gamma \neq 1$ then numerical integration must be used to compute the moments and hence the relationships between the spectral parameters. For Ochi and Gamma spectra parameter relationships are given by:

$$H_s = 4\sqrt{m_0} = 4\left[\frac{\alpha}{s}\Gamma\left(\frac{r-1}{s}\right)\left(\frac{r}{s}f_p^s\right)^{\frac{1-r}{s}}\right]^{1/2} \qquad [4.7]$$

$$T_e = \frac{m_{-1}}{m_0} = \frac{\Gamma\left(\frac{r}{s}\right)}{\Gamma\left(\frac{r-1}{s}\right)}\left(\frac{s}{r}\right)^{\frac{1}{s}}T_p \qquad [4.8]$$

$$T_m = \frac{m_0}{m_1} = \frac{\Gamma\left(\frac{r-1}{s}\right)}{\Gamma\left(\frac{r-2}{s}\right)}\left(\frac{s}{r}\right)^{\frac{1}{s}}T_p \qquad [4.9]$$

$$T_z = \sqrt{\frac{m_0}{m_2}} = \left[\frac{\Gamma\left(\frac{r-1}{s}\right)}{\Gamma\left(\frac{r-3}{s}\right)}\right]\left(\frac{s}{r}\right)^{\frac{1}{s}}T_p \qquad [4.10]$$

For the JONSWAP spectrum functions of γ can be defined to determine the parameter relations as follows:

$$H_s = g_h(\gamma)T_p^2\alpha^{1/2} \qquad [4.11]$$

$$T_e = g_e(\gamma)T_p \qquad [4.12]$$

$$T_m = g_m(\gamma)T_p \qquad [4.13]$$

$$T_z = g_z(\gamma)T_p \qquad [4.14]$$

The values of the functions g_h, g_e, g_m and g_z are shown in Figure 4.2 for $1 \leq \gamma \gamma > 1000 \leq$ 10,000. Note that the period parameter relations are approximated by a logarithmic function for smaller values of γ but tend towards 1 for $\gamma > 1000$. Note that these relations assume that the cut-off frequency in Eq. 4.5 is infinite. This is not the case of course, but has negligible effect if the cut-off frequency is greater than 3 f_p.

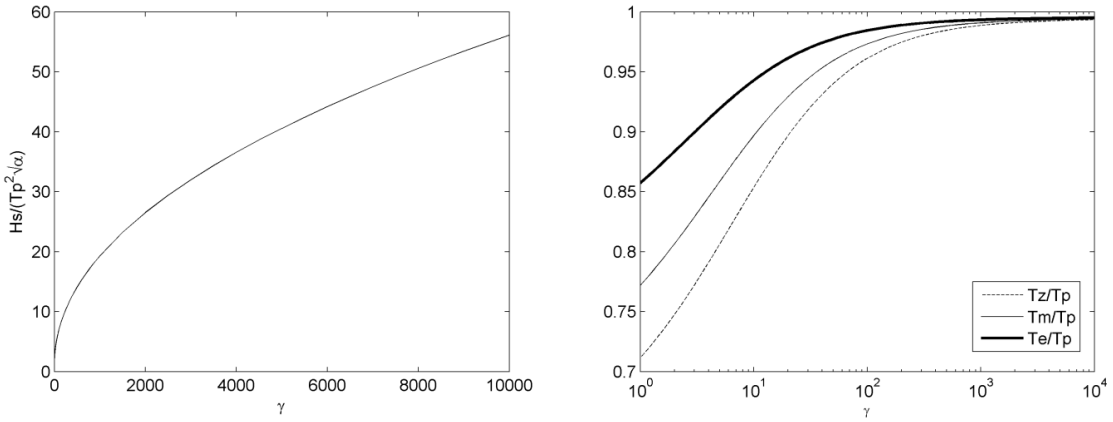

Figure 4.2. Values of the functions g_h, g_e, g_m and g_z which determine parameter relations for the JONSWAP spectrum.

For the spectra with three free parameters the third free parameter (other than α and β) controls the bandwidth or equivalently the peakedness of the spectrum. To make this precise, the peakedness of a spectrum will be defined as the ratio E (f_p) / E_{p0} where E_{p0} is the peak spectral density of a Bretschneider spectrum with the same H_s and T_e, given by

$$E_{p0} = H_s^2 T_e \frac{\exp(-5/4)}{4\Gamma(5/4)} \left(\frac{5}{4}\right)^{\frac{5}{4}} \qquad [4.15]$$

Figure 4.3 shows the peakedness of JONSWAP, Ochi and Gamma spectra against r and γ. The peakedness increases approximately linearly with r for Gamma spectra, and approximately logarithmically with r and γ for Ochi and JONSWAP spectra respectively. In fact for $\gamma < 100$, to a good approximation the peakedness of the JONSWAP spectrum is equal to 1 + ln (γ).

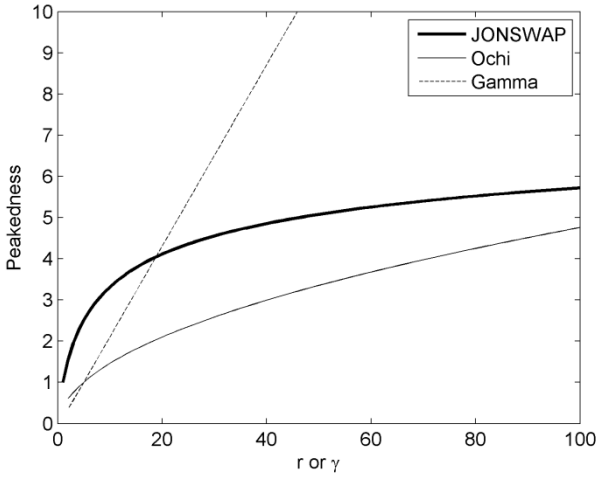

Figure 4.3. Spectral peakedness against *r* for the Ochi and Gamma spectra and against *γ* for the JONSWAP spectrum.

The most commonly used multimodal spectral forms are formulated as the summation of either JONSWAP, Gamma or Ochi spectra. Ochi and Hubble (1976) proposed a six-parameter spectrum formed as the sum of two Ochi spectra. However, each of the six free parameters was given as a function of H_s (together with ten spectra representing a 95% confidence interval), so in essence this is a one parameter spectrum. Guedes Soares (1984) proposed a bimodal spectrum formed as the sum of two JONSWAP spectra, but with γ fixed as 2 for both components, resulting in a four parameter spectrum. Torsethaugen (1993) and Torsethaugen and Haver (2004) have proposed a form consisting of two JONSWAP spectra. However, the values of the parameters of each spectrum are determined by the values of H_s and f_p, so the number of free parameters is reduced from six to two. Finally, Boukhanovsky and Guedes Soares (2009) modelled multi-modal spectra as the summation of Gamma spectra, imposing no restrictions on the parameter values, resulting in a true six parameter spectrum.

In this study the use of 3-, 4- and 6-parameter spectra will be investigated and compared to the use of Bretschneider spectra. The 3-parameter spectra correspond to the JONSWAP, Ochi and Gamma formulations described above and the 6-parameter spectra are formed as the sums of two such spectra. The 4-parameter spectra are also formed as the sums of these types of spectra, but with the bandwidth parameter for each spectrum (γ in the case of JONSWAP spectra and r in the case of Ochi or Gamma spectra) set at a fixed value. Following Guedes Soares (1984) the value of γ for the 4-parameter JONSWAP spectra will be fixed at 2. To give spectra with similar peakedness for the 4-parameter Ochi and Gamma spectra r will be fixed at 10 and 7 respectively for these spectra. The use of other fixed values of peakedness or values which vary as a function of the H_s and T_e of each partition may potentially give better results but this will not be considered further here. The influence of the inclusion of peakedness as a free parameter will be assessed through comparison between 2- and 3-parameter spectra and the 4- and 6-parameter spectra,

4.3 Parameterisation of bimodal spectral shapes

Through a change in the parameterisation used to describe the 4- and 6-parameter spectra it is possible to place theoretical limits on the range of possible shapes, in terms of the H_s and T_e of each component system (or partition). This change of parameters also provides a systematic method for describing how the shapes vary and provides a two-dimensional space which covers all possible shapes for a particular 4-parameter formulation.

First note that the moments of the spectrum are the sum of the moments of each partition:

$$m_n = m_{ns} + m_{nw}, \quad [4.16]$$

where m_n is the n^{th} moment of the spectrum and m_{ns} and m_{nw} are the n^{th} moments of the swell and wind sea partitions respectively. Here the terms swell and wind sea are used to denote the lower and higher frequency partitions respectively and are not intended to imply any particular qualities about the sea state. They are also not intended to be interpreted as necessarily representing waves generated in separate events. However, this is a reasonable conclusion when the two components are sufficiently separated in frequency.

From the moment definitions it is possible to obtain:

$$H_s^2 T_e = H_{ss}^2 T_{es} + H_{sw}^2 T_{ew}, \quad [4.17]$$

where H_{ss}, T_{es}, H_{sw} and T_{ew} are the significant wave height and energy periods or the swell and wind sea partitions respectively. This can also be derived from the principle of conservation of power. Normalised parameters for each partition can be defined as follows:

Normalised swell and wind sea heights: $H_{sn} = H_{ss}/H_s, \quad H_{wn} = H_{sw}/H_s.$ [4.18]

Normalised swell and wind sea periods: $T_{sn} = T_{es}/T_e, \quad T_{wn} = T_{ew}/T_e.$ [4.19]

Normalised swell and wind sea power: $P_{sn} = P_s/P, \quad P_{wn} = P_w/P.$ [4.20]

Normalised swell and wind sea steepness: $s_{sn} = s_{es}/s_e, \quad s_{wn} = s_{ew}/s_e.$ [4.21]

Normalised separation of the swell and wind sea periods: $dT_n = T_{sn} - T_{wn}.$ [4.22]

Here s_e is the significant steepness defined in terms of T_e as $s_e = 2\pi H_s/gT_e^2$, rather than the more common definition in terms of T_z. From the definitions above the following relations hold:

$$H_{sn}^2 + H_{wn}^2 = 1, \quad [4.23]$$

$$P_{sn} + P_{wn} = 1, \quad [4.24]$$

$$T_{wn} \leq 1 \leq T_{sn}. \quad [4.25]$$

From this it follows that the normalised periods, powers and steepnesses can be expressed in terms of the normalised heights and separation:

$$T_{sn} = 1 + H_{wn}^2 dT_n, \quad T_{wn} = 1 - H_{sn}^2 dT_n. \quad [4.26]$$

$$P_{sn} = H_{sn}^2 T_{sn}, \qquad P_{wn} = H_{wn}^2 T_{wn}. \qquad [4.27]$$

$$s_{sn} = H_{sn}/T_{sn}^2, \qquad s_{wn} = H_{wn}/T_{wn}^2. \qquad [4.28]$$

So it follows that for a spectrum with a given H_s and T_e, the significant wave heights and periods of each partition are determined by the normalised swell height H_{sn}^2 and normalised separation dT_n alone. Figure 4.4 shows contours of the normalised swell and wind sea periods, powers and steepness plotted for a range of H_{sn}^2 and dT_n.

Examples of spectral shapes for a range of values of H_{sn} and dT_n are shown in Figure 4.5. A JONSWAP spectrum with $\gamma = 2$ has been used for both partitions. Frequencies have been normalised by $f_e = 1 / T_e$ and spectral densities are normalised by E_{p0}. Note that the wind sea partition for $H_{sn}^2 = 5/6$, $dT_n = 1$ is not visible within the axes limits used here, since the wind sea peak is around $5f / f_e$.

Also note that spectra with $dT_n dT_n$ close to zero or H_{sn}^2 close to zero or one all correspond to unimodal shapes.

For a spectrum with a given H_s and T_e there are two factors which limit the range of possible combinations of H_{sn} and dT_n: the steepness of the wind sea and the maximum swell period at the site. As the steepness of the overall sea state, s_e, increases, the range of possible values of s_{wn} will reduce. For example, if the limiting sea steepness is $s_{ew} = 0.06$ and $s_e = 0.04$ then the limiting value is $s_{wn} = 1.5$, whereas if $s_e = 0.02$ then the limiting value is $s_{wn} = 3$. Similarly, if the maximum recorded swell period at a site is $T_{es} = 20$s, then for a spectrum with $T_e = 10$s the maximum value of T_{sn} is 2, whereas for a spectrum with $T_e = 5$s the maximum value of T_{sn} is 4. Therefore for a spectrum with a given H_s and T_e the range of possible shapes of 4-parameter spectra is bounded by the contours of maximal wind sea steepness and maximal swell period.

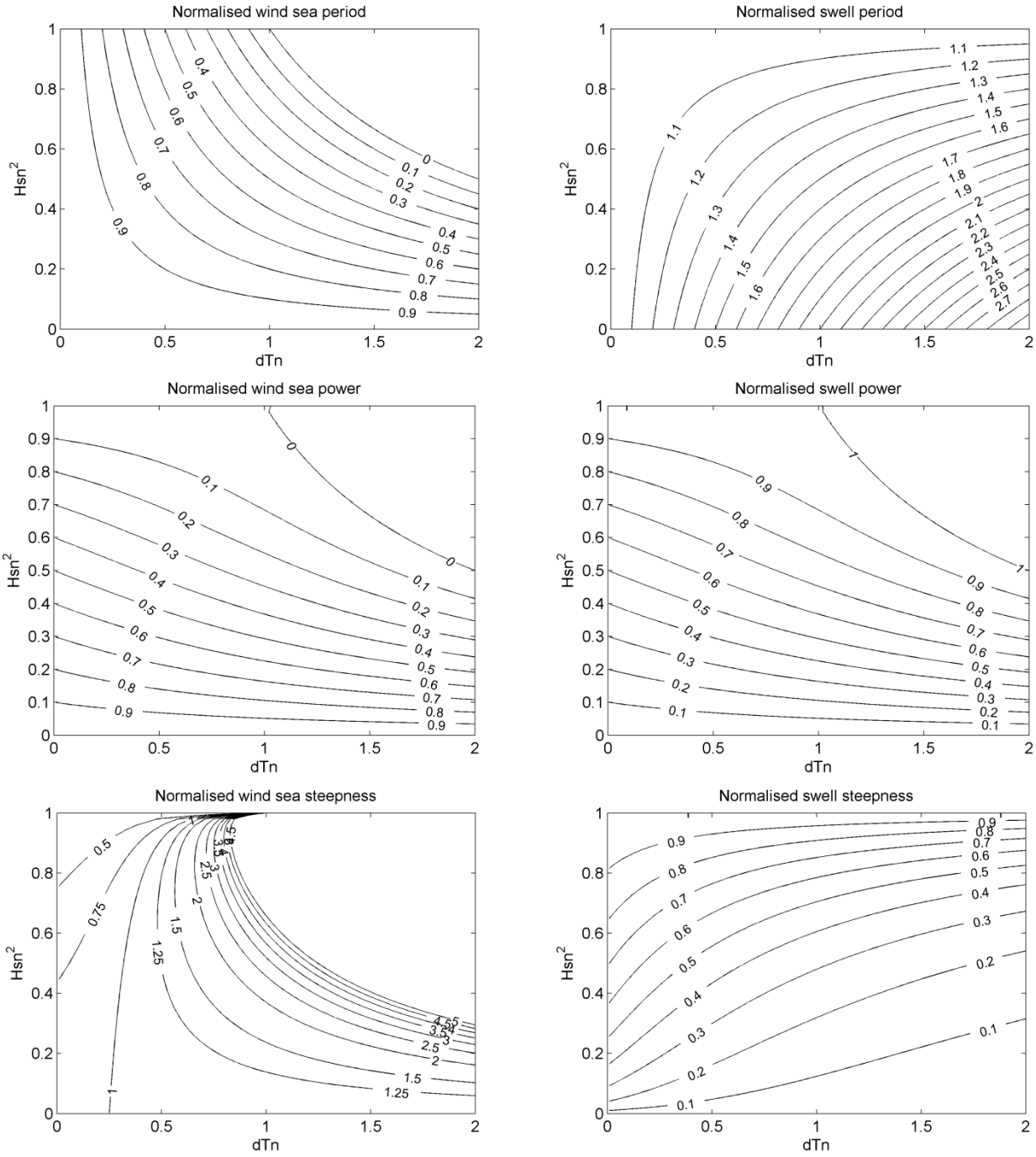

Figure 4.4. Contours of normalised swell and wind sea periods, powers and steepness as functions of H_{sn}^2 and dT_n.

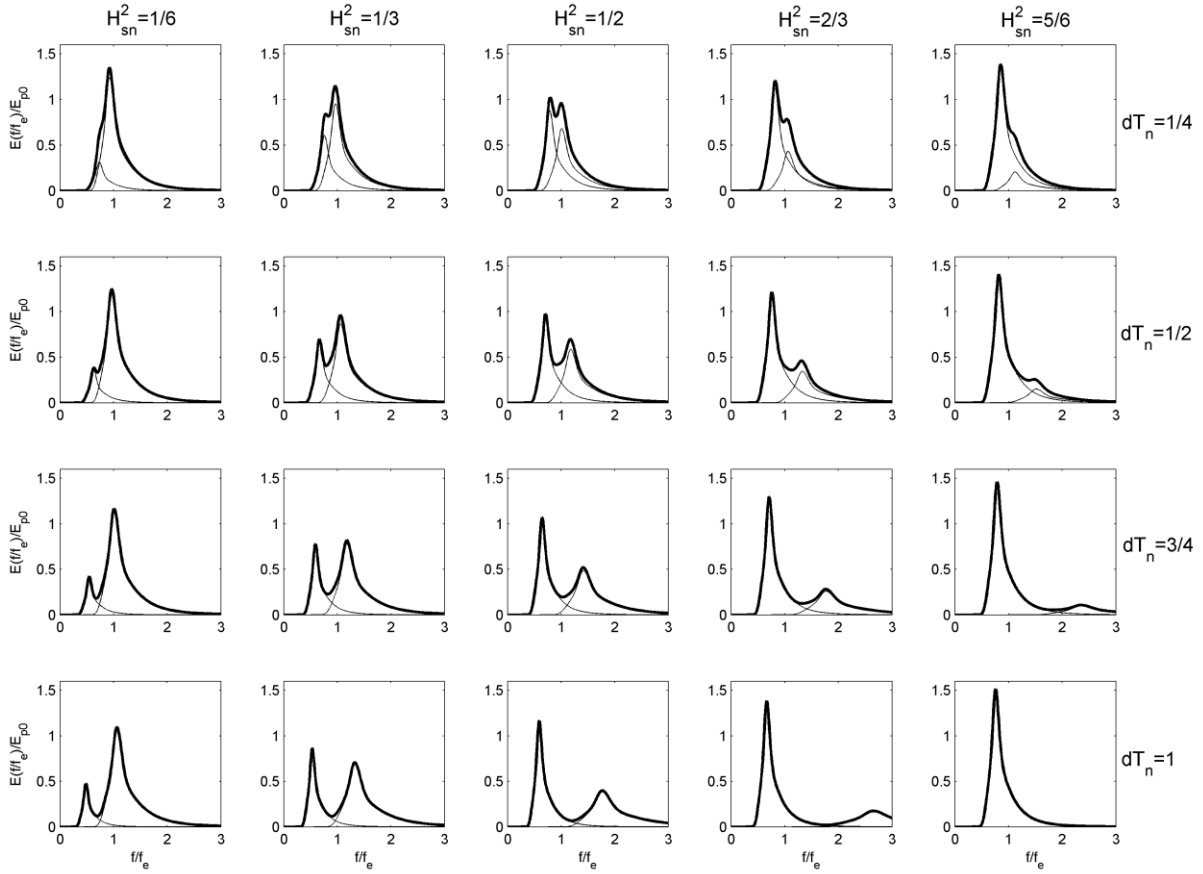

Figure 4.5. Spectral shapes for a range of values of H_{sn} and dT_n. A JONSWAP spectrum with γ = 2 has been used for both partitions. The energy of the swell partition increases from left to right (H_{sn}^2 values are noted at the top of each column) and the separation of the peaks increases from top to bottom (dT_n values are noted at the right of each row).

4.4 Method for spectral fitting

Bretschneider spectra are not usually fitted to measured spectra in a least squares sense, but are determined by the moments of the measured spectra and chosen so that they match the measured values of H_s and T_e, T_m or T_z. The ratios between T_e, T_m and T_z for a Bretschneider spectrum are fixed, so the Bretschneider spectrum corresponding to the measured H_s and T_e may differ from that corresponding to the measured H_s and T_z. In this study the measured H_s and T_e will be used to determine the Bretschneider spectra (initial tests showed that this gave a better fit than using T_m or T_z).

In contrast, spectra with a greater number of free parameters are usually fit to the spectrum using some kind of fitting algorithm. The initialisation of the fitting algorithm is critical to its performance, especially in the cases of the four and six parameter spectra. If the fitting algorithm is initialised with a poor first guess then it is unlikely to converge to the global best fit. In many studies a partitioning algorithm is used to determine the first guess parameters for the fitting algorithm (e.g. Guedes Soares, 1984; Keribriou et al., 2007). This was also the approach adopted in D2. Criteria are chosen to identify 'separate' wave systems making up the spectrum. The parameters of the partitions which are identified are then used to determine the parameters used to initialise a fitting algorithm. Regardless of the criteria used to determine what constitutes a significant peak there will be some spectra which are neither determined to be significantly bimodal nor are well described by standard unimodal shapes. In these cases it would be advantageous to decouple to performance of the fitting algorithm from the

performance of the partitioning algorithm. The approach taken here is not to use a partitioning algorithm, but to attempt to fit all spectra with models of the same number of parameters and to use the fitting algorithm to discard the fitted peaks which are deemed insignificant, thereby only using a unimodal model if it is a better fit than a bimodal model. This approach has the advantage over the partitioning and fitting approach in that it allows a greater flexibility in the initial guesses for the fitting algorithm. Comparisons between the two methods (not presented here) have confirmed that removing the portioning algorithm from the fitting process significantly improves the fit of the spectra on average.

The procedure used for spectral fitting is as follows (here E_m and E_f denote the measured and fitted spectra, respectively):

- Firstly a unimodal spectrum is fit to the highest peak in the spectrum:
  - The first guess is based on a spectrum with the measured peak frequency, f_p, measured peak spectral density, $E_m(f_p)$, and a peakedness of 1.5 in the cases where this is a free parameter.
  - A simplex search technique is used to find the parameters which minimise the squared distance between the measured and fitted unimodal spectra $\int_0^\infty [E_m(f) - E_f(f)]^2 \mathrm{d}f$.
- In the two-peaked cases a second peak is fit as follows:
  - The first guess parameters for the highest peak are based on the optimised values found in the first stage. A first guess for the peak frequency of the second peak, f_{p2}, is made as the frequency corresponding to the maximum of the curve $E_f(f) - E_m(f)$ in the section with the maximum positive area (i.e. this is the largest area not covered by the fitted unimodal model). The first guess for the peak spectral density of the second partition is taken as $E_f(f_{p2}) - E_m(f_{p2})$, and a peakedness value of 1.5 is used in the cases where this is a free parameter.
  - A simplex search technique is used again to find the parameters which minimise the squared distance between the measured spectrum and a spectrum formed of two partitions.

Note that in contrast to the Bretschneider spectra, the fitted spectra are not forced to match the H_s and T_e of the measured spectra.

4.5 Data and spectral processing

Three datasets have been selected for the comparison of the fits of the various types of spectra. Data from the US National Data Buoy Centre (NDBC) has been used since there are many long records (exceeding 20 years) and all data are freely available[1]. The buoys used are in locations with differing wave climate characteristics. One is on the Atlantic coast of the US, east of Virginia where the wave climate is wind-sea dominated. The second is on the Pacific coast of the US, off central California where the wave climate is a mixture of wind sea and swell conditions; and the third is near Hawaii which has a swell-dominated climate. Details of the buoy locations and available data are presented in Table 4.2. A range of depths is shown since the locations of the buoys have changed slightly over time

[1] ftp://ftp.nodc.noaa.gov/pub/f291/

(after maintenance or replacement of buoy systems). However the locations and depths are constant enough so that the wave climate at the buoy locations can be considered constant over time.

The annual mean power levels at the three sites are 10.4 kW/m (Virginia), 29.1kW/m (California) and 31.9kW/m (Hawaii). The joint distributions of H_s with T_e and H_s with *MDIR* for the three locations are shown in Figure 4.6. Note that although the most frequently occurring direction at the Hawaii buoy is from the east, nearly all the energetic conditions, where H_s exceeds 4m, come from between north west and north east. The mean measured spectrum for each location is shown in Figure 4.7. Buoy 44014 has a peak in the mean spectrum around 9s and buoys 46042 and 51001 both have peaks in the range 12-14s. At buoy 51001 there is also a smaller second peak caused by the frequent presence of the easterly wind sea on top of the northerly swell.

Buoy Number	Location	Water depth [m]	Non-directional data	Directional data
46042	27 NM West of Monterey Bay, California	640 – 2115	04/1988-12/2010	04/1988-12/2010
44014	64 NM East of Virginia Beach, Virginia	41.8 – 53.6	10/1990-12/2010	10/1990-12/2010
51001	170 NM West Northwest of Kauai Island, Hawaii	3252 – 3430	02/1981-11/2009	05/2005-11/2009

Table 4.2. Locations and data availability for the buoys used in this study.

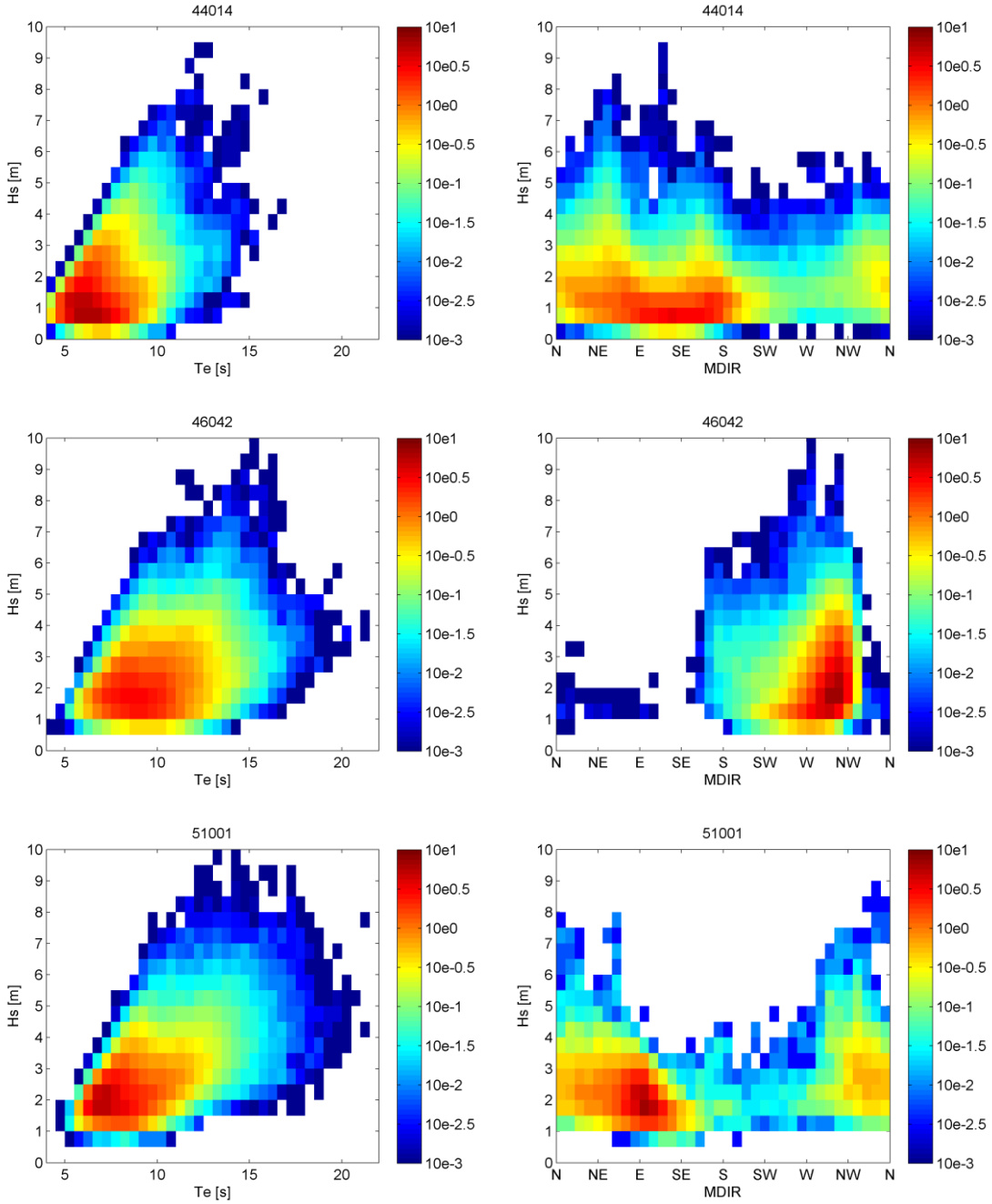

Figure 4.6. Parameter distributions for the three buoy locations. Left: Joint distribution of H_s and T_e. Right: Joint distribution of H_s and *MDIR*. (Colour indicates percentage occurrence in logarithmic scale).

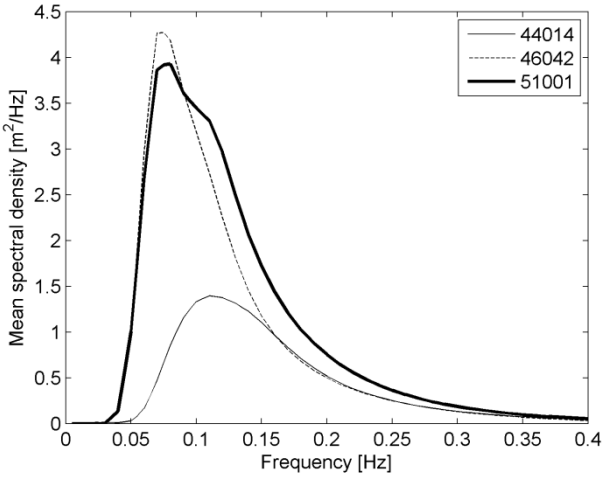

Figure 4.7. Mean spectral shape at the three buoy locations.

The data sampling and processing methods used by the NDBC have changed over the years and in some instances the size and shape of the buoys has also changed. Buoys 44014 and 46042 are both 3m discus shaped buoys, whereas buoy 51001 initially had a 6m boat shaped hull, before being changed to a 3m discus buoy in May 2005 (coinciding with the start of the directional data collection). The wave data sampling and processing procedures are discussed in detail in NDBC (1996) and are summarised in Table 4.3 below. All systems make measurements once per hour. Buoys 44014 and 46042 used DACT DWA processing units initially before being upgraded to the WPM systems in June 2006 and October 2004 respectively (although buoy 44014 also used the WPM processor for the period June 1995 – March 1997). Buoy 51001 initially used the GSBP processor, before being upgraded to the DACT WA processor in August 2001, and then to the WPM processor in May 2005 (coinciding with change in the buoy hull and the start of the collection of the directional data).

	GSBP	**DACT WA**	**DACT DWA**	**WPM**
Record length	1200s	1200s	1200s	2400s
Sampling rate	1.5 Hz	2.56 Hz	2.0 Hz	1.7066 Hz
Analogue filter	0.5 Hz	0.5 Hz	None	None
Digital filter	None	None	0.39 Hz	None
Segment length	N/A	100s	100s	N/A
Frequencies resolution and range	0.03-0.50 @0.01Hz	0.03-0.40 @0.01Hz	0.03-0.40 @ 0.01Hz	0.0325-0.925 @0.005Hz; 0.1-0.35 @ 0.01Hz; 0.365-0.485 @0.02 Hz
Equivalent degrees of freedom of spectral estimates	48	33	33	24

Table 4.3. NDBC buoy system parameters

The GSBP spectra were calculated using covariance (autocorrelation) techniques rather than an FFT. For each 20-minute acceleration record consisting of 1800 data points sampled at 1.5 Hz, an acceleration covariance (autocorrelation) function is calculated for up to 75 lags. Acceleration spectra are computed from the covariance values and a Hanning window is applied to reduce spectral leakage. The acceleration spectra are corrected for the hull-mooring response before the elevation spectra are computed. For data processed by covariance techniques, the equivalent degrees of freedom, v, of spectral estimates are given by $v = 2N / M$, where N is the number of data points and M is the number of covariance lags. However, adjacent spectral estimates are not independent.

The processing method used by the DACT WA and DACT DWA are identical except for the sampling frequencies and filtering (also the DWA processes directional data, but the method for deriving cross-spectra are essentially the same as for auto-spectra). Data are divided into 23 segments with 50% overlaps and Hanning is performed. An FFT is used to give elevation spectra which are corrected for windowing and averaged over the segments. For data processed by FFTs with data segmenting, the equivalent degrees of freedom, v, of spectral estimates is given by

$$v = \frac{2J}{\left(1+\frac{0.4(J-1)}{J}\right)} \qquad [4.29]$$

where J is the number of overlapping segments.

For the WPM processor, no filtering, segmenting or Hanning is used. For data processed by FFTs without data segmenting, the degrees of freedom for a frequency band are given by twice the number of Fourier frequencies within the band. Data are processed to give a constant 24 DOF for all frequencies. For frequencies below 0.1Hz spectral estimates are based on 4096 data points (40 minutes) and reported at intervals of 0.005Hz. For frequencies between 0.1 Hz and 0.35 Hz spectral estimates are based on 2048 data points (20 minutes) and reported at intervals of 0.01Hz. For frequencies above 0.35 Hz spectral estimates are based on 1024 data points (10 minutes) and reported at intervals of 0.02Hz.

For all the methods described above, the 100α percent confidence interval for a spectral estimate with v degrees of freedom is given by:

$$\hat{S}(f)\left(\frac{v}{\chi^2_v((1+\alpha)/2)}\right) \leq S(f) \leq \hat{S}(f)\left(\frac{v}{\chi^2_v((1-\alpha)/2)}\right) \qquad [4.30]$$

where $\chi^2_v((1-\alpha)/2)$ and $\chi^2_v((1+\alpha)/2)$ denote the $100((1-\alpha)/2)^{\text{th}}$ and $100((1+\alpha)/2)^{\text{th}}$ percentiles for a chi-squared random variable with v degrees of freedom respectively, and $\hat{S}(f)$ is the estimate of $E(f)$. For the data used in this study the upper and lower points of a 90% confidence interval for spectral estimates is shown in Table 4.4.

v	5% point	95% point
24	0.66	1.73
33	0.70	1.58
48	0.74	1.45

Table 4.4. Confidence limits as a fraction of the spectral estimate $\hat{E}(f)$ for several values of v.

Due to the changes in the frequency range and resolution reported by the buoys all spectra have been interpolated to a resolution of 0.005Hz and range 0.03-0.40Hz (spectral parameters have been calculated by integration of the spectra over this range). This increase in frequency resolution will mean that all adjacent spectral estimates are correlated (except for the data from the WPM processors at frequencies below 0.1Hz). However, it was deemed more important to keep a constant frequency resolution so that each frequency carries equal weight in the fitting algorithm and the higher resolution was chosen to better resolve the shape of the spectrum around the spectral peak.

Note that the changes in the frequency range reported by the buoys will not affect results as all spectra have been cropped to the same range. The sampling frequency also will not affect the results as the

Nyquist frequency is always greater than the upper limit of the frequency range used here. However, the sampling duration and frequency resolution reported does have a significant effect on the results. This is further discussed in Section 4.6.

Some quality controls have been applied to the data by the NDBC (see NDBC 2003 for details); however there were some bad data remaining so further quality controls have been applied. The joint distributions of parameters have been examined to ensure that parameters are within realistic ranges for H_s with T_e, H_s with *MDIR* and T_e with T_z. Any clearly outlying points have been removed from the analysis.

4.6 Accuracy of fitted spectra

The goodness-of-fit of a fitted spectrum is quantified by the integral of absolute difference between the measured and fitted spectrum, normalised by m_0:

$$\Delta = \frac{1}{m_0}\int_0^\infty |E_m(f) - E_f(f)|\mathrm{d}f \qquad [4.31]$$

where E_m is the measured omnidirectional spectrum and E_f is the fitted spectrum. The quantity Δ is referred to as the deviance of the fitted spectrum. It is a measure of the area of the measured spectrum which is either above or below the fitted spectrum, normalised by the total area under the measured spectrum.

It was noticed that the deviance of the various types of spectra changes over time, both in terms of the average deviance and of the relative performance between spectra, depending on the method used to calculate the spectra and the degrees of freedom of the spectral estimates. Therefore the results have been separated both between locations and between processing types. The mean deviances of the various types of fitted spectra are listed in Table 4.5. The results are also presented as a percentage of the mean deviance for the Bretschneider spectra in Table 4.6. The mean deviance binned by the H_s and T_e of the measured spectra are shown in Figures 4.8 and 4.9. The results are shown for buoy 46042 (California) for the period using the DACT processing. Although, the magnitudes of the mean deviances change between buoys and between processing types, the patterns with H_s and T_e remain approximately the same.

Free parameters	Formulation	44014		46042		51001		
		DACT	WPM	DACT	WPM	GSBP	DACT	WPM
2	Bretschneider	0.442	0.471	0.445	0.483	0.355	0.377	0.407
3	JONSWAP	0.285	0.316	0.298	0.329	0.263	0.281	0.314
	Ochi	0.279	0.330	0.279	0.347	0.216	0.240	0.312
	Gamma	0.286	0.339	0.282	0.354	0.218	0.243	0.316
4	JONSWAP	0.186	0.233	0.190	0.248	0.180	0.184	0.224
	Ochi	0.314	0.312	0.339	0.315	0.358	0.354	0.336
	Gamma	0.219	0.285	0.209	0.310	0.164	0.190	0.267
6	JONSWAP	0.145	0.181	0.149	0.185	0.119	0.136	0.179
	Ochi	0.163	0.210	0.168	0.222	0.122	0.149	0.210
	Gamma	0.172	0.219	0.168	0.229	0.123	0.149	0.217

Table 4.5. Mean deviance of various types of fitted spectra for the three buoy locations.

Free parameters	Formulation	44014		46042		51001		
		DACT	WPM	DACT	WPM	GSBP	DACT	WPM
3	JONSWAP	64.5	67.1	67.0	68.1	74.1	74.4	77.1
	Ochi	63.1	70.1	62.7	71.8	61.0	63.6	76.6
	Gamma	64.7	72.0	63.4	73.3	61.3	64.4	77.7
4	JONSWAP	42.1	49.5	42.7	51.3	50.7	48.8	55.0
	Ochi	71.0	66.2	76.2	65.2	100.8	93.9	82.6
	Gamma	49.5	60.5	47.0	64.2	46.2	50.4	65.6
6	JONSWAP	32.8	38.4	33.5	38.2	33.5	36.2	44.0
	Ochi	36.9	44.5	37.8	46.0	34.4	39.6	51.7
	Gamma	38.8	46.5	37.8	47.4	34.7	39.6	53.3

Table 4.6. Mean deviance for the various types of fitted spectra as a percentage of the mean deviance for the Bretschneider spectra over the same period.

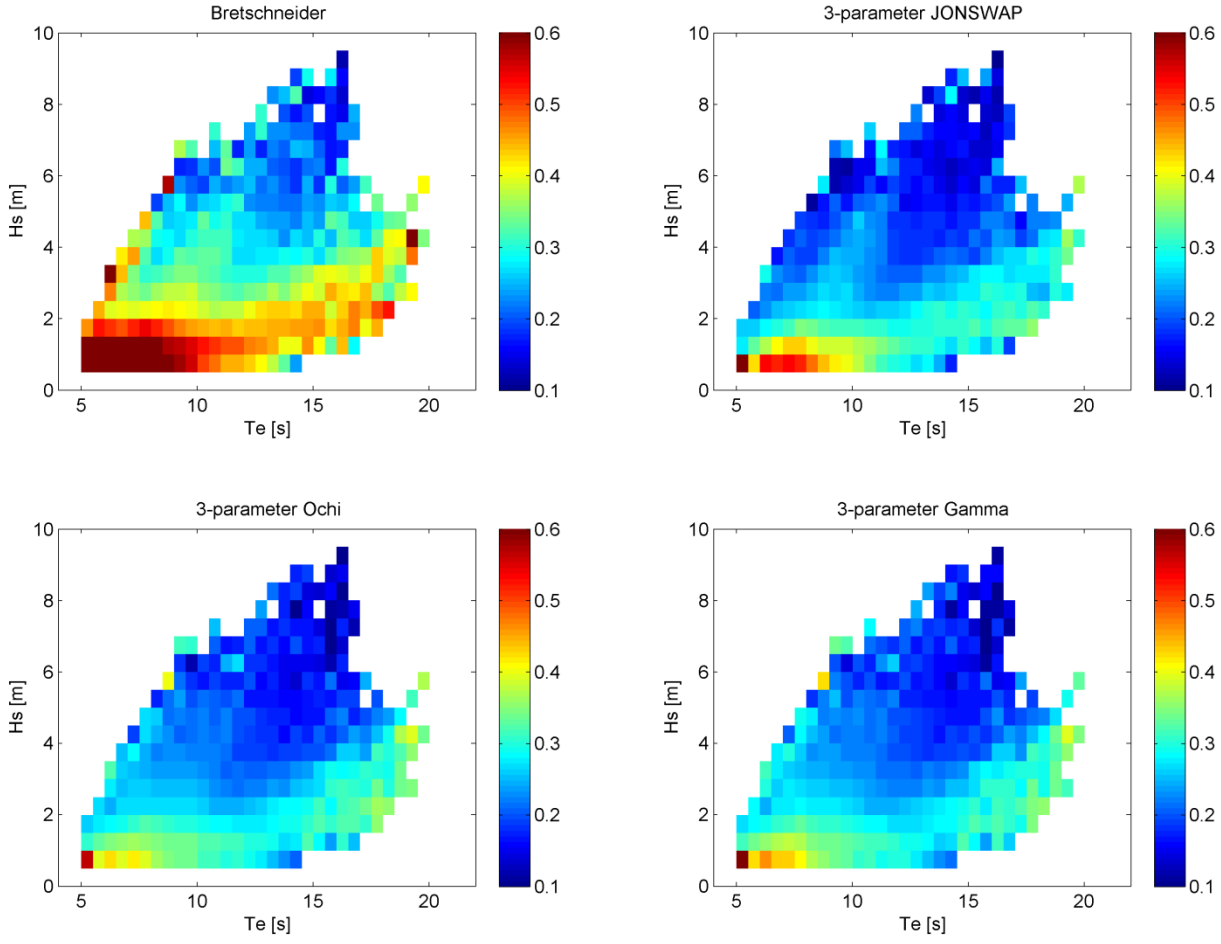

Figure 4.8. Mean deviance of Bretschneider and fitted 3-parameter spectra, binned by H_s and T_e.

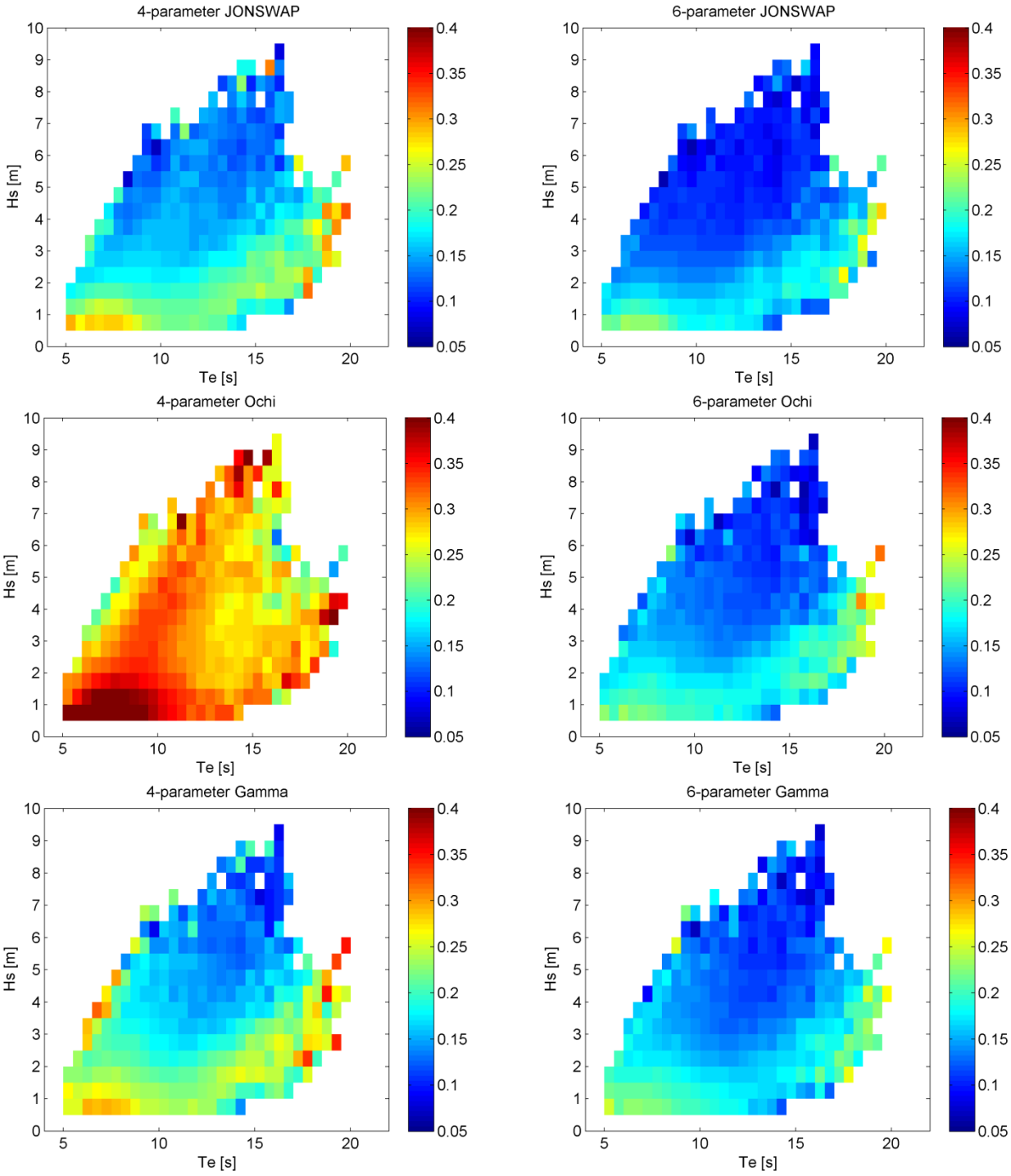

Figure 4.9. Mean deviance of fitted 4- and 6-parameter spectra, binned by H_s and T_e.

The results can be summarised as follows:

- The fits of all the types of spectra considered here improves as the DOF of the spectral estimates increase, due to the decrease in the variability of spectral estimates.
- For the GSBP data, there is a relatively high level of smoothing which results in broadening of the spectra with increased energy in the high- and low-frequency tails and decreased energy in the spectral peak. The shape of the spectra from the WPM data are better resolved around the

spectral peak than those from the DACT and GSBP data due to increased resolution for frequencies less than 0.1Hz and the decreased level of smoothing.

- The fit of the all types of spectra is worst for low sea states and long period swells. The deviances decrease for higher sea states as spectral shapes tend toward standard unimodal forms.
- For steeper seas the fits of the 3-, 4- and 6-parameter JONSWAP spectra are better than that for Ochi or Gamma spectra with the same number of parameters. This is understandable, considering that the JONSWAP spectrum was formulated specifically for fetch-limited seas.
- The fit of 3-, 4- and 6-parameter JONSWAP spectra improves relative Ochi or Gamma spectra with the same number of parameters as the level of smoothing decreases. This is because JONSWAP spectra can resolve narrow peaks whilst keeping energy in the spectral tail, whereas Ochi and Gamma spectra remove energy from the tail in more peaked spectra. However, Ochi and Gamma spectra perform better than JONSWAP spectra in swell dominated conditions when there is relatively little energy in the high-frequency tail.
- The fit of the 4-parameter JONSWAP spectra is significantly better on average than that of the 3-parameter JONSWAP spectrum, implying that the addition of a second peak is more important than including the peakedness of spectrum as a free parameter. However, for the steepest seas and the longest swell conditions where spectra are more peaked, the 3-parameter JONSWAP spectra perform better than the 4-parameter JONSWAP spectra.
- The 4-parameter Ochi spectra performed poorly and generally worse than the 3-parameter Ochi spectra. This may be due to a poor choice in the value of r for each partition. The performance of the of 4-parameter Gamma spectra was better, but generally worse than the performance of the 4-parameter JONSWAP spectrum.
- The difference in performance between the three types of spectral shape is much smaller than the difference in performance due to inclusion of further parameters. However spectra formed as sums of JONSWAP spectra provide a marginally better fit overall at all three locations (at least for the WPM records which have the highest resolution and are therefore likely to be more representative).

Examples of measured and fitted 4-parameter JONSWAP spectra with Δ=0.1, 0.3 and 0.5 are shown in Figure 4.10 for data from buoy 46042. For each value of Δ five spectra with Δ within ±0.05 of this value have been selected at random. Qualitatively, for $\Delta \leq 0.3$ the fit is good, whereas for $\Delta \geq 0.5$ the fit can be considered as merely indicative of the shape. The distribution of Δ for the Bretschneider and 3-, 4- and 6-parameter JONSWAP spectra is shown in

Figure 4.11, again using data from buoy 46042. The improvement in the performance with the inclusion of extra free parameters is clear. For the 3 parameter JONSWAP spectra 57% have $\Delta \leq 0.3$ and 89% have $\Delta \leq 0.5$ whereas this increases to 88% and 99.5% respectively for the 4-parameter JONSWAP spectra and 97% and 99.9% for the 6-parameter JONSWAP spectra.

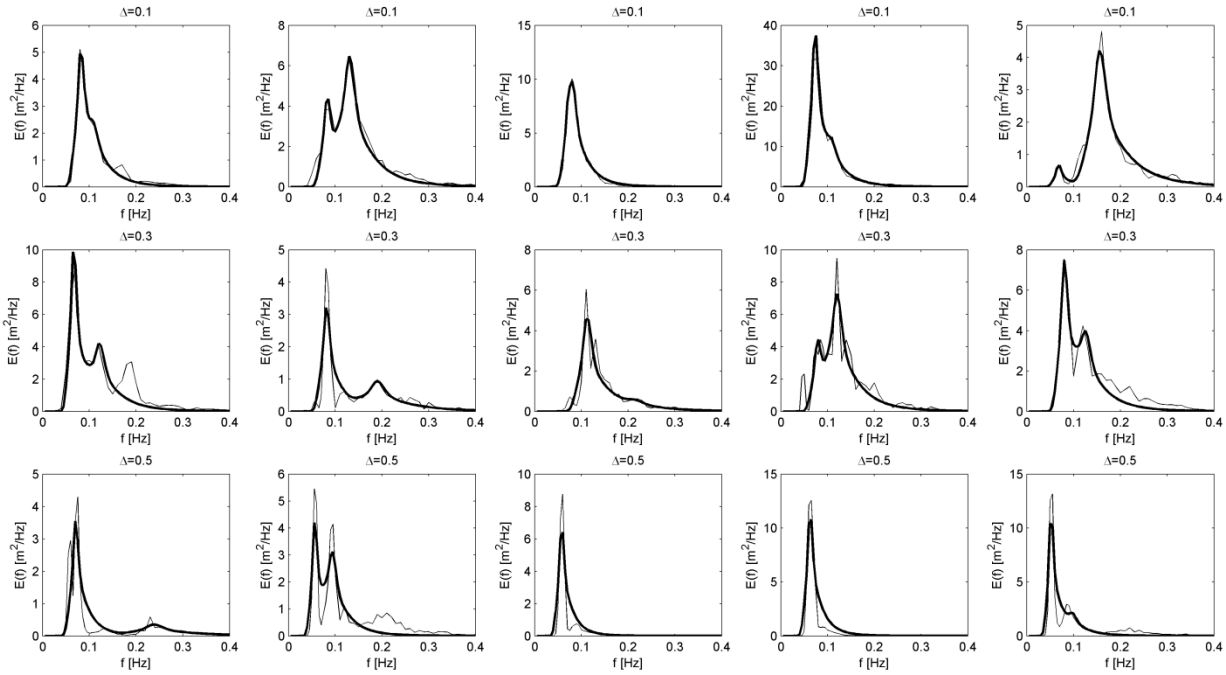

Figure 4.10. Examples of measured spectra (thin lines) and fitted 4-parameter JONSWAP spectra (bold lines) for buoy 46042 and Δ = 0.1, 0.3 or 0.5.

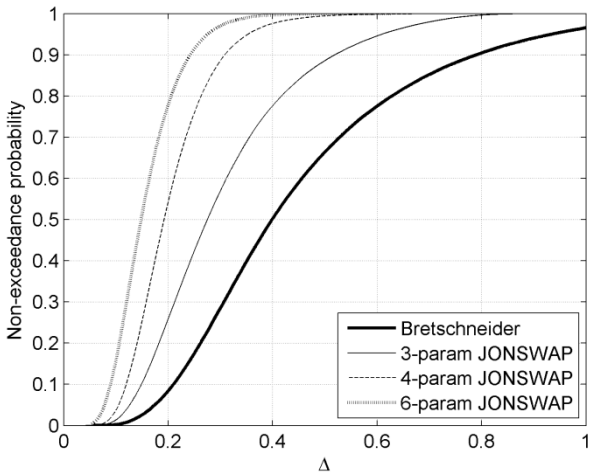

Figure 4.11. Distribution of Δ for buoy 46042 for 2-, 3-, 4- and 6-parameter JONSWAP spectra.

The fitted spectra are not forced to match the measured values of H_s and T_e so it is important to quantify the differences. A scatter plot of fitted against measured H_s and T_e (coloured by the mean deviance of the spectra within each bin) is shown in Figure 4.12 for the 4-parameter JONSWAP spectra fitted to data from buoy 46042. It is clear that overall the fitted H_s matches the measured H_s very well, but for the fitted spectra with higher deviance the difference in measured and fitted T_e can be significant. Overall though, the agreement is good, with a standard error in the fitted H_s of 4% and a bias of -0.04m and for T_e the standard error is 5.2% with a bias of 0.02s. The bias and standard error in H_s for the 3-parameter JONSWAP spectra was -0.17m and 7.5% and for T_e the figures are 0.50s and 15%. For the 6-parameter JONSWAP spectra bias and standard error in H_s was -0.02m and 2.2% and for T_e the figures are 0.007s and 3.9%. Note that it was initially attempted to force the fitted spectra to

match the measured H_s and T_e, but this was found to increase the deviance of the fitted spectra and bias and standard deviation of the estimated WEC power (discussed in Section 4.8).

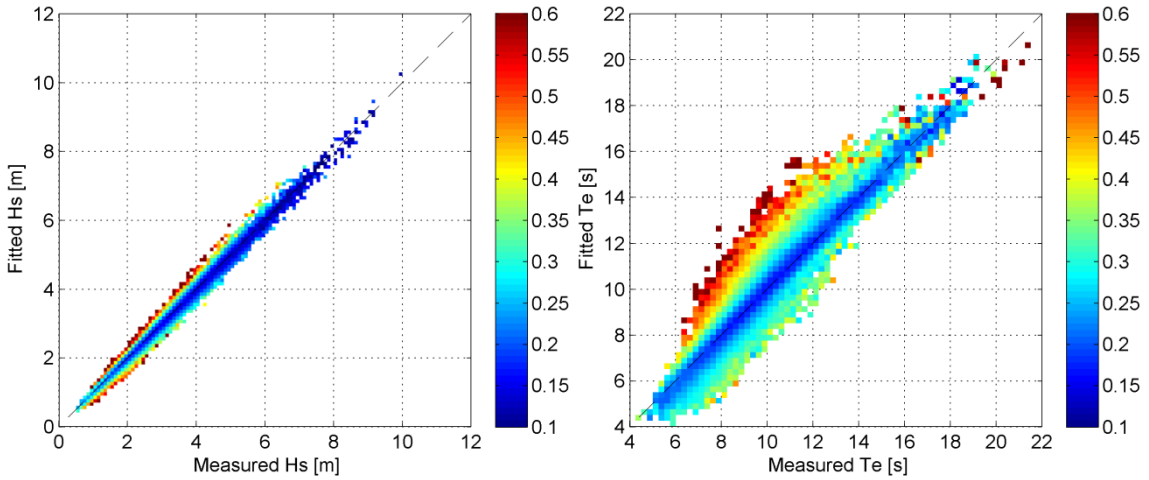

Figure 4.12. Left: Scatter plot of fitted H_s against measured H_s for the 4-parameter JONSWAP spectra. Right: Scatter plot of fitted T_e against measured T_e for the 4-parameter JONSWAP spectra. Colour denotes the mean deviance in each bin.

It is also interesting to consider the bias and standard deviation of the fitted spectral densities relative to the measured values. These are shown for each buoy in Figures 4.13-4.15. The patterns in bias and standard deviation for the three locations were broadly similar, relative to the position of the mean spectral peak. The Bretschneider spectra show a large positive bias of around 20-30% at frequencies around the mean spectral peak and a negative bias away from the peak. The size of the bias for the three parameter spectra is much lower, but follows a similar pattern in terms of where it is positive and negative, although at buoy 44014 all the 3-parameter spectra tend to underestimate spectral densities. The bias of the 4- and 6- parameter JONSWAP spectra is close except that the energy in the tail is slightly better estimated by the 6-parameter spectra due to its greater flexibility in shape. The standard deviations of the 3-parameter JONSWAP spectra close to the spectral peak are similar to those of the 4-parameter spectra, but the 4-parameter spectra have slightly lower standard deviations in the tail. This is because the 4 parameter spectra have a greater flexibility to adjust for differing levels of energy in the spectral tail.

The reason that the 4-parameter spectra are able to model a wide range of spectral shapes fairly accurately is that there are relatively few spectra which have a peakedness exceeding that of a JONSWAP spectrum with $\gamma = 2$ (a peakedness value of 1.60). As discussed in Section 4.3 the 4-parameter JONSWAP spectrum is able to model a wide range of spectral shapes lower peakedness values (see Figure 4.5). The distribution of spectral peakedness values measured for buoy 46042 and the mean peakedness binned by H_s and T_e are shown in Figure 4.16. The most peaked spectra occur in very steep conditions (strongly driven wind seas) and in long period swells, with the very longest swells having a mean peakedness of over 2. However, 93% of the spectra measured at buoy 46042 have a peakedness less than 1.6 and 99% have a peakedness less than 2.

The mean shape of measured and fitted JONSWAP spectra with a measured peakedness greater than 2 (a total of 2251 records) is shown in Figure 4.17. Note that the mean height of the normalised spectra is less than 2 as the location of the peak with T_e varies. Both the 3- and 6- parameter spectra do better than the 4-parameter spectra in these cases due to their ability to vary the peakedness of the spectrum, although 3-parameter JONSWAP spectrum slightly underestimates the energy in the tail.

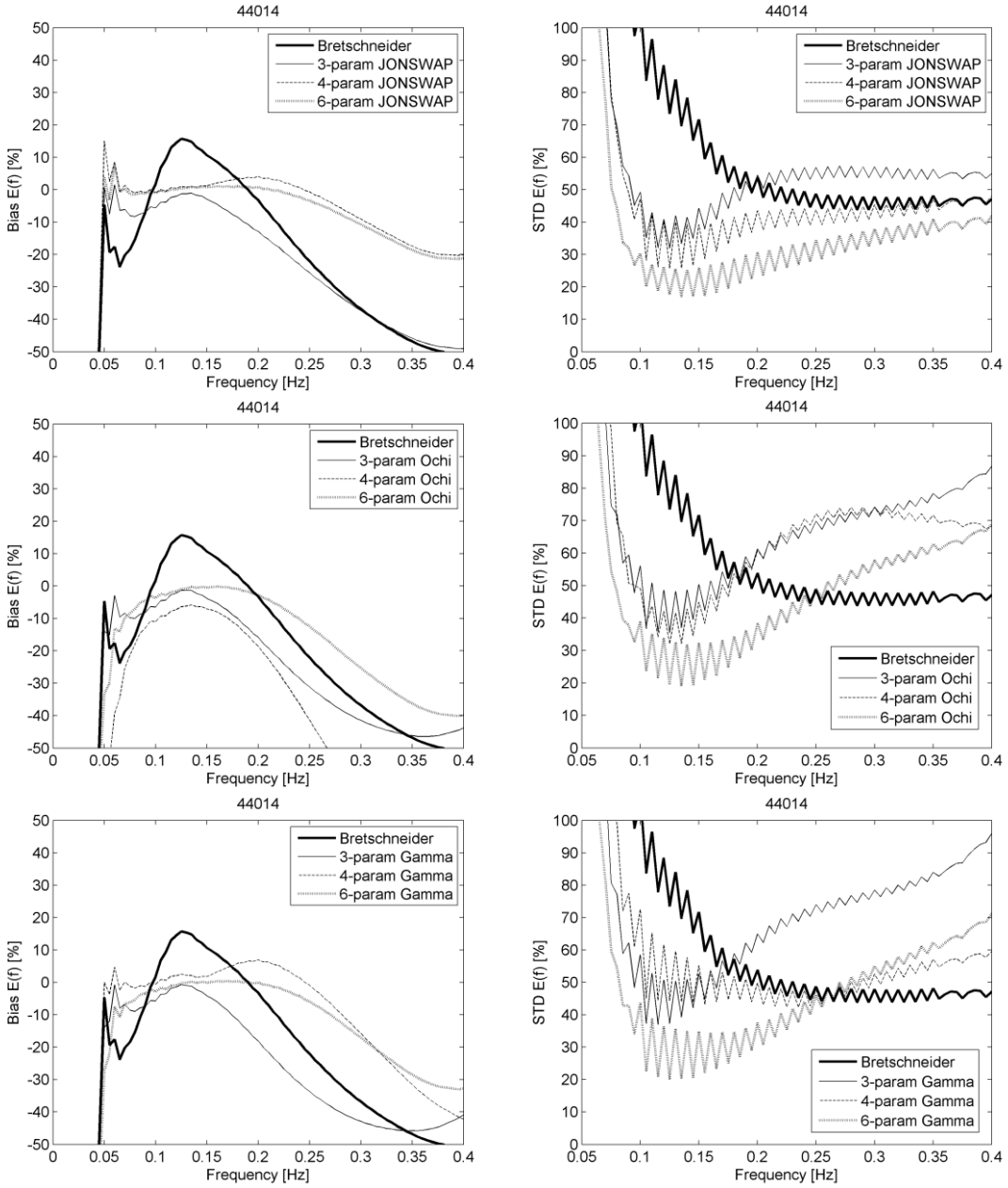

Figure 4.13. Bias and standard deviation in fitted spectra for buoy 44014.

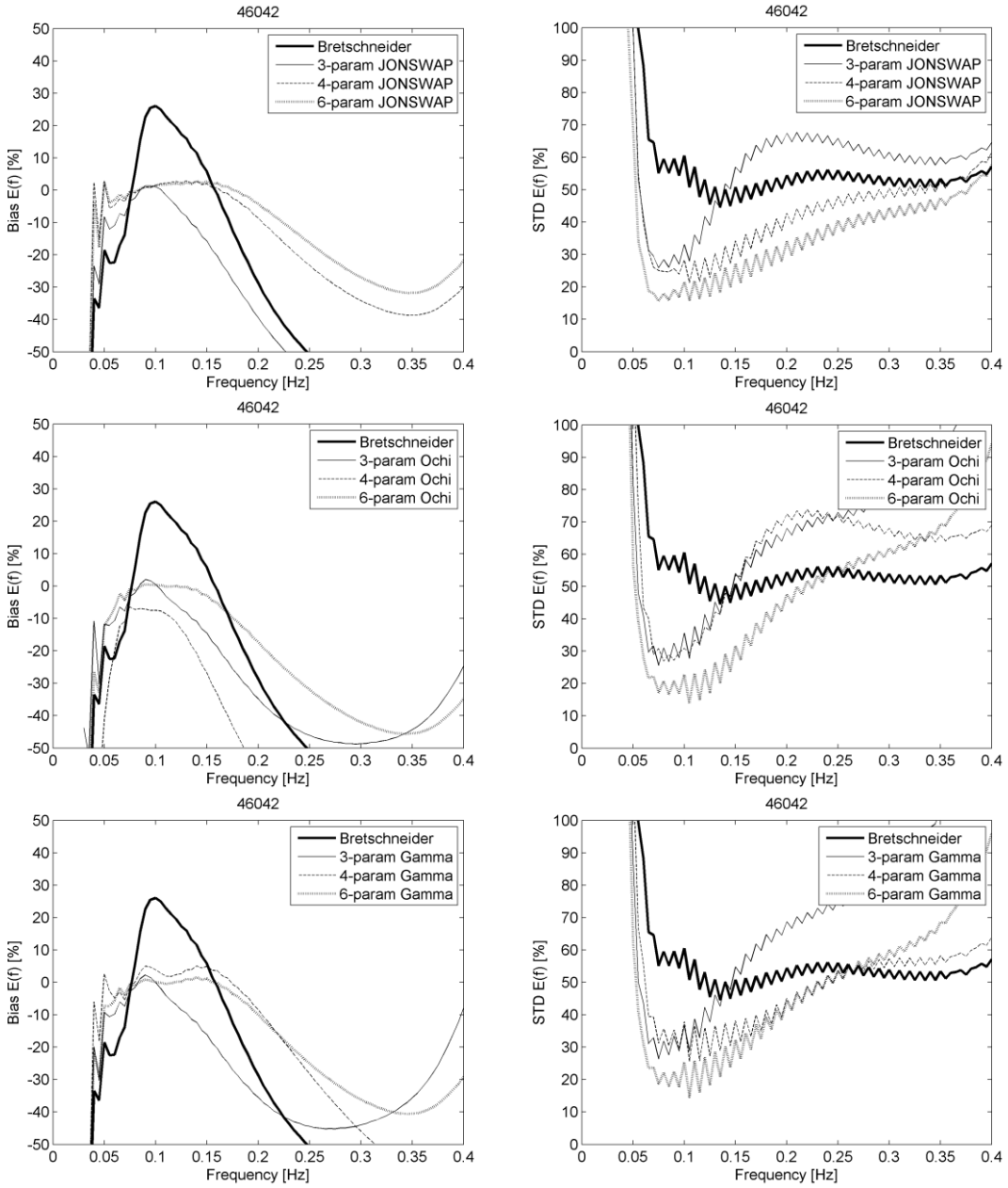

Figure 4.14. Bias and standard deviation in fitted spectra for buoy 46042.

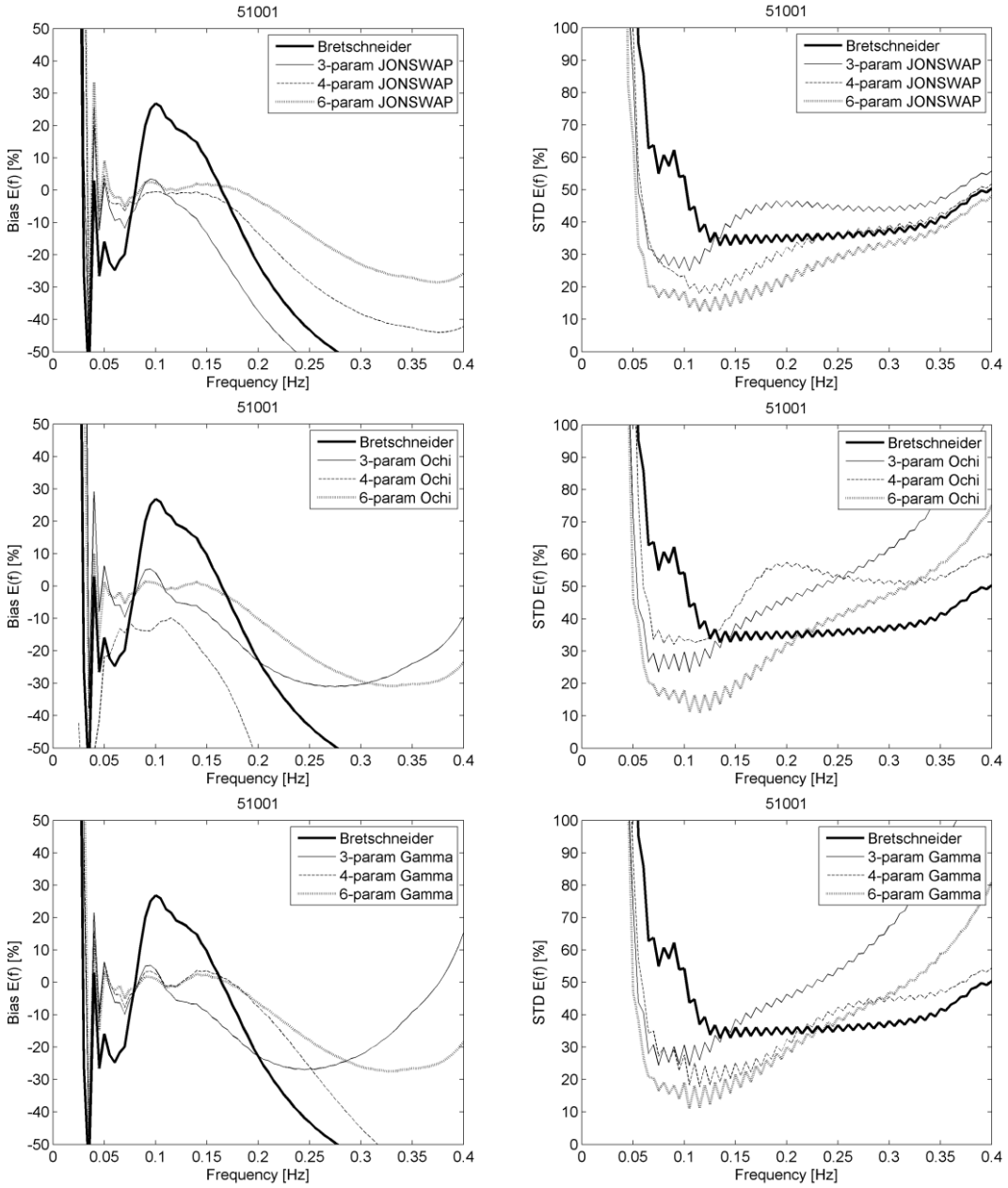

Figure 4.15. Bias and standard deviation in fitted spectra for buoy 51001.

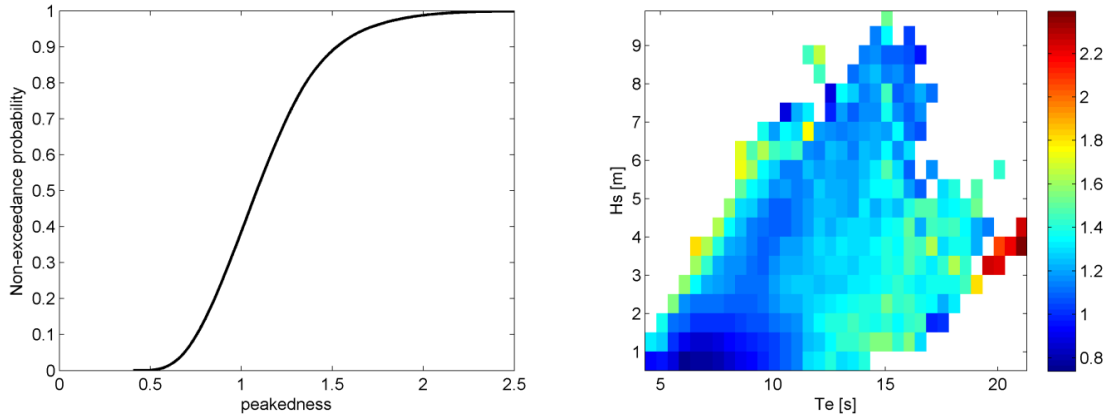

Figure 4.16. Left: distribution of peakedness of measured spectra at buoy 46042. Right: Mean peakedness of spectra measured at buoy 46042, binned by H_s and T_e.

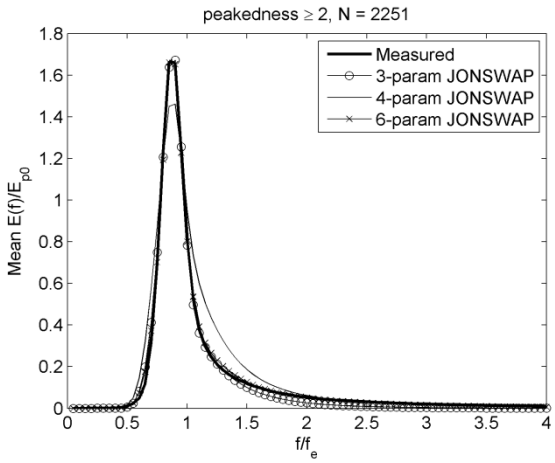

Figure 4.17. Mean normalised spectral shapes for measured and fitted spectra where the measured peakedness exceeds 2.

4.7 Analysis of observed shapes

Since the majority of spectra are well described by 4-parameter spectra, the parameterisation described in Section 4.3 can be used to examine the range of observed shapes. Data from buoy 46042 and the partitions of the 4-parameter JONSWAP spectra will be considered (although the parameters from the fitted Gamma spectra were close to these). Note that the partition parameters have been normalised by the H_s and T_e of the fitted spectra rather than the measured spectra.

The frequency of occurrence of spectra with various shapes, described by parameters H_{sn} and dT_n, is shown in Figure 4.18. For the cases where the fitting algorithm discarded the second partition as insignificant the normalised swell height has been set to one, the normalised wind sea height and normalised period separation are set to zero. These cases accounted for 6% of spectra at buoy 44014, but only 3% and 1% of spectra at buoys 46042 and 51001 respectively, due to the near-constant occurrence of swell at these locations. Despite the differences in the wave climates, the range of observed partition parameters was similar at all three locations, being mainly clustered around higher values of H_{sn}^2 and dT_n in the range 0.25 – 1, corresponding to a dominant swell peak with a smaller

wind sea. Values of dT_n greater than one are relatively rare, with 96% of spectra having $dT_n < 1$ and 99.8% having $dT_n < 1.5$.

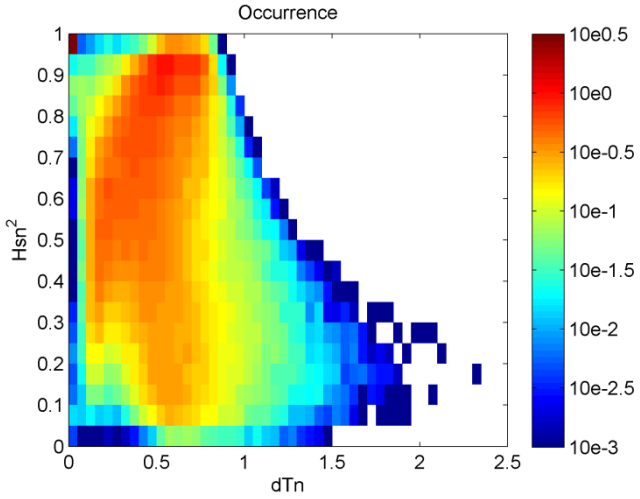

Figure 4.18. Occurrence of partition parameters from buoy 46042. Colour scale denotes percentage occurrence.

Figure 4.19 shows the range of observed H_{sn}^2 and dT_n, binned by H_s and T_e, for 2.25m $\leq H_s \leq$ 2.75m, (consisting of 29,499 records) and T_e in bins of size 1s. The observed range of parameters nearly all fall within the predicted bounds corresponding to $s_{ew} = 0.06$ and $T_{es} = 25$s, with only a couple falling just outside the bounds. However, the observed range of parameters does not always fill the range of valid parameter space, with values of dT_n greater than 1 being rare. The predicted bounds corresponding to $s_{ew} = 0.06$ and $T_{es} = 25$s were found to be equally valid over the entire range of H_s.

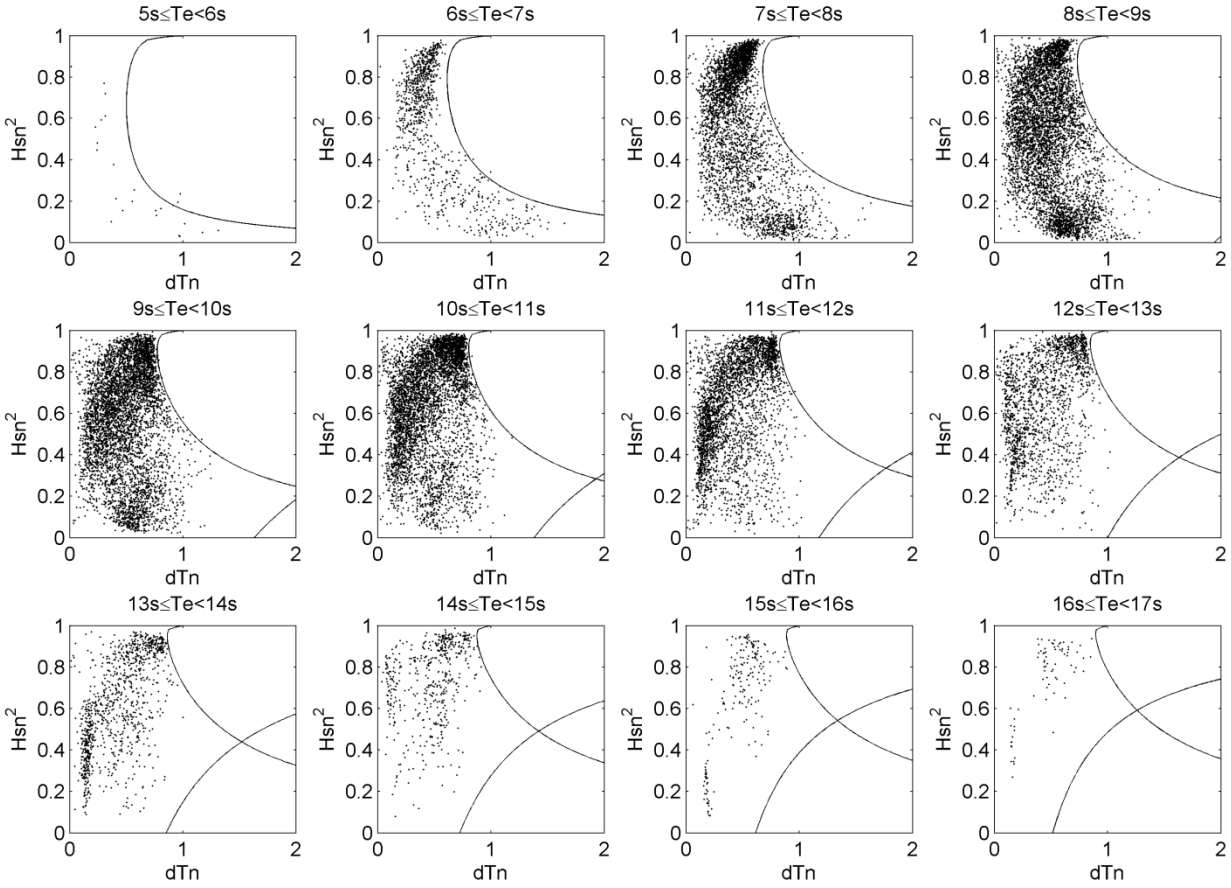

Figure 4.19. Observed range of partition parameters from buoy 46042 for spectra within the range $2.25 \leq H_s \leq 2.75$m, binned by T_e. Bounding lines of $s_{ew} = 0.06$ and $T_{es} = 25$s are also shown.

Fitting spectra with two-peaked models and using the parameterisation described above provides a powerful method of sorting spectral shapes. Figure 4.20 shows the observed range of spectral shapes for buoy 46042, sorted by the fitted values of H_{sn}^2 and dT_n, in bins of size 0.05 × 0.05 for a subset of bins (at a resolution of 0.05×0.05 there are 800 bins covering the area $0 \leq H_{sn}^2 \leq 1$, $0 \leq dT_n \leq 2$). Frequencies have been normalised by f_e and spectral densities have been normalised by E_{p0}. For each bin shown, the mean spectral shape is shown together with the 5%-95% range of spectral densities at each normalised frequency. It worth emphasising that these bounds cover *all* observed spectra, not just those for a restricted range of H_s and T_e. Even without considering the peakedness of each partition the method is highly effective at sorting spectral shapes, with the 90% confidence intervals for the spectral shapes being relatively narrow compared to the confidence intervals for the spectral estimates themselves (see Table 4.4). However, the width of the confidence interval below the spectral peak is often somewhat wider than would be expected from sampling variability alone, indicating that there are some small swell components which are not captured by the 4-parameter JONSWAP spectra.

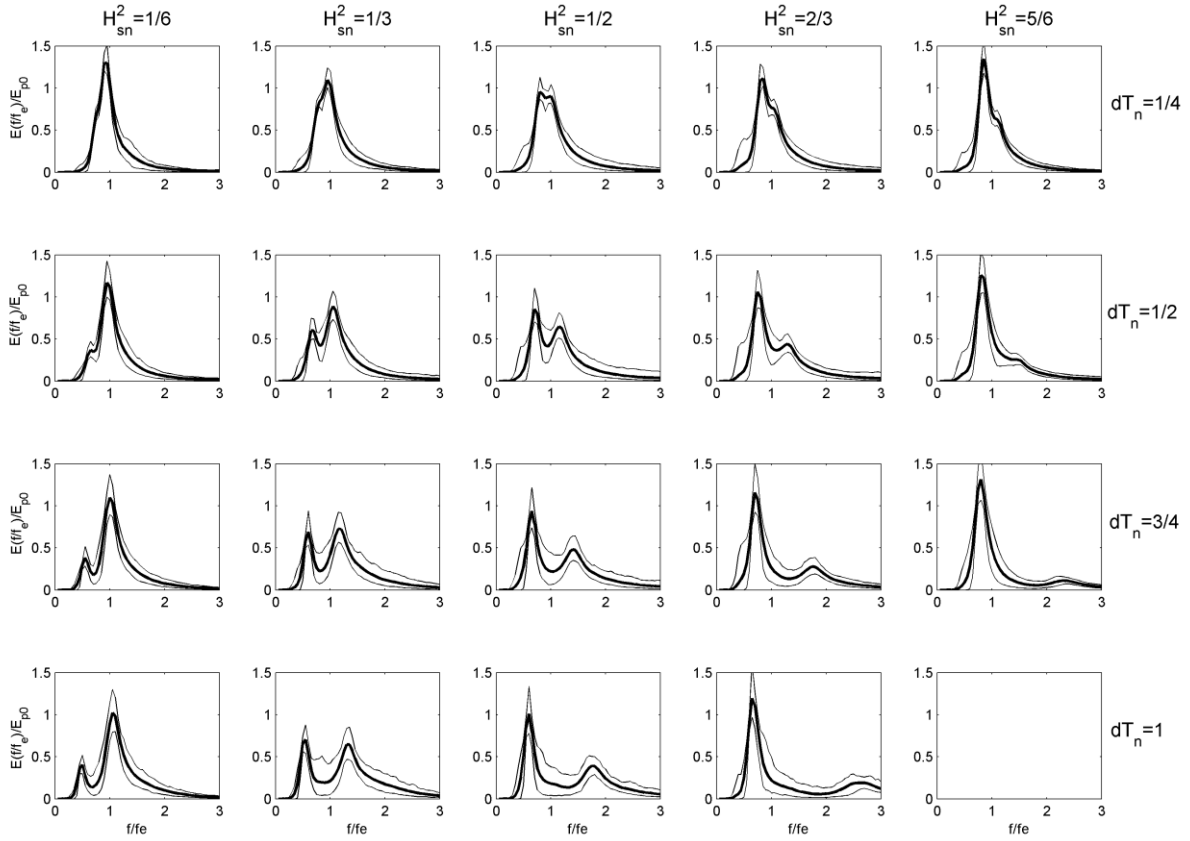

Figure 4.20. Observed range of spectral shapes from buoy 46042 for a range of normalised swell heights and normalised period separations. Frequencies have been normalised by f_e and spectral densities are normalised by E_{p0}. Bold lines show mean spectra within each bin, thin lines show the 5%-95% range at each normalised frequency.

4.8 Effect of parameterisation on the accuracy of energy yield prediction

As discussed in D1b, there is a compromise between the number of parameters used to describe a sea state (and hence the number of numerical simulations required to predict the response over the entire climate) and the accuracy of the predicted energy yield. Recently Saulnier et al. (2011) presented a study on the use of various spectral bandwidth parameters for performance assessment of WECs (used in addition to H_s and T_e). It was shown that while the use of certain bandwidth parameters can improve the accuracy of predicted performance of certain WECs at certain locations over certain ranges of conditions, there was no single bandwidth parameter which was effective at predicting performance of all WEC types at all locations, over all conditions. These results suggest that three parameters are still insufficient for predicting the performance of a WEC. This was mirrored in the results presented in Section 4.6 which showed that while including a third parameter improves the fit of the spectra (i.e. the description of the spectrum and therefore hopefully the WEC response) compared to Bretschneider spectra, the use of 4-and 6-parameter models significantly improves the fit .

The effect of the use of the various parameterisations discussed in the preceding sections on the predicted energy yield of several theoretical WECs will be investigated in this section. To obtain preliminary results regarding the effects of wave climate parameterisation on the energy yield, the response of a WEC will be predicted using a linearised capture width curve, defined as a function of frequency. In reality nonlinearities introduced by e.g. the hydrodynamic response, PTO and mooring forces will mean that the capture width curve will depend on both the sea state and applied forces (namely the PTO and moorings). Nevertheless, the work conducted as part of WG1 WP2 on spectral modelling of WECs has indicated that a linearised response can be used for each sea state in a spectral

approach, with potential applications in energy yield estimates for large arrays of WECs (see WG1 WP2 D1).

In this exercise instead of using a capture width curve which varies with the sea state (as would be the case for a realistic WEC), four curves will be used. This can be interpreted as representing either different WEC types or the changing response of a single WEC type with sea state or applied forces. The four curves used are shown in Figure 4.21. They represent devices with a narrowband response with peaks at 0.075 Hz, 0.1 Hz and 0.14 Hz and a broadband response centred at 0.1Hz. All curves have been normalised to have a peak capture width of 1m. However, results are presented in terms of percentage bias and standard deviation, so this normalisation does not affect the results. Although the capture width curves of individual devices may vary considerably in shape from the curves used here, the use of different peak response frequencies, response bandwidths and different wave climates should give a first indication of the accuracy of the use of various sea state parameterisations.

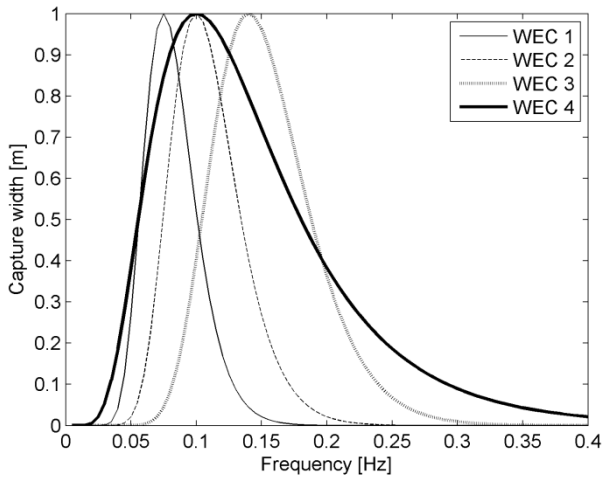

Figure 4.21. Capture width curves for example WECs

The mean power transported per meter crest length is given by

$$P = \rho g \int_0^\infty c_g(f,h) E(f) \mathrm{d}f \qquad [4.32]$$

where ρ is the water density, g is the acceleration due to gravity, $c_g(f,h)$ is the wave group velocity, h is the water depth, and $E(f)$ is the omnidirectional spectral density. Using the capture width curves a similar equation can be used to calculate the mean power output of a WEC for a given spectrum:

$$P_{WEC} = \rho g \int_0^\infty c_g(f,h) E(f) CW(f) \mathrm{d}f \qquad [4.33]$$

where $CW(f)$ is the capture width of the WEC. It is assumed for now that the WEC or array response is not sensitive to direction. This is a reasonable first approximation for single devices but may prove less reliable for arrays. The effect of this assumption will be investigated further in future work.

The accuracy of the predicted energy yield for various parameterisations will be considered by comparing the calculated power using the measured and fitted spectra for each individual spectrum. In a real situation the use of fitted spectra in this way does not provide any advantage over using the measured spectra as the same number of calculations of power must be made (on top of the spectral fitting itself). However, this comparison gives an indication of how well the parameterisation performs on the whole.

Results are presented in terms of the bias and standard deviation in power for each WEC type considered above, as a percentage of the mean power for that WEC calculated from the measured spectrum. Whilst the bias in mean power is the most important statistic for energy yield prediction, the standard deviation of the power from the measured versus fitted spectra is also important for optimising machine and array design.

The percentage bias and standard deviation in power for each WEC at each location are presented in Tables 4.7-4.9. Results for the 4-parameter Ochi spectra have been excluded due to its poor performance in describing spectral shapes. The biases in the predicted power binned, by H_s and T_e, for the Bretschneider and JONSWAP spectra are shown in Figures 4.22-4.25.

The Bretschneider spectra give a significant bias in the mean power prediction which varies with both location and WEC response. The size of the bias is lowest where the peak WEC response is closest to the peak of the mean spectrum, but can be of the order 8-12% when the peak WEC response is further away from the mean spectral peak. Figure 4.22 shows that for certain H_s and T_e the bias in the predicted response can be very large - of the order ±100%. However, these sea states account for a relatively small amount of the total available power so do not strongly affect the results. Note that in this example since the WEC response is assumed to be linear the bias could have been calculated by multiplying the bias in fitted spectra (Figures 4.13-4.15) by the WEC capture width curve. The standard deviation in the power estimates from the Bretschneider spectra is uniformly high for WECs 1-3 which have a narrow bandwidth response but is significantly lower for WEC 4 which has a broader bandwidth response.

All the 3-parameter spectra tended to underestimate the mean power of each WEC, which is unsurprising considering that the 3-parameter spectra tended to underestimate the spectral densities at frequencies above and below the spectral peak. The standard deviations tended to be lower than that from the Bretschneider spectra for the narrowband WECs (1-3) but somewhat surprisingly gave larger standard deviations and biases than using the Bretschneider spectra for WEC 4. This is because in many conditions WEC 4 captures around 80%-90% of the available power and the Bretschneider spectra are forced to have the same total power as the measured spectra (since they have the same H_s and T_e).

The 4-parameter spectra showed very little bias in power for all WEC types and all locations. Figure 4.24 shows that the bias does not vary much with H_s and T_e. For $T_e < 6$s the power for WEC 1 is significantly underestimated. Figure 4.26 shows the mean measured and fitted 4-parameter JONSWAP spectrum for seas with $T_e < 6$s. It is clear that the reason that the power for WEC 1 is underestimated is that the 4-parameter JONSWAP spectrum underestimates the small swell component in the mean measured spectrum which occurs at the peak response frequency of WEC 1. Similarly the power for WECs 2 and 3 is overestimated for longer period spectra where the measured spectra tend to be more peaked than the 4-parameter JONSWAP spectrum. Figure 4.26 also shows the mean measured and fitted 4-parameter JONSWAP spectrum for seas with $2 \leq H_s \leq 3$m and $12 \leq T_e \leq 13$s. The amount of energy between 0.1 and 0.15Hz, where WECs 2 and 3 are tuned, is overestimated by the 4-parameter JONSWAP spectra, resulting in the positive bias. The standard deviation from the 4-parameter JONSWAP spectra was also significantly lower than for the Bretschneider spectra for WECs 1-3 and a similar size for WEC 4.

The 6-parameter spectra did not significantly improve the bias in estimate of mean power over the 4-parameter spectra (and were even slightly worse at buoy 44014), but the pattern of bias with H_s and T_e was more constant than for the 4-parameter spectra (see Figure 4.25). However the standard deviation in power estimation does reduce for the 6-parameter spectra, especially at buoy 44014.

Type	WEC 1		WEC 2		WEC 3		WEC 4	
	Bias [%]	STD [%]	Bias [%]	STD [%]	Bias [%]	STD [%]	Bias [%]	STD [%]
Bretschneider	-6.9	28.7	2.9	22.5	8.8	20.5	2.2	8.1
3P JONSWAP	-5.9	28.6	-4.5	16.6	-4.0	15.1	-5.1	13.8
3P Ochi	-7.4	22.3	-5.3	15.9	-4.7	17.1	-6.2	15.0
3P Gamma	-6.4	21.3	-4.7	15.3	-4.7	18.8	-5.8	14.7
4P JONSWAP	-0.1	21.2	0.1	10.6	1.0	9.9	0.4	11.9
4P Gamma	-0.4	15.8	0.6	9.1	2.1	9.1	0.9	10.1
6P JONSWAP	-0.6	11.2	-0.3	4.5	0.3	3.9	-0.2	4.4
6P Ochi	-5.9	13.5	-3.2	7.7	-1.5	5.9	-3.5	7.3
6P Gamma	-4.3	12.6	-2.2	7.0	-0.7	4.2	-2.3	6.2

Table 4.7. Bias and standard deviation in power prediction from fitted spectra for buoy 44014.

Type	WEC 1		WEC 2		WEC 3		WEC 4	
	Bias [%]	STD [%]	Bias [%]	STD [%]	Bias [%]	STD [%]	Bias [%]	STD [%]
Bretschneider	0.6	18.0	13.1	20.2	13.1	16.6	5.5	8.6
3P JONSWAP	-4.3	11.4	-2.7	11.4	-8.3	24.3	-5.6	10.2
3P Ochi	-4.1	10.1	-2.8	10.3	-8.2	20.3	-5.4	9.8
3P Gamma	-3.8	10.0	-3.0	10.5	-9.1	20.6	-5.5	9.7
4P JONSWAP	-1.2	8.2	0.5	8.5	1.1	11.8	-0.5	8.2
4P Gamma	-0.5	7.1	1.9	7.5	2.5	8.1	0.5	6.7
6P JONSWAP	-0.7	4.0	0.6	4.2	1.4	6.4	-0.1	3.4
6P Ochi	-2.3	5.4	-0.8	3.8	-1.9	7.7	-2.4	4.3
6P Gamma	-1.8	5.3	-0.4	3.2	-0.4	5.2	-1.5	3.7

Table 4.8. Bias and standard deviation in power prediction from fitted spectra for buoy 46042.

Type	WEC 1		WEC 2		WEC 3		WEC 4	
	Bias [%]	STD [%]	Bias [%]	STD [%]	Bias [%]	STD [%]	Bias [%]	STD [%]
Bretschneider	-1.9	19.7	12.3	21.2	13.6	12.6	5.1	9.0
3P JONSWAP	-5.0	12.3	-2.9	11.0	-7.9	20.6	-5.8	9.9
3P Ochi	-2.6	8.6	-1.3	8.1	-5.2	15.7	-3.2	7.6
3P Gamma	-2.7	9.1	-1.5	8.5	-5.6	15.9	-3.5	7.8
4P JONSWAP	-3.2	8.9	-2.0	7.9	-2.0	9.1	-2.7	7.5
4P Gamma	-1.9	7.7	0.0	6.3	0.6	6.0	-0.9	6.0
6P JONSWAP	-1.0	5.1	0.3	4.8	0.8	4.6	-0.2	3.8
6P Ochi	-1.8	4.8	-0.6	3.5	-0.8	5.2	-1.4	3.4
6P Gamma	-1.3	4.7	-0.3	2.9	0.0	3.0	-0.8	2.9

Table 4.9. Bias and standard deviation in power prediction from fitted spectra for buoy 51001.

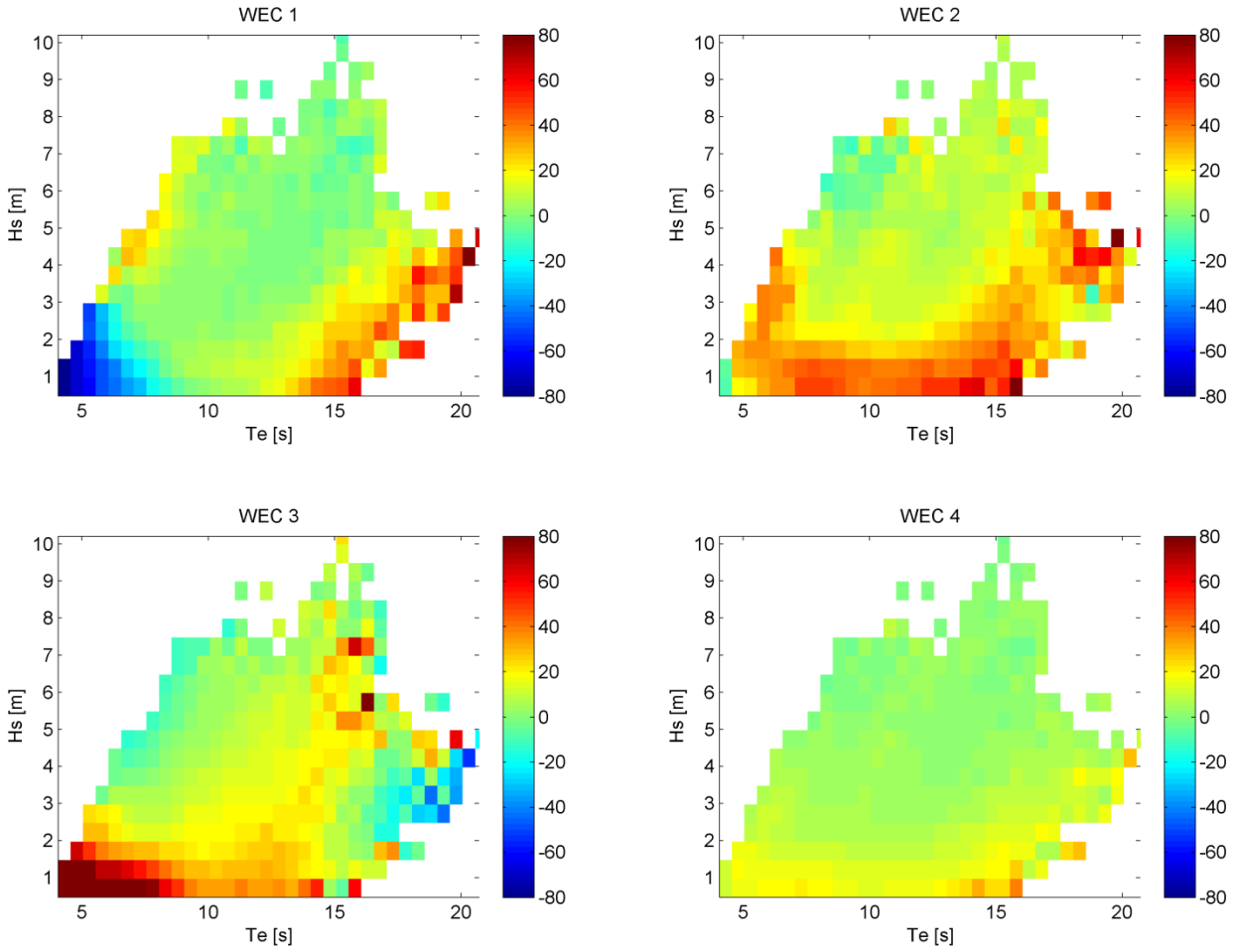

Figure 4.22. Percentage bias in power prediction from Bretschneider spectra, binned by H_s and T_e for buoy 46042.

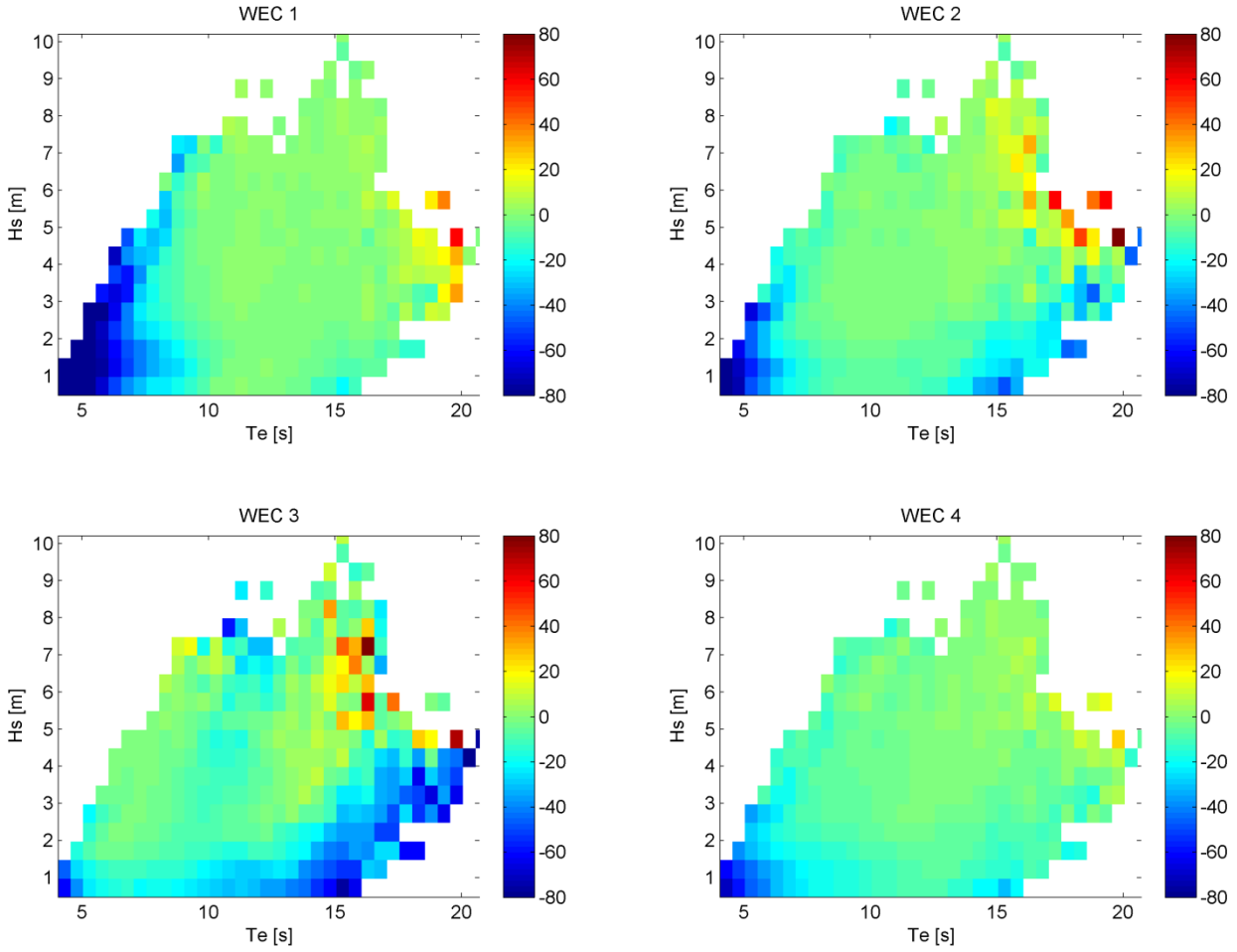

Figure 4.23. Percentage bias in power prediction from 3-parameter JONSWAP spectra, binned by H_s and T_e for buoy 46042.

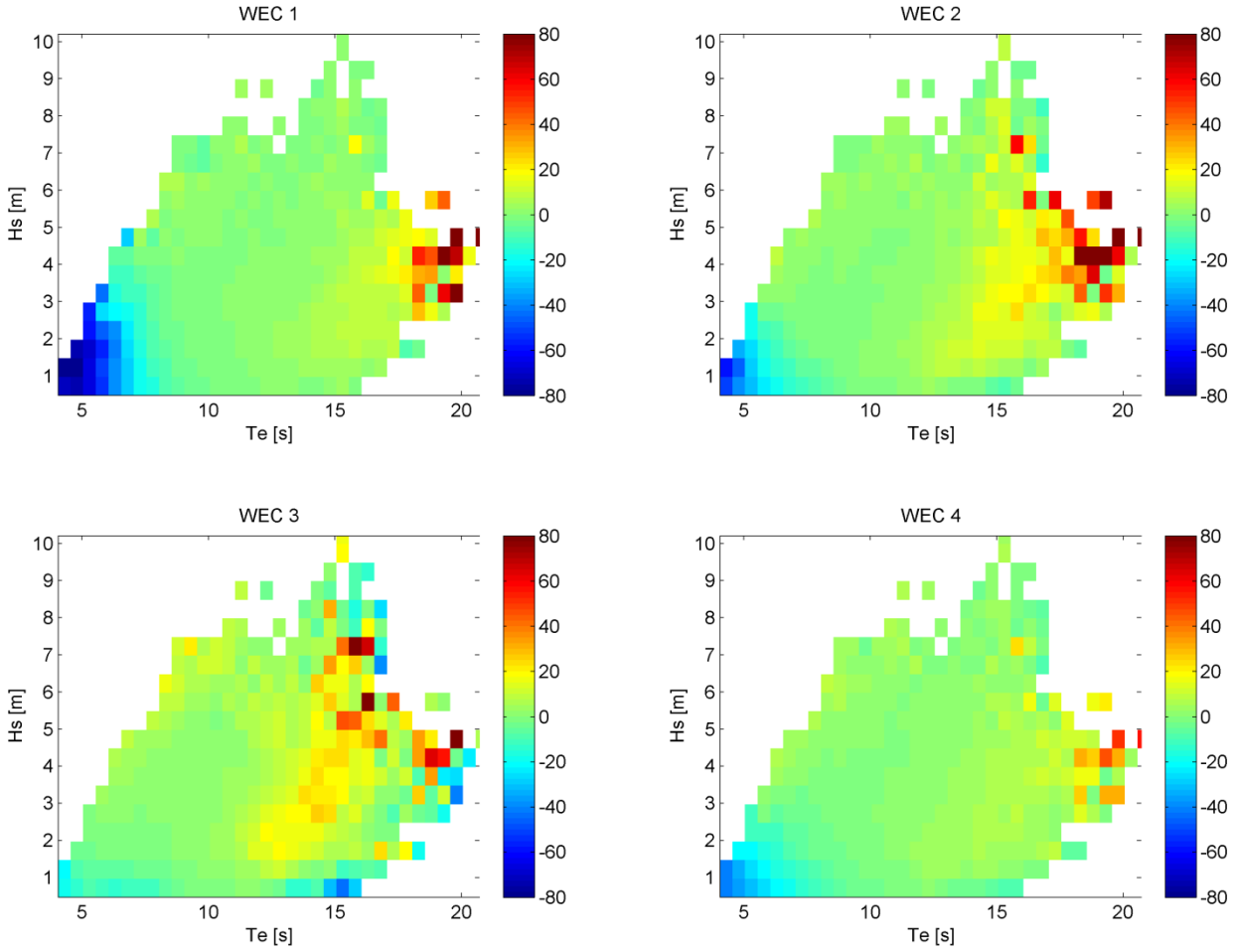

Figure 4.24. Percentage bias in power prediction from 4-parameter JONSWAP spectra, binned by H_s and T_e for buoy 46042.

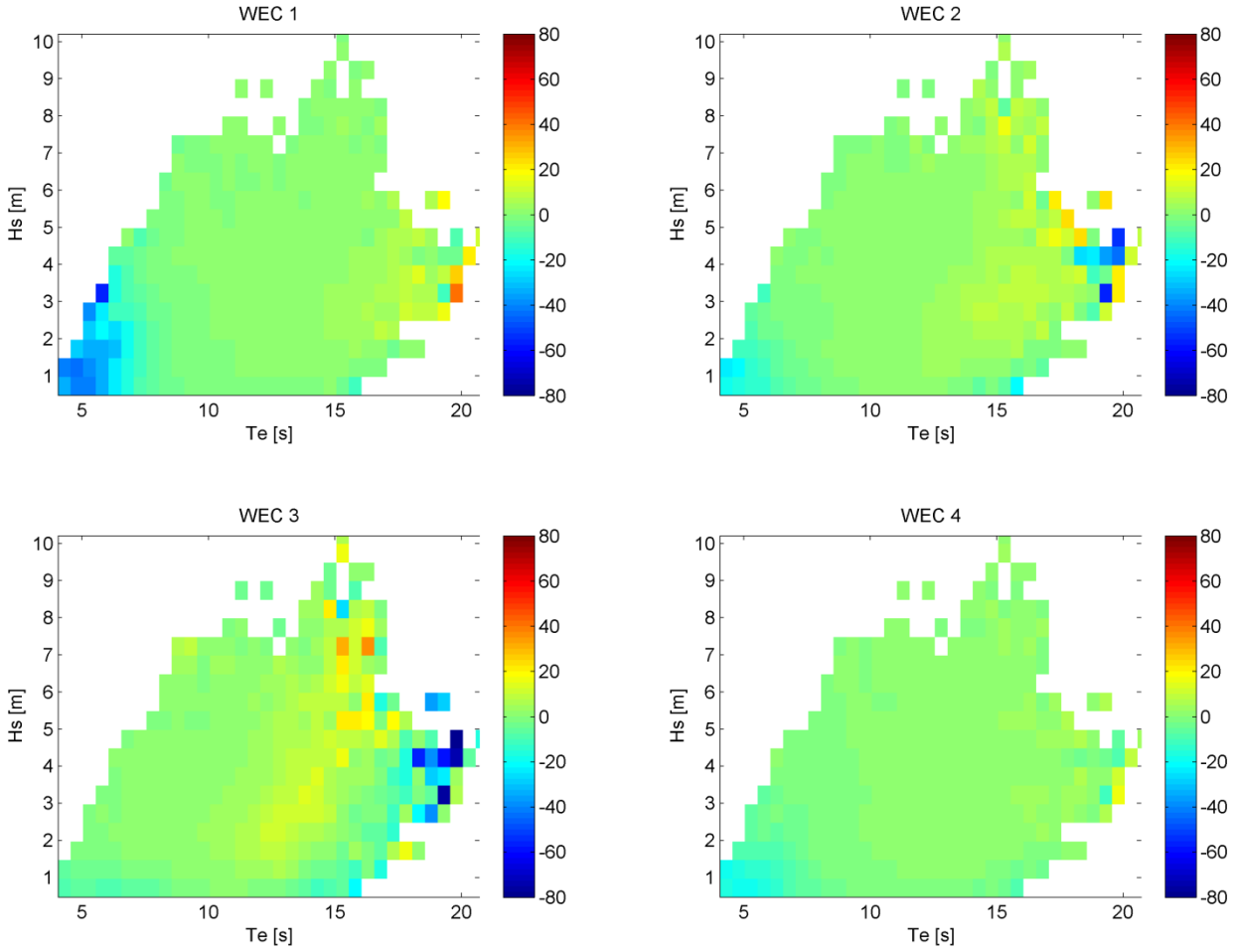

Figure 4.25. Percentage bias in power prediction from 6-parameter JONSWAP spectra binned, by H_s and T_e for buoy 46042.

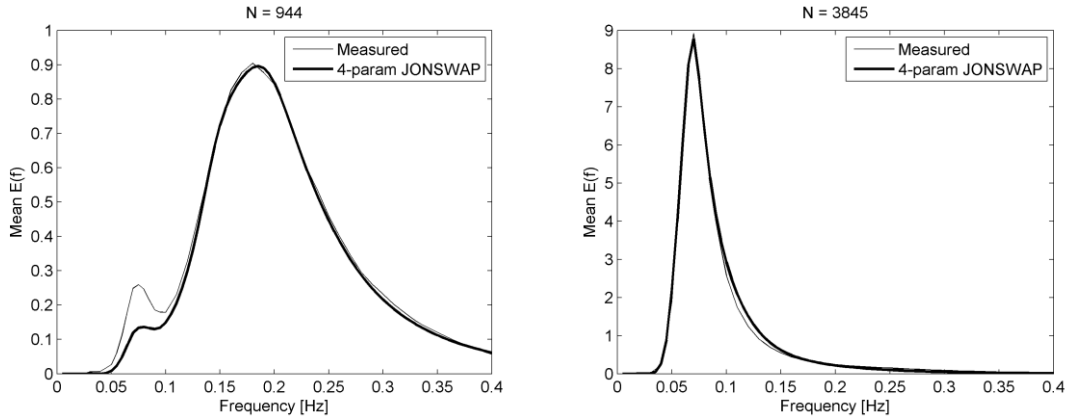

Figure 4.26. Mean measured and fitted 4-parameter JONSWAP spectrum for data from buoy 46042. Left: spectra with $T_e \leq 6$s. Right: spectra with $2 \leq H_s \leq 3$m and $12 \leq T_e \leq 13$s.

If it is assumed now that the response shown in Figure 4.21 are relative capture widths (i.e. with units W/m), then the ratio P_{WEC} / P is the fraction of the available power captured by the WEC. As in this

example the WEC response is assumed to be linear, this ratio is dependent only on T_e and the shape of spectrum and not on H_s. The percentage of available power captured by each WEC is shown in Figures 4.27-4.30, plotted against H_{sn}^2 and dT_n of the fitted 4-parameter JONSWAP spectra and binned by T_e, using data from buoy 46042. Note that this is the power capture calculated using measured spectra rather than the fitted spectra, and the fitted spectra are only used to sort the data. These plots show the variation in percentage power capture with T_e and spectral shape. The wide range of power capture for a given T_e – up to a factor of 4 – due to the variability in spectral shape is clear. It is also clear that the variation in power for a given T_e seems to be well determined by the parameters H_{sn} and dT_n. This is evident from the strong banding of the response with H_{sn} and dT_n. This is perhaps unsurprising since the fitted values of H_{sn} and dT_n were shown to provide a powerful method of sorting spectral shapes (see Figure 4.20). For all the WECs the response for values of dT_n close to zero and H_{sn} close to zero or one is roughly constant for a given T_e, since these all correspond to a spectrum close to a unimodal JONSWAP spectrum with $\gamma = 2$. Performance generally decreases as the peak separation increases and central values of H_{sn}^2. However, for the narrowband WECs (1-3) the performance can have an s-shaped profile with H_{sn}^2 at larger dT_n (i.e. for fixed dT_n the performance decreases, increases and decreases again as H_{sn} varies). This occurs in sea states with T_e close to the WEC's peak response where either a large swell or wind sea peak coincides with the WECs peak response (see e.g. the response of WEC 1 for $9 \leq T_e \leq 9.5$s).

It is also interesting to plot the bias in the predicted power from the fitted spectra in this way. Figures 4.31 and 43.2 show the bias in the power predicted for WEC 1 from Bretschneider and 4-parameter JONSWAP spectra. The Bretschneider spectra have a bias which varies significantly for each T_e, but the 4-parameter JONSWAP spectra generally have a relatively low and constant bias. The bias at low values of T_e is caused by the underestimation of swell in these cases, discussed previously.

From the discussion above it is clear that assuming a Bretschneider spectrum in place of the measured spectra can give a significant bias in the predicted energy yield and high standard deviation in the response for individual sea states. The use of the 3-parameter spectra considered here generally results in a negative bias, but the 4- and 6-parameter spectra give almost unbiased predictions with low standard deviation in the predicted response. It should be emphasised that such findings are preliminary, as other capture width or equivalent WEC performance parameterisations may lead to other conclusions. This issue will be addressed in the development programme leading to the Beta 2 version of the PerAWaT (wave) software tool(s). Nevertheless the results are encouraging in what concerns the ability of using a 4- and 6- parameter spectra to describe the local wave climate without compromising the energy yield estimate (when compared to the use of the measured spectra).

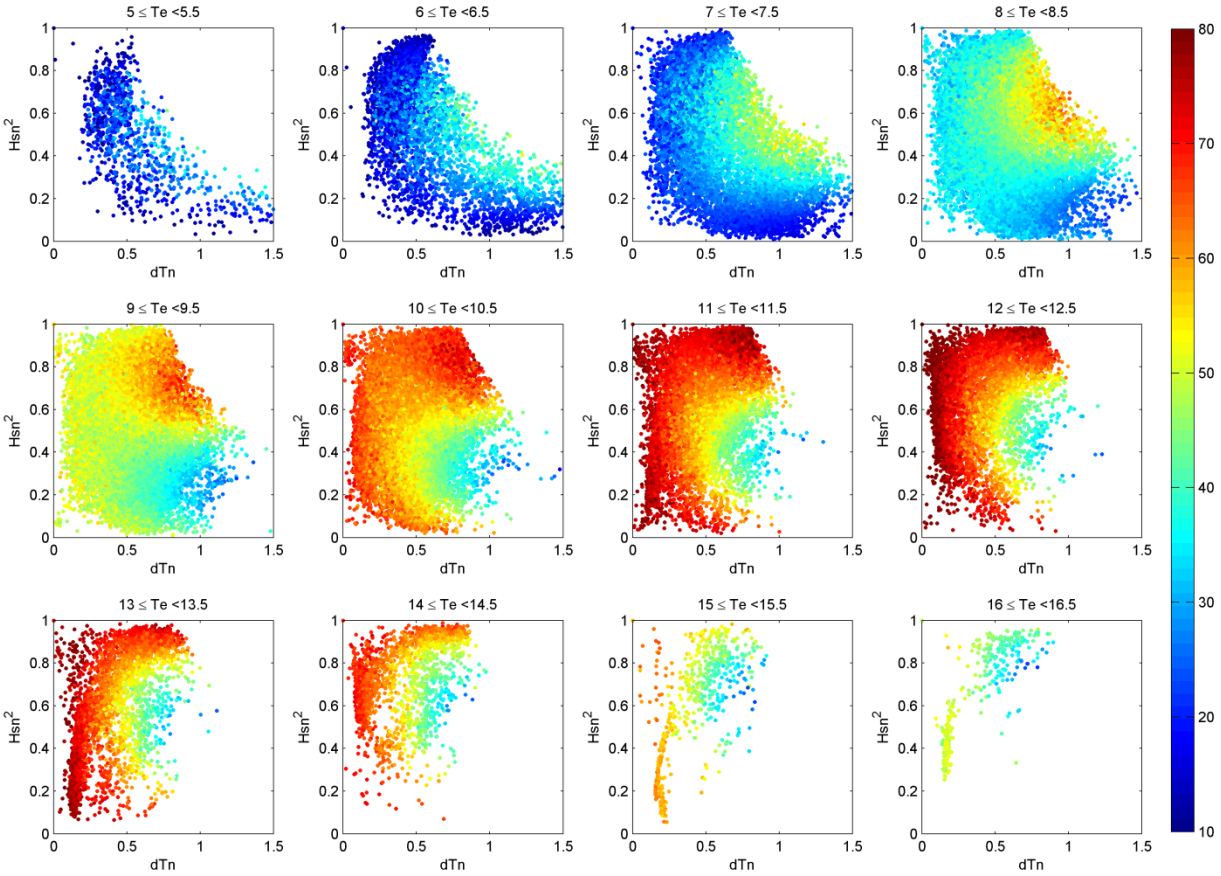

Figure 4.27. Percentage of available power absorbed by WEC 1 (colour scale) plotted against H_{sn}^2 and dT_n of fitted 4-parameter JONSWAP spectra for data from buoy 46042, binned by T_e.

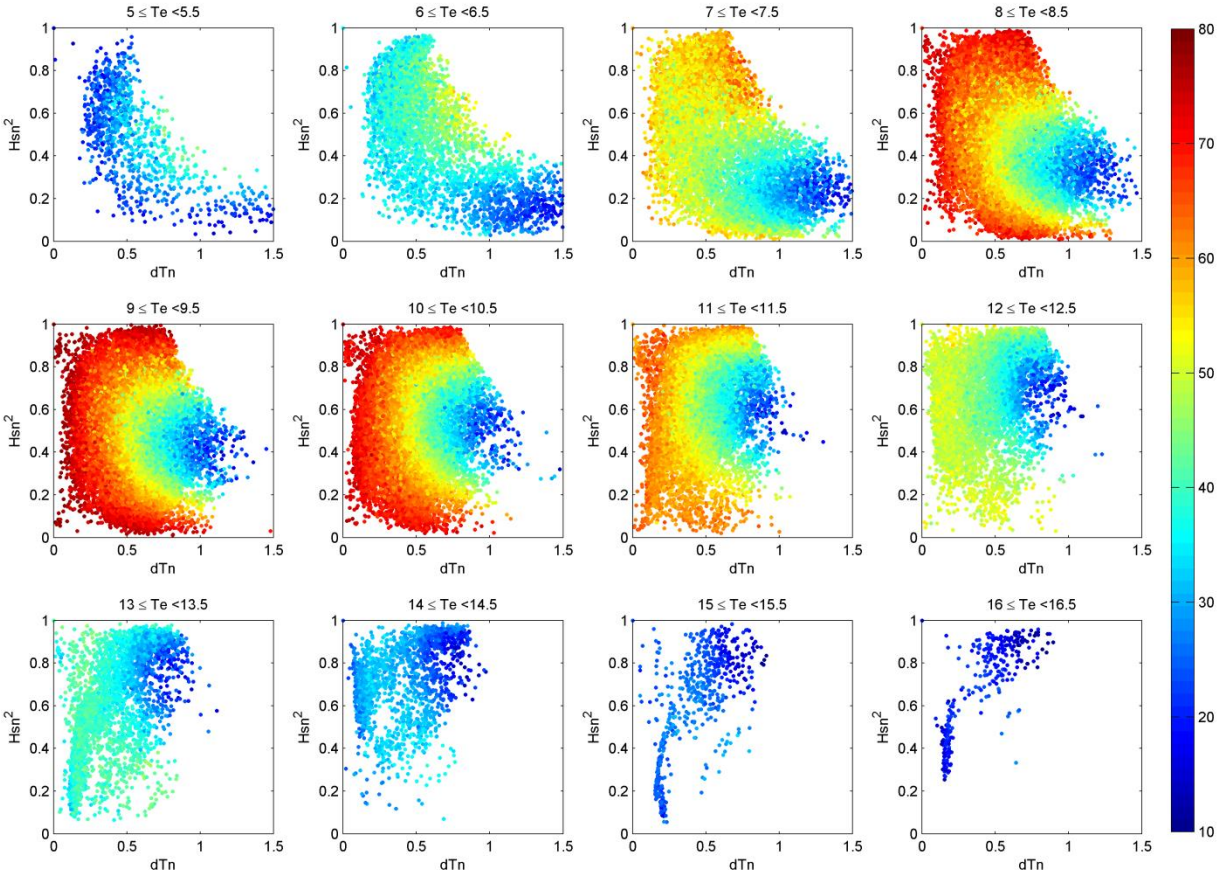

Figure 4.28. Percentage of available power absorbed by WEC 2 (colour scale) plotted against H_{sn}^2 and dT_n of fitted 4-parameter JONSWAP spectra for data from buoy 46042, binned by T_e.

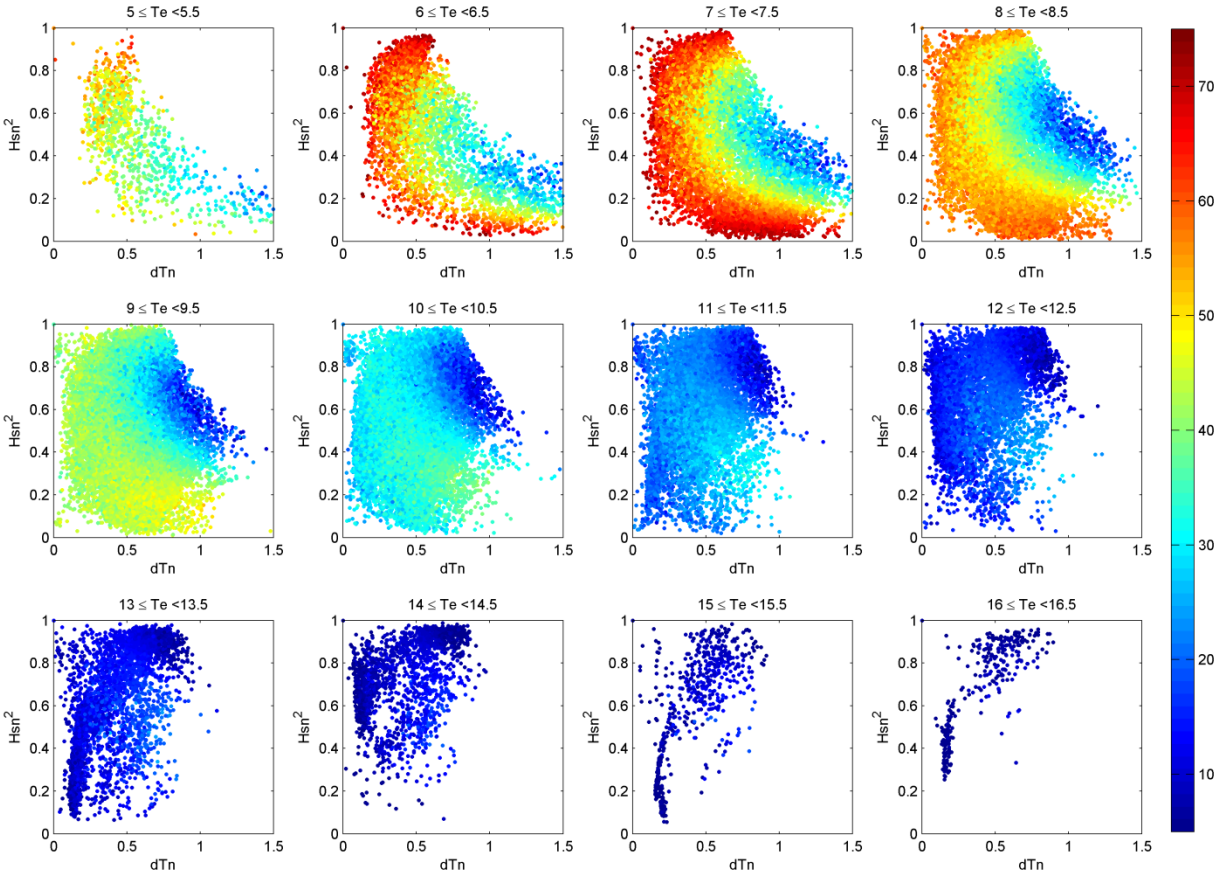

Figure 4.29. Percentage of available power absorbed by WEC 3 (colour scale) plotted against H_{sn}^2 and dT_n of fitted 4-parameter JONSWAP spectra for data from buoy 46042, binned by T_e.

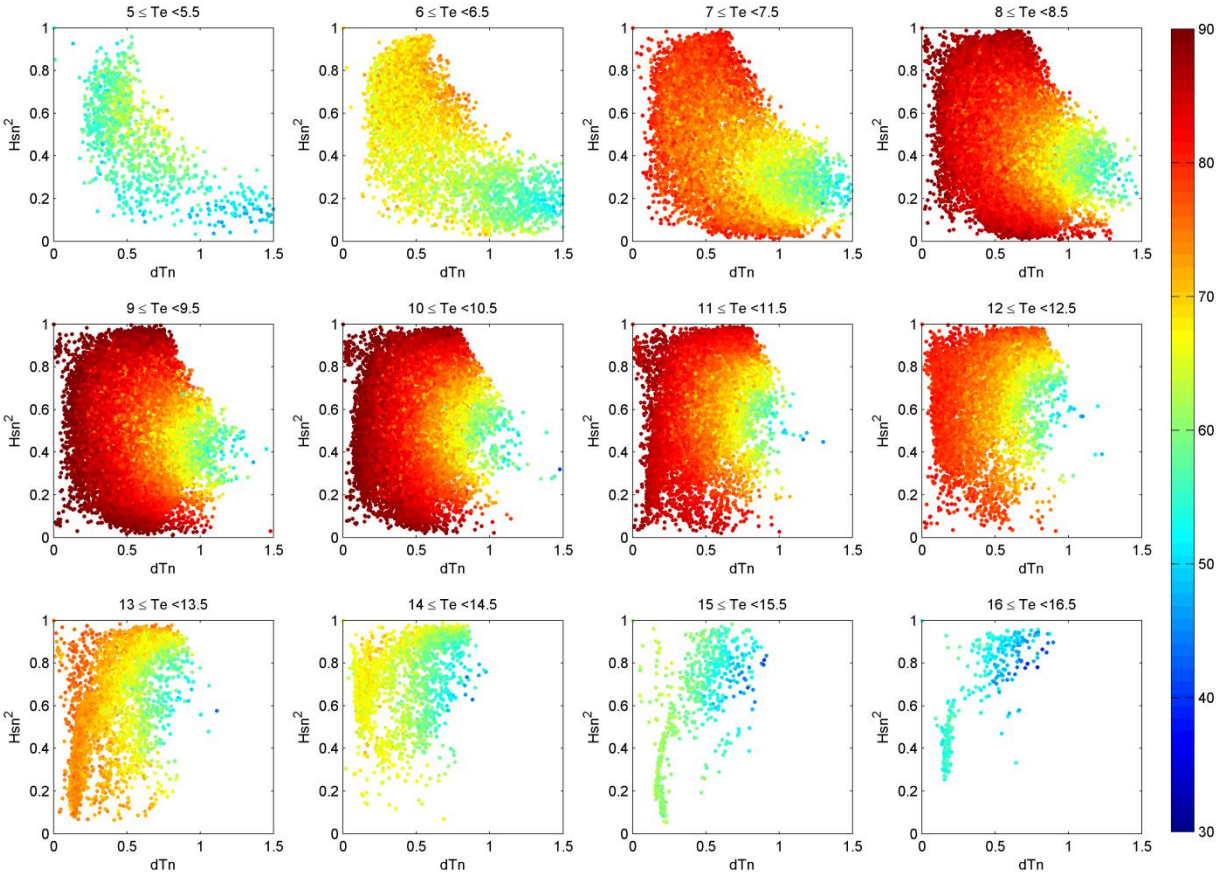

Figure 4.30. Percentage of available power absorbed by WEC 4 (colour scale) plotted against H_{sn}^2 and dT_n of fitted 4-parameter JONSWAP spectra for data from buoy 46042, binned by T_e.

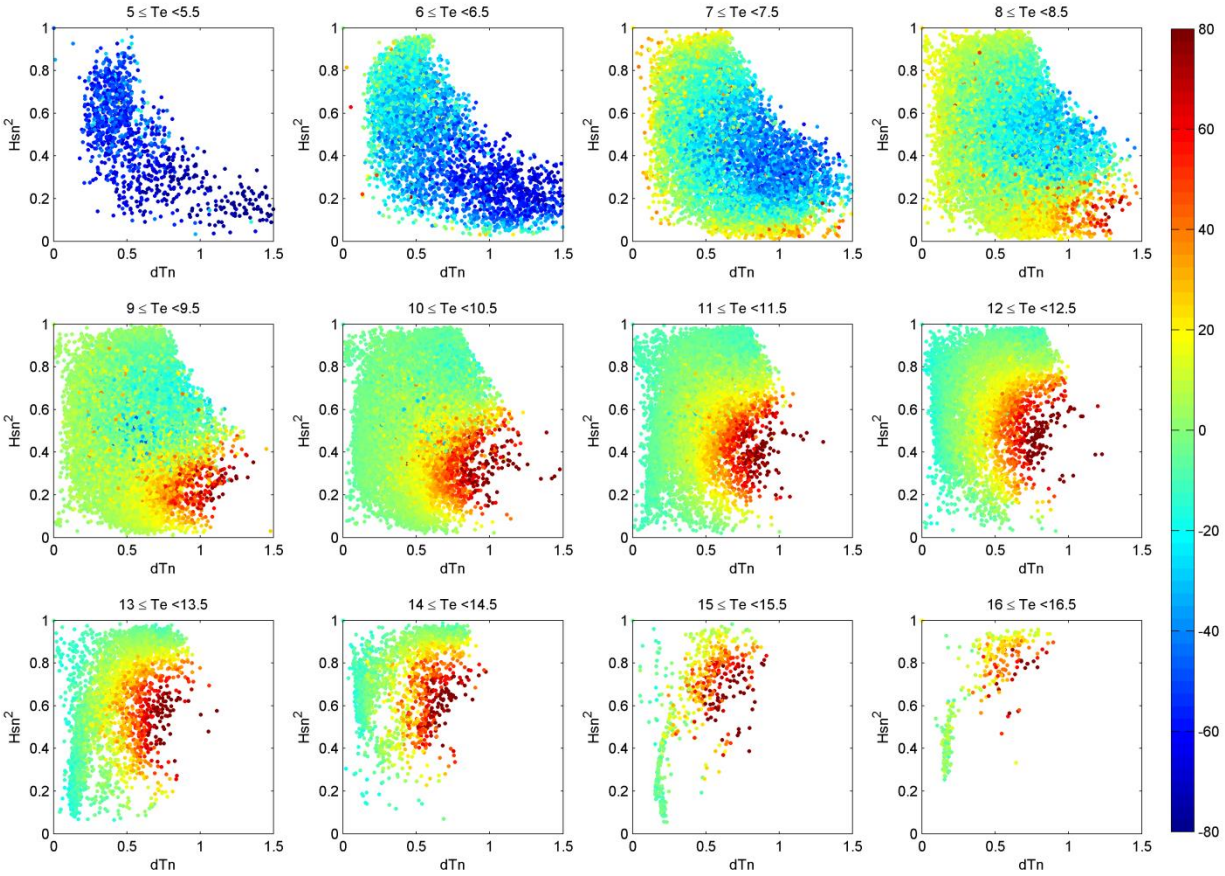

Figure 4.31. Percentage bias in predicted power from WEC 1 (colour scale) from Bretschneider spectra plotted against H_{sn}^2 and dT_n of fitted 4-parameter JONSWAP spectra for data from buoy 46042, binned by T_e.

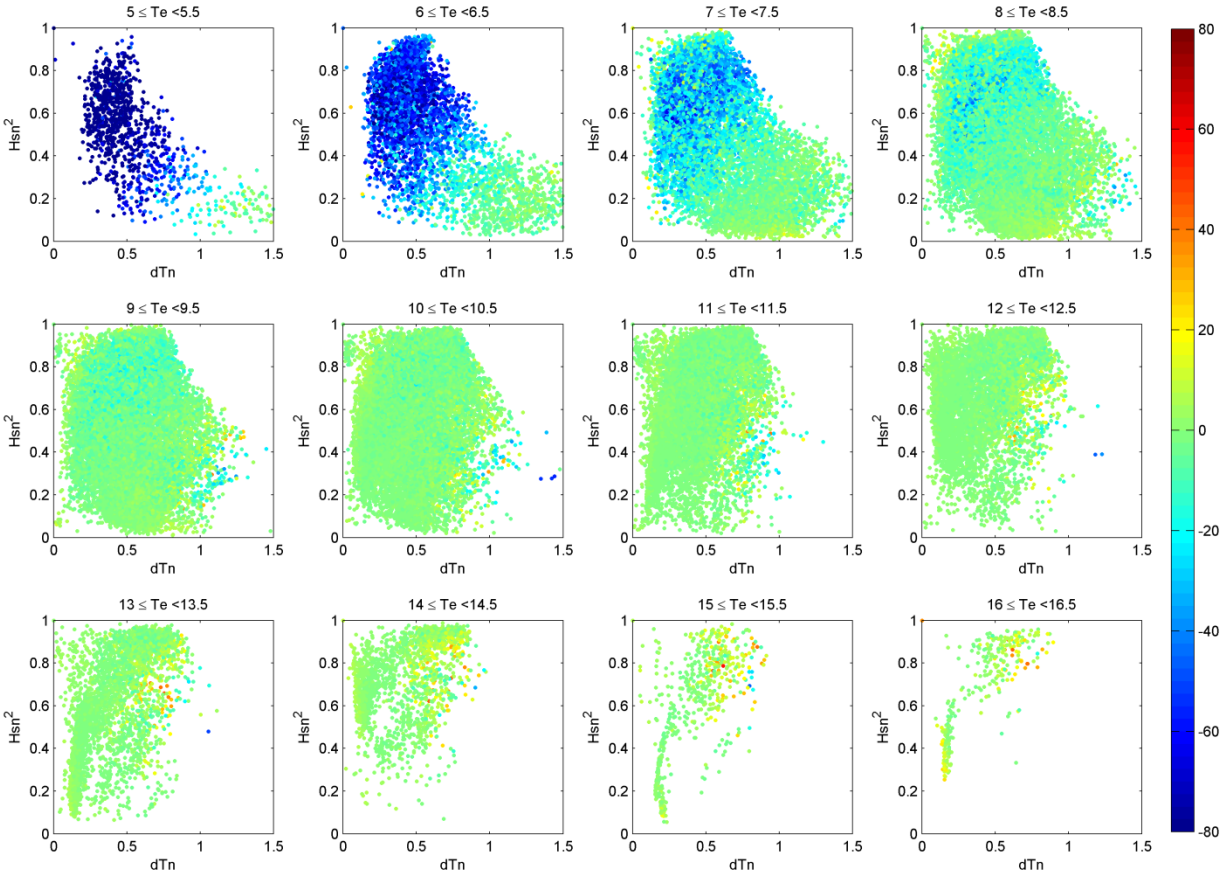

Figure 4.32. Percentage bias in predicted power from WEC 1 (colour scale) from 4-parameter JONSWAP spectra plotted against H_{sn}^2 and dT_n of fitted 4-parameter JONSWAP spectra for data from buoy 46042, binned by T_e.

4.9 Conclusions and next steps

Accurate description of the wave climate is of key importance to the prediction of energy yield. If all aspects of the WEC response are linear then the energy yield can be predicted from the mean spectrum at the site and only one spectral shape is required for simulations. However, if there are any nonlinearities in the machine response then simulations will need to be made over a range of spectral shapes from which results at intermediate points can be estimated by interpolation. This requires a method for parameterising the sea state. The accuracy of three types of spectral model with 3-, 4- and 6- parameters has been calculated and compared to the use of the standard 2-parameter Bretschneider spectrum.

The 3-, 4- and 6-parameter JONSWAP spectra give the best description of spectra at the three locations considered, compared to the Ochi and Gamma spectra with the same number of parameters. Moving from 2-parameter spectra (Bretschneider) to 4-parameter JONSWAP spectra decreases the deviance by approximately 50%, but adding another 2 free parameters only decreases the deviance by a further 10%. This implies that 4-parameter spectra provide a reasonable compromise between accuracy of description and the number of parameters used.

A systematic method of describing the shapes of 4-parameter spectra has been introduced. This allows bounds on the range of possible shapes for a spectrum with a given H_s and T_e to be formulated, which

were shown to match well with observations. It has been demonstrated that this provides a powerful method of sorting observed spectral shapes.

Initial investigations into the effect of the sea state parameterisation on energy yield prediction were presented using four theoretical capture width curves and data for three locations. It was shown that the use of Bretschneider spectra to predict power capture can give significant biases in the mean power prediction which vary with both location and WEC response. These biases can be of the order of 10% for certain WEC types and over ±100% for certain values of H_s and T_e. However the sea states with such large biases account for very little of the available wave power, so do not strongly affect the average. The 4-parameter JONSWAP spectra showed very little bias in power for all WEC types and all locations considered (although further investigations with data from other regions and other CW curves will be needed to confirm the validity of this approach in general). The 6-parameter spectra did not significantly improve the bias relative to the 4-parameter JONSWAP spectra, but did significantly improve the standard deviation (unsurprising, considering the improvement in deviance relative to the 4-parameter spectra). Finally, it was shown that the fitted parameters H_{sn}^2 and dT_n of the 4-parameter JONSWAP spectra explain much of the variance in power production due to spectral shape.

The effect of power matrix resolution on energy yield prediction has not yet been considered. Due to the time required for the time-domain simulations it is not practical to calculate the response of a WEC or an array for every measured or fitted spectra in the historic data. So to predict the long-term energy yield results must be calculated for a discrete range of conditions from which performance in other sea states can be estimated by interpolation. (The approach which is most commonly adopted is to use a power matrix, where results are calculated for discrete values of H_s and T_e, usually assuming a Bretschneider spectrum). It will be necessary to conduct experiments to investigate the effect of using various parameter resolutions within the power matrix and using different interpolation and extrapolation algorithms. The results of these investigations should show the relationship between the number of simulations required and the accuracy of energy yield prediction.

Directional aspects have also not been considered so far. Directional spreading is likely to have a significant impact on the prediction of energy yield for arrays of WECs, since waves travelling in different directions will move energy into the wake behind a WEC and thus change the wake characteristics relative to that for unidirectional waves (see e.g. Folley and Whittaker, 2009).

5 MOORINGS MODULE

5.1 Overview of the development strategy

WaveDyn uses a multi-body dynamics approach and as such any part of the WEC that moves relative to other parts will be modelled as a single body in this system (see Section 2).

As outlined in WG1 WP1 D2, in the initial implementation the mooring lines are not modelled as bodies in the system, but are treated separately as applied forces (and moments) that affect the overall response. The effects of the moorings are introduced through a 'look-up table' approach, which in the time-domain formulation allows nonlinear representations of the above mentioned applied forces (and moments) with regard to body displacement, velocity and acceleration.

A nonlinear representation of the mooring line effects can be achieved through the specification of a look-up table database which relates general properties of the line (like stiffness and damping) to its motions. These general properties can be obtained separately through numerical modelling or experimental tests for the mooring lines. This data is then used by WaveDyn for estimating the forces and moments associated with the specific mooring line arrangements.

This is done for two main reasons:

- To fully model a mooring line as a flexible body is computationally intensive. The look-up table approach offers a more efficient alternative to this, and thus can be seen as a starting point.
- The current multi-body approach places some restrictions on the configuration of the multi-body system. Specifically it requires the system to have a tree-like topology, with exactly one possible path to ground from anywhere in the structure. Multiple mooring-line bodies in the structure would violate this rule, while multiple mooring line force profiles do not.

The look-up tables are selected by the user at runtime from a database of predefined mooring elements or strategies. For some applications, however, this approach may be inadequate and in this case task-specific "custom" tables are to be calculated on demand, using alternative moorings software or industry standard codes. Procedures to populate the look-up tables for predefined mooring configurations that can be simulated using alternatives approaches are currently being developed.

In a similar approach to that followed in other sections of this report, the development guidelines for the moorings module (drafted in WG1 WP1 D2) are summarised in the bullet points below:

- Improve post-processing capabilities, including a graphical tool to allow the user to visualise the mooring line shapes and configurations;
- Compare look-up-table approach to Morison-element approach for different simulation cases, to determine the degree of similarity in results;
- Based on conclusions from the previous step, make a decision as to whether to the currently functionality is sufficient, or there is a need to add the Morison-element approach to the existing code, or in alternative to create a run-time link to a third-party tool, or to continue with just the look-up-table approach;
- Investigate the possibility of creating a finite-state model of the mooring system with the aim of carrying out convolutions in the time-domain to represent frequency-dependent impedance;
- Adding static-analysis capability to the software so that a realistic equilibrium state to be computed. This equilibrium state is used as the starting-point for time-domain simulations.

The initial efforts described in this report were concentrated in providing a suitable platform for the time-domain modelling of nonlinear applied forces / moments via look-up tables, while improving and further developing the post-processing capabilities and user interface.

As previously mentioned procedures to populate the look-up tables for predefined mooring configurations that can be simulated using alternatives approaches are currently being developed. However this may need to be complemented by a more explicit mooring-line model based on a Morison-element approach. The next immediate steps will aim to quantify the need for this explicit procedure for typical mooring configurations associated with each FDC (see Section 9).

5.2 Details of the implementation: the look-up table approach

The kinematics and loads on each look-up table are given in the mooring line's own coordinate system, which is illustrated in Figure 5.1. Each mooring line has an origin at the anchor point with the *z*-axis of this coordinate system being vertical (as is the global *z*-axis), and the *xz* plane containing both the anchor point and the attachment point ($\underline{p}$; see Figure 5.1).

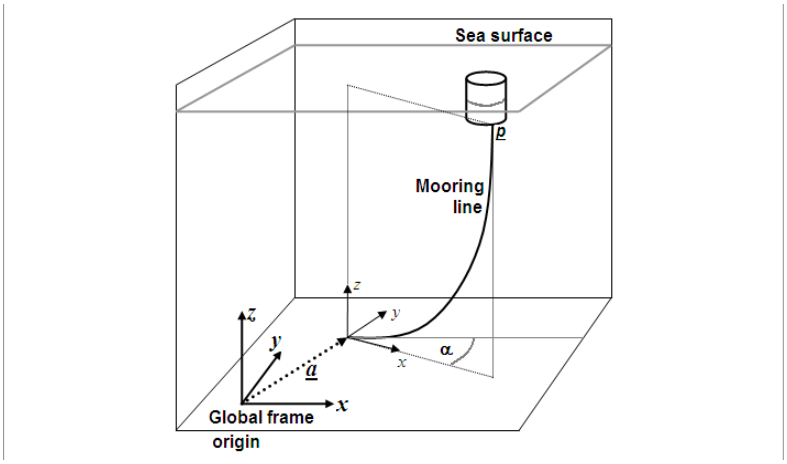

Figure 5.1. The mooring line layout, illustrating the basis of the mooring line's coordinate system.

For each mooring line, the displacement, velocity and acceleration vectors which are used in the look-up tables refer to the line's attachment point $\underline{p}$, and are expressed in that mooring line's coordinate system. The displacement vectors are measured relative to $\underline{p}$'s equilibrium position $\underline{p}_{eq}$, which is its steady-state position in the absence of any waves. Thus the displacement vector to use in the look-up, $\underline{p}_m$, is given by:

$$\underline{p}_m = R(\underline{p} - \underline{p}_{eq}) \qquad [5\text{-}1]$$

where both $\underline{p}$ and $\underline{p}_{eq}$ are expressed in the global frame.

The transformation from the global frame to the mooring-based frame consists of two elements: a translation given by vector $\underline{a}$ (the position of the anchor in global coordinates), and a rotation by an angle α about the z-axis:

$$\underline{x}_m = R\underline{x}_g - \underline{a} \qquad [5\text{-}2]$$

where:

$\underline{x}_m$ is a position vector in mooring-based coordinates;

$\underline{x}_g$ is the same position in space but expressed in global coordinates;

R is the rotation matrix corresponding to a rotation by angle α about the *z*-axis, where the rotation direction is from the mooring x-axis towards the global *x*-axis (anticlockwise in Figure 5.1).

The resultant force on the body due to each mooring line (*i*) is calculated from the look-up table which specify the functional relationship between the displacements, velocities, accelerations and incident wave frequency to the stiffness, damping and inertia of the mooring line (respectively).

The force on the mooring lines is thus given by:

$$\left(F_m\right)_i = \sum_{i=1}^{n} \left(\mathbf{K}\, x + \mathbf{B}\, \dot{x} + \mathbf{M}\, \ddot{x}\right)_i , \qquad [5\text{-}3]$$

where x, $\dot{x}$, $\ddot{x}$ are six component vectors (in surge, sway, heave, roll, pitch and yaw) associated with the displacements, velocities and accelerations of the n^{th} mooring line attachment point connected to the body, respectively. The matrices **K**, **B** and **M** are respectively the stiffness, damping and inertia matrices defined by the coefficients in the look-up table associated with the displacements (x) and incident wave frequency (ω). For each line, these matrices are defined by 36 (6x6) components, which relate the forces exerted in a certain direction to the motions on a different direction. For example, the term (k_{31} x_1) represents the stiffness force in heave due to the displacements in surge. The most significant technical difference between this implementation and that described in WG1 WP1 D2 is that $\left(F_m\right)_i$ may, in the time-domain formulation, be a nonlinear applied force / moment.

The moorings module has its own input/output (I/O) functionality; this allows it to parse the relevant section of the common data file which holds all information about the WEC and the simulation. For each mooring line, the relevant information is within a special block demarcated by the symbols

{MOORING

...

}MOORING,

and consists of:

- The mooring line's name;
- The body which it is attached to;
- The position of the attachment point (expressed in the body-fixed coordinate system of the attached body);
- The position of the anchor (expressed in the global coordinate system);
- The stiffness, damping and inertia matrices (stored as 6-by-6 arrays of look-up tables, all quantities being expressed in the frame of reference of the mooring line).

Once this information has been read in, the coordinating (WaveDyn core) code starts the simulation. Firstly the core WaveDyn code passes on relevant details to the mooring module about the current state of the system. For each mooring line, the required information is the current position and velocity (both linear and rotational) of the body to which the line is attached. The mooring module can then calculate, in the mooring line coordinate system, both the velocity of attachment point $\underline{p}$ and its relative displacement from its equilibrium position. Once these values are known it can perform the look-up operation to obtain the loads, which it then transformed back into the global coordinate system. Before the loads can be applied to the bodies, a further step is needed: in the multi-body code the loads are applied at the proximal node of the body. In general, the proximal node of the body is

not at the same point in space as the attachment point of the mooring. This means the loads need to be transformed into a new set of loads acting at the proximal node. The transformed mooring and other loads (PTO and hydrodynamic) are then applied to the body or bodies by the multi-body module (MBCore) code.

5.3 Case study: moored truncated cylinder

As an example of the application of the WaveDyn moorings module, the data associated with the mooring configuration published in Jonkman (2010) is used and applied to a floating truncated cylinder (the same FDC as used in Section 8).

It should be noted that the properties of the mooring lines used in this example are suitable for a slacked moored floating spar which is distinct from the structure considered in this example (the most obvious difference between the two scenarios is the overall water depth). However the properties of these mooring lines can be used with the cylindrical geometry to give a first qualitative overview of the main implementation characteristics of the moorings module in WaveDyn.

Table 5.1 presents the main properties associated with the mooring lines used in this example.

Property	Value
Depth to anchors below SWL (water depth)	320 m
Depth to fairleads below SWL	4 m
Horizontal distance from fairlead to anchor	846.67 m
Radius to fairleads from platform centreline	10 m
Unstretched mooring line length	902.2 m
Mooring line diameter	0.09 m
Equivalent mooring line mass density	77.7066 kg/m
Equivalent mooring line weight in water	698.094 N/m
Equivalent mooring line extensional stiffness	384,243 kN

Table 5.1. Mooring lines properties for the test cylinder; adapted from Jonkman (2010).

Figure 5.2 gives a schematic representation of the test case considered in this example. The cylinder is moored with three lines attached to the fairleads at a depth equal to 4m bellow the still water line. The anchors (fixed to the inertia frame) are located at a (water) depth of 320 m below the mean free-surface and at a radius of 853.87m from the centreline. The three lines are connected to the three fairleads which are located on a plane parallel to the mean free-surface and spaced uniformly around the cylinder at 120º angle.

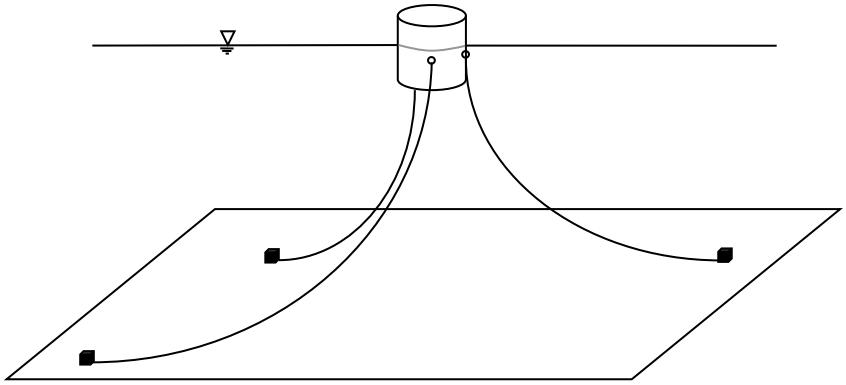

Figure 5.2. The mooring arrangement for the test cylinder. Three identical catenary mooring lines are represented, spaced evenly at 120° intervals around the cylinder.

The load-displacement relationships for this system were derived numerically by considering discrete combinations of the displacements in all modes of motion which serve as basis to derive the coefficients used in the look-up tables. These relationships were originally calculated from the line characteristics given in Table 5.1 using FAST (a modelling code developed for the wind industry). It should be noted that in this example, these relationships take into account the combined effect of the mooring arrangement with the three lines and also that only the stiffness properties of the mooring lines are taken into account, i.e. neither damping nor the inertial properties of the lines were considered.

The procedure to obtain the load-displacement relationships consisted in recording the reaction force in the mooring lines at the attachment point that resulted from the combinations from discrete displacements of the line. A very large number of simulations were required to cover all the possible combinations and to fill the lookup table. Jonkman (2010) reports to have performed 1,574,573 simulations to obtain these relationships associated with variations in surge, sway, heave, roll, pitch and yaw in a corresponding number of steps equal to $13 \times 13 \times 7 \times 11 \times 11 \times 11$, respectively. The details of the procedure can be found in Jonkman (2010). Figure 5.3 to Figure 5.5 show load-displacement relationships obtained when each DOF is varied independently.

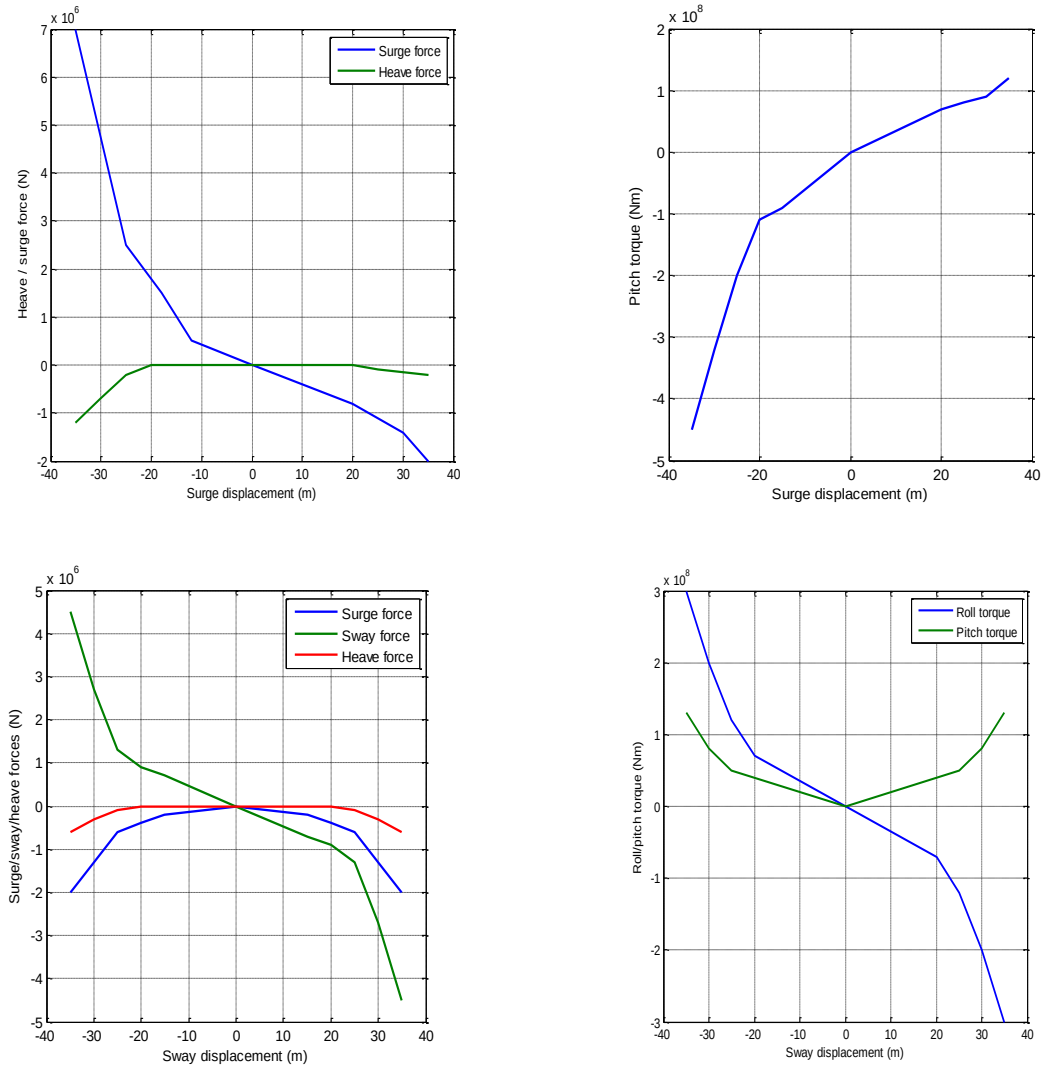

Figure 5.3. Load-displacement relationships of the mooring lines which derive the look-up tables.

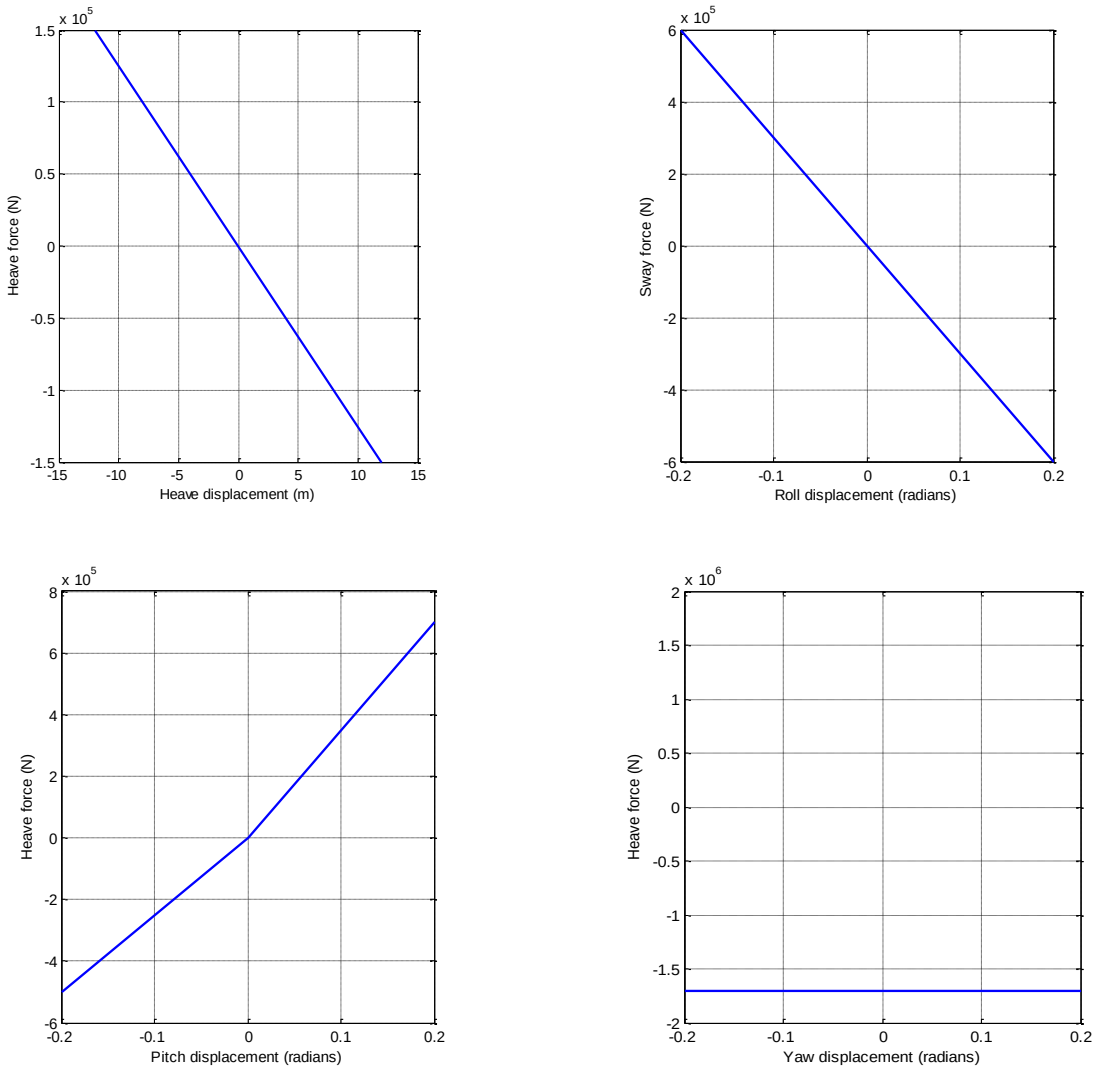

Figure 5.4. Load-displacement relationships of the mooring lines using the look-up tables (cont.)

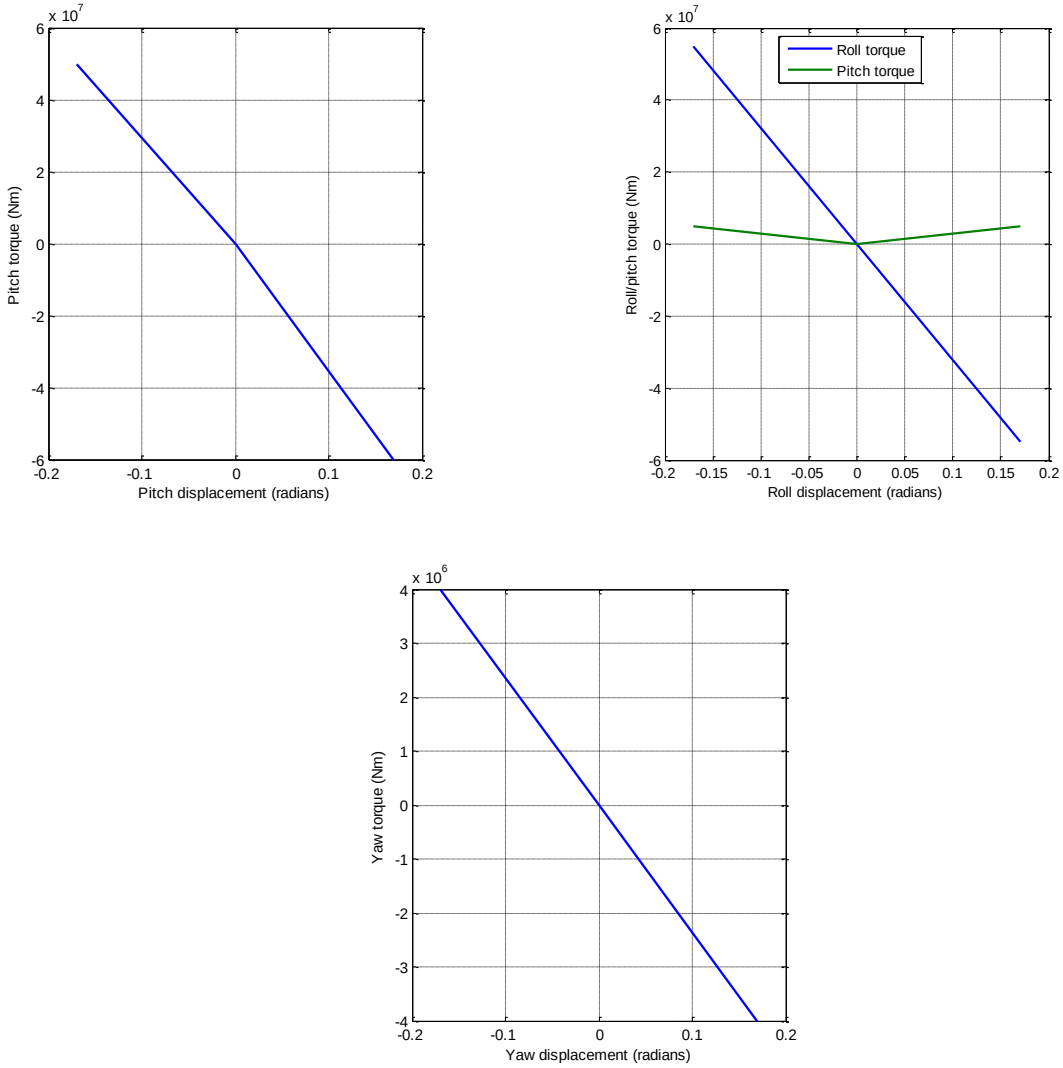

Figure 5.5. Load-displacement relationships of the mooring lines using the look-up tables (cont.)

Representative results can be obtained by monitoring the time history response of the moored cylinder. The simulations were performed for regular and irregular waves, using a Pierson-Moskowitz spectrum with H_s=2.5m (T_p=7.9). For regular waves the simulations were carried out over a total duration of 900s (15min) whereas for the irregular waves a simulation length of 1800s (30min) was used.

Figure 5.6 shows the initial results which compare the displacements in heave for a freely floating and a moored cylinder. The large amplitudes of the initial transients were found to be related to the additional weight of the mooring lines, which unbalance the buoyancy force on the cylinder (note that this is proportional to the cylinder's draft). The steady state equilibrium position (0.54m below the free-surface) is used to estimate the weight of the mooring lines. To keep the same draft on the cylinder, the additional mass of the mooring lines is subtracted from the mass of the cylinder so that the cylinder plus the mooring lines are in balance with the buoyancy force of the cylinder. The mass and moments of inertia of the cylinder used for the simulations in the present section are given in Table 5.2.

Figure 5.7 shows the displacements in surge, sway and heave for the moored cylinder. In surge the superposing effect of a higher period oscillation of about 140s (and amplitude of 0.7m) is clear, and

this is due to the mooring lines in addition to the oscillations related to the incident wave. In sway, as expected, there is no displacement as the waves do not excite the cylinder in this direction. In heave, the oscillations are small and of about $1/10^{th}$ of the amplitude of the incident wave. Note that the transient effects observed for the first cylinder are not present, as the weight of cylinder was adjusted to include the mooring lines weight.

Figure 5.8 shows the comparison of the time series displacements in surge and heave for a freely floating and a moored cylinder when the incident wave has a period and amplitude equal to 5s and 1m. The time series responses for irregular waves are shown in Figure 5.9. As expected, the free cylinder drifts away in surge from its starting point whereas the moored cylinder oscillates about its mean position with no drift. The amplitudes of the oscillations in heave are about the same for both cases showing that the mooring lines are not restraining the cylinder in this DOF.

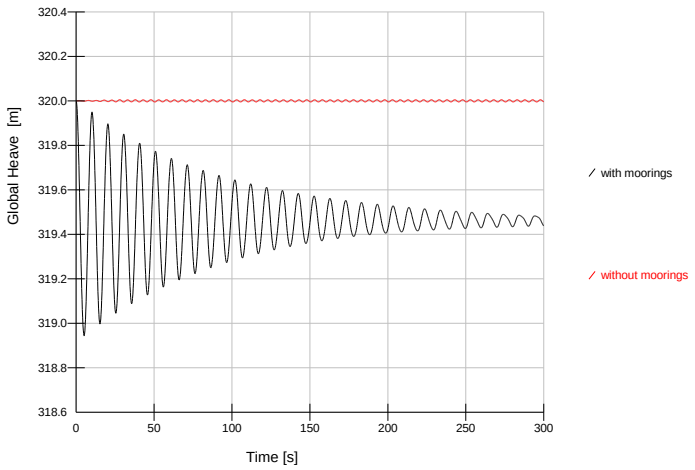

Figure 5.6. Initial simulations: Comparison between heave displacement for a moored and a freely floating cylinder. The initial transient motion of the moored cylinder is due to the instantaneous unbalance between the buoyancy force and joint weight of the cylinder and mooring lines.

Table 5.2. Properties of the cylinder used in the simulations of the present section.

Mass of the mooring lines	173887.15 [kg]
Mass of the cylinder used in Section 8	6440240.12 [kg]
Mass of the cylinder used in the simulations of the present section.	6267109.59 [kg]
Moments of Inertia at the principal axis of the cylinder used in the present section.	Ixx = Iyy = 218139290.35 [kg m^2] Izz = 168246318.16 [kg m^2]

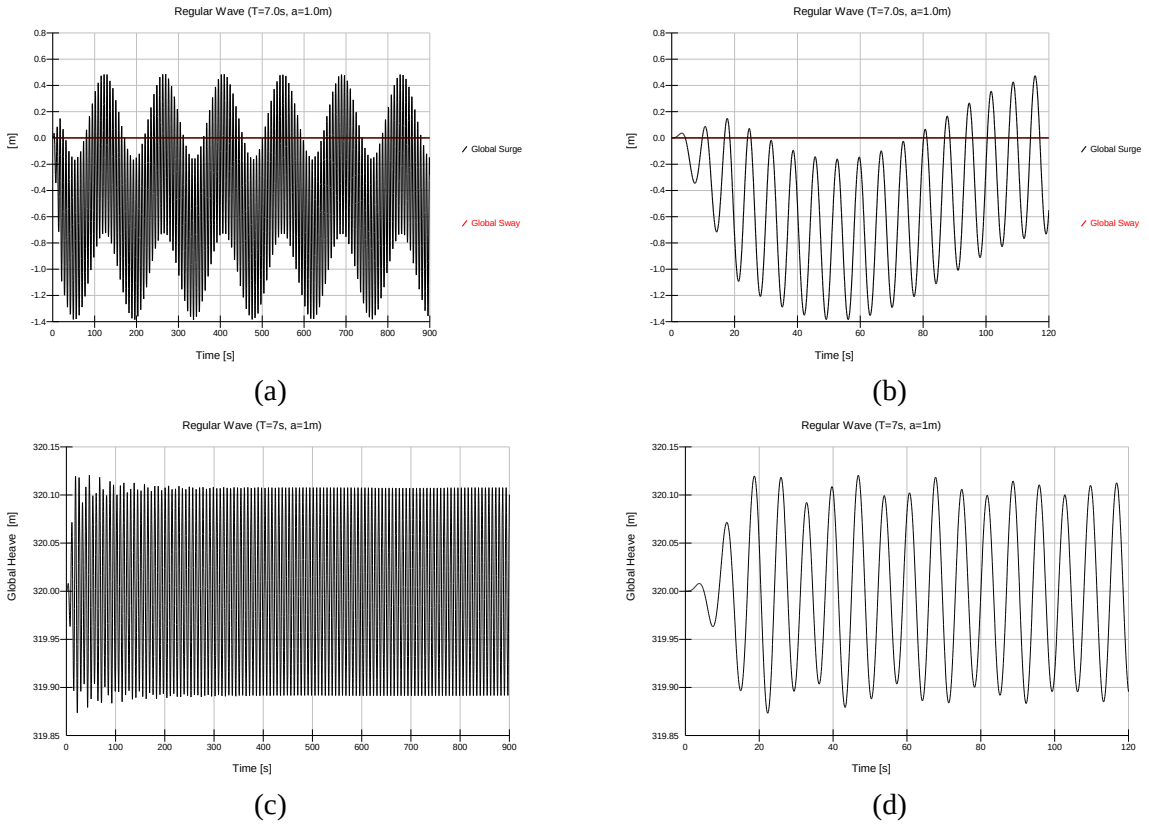

Figure 5.7. Time series of the motions of the moored single cylinder (a) Surge (black) and sway (red) motions for a 15 min simulation, (b) first 120s of the simulation for surge and sway. (c) Heave motion correspondent to 15min simulation (d) first 120s for the heave motion simulation.

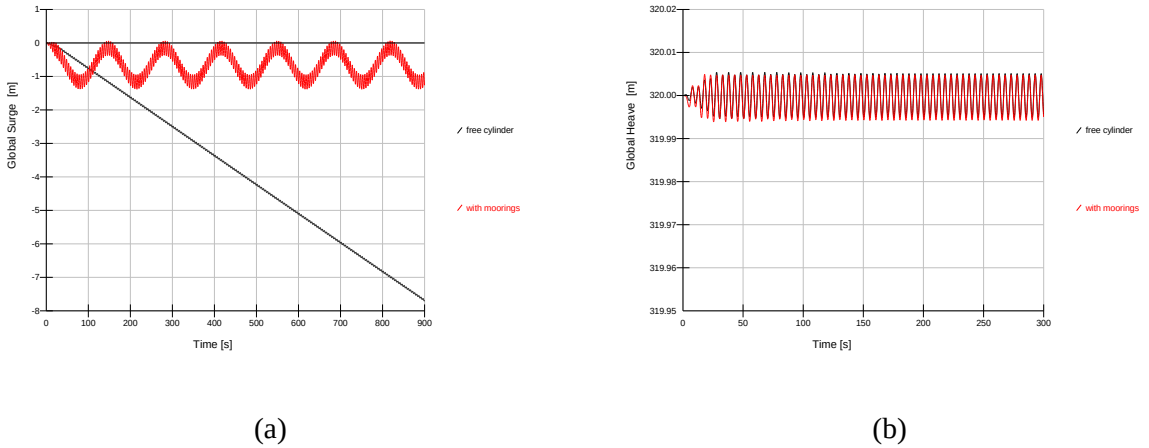

Figure 5.8. Comparison between a moored and a freely floating cylinder obtained with WaveDyn for a regular wave (*T*=5s, *a*=1m).

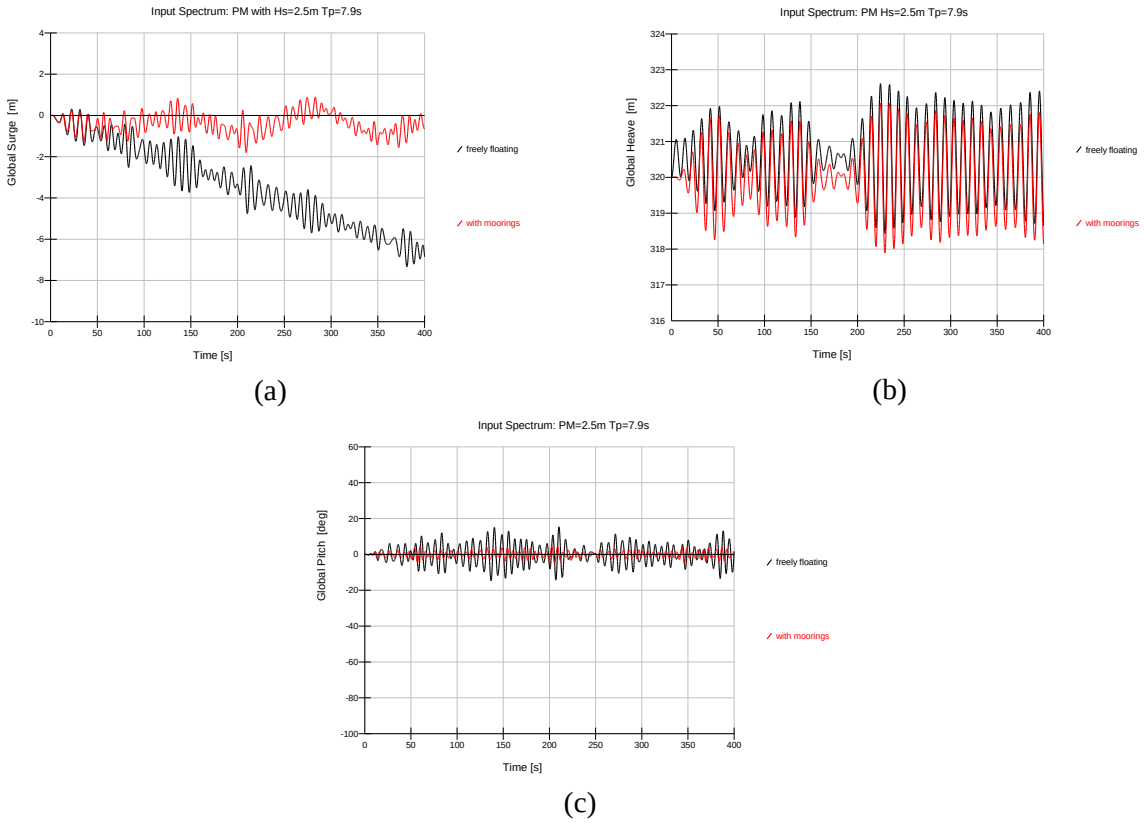

Figure 5.9. Comparison between the displacements of a moored and a freely floating truncated cylinder for irregular waves. The input spectrum is a PM with H_s=2.5m (T_p=7.9s).

The time series of the mooring forces in surge and heave for a PM spectrum (with H_s=2.5m and T_p=7.9s) are shown in Figure 5.10. In surge , the mooring forces oscillate with maximum amplitude of about 200kN. In heave the amplitude of the oscillations is small around a steady force equal to about 1700kN which is the force corresponding to the weight of the mooring lines (see also Table 5.2).

An initial verification procedure of the computations performed by the moorings module is performed by comparing the mooring forces output from WaveDyn and the mooring force obtained via the relationship given by Equation [5-3], using the motions computed by WaveDyn. This is shown in Figure 5.11 for the same input PM spectrum. The agreement is good, giving evidence that the implementation of the mooring forces module is behaving as expected.

The current implementation allows the description of linear and nonlinear mooring force profiles in the time-domain. Such feature allows the definition of the mooring loads to be monitored experimentally in WG2, thus the primary objective of the moorings module has been achieved. Further steps, mostly related to verification exercises (as the one described in the previous paragraph), are still needed to infer if the formulation is applicable to a wide range of mooring configurations. Such steps are outlined in Section 9.

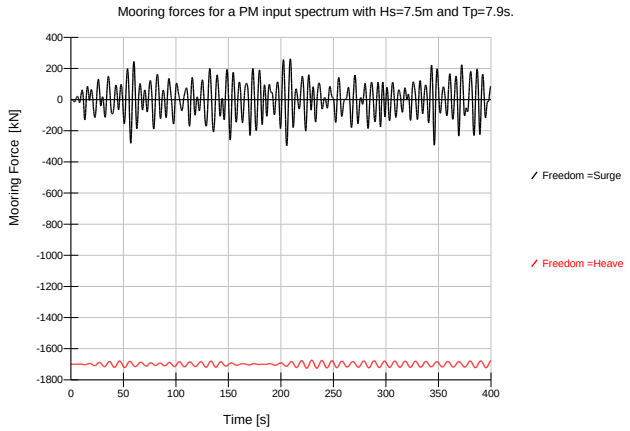

Figure 5.10: Mooring forces in surge (black) and heave (red) associated with a PM spectrum with H_s=2.5m (T_p=7.9s).

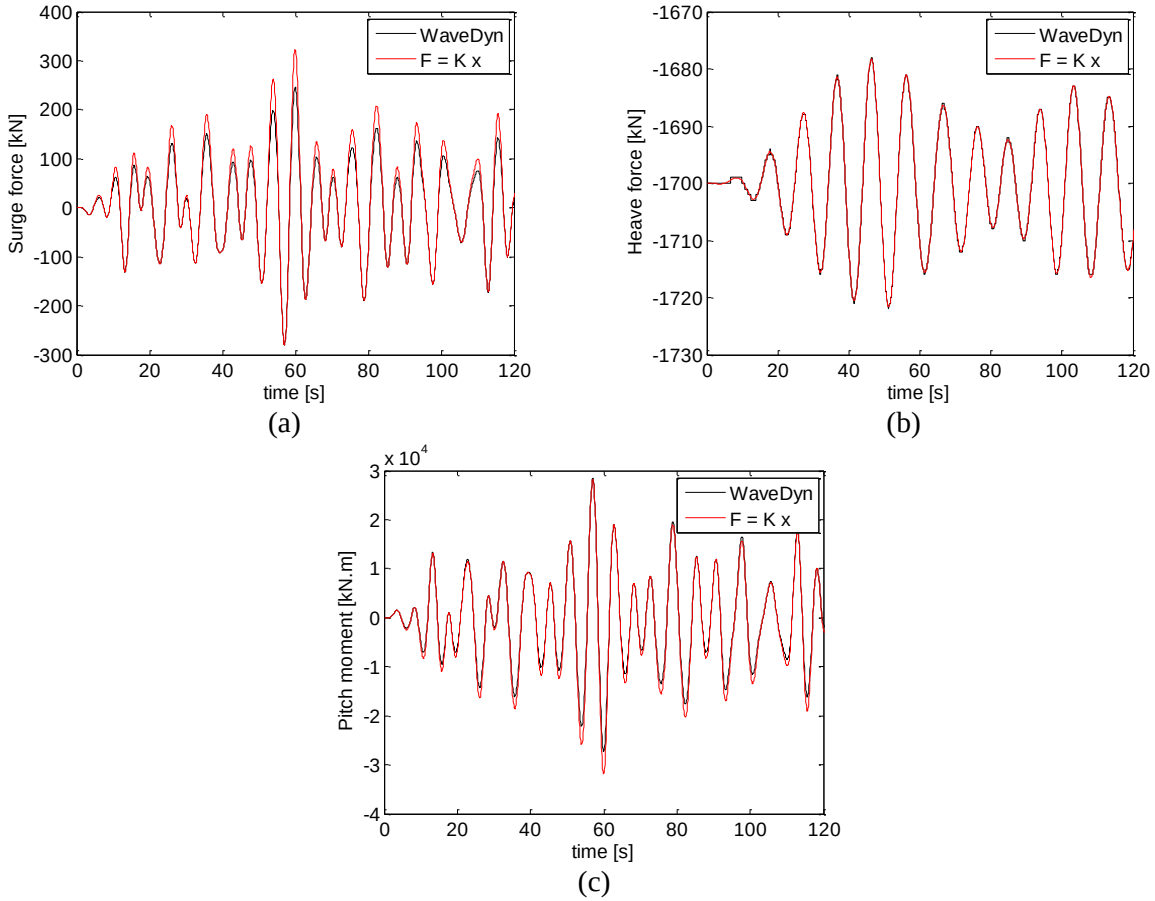

Figure 5.11: Comparison between the mooring forces / moments obtained with WaveDyn and computed externally through Equation 5-3 using the stiffness coefficients from the load-displacement relations given by Figures 5.3 to 5.5.

6 POWER TAKE-OFF (PTO) AND CONTROL MODULES

The frequency-domain PTO model presented in WG1 WP1 D2 relies on a explicit, linear mathematical formulation that allows a PTO force to be applied to any joint in the WEC structure as a function of the joint freedom displacements and velocities. As with the other applied force calculation modules, an object-orientated software architecture supports a multi-body implementation whereby a set of 'PTO bodies' are constructed for the joints in the system at which forces are to be applied; these bodies complete the PTO force calculations and are managed by an overall containing object referred to as the PTO structure. The PTO structure represents the interface with the high level WaveDyn co-ordinating code, including the numerical integrator. This multi-body setup allows more advanced PTO modelling capability to be added to the code through the development of new PTO body types, which can be specified as alternatives to the linear bodies developed for the frequency-domain implementation. The time-domain PTO bodies may support complex, nonlinear or discontinuous PTO characteristics that more closely represent real PTO designs. In line with the 'Next Steps' outlined in the Section 9.2 of the WG1 WP1 D2 report, the recent PTO and control system implementation work has focused on the implementation of these more complex PTO bodies in the WaveDyn code.

Two new types of PTO body have been developed for the time-domain; the most advanced of these is a simplified hydraulic or electrical rectification and smoothing system that incorporates an internal 'charge' state solved for by the central WaveDyn integrator. The charge integration for these bodies is the first applied force calculation module state variable to be handled in WaveDyn (previously the integrator dealt with structural, MBCore states only) and has led to some development in the software format of both the PTO module and the central integrator since that presented in WG1 WP1 D2. An overview of the latest PTO software architecture is given in Section 6.1 below, whilst Section 6.2 presents the input parameters. Sections 6.3, 6.4 and 6.5 describe the mathematical basis and implementation process for the new PTO bodies and their associated control parameters. The central WaveDyn integrator is described in Section 2.3; the integrator code now more comprehensively supports the solution of an unspecified number of calculation module states, providing a basis for the completion of a PTO and control system DLL interface.

6.1 PTO applied force calculation module: software architecture

The basis of the PTO module software architecture follows a very similar design to that of the hydrodynamics module described in Section 3 and was initially presented in Section 6.4 of WG1 WP1 D2. In this initial formulation a set of lower level PTO body objects representing linear PTO models for joints in the structure was contained within a single PTOStruct object. The central WaveDyn code could call the PTOStruct object passing a set of joint kinematics to the PTO bodies and could then request that a set of PTO loads to be returned. The two level body-structure architecture has been largely maintained for the latest implementation however the kinematics setting and load calculation functions have been combined into a single function, named CalStateDevApp that accepts a structure containing the PTO body kinematics and any state values as its argument and returns the loads as well as any internal state derivatives for use by the central WaveDyn integrator. The explicitly defined input-output structure of this single function avoids the need to store the body kinematics in memory once they have been 'set' and removes the need to call the calculation module functions in the correct order. Additional arguments to the CalStateDevApp function allow the integrator to indicate to the PTO module whether the loads and state derivative calculation is simply an intermediate integrator call, as this is required for some integration algorithms (such as a Runge-Kutta type technique), or a complete timestep call in which the actual system states and loads are determined. The states passed to the calculation module for a complete timestep call may be checked for validity by the PTO module at the start of the CalStateDevApp function and the loads calculated may additionally be written to the simulation output buffer, if the timestep has been marked as an output timestep by the coordinating WaveDyn code.

At the start of the simulation, the coordinating code calls an initialisation function for the module, at which point the PTOStruct examines the PTOBody types that have been constructed during the input file parsing process and returns a list of any states, with assigned initial values, to be included in the time-domain integration process. The overall code structure is illustrated schematically in Figure 6.1 below.

6.2 PTO and control modules: input parameters

As described in Figure 6.1, the WaveDyn engineering code is capable of reading user input provided in the .IN file plain text format described in WG1 WP1 D2, Section 2.7, or an equivalent .xml data tagged version generated by the prototype user interface. The input parameters themselves are the same in both input files types, it is simply the format that differs, and in both cases the PTO and control applied force calculation module input parameters are contained within a tagged sub-block of the body data. This is marked by "<pto" and ">pto" tags in the .IN file and "<PowerTakeOff>" and "<\PowerTakeOff>" tags in the xml files. The PTO body type is determined from a type parameter in these blocks which allows an instance of the correct PTO Body object, constructed with the remaining parameters, to be added to the PTOStruct in the WaveDyn model. The input parameters required for each of the PTO Body models are overviewed in Sections 6.3 to 6.5.

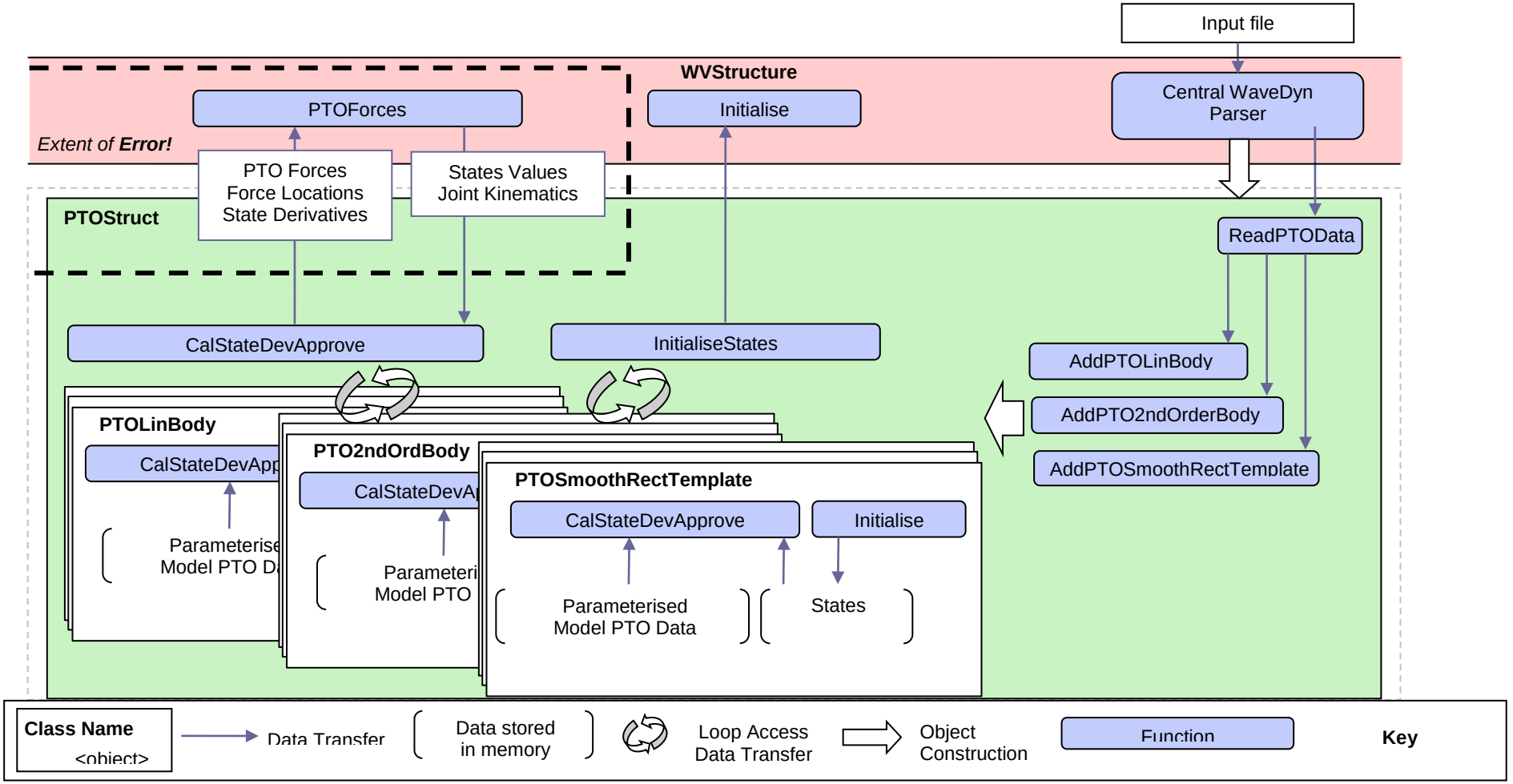

Figure 6.1. PTO Force Calculation Module Class Architecture and Key Functions.

6.3 First-order (linear) explicit PTO model

The initial PTO Calculation Module formulation, designed to support the requirements of a frequency-domain analysis as well as time-domain simulations, allows the user to specify parameters for a mathematical PTO force expression with a simple, parameterised spring-damper form:

$$\underline{f}_{PTO} = -\underline{B}^T \underline{\dot{x}} - \underline{K}^T \underline{x} - \underline{E} \qquad [6.1]$$

where:

$\underline{x}$ is the vector of joint freedom translational and angular displacements,

$\underline{B}$ is the vector of PTO damping values for each freedom,

$\underline{K}$ is the vector of stiffness coefficients,

$\underline{E}$ is a vector of preloads. Note that this must be set to zero for a frequency-domain analysis.

The force $\underline{f}_{PTO}$ is applied to the freedoms in the SlidingJoint and Hinge structural bodies. Equation 6.1 may be evaluated directly from the kinematic data arguments to the CalStateDevApp PTOLinBody member function containing the instantaneous $\underline{x}$ and $\underline{\dot{x}}$ values. The input parameters embodied in the damping, stiffness, pre-load and control variables are provided by the user in the .IN file "<pto >pto" sub-block using the parameter order shown in Table 6.1.

<pto >pto Sub-block Parameters; PTOType = Simple			
Input Parameter (as presented in the .IN file)	**Data Format**	**Parser Dependencies**	**Description**
`PTOType`	`= Simple`		
`Damping`	Vector of double precision floating point numbers	None Parameter is compulsory, but may be set to zero.	Vector of PTO damping coefficients for each joint freedom. Energy dissipated is assumed to be converted by the PTO mechanism and is recorded in the PTO absorbed power output data series.
`Stiffness`	Vector of double precision floating point numbers	None Parameter is compulsory, but may be set to zero.	Vector of PTO stiffness coefficients for each joint freedom.
`Pre-load`	Vector of double precision floating point numbers	None Parameter is compulsory, but may be set to zero.	Vector of Pre-load values permanently applied to the joint.

Table 6.1. PTO sub-block .IN file parameters for the initial, linear PTO model.

A user may passively control the linear explicit PTO bodies through variation of the stiffness and damping terms; in doing this, it is possible to adjust the system reactance and hence peak response frequency, or to simple obtain an overall optimum damping level for energy capture. Use of the more complex, second-order model described in Section 6.4 alternatively allows modulation of the PTO settings to be expressed using a control coefficients format (the second-order terms simply being set to zero if the linear format described by Equation 6.1 is still required). A more detailed discussion on PTO tuning is provided in both the Methodology Report, WG1 WP1 D1b, Section 3.6.2 and in multiple texts including Falnes (2002), Cruz (2006) and Livingstone and Plummer (2010).

6.4 Second-order explicit PTO model

The time-domain WaveDyn formulation allows much more complex mathematical models than the simple case presented in Section 6.3 to be supported. Indeed, any explicit mathematical function of the joint kinematics could be readily incorporated into the code without significant effort. In reality, however it is difficult to support such an open-ended model from a user input perspective and so the second PTOBody type limits the input to a more complex, but restricted second-order formulation that takes the form:

$$\underline{F}_{PTO} = -\underline{A_c}^{T}\,\underline{A}^{T}\,\underline{\dot{x}}|\underline{\dot{x}}| - \underline{B_c}^{T}\,\underline{B}^{T}\,\underline{\dot{x}} - \underline{C_c}^{T}\,\underline{C}^{T}\,\underline{x}|\underline{x}| - \underline{K_c}^{T}\,\underline{K}^{T}\,\underline{x} - \underline{E_c}\,\underline{E} \qquad [6.2]$$

where, in addition to the parameters defined in Section 6.3, the following vectors describe values for each joint freedom as follows:

$\underline{A_c}$ Control Square Law Damping

$\underline{A}$ Square Law Damping

$\underline{B_c}$ Control Damping

$\underline{C_c}$ Control Square Law Stiffness

$\underline{C}$ Square Law Stiffness

$\underline{K_c}$ Control Stiffness

$\underline{E_c}$ Control Pre-Load

As with Equation 6.1, Equation 6.2 may be evaluated directly from the joint kinematics passed as arguments to the CalStateDevApp function and the user supplied PTO settings, which have the .IN file parameter names listed in Table 6.2.

<pto >pto Sub-block Parameters; PTOType = 2ndOrder			
Input Parameter (as presented in the .IN file)	**Data Format**	**Parser Dependencies**	**Description**
PTOType	= 2ndOrder		
ControlSquareLawDamping	Vector of double precision floating point numbers	None Parameter is compulsory, but may be set to zero.	Vectors of control values used to modulate the set of PTO parameters defined below. These are set as unit vectors if the full PTO coefficient values are to be used unchanged.
ControlDamping			
ControlSquareLawStiffness			
ControlStiffness			
ControlPre-load			
SquareLawDamping			Vector of PTO square law damping coefficients for each joint freedom. Energy dissipated is assumed to be converted by the PTO mechanism and is recorded in the PTO absorbed power output data series.
Damping			Vector of PTO damping coefficients for each joint freedom. Energy dissipated is assumed to be converted by the PTO mechanism and is recorded in the PTO absorbed power output data series.
Stiffness			Vector of PTO stiffness coefficients for each joint freedom.
Pre-load			Vector of Pre-load values permanently applied to the joint.

Table 6.2. PTO sub-block .IN file parameters for 2nd Order PTO model.

The results of test simulations run using both the second-order PTO model and the simple, linear model allow the two implementations to be compared. Figure 6.2 to Figure 6.5 illustrate the effect of a second-order PTO model on the heaving point absorber case study presented in Section 8 of WG1 WP1 D2 (see also Section 8.1 of this report). The results presented here for regular waves with a frequency of 0.7rad/s and a wave amplitude of 1m. The PTO settings selected in each case lead to a similar heave response amplitude (a linear damping of 2MNs/m and a square law damping of 6MNs/m) but significant differences in the PTO force experienced at the sliding joint and, as a result, the power absorbed by the system. The difference in the body kinematics may be expected to become more pronounced as the wave amplitude increases.

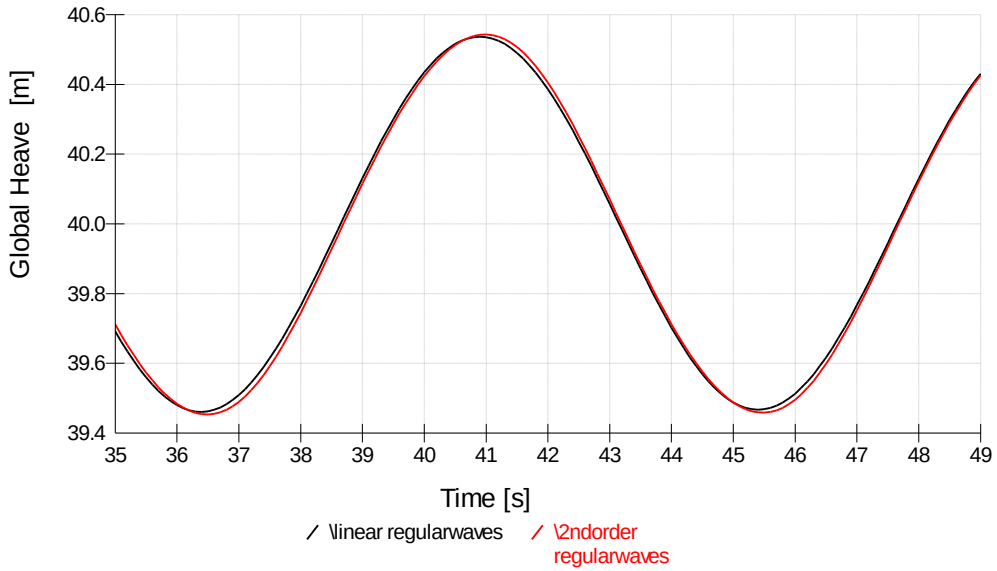

Figure 6.2. Cylinder heave displacement with both linear and 2nd order PTO models.

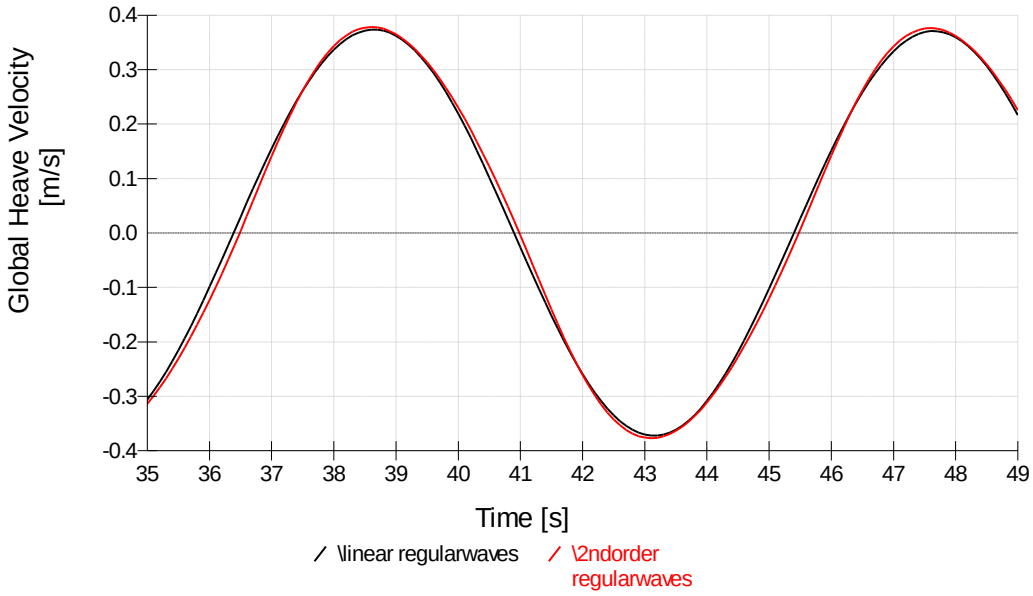

Figure 6.3. Cylinder heave velocity with both linear and 2nd order PTO models.

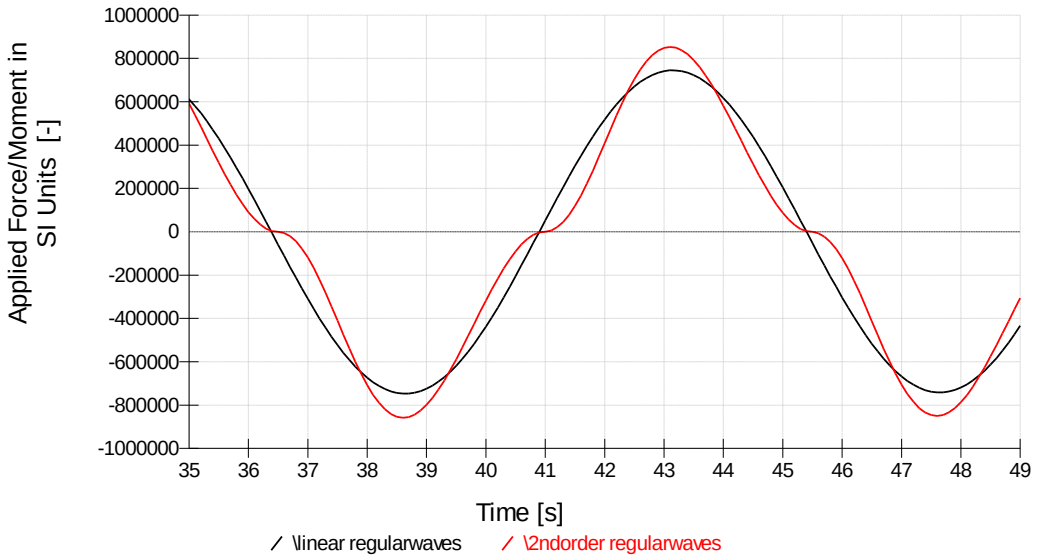

Figure 6.4. Applied PTO force for the heaving cylinder under both linear and 2nd order PTO models.

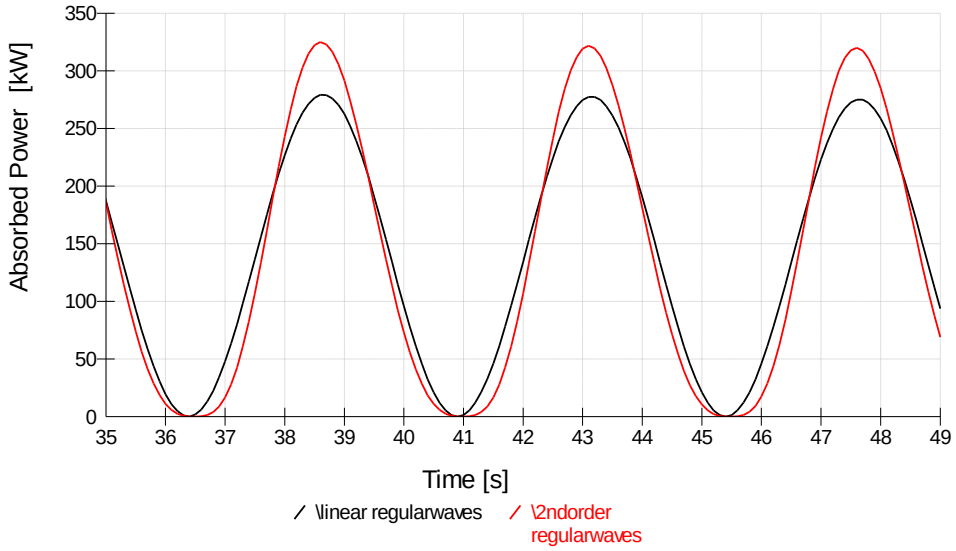

Figure 6.5. Absorbed PTO power for the heaving cylinder under both linear and 2nd order PTO models.

6.5 Smoothing-rectification PTO template: control and implementation

The smoothing and rectification PTO template implementation is more complex than the simple explicit models described in Sections 6.3 and 6.4 above. This is the first of a set of potential PTO 'template' models; the templates are specifically designed to capture the salient features of a certain type of PTO, avoiding the need to model the complete machine design down to an individual component level. The template allows the potential performance and critical load levels on the WEC to be assessed and may require interaction with the WaveDyn integrator so that the internal system states can be solved.

The mathematical basis for the smoothing-rectification PTO template implementation was given in the methodology report, WG1 WP1 D1b, Sections 3.6.1 and 5.5.4. The model consists of five parts, or sub-models, which may be briefly summarised as:

1. The actuator model: the primary interface between wave-activated bodies and the PTO mechanism. The force applied to the actuator is used to pump a working 'flow' around the PTO circuit. The term 'flow' is loose and may refer to a hydraulic fluid or an electrical current (or indeed anything that may be modelled sufficiently accurately by the mathematical equations presented). The flow has both a potential (pressure or voltage) and flow rate (or current).

2. The rectifier model: designed to simulation the rectification of the actuator flow, including a loss model in which valve losses and component resistances may be applied in a simplified, lump format.

3. A smoothing model: a flow capacitance designed to smooth ripples in the actuator flow so as to allow a more constant flow rate to be drawn through the load-drive element with limited variation in flow potential.

4. The load-drive element: converts some of the energy in the flow to a mechanical, rotational form used to drive the generator load. The conversion occurs with a specified efficiency and a limit on the maximum allowable flow rate.

5. The generator model: an additional electrical efficiency term for the electrical generator and power converter operations.

Each of the sub-models operates with additional, designated control variables allowing the template operations to be continuously adjusted. The control points and the interactions between the sub-models is shown in WG1 WP1 D1b, Figure 3.5, which has been reproduced in Figure 6.6 below. The mathematical calculations completed for each sub-model are described in Table 6.3. The `CalStateDevApprove` function for the PTO template bodies completes the calculations following the algorithm described below. The calculations are referenced directly to Table 6.3 using cross-referencing tags following a **/1/, /2/, …,/N/** format. The user-defined models are not yet supported in the code (see Section 9.2). `CalStateDevApprove` receives the instantaneous time and joint kinematics as its input arguments. Pointers to the body internal charge states are contained within a PTOStruct state list (these are established during the PTOStruct Initialisation call) and are used to set the states for all the PTO models prior to the calculations being completed.

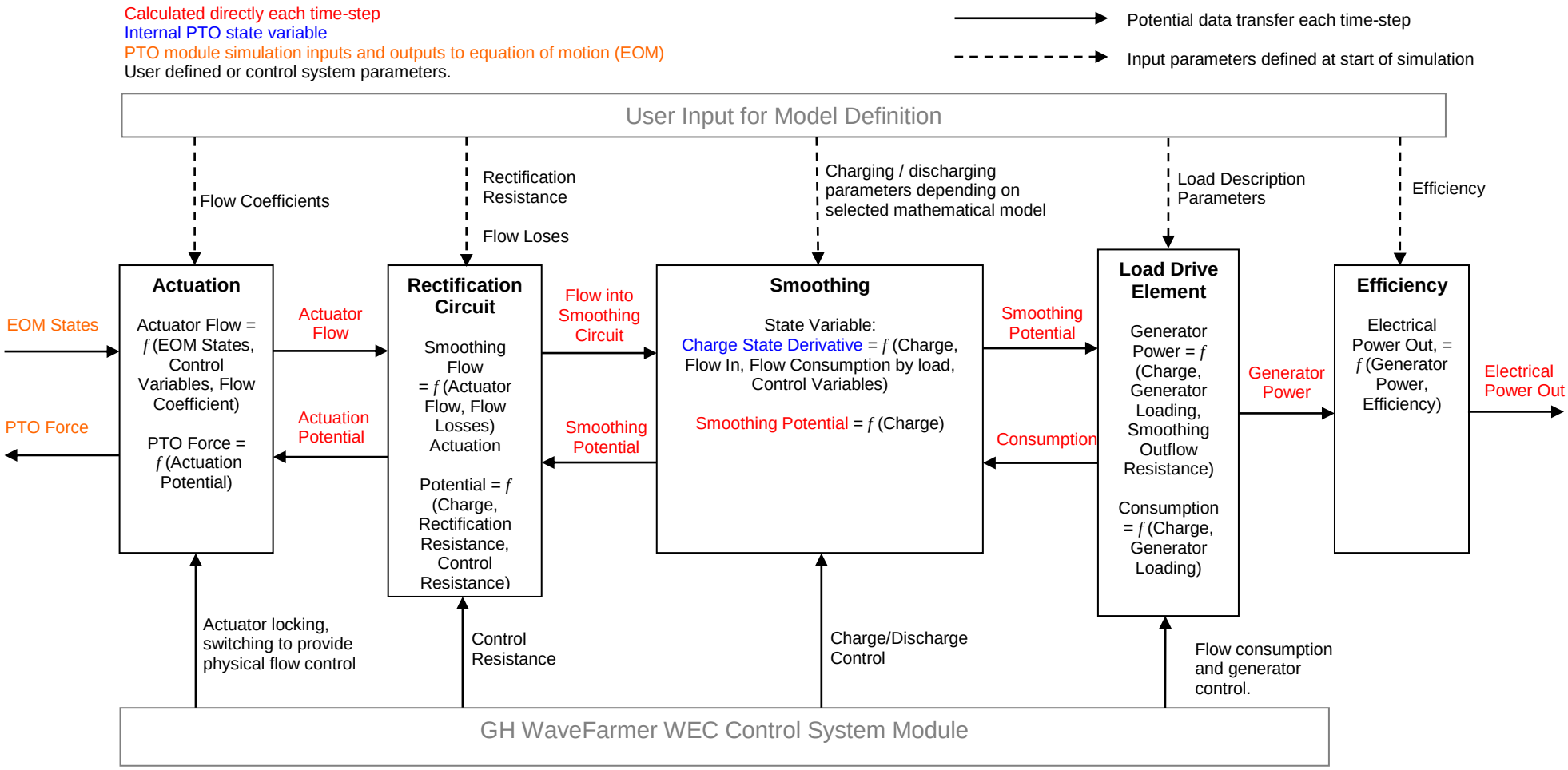

Figure 6.6. The smoothing-rectification PTO template sub-model interactions, including control and user supplied variables .

The smoothing-rectification PTO template calculation algorithm can be summarised in the following key steps:

- Check state values are within a realistic set of allowable limits (ensure charge state is not less than zero).
- Calculate the smoothing potential (pressure or voltage) in the accumulator or capacitor directly from the charge state **/1/**. The user may have selected an electrical capacitor or hydraulic accumulator model.
- Calculate the actuator flow from the velocity of the joint freedoms. **/2/**
- Calculate the actuation potential from the smoothing potential, the rectified actuator flow rate and the rectification resistances and the control terms. **/3/**
- Determine the PTO force on the actuator from the actuation potential. This is passed back to the coordinating level of WaveDyn code, where it is applied to the joint the in the MBCore structure. **/4/**
- Calculate the the flow in to the smoothing element (accumulator or capacitor). Both a constant leakage loss and a flow loss in proportion the actuation potential are applied. **/5/**
- On the generator side of the smoothing system, calculate the load-drive element flow consumption from the smoothing potential (the potential within the accumulator or capacitor element; the assumption is made that this is approximately the full potential difference across the load drive). The consumption flow is limited by a user input peak value. **/6/**
- Use the load-drive element flow consumption and the smoothing circuit flow potential to calculate the generator drive power (again assuming that the smoothing circuit flow potential is equivalent to the potential drop across the drive). **/7/**
- Apply electrical efficiency terms to the drive power to obtain an estimate for the electrical power output. **/8/**
- Calculate the charge state derivative as the net flow into the smoothing element. Return this value to the WaveDyn numerical intergrator. **/9/**
- Record all calculation variable values to the output data streams if an output timestep has been called.

Table 6.3. The mathematical formulation of the Smoothing-Rectification PTO Template.

Actuation			
User Defined Parameters			
Name	*Symbol*		*Description*
Flow Coefficient	C_F		Simple velocity coefficient used to calculate PTO 'flow' rate
Control Parameters			
Name	*Symbol*		*Description*
Actuator Locking	I_{LOCK} B_{LOCK}		Variables used to 'lock' actuator motion by applying a damping B_{LOCK} whenever the Boolean parameter I_{LOCK} is set to 'true'.
Control Flow Coefficient	C_{FC}		Controller defined flow coefficient term. Used to mimic discreet actuator switching or other form of variable flow actuation.
Inputs and Outputs (I/O) (Working Variables)			
Name	*Symbol*	*I/O*	*Description*
EOM States	$\underline{z}$	I	Equation of motion states – typically body displacement, z_1 and velocity, z_2.
Actuation Potential	Γ_A	I	Potential Difference across actuator
PTO Force	f_{PTO}	O	Instantaneous power take-off force output.
Actuator Flow	Q_A	O	Energy carrying flow rate out from actuation component.
Calculations – User may select from multiple calculation models if available			
Calculation Name	*Model Number*		*Model Description*
Actuator Flow /2/	1		$Q_A = \left(C_F + C_{FC}\right) z_2$
	2		User Defined. Format must fit: $Q_A = f\left(C_F, C_{FC}, \underline{z}\right)$
PTO Force /4/	1		$f_{PTO} = \left(C_F + C_{FC}\right)\Gamma_A + B_{LOCK} z_2$
	2		User Defined. Format must fit: $f_{PTO} = f\left(C_F, C_{FC}, \Gamma_A, \underline{z}, B_{LOCK}\right)$

Rectification Circuit			
User Defined Parameters			
Name	*Symbol*		*Description*
Rectification Proportional Flow Loss Coefficient.	C_{L-RP}		Proportional loss coefficient. Allows user to specify a flow loss in proportion to the actuator potential. Loss is representative of a leakage in a hydraulic system.
Rectification Constant Flow Loss	Q_{L-RC}		Constant flow leakage loss regardless of pressure or flow rate.
Rectification Resistance	R_R		Flow resistance due to valves or resistors in the rectification circuit.
Control Parameters			
Name	*Symbol*		*Description*
Control Resistance	R_{RC}		A controllable flow resistance.
Control Potential	Γ_C		Additional controller induced actuator potential
Inputs and Outputs (I/O) (Working Variables)			
Name	*Symbol*	*I/O*	*Description*
Actuator Flow	Q_A	I	Energy carrying flow rate out from actuation component.
Smoothing Potential	Γ_S	I	Potential difference across generator power-train. Maintained by smoothing circuit.
Actuation Potential	Γ_A	O	Potential difference across actuator
Smoothing Flow	Q_S	O	Energy carrying flow rate out into smoothing circuit.
Calculations **(User may select from multiple calculation models if available)**			
Calculation Name	*Model Number*		*Model Description*
Actuation Potential /3/	1		$\Gamma_A = \Gamma_S + \lvert Q_A \rvert \left(R_R + R_{RC} \right) + \Gamma_C$
	2		User Defined. Format must fit: $\Gamma_A = f\left(\Gamma_S, R_R, R_{RC}, Q_A, \Gamma_C\right)$
Smoothing Flow /5/	1		$Q_S = \lvert Q_A \rvert - C_{L-RV}\Gamma_A - Q_{L-RC}$
	2		User Defined. Format must fit: $Q_S = f\left(C_{L-RP}, Q_{L-RC}, Q_A, \Gamma_A\right)$

Smoothing Circuit			
User Defined Parameters (Note than in this case, use is dependant on calculation selection)			
Name	*Symbol*		*Description*
Accumulator Pre-Charge Potential	Γ_0		Pre-charge pressure for the gas accumulator model.
Accumulator Size	Φ_0		Total accumulator volume for the gas accumulator model.
Capacitance	C_y		Capacitance for the electrical model.
Polytropic Index	n		Polytropic index for the accumulator gas expansion and compression process (assumed constant).
Other User Defined Parameters	$C_{SU\_1}, C_{SU\_2}, \ldots$		User defined constants for use in a user defined smoothing model.
Control Parameters			
Name	*Symbol*		*Description*
User defined control variable	V_{SU_1}		Control variable for use with a user defined smoothing potential mathematical model.
Inputs and Outputs (I/O) (Working Variables)			
Name	*Symbol*	*I/O*	*Description*
Smoothing Flow	Q_S	I	Energy carrying flow rate into smoothing circuit.
Consumption	Q_C	I	Energy carrying flow passing though the generator power train.
Smoothing Potential	Γ_S	O	Potential difference across generator power-train. Maintained by smoothing circuit.
Calculations – User may select from multiple calculation models if available			
Calculation Name	*Model Number*		*Model Description*
Charge State Derivative **/9/**	1		$\dot{\Phi} = Q_S - Q_C$
Smoothing Potential **/1/**	1		Gas Accumulators System (Polytropic) $\Gamma_S = \Gamma_0 \left(\frac{\Phi_0}{\Phi_0 - \Phi} \right)^n$
	2		Electrical Capacitor System $\Gamma_S = \frac{\Phi}{C_y}$

	3	User Defined. Format must fit $\Gamma_S = f\left(\Phi, V_{SU\_1}, \ldots\right)$
States		
State Name	*Description*	*State Derivative Calculation Name*
Charge, Φ	Quantity of fluid or charge stored in the smoothing circuit.	Smoothing Potential

Load Drive Element			
User Defined Parameters			
Name	*Symbol*		*Description*
Load Resistance	R_L		Loading on the generator drive components.
Smoothing Outflow Resistance	R_{OUT}		Resistance to outflow from the smoothing model.
Powertrain Mechanical Efficiency	η_{DM}		'Mechanical' efficiency of generator drive componentry.
Powertrain Volumetric Efficiency	η_{DV}		Volumetric efficiency of generator drive componentry.
Control Parameters			
Name	*Symbol*		*Description*
Powertrain Control Resistance.	R_{DC}		Control resistance used to modulate flow to the powertrain.
Maximum Consumption	Q_{DC_MAX}		Controller applied limit on the powertrain flow consumption.
Inputs and Outputs (I/O) (Working Variables)			
Name	*Symbol*	*I/O*	*Description*
Smoothing Potential	Γ_S	I	Potential difference across generator power-train. Maintained by smoothing circuit.
Consumption	Q_C	O	Energy carrying flow passing though the generator power train.
Generator Power	P_G	O	Generator Drive Power
Calculations – User may select from multiple calculation models if available			
Calculation Name	*Model Number*		*Model Description*
Consumption **/6/**	1		$Q_C = MIN\left(\frac{1}{\eta_{DV}}\frac{\Gamma_s}{R_{OUT}+R_L+R_{DC}}, \frac{Q_{DC\_MAX}}{\eta_{DV}}\right)$
Generator Drive Power **/7/**	1		$P_G = \eta_{DM}\eta_{DV}Q_C\Gamma_S$

Electrical Generator (Simple Efficiency Model)			
User Defined Parameters			
Name	*Symbol*		*Description*
Generator Efficiency	η_{GEN}		Electrical generator efficiency.
User Defined Parameters	C_{SU_1}, C_{SU_2},…		User defined constants for electrical generator model. May be used to describe power electronics effects thereby providing a more comprehensive model of the generator and power converter until a more sophisticated electrical model is available.
Inputs and Outputs (I/O) (Working Variables)			
Name	*Symbol*	*I/O*	*Description*
Generator Power	P_G	I	Generator input power
Electrical Power Output	P_E	O	Electrical power output
Calculations – User may select from multiple calculation models if available			
Calculation Name	*Model Number*		*Model Description*
Electrical Power Output **/8/**	1		$P_E = \eta_{GEN} P_G$
	2		User defined model $P_E = f\left(P_G, C_{SU\_1}, C_{SU\_2}, ...\right)$

The .IN file input format for the user-supplied data listed in Table 6.3 is given in Table 6.4 below.

<pto >pto Sub-block Parameters; PTOType = 2ndOrder			
Input Parameter (as presented in the .IN file)	**Data Format**	**Parser Dependencies**	**Description**
PTOType	= SmoothRect		
SmoothingPotenModel	Integer Number	None	< 0 indicates a hydraulic accumulator model. = 0 indicates an electrical capacitor model. > 0 indicates another, user-supplied model.
FlowCoeff	Double precision, floating point number.		Actuator flow coefficient. Relates joint velocity to system flow rate.
RectFlowLossPropActPCoeff			Rectification potential flow loss coefficient. Flow loss in proportion to the actuator potential.
ConstantRectFlowLoss			Constant flow leakage from the rectification circuit.
RectResistance			Flow resistance due to valves or resistors in the rectification circuit.
PolyTropIndex			Polytropic index for the accumulator gas compression and expansion process. Not used for the electrical capacitor model.
AccPreChargePot			Gas pre-charge pressure for the accumulator. Not used for the electrical capacitor model.
AccSizeCap			Accumulator or capacitor size.
LoadResist			Load resistance – constant damping or resistance value to represent the load provided by the generator and power-train.
SmoothOutResist			Resistance to outflow from the capacitor or accumulator.
PowerTMechEff			Mechanical efficiency of generator drive componentry.
PowerTVolEff			Volumetric efficiency of generator drive componentry.
GenElecEff			Generator and power-train electrical efficiency.
MaxConsump			Limit on flow consumption by the generator drive componentry.

Table 6.4. PTO sub-block .IN file parameters for the Smoothing-Rectification PTO Template.

As for the second-order PTO model (Section 6.4), initial PTO template test simulations have been completed using the point-absorber FDC model (heaving point absorber). The hydraulic system mimics that shown in Figure 6.7, although the pressure drop across the hydraulic motor created by the combined high and low-pressure accumulators must be modelled using the single accumulation element in the PTO template. The 'flow constraint' valve operates as a limit on the maximum flow rate allowed through the hydraulic motor and may in reality take the form of a pressure-compensated flow control valve, which would have additional dynamic properties. The rectification and accumulator outflow resistances in the PTO template model and losses are not shown in Figure 6.7.

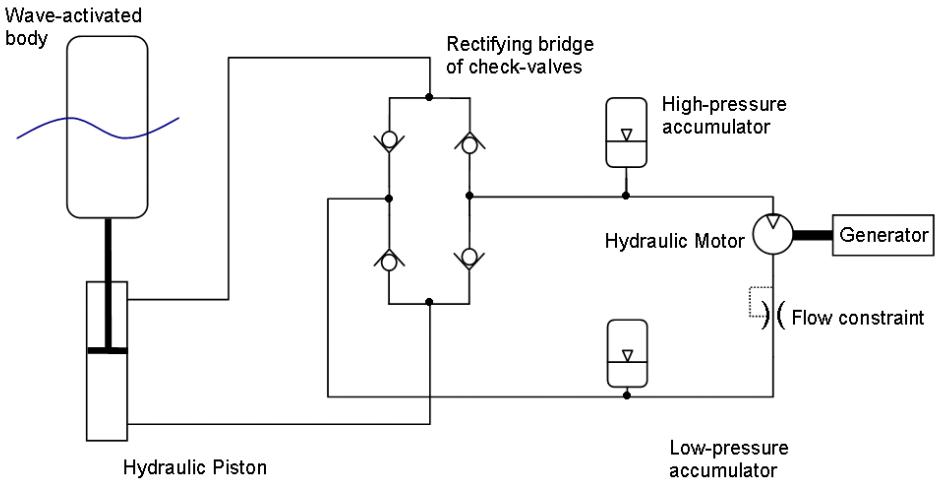

Figure 6.7. Simple hydraulic accumulator PTO system.

The WaveDyn inputs for all of the PTO template parameters are listed below. All parameters are in S.I units:

```
SmoothingPotenModel = -1
FlowCoeff = 0.03
RectFlowLossPropActPCoeff = 1e-12
ConstantRectFlowLoss = 0.00001
RectResistance = 200
PolyTropIndex = 1.3
AccPreChargePot = 6000000
AccSizeCap = 0.1
LoadResist = 100000
SmoothOutResist = 100
PowerTMechEff = 0.95
PowerTVolEff = 0.95
GenElecEff = 0.98
MaxConsump = 0.008333
```

The results from a sample simulation run for regular waves with a 0.4rad/s angular frequency and a 1m wave amplitude are shown in Figure 6.8 to Figure 6.13. The smoothing effect provided by the accumulator is clearly visible and could be improved further by using a larger accumulator or through a user specific control system modulation of the accumulator outflow. The more complex model, which includes loss terms, allows a more realistic assessment of device performance to be obtained than is possible with the simple (explicit) mathematical PTO models.

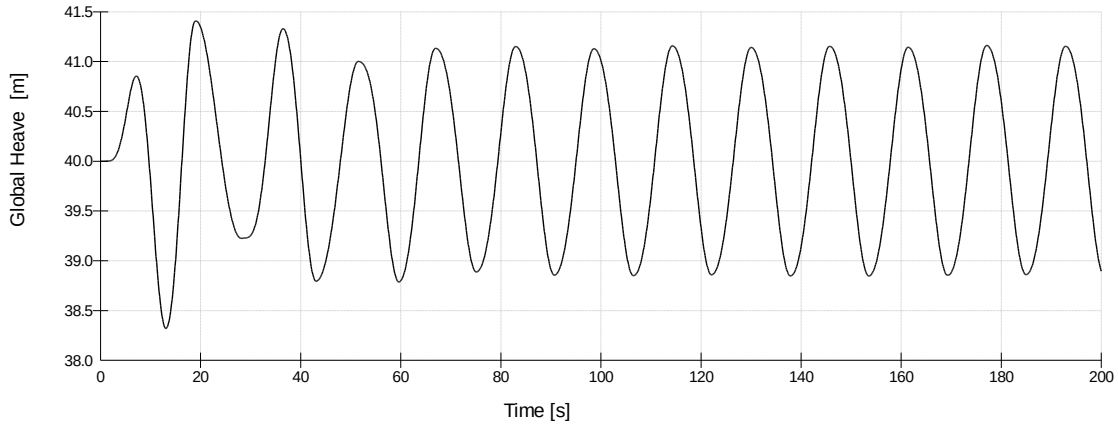

Figure 6.8. Cylinder heave displacement time-series as the cylinder pushes fluid in to the hydraulic accumulator.

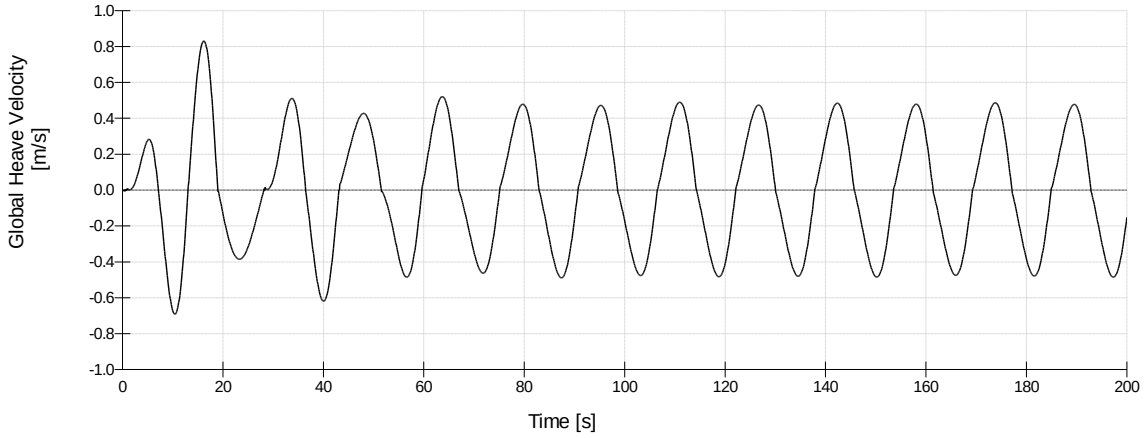

Figure 6.9. The pressure maintained by the accumulator system distorts the velocity time-series away from the symmetric periodic form obtained with the linear and 2nd order PTO models.

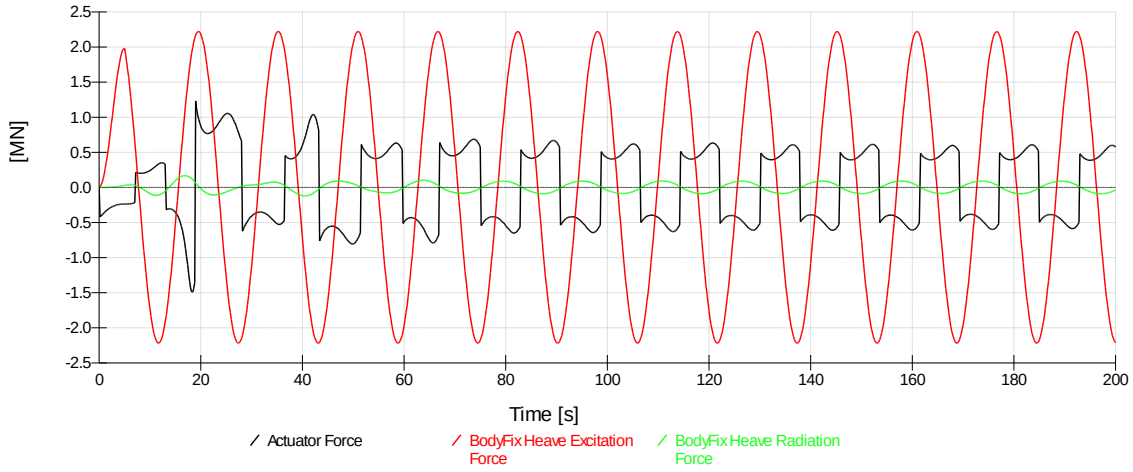

Figure 6.10. Excitation force, radiation force and PTO actuator force time series. The PTO actuator motion is consistently opposed by the high accumulator pressure.

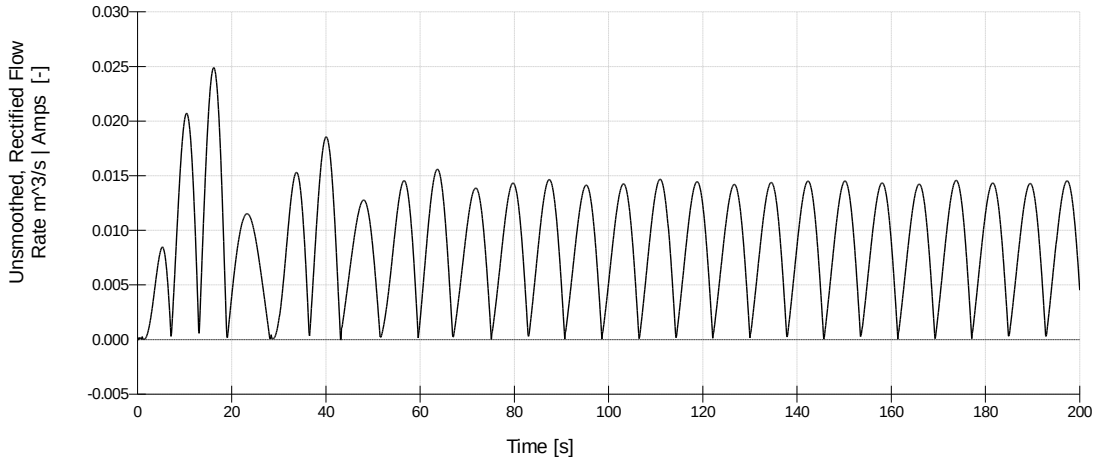

Figure 6.11. The unsmoothed flow passing from the rectification circuit to the hydraulic accumulator.

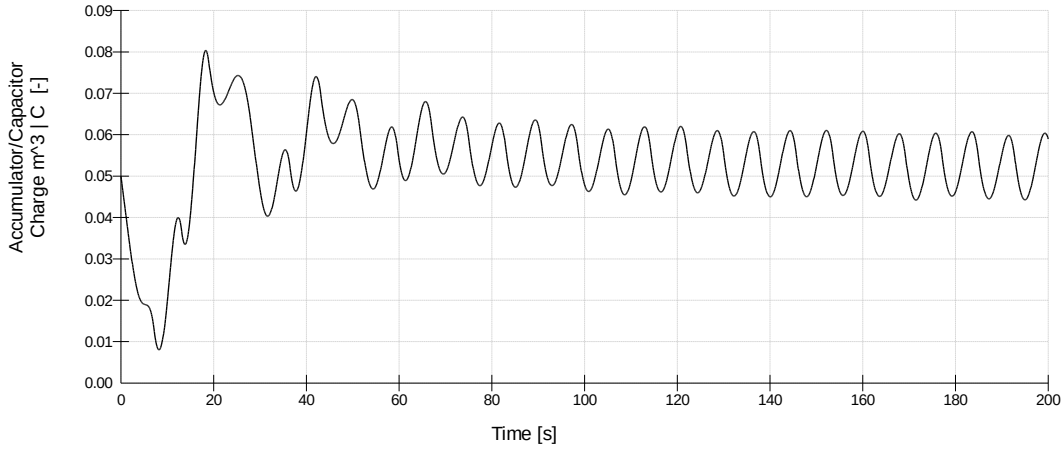

Figure 6.12. Variation in accumulator charge. A larger accumulator would allow still smaller charge variation and a more constant potential drop across the generator drive-train.

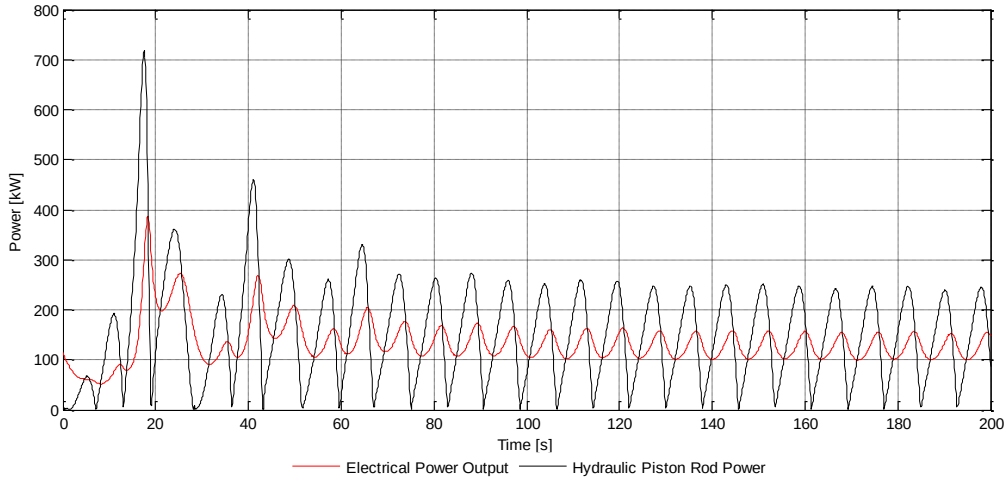

Figure 6.13. Comparison between the power in the PTO joint and the smoothed electrical output.

The control parameters for the smoothing-rectification PTO template are much more complex than for the simple, explicit mathematical models presented in Sections 6.3 and 6.4, however control variables positioned throughout the mathematical formulation (see Table 6.3) support a number of strategies. Basic tuning and latching control techniques for systems of this type are presented in Falcão (2007; 2008) and Livingstone and Plummer (2010).

7 OPTIMISER MODULE

7.1 Overview of the development strategy

The role of the optimiser module is to assist in the design a wave farm under realistic engineering constraints. In the Frequency-Domain Implementation Report (WG1 WP1 D2) the foundations of the implementation were laid. Since the overall approach has been retained in the current implementation, a brief summary is given in Section 7.2 along with an update on certain aspects of it. Up until this point, the optimiser has been integrated with an equation of motion solver that operates in the frequency-domain. The major advance in the current implementation is the integration of the optimiser module with the time-domain version of the equation of motion solver (WaveDyn), which is detailed Section 7.3. This implementation step allows a characterisation of WECs including their major subsystems like the PTO, which is more detailed than frequency- or spectral-domain calculations (allowing verification of the latter approaches). This last task was in the list of next-steps given in the aforementioned report:

- Improve the optimisation of array layout by using different settings with the Genetic Algorithm or possibly employing an alternative procedure.
- Investigate the trade-off between efficiency and accuracy in the computation of the hydrodynamic solution for the layout optimisation objective function.
- Investigate the suitability of local optimisation routines to the problem of PTO coefficient optimisation and possibly use an alternative approach.
- Integrate the optimiser module with the time-domain WaveDyn tool for the objective function.
- Investigate procedures for estimating the interaction effects between WECs and incorporate into the optimiser module.

The remaining items from this list represent technical investigations regarding the operation of the optimiser and are covered in the latter part of this section (namely Sections 7.4-7.7). Several case studies demonstrating the functionality of the optimiser described in the current section are presented in Section 8.

7.2 Details of the implementation

In this section, the implementation of the optimiser module will be briefly described, detailing the optimisation problem to be solved, the development plan for the optimiser and the optimisation algorithms themselves. Advances in functionality are detailed as well as a summary of existing features previously described in the Frequency-Domain Implementation Report (WG1 WP1 D2).

7.2.1 Problem definition

The problem that must be solved may be defined in terms of several collections of information that interact with each other within the optimiser. These may be conveniently categorised using the following labels:

- Objective function: the quality of a design that is required to be enhanced or reduced
- Fixed inputs: the variables that the optimiser receives from other modules or user input
- Constraints: the features of the solution that must be satisfied by the output from the optimisation

- Penalties: factors that lower the estimation of how suitable a particular solution is without excluding it from the optimisation
- Design variables: the quantities that can be altered by the optimisation algorithm in order to change the features of the solution

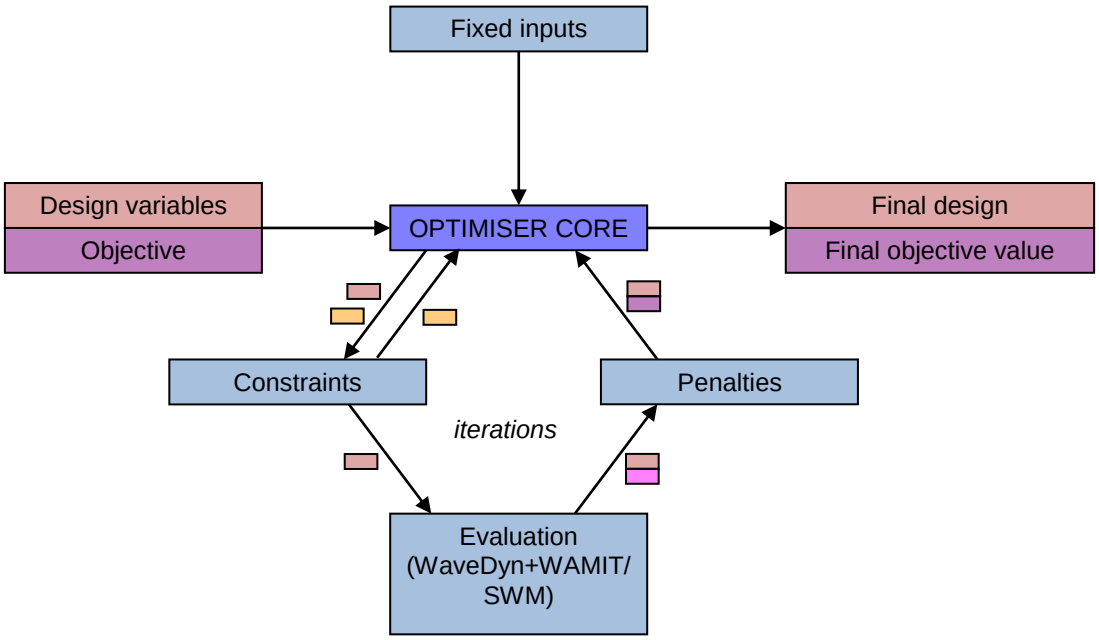

Figure 7.1. Structure of optimisation algorithm.

The general structure of an optimisation algorithm, including the above mentioned categories of information, is shown in Figure 7.1. The sets of design variables pass around the system leading to multiple evaluations of the objective function by other modules of the software (such as WaveDyn or potentially the spectral wave model under development in WG1 WP2). This is often the most time-consuming part of the whole process since it generally involves the assessment of many different physical scenarios. It should be noted that in a time-domain approach, the call to the objective function is more computationally intensive than an equivalent call to a purely frequency-domain solver, although it has the ability to more accurately represent the WEC behaviour.

The variables that are used in the current implementation of the optimiser module in each of the categories specified above are described below in more detail.

Objective function

- Maximisation of the absorbed power in a certain wave climate

An alternative objective that will be treated in future developments of the tool is the minimisation of the total cost of energy. Although this may change the results of the optimisation, the functionality of the software will not be significantly altered, since the modular nature of the tool allows other objective functions to be inserted into the optimisation procedure. In the interim period, the maximisation of total absorbed power will remain the objective.

Fixed inputs

- Sea-state
- Water depth
- Number of WECs in the array
- Geometry of each WEC
- Modes in which the WEC can move
- Modes of motion in which power is converted

The current implementation of the software is now able to load a single multi-body WEC definition and subsequently perform optimisation on the array design variables described below. Further information on this process is contained in Section 7.3.

Design variables

- Layout of WECs within the array
- PTO settings for each WEC

Either of these sets of variables may alternatively be entered by the user as fixed inputs with the optimisation performed on the remaining set. They both may have a significant influence on the performance of the array as a whole due to their effect on the hydrodynamic interactions between WECs. In the following paragraphs, the way that each is represented as design variables is described.

Firstly, the variables associated with the array layout are defined. In the general case, the layout of an array of WECs may be described using an x and a y coordinate for every converter following the first (as well as a machine heading if the WEC is not axially symmetric). However, in the present implementation a formation pattern is defined to which all layouts must conform. This consists of a 'regular grid,' where WECs are placed at the intersections of two sets of equally spaced parallel lines. Although this is a more restrictive definition than WECs existing in any location, there are a number of reasons why it might be more attractive. The first is that it significantly reduces the number of variables needed to describe arrays of many bodies. This reduction in the size of the search space has the potential to lead to an improvement in optimiser efficiency. Secondly, free optimisation of the layout (that is, without formation patterns imposed) has been seen to produce regular arrangements in a number of scenarios (Child and Venugopal, 2010). Hence it is anticipated that a regular grid regime would assist the optimisation in finding configurations more effectively without the resulting objective function being significantly affected. Future implementations of the tool may allow irregular spacing of WECs, although it should be noted that a larger amount of computational effort would be required due for this to the increased size of the search space.

The regular grid formation of an array of N WECs, illustrated in Figure 7.2, is defined as follows. Firstly two directions are defined, making angles ψ and σ with the positive x-direction (mean incoming wave direction). Next, a grid is constructed such that lines are placed at regular intervals with spacing p in the direction defined by ψ and s in the σ-direction. An integer number of adjacent gridlines M are chosen in the σ-direction, and a sufficient number, ceil(N/M), in the ψ-direction such that their product of the two values is at least as big as the number of WECs. The intersections of the chosen gridlines then define the potential WEC locations. These positions are filled by WECs sequentially in a down-wave direction from the most up-wave point of the array until all N converters have been allocated a position. In the case that more than one candidate for the final WEC location share the same x-coordinate, preference is given to the one with the least y-coordinate, without loss of generality.

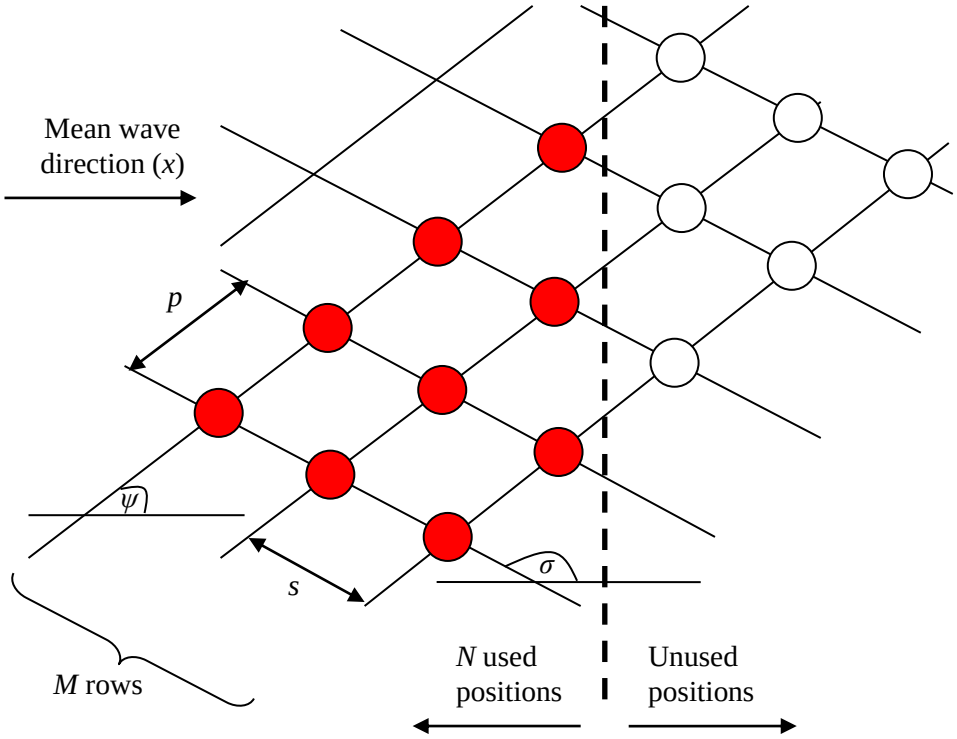

Figure 7.2. Regular grid definition sketch (axially symmetric WECs).

There are therefore five parameters that govern any particular instance of arrays of axially symmetric WECs using this formation: [ψ, σ, p, s, M]. In the case of non-axially symmetric WECs, a sixth parameter (the WEC heading) is generally required in addition to these variables. However, where only unidirectional waves are considered, the WEC heading for all WECs may be set in advance of any optimisation, thus reducing the set of parameters to those given above.

The other main set of design variables involves the characteristics of the PTO for each WEC, bearing in mind that each WEC may have multiple PTO modes. Depending on the PTO options and / or control strategies that are permitted by the constraints (see also Section 6), these parameters will take a different form. For example, if only a dissipative component is to be considered then the PTO settings may be expressed as a collection of damping coefficients, one for each mode in which power is converted, for each WEC in the array. If a reactive component is also permitted, then there are twice this number of parameters; a spring and a damping coefficient for each mode as previously mentioned. The use of a time-domain equation of motion solver will also allow the use of additional definitions of each individual PTO subsystem, via for example, the PTO templates (see Section 6). Further work will address the definition of WEC parameterisations to exchange information with the optimiser module. These would be similar to the wave climate parameterisation described in Section 4 and may be formed utilising the functionality of WaveDyn.

Constraints / Penalties

- Minimum spacing between WECs
- Minimum and maximum PTO settings
- Allowable control strategies to be tested

One constraint that is required in any layout optimisation is that of the minimum distance between array elements. This serves two main purposes: the first is to ensure that arrangements are not created with intersecting bodies. The second stricter condition is that WECs should be far enough apart that the chance of collision is small, even in highly energetic seas. For point-absorber WECs, a simple minimum centre-to-centre spacing condition may be employed for this purpose. The situation for an array of attenuators (the other FDC under analysis) requires deeper consideration. The approach taken here is to insist that the WECs should not collide if the mooring of the tail of the converters becomes unattached whilst that located at the nose remains. This rationale also allows the positions and constraints on this type of WEC to be expressed in the same way as for point-absorbers. Distances between WECs of more than two attenuator lengths may in fact be necessary due to access requirements for operation and maintenance, although these constraints may be dealt with in a similar way.

An array of attenuators is thus defined such that the WEC positions generated by the optimisation routine relate to the locations of the noses of the converters. The minimum spacing constraints may then be expressed by imposing a minimum distance between any two WEC positions, as indicated in Figure 7.3.

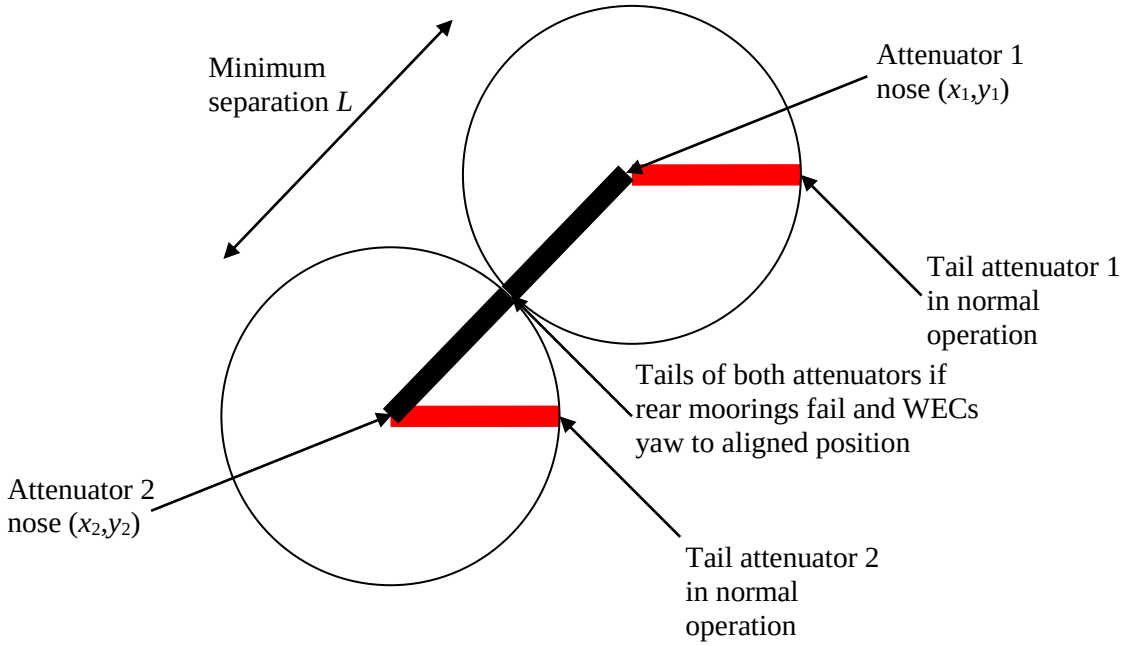

Figure 7.3. Layout definition and constraint for arrays of attenuators.

In addition to a minimum spacing condition it may also be necessary to place an upper limit on the physical size of the array due to, for example, the finite dimensions of the leased area for a particular site. There are several ways that this may be performed, although the parameterisation of the array layout lends itself to one in particular that has been implemented thus far. Hence the maximum size of the array is determined by an upper limit being placed on the following parameters

- The spacings s and p between WECs along the gridlines defined by the regular grid
- The number of rows M and columns ceil(N/M) defining the regular grid

An example of an optimisation involving these constraints is described in Section 8. Future implementations of the tool may impose stricter conditions by forcing the evaluation of the objective

function to be zero for a layout that exceeds a certain measure of array size (effectively implementing an exclusion criteria).

7.2.2 Detailed development plan

The development of the optimiser module has been decomposed into several 'scenarios' as detailed in the Frequency-Domain Implementation Report (WG1 WP1 D2). Scenarios 1A and 1B relate to the Beta 1 version of the software, whereas the more advanced Scenarios 2A and 2B (also preliminary described below) will only be implemented in the Beta 2 version.

Scenario 1A

In this approach, the optimisation problem is handled using an exhaustive method. A fixed set of cases and associated design variables are determined before evaluation of the solutions is made. The final design is then determined by comparing the objective function values, penalties and whether or not the constraints are satisfied, before one is selected. This corresponds to one long iteration of the loop shown in the lower half of Figure 7.1.

Note that meaningful exhaustive optimisation was possible in the PTO optimisation of small arrays using a purely frequency-domain approach. However, in the time-domain the solution of the equations of motion is a more lengthy procedure. Therefore although the tool is capable of testing a small number of array solutions, an effective optimisation is likely to be associated prohibitively long computational run times. Moreover the results and discussion from exhaustive optimisation were contained in the frequency-domain implementation report (WG1 WP1 D2) and so no further discussion of Scenario 1A will be contained in this report.

Scenario 1B

Scenario 1B involves the evaluation of solutions at every stage of an iterative procedure. Thus, the algorithm generates solutions automatically which are evaluated by WaveDyn (and WAMIT if necessary) before adaptively generating further designs based on the success or failure of these initial solutions. This process corresponds to several executions of the loop pictured in the lower half of the optimisation scheme of Figure 7.1. Scenario 1B corresponds to the current stage of development and so a more detailed description of the algorithms used is contained in Section 7.2.3.

Scenario 2A

Scenario 2A involves the inclusion of the capability to estimate the hydrodynamic interactions between WECs within the software. Hence the characteristics of an individual WEC will be obtained prior to the execution of the optimiser module, and all other calculations will be done within the software package. It is anticipated that this could lead to an improvement in the efficiency of the optimiser. There are several options for the method by which to estimate the hydrodynamic interactions, the principal candidates of which are surveyed in Section 7.7 in anticipation of their use in this scenario.

Scenario 2B

Scenario 2B involves the use of the spectral wave methodology developed by QUB in WG1 WP2 as the design evaluation tool. This entails using a spectral solver to estimate the local sea states at each array location and a spectral-domain representation of the WEC response to describe the WEC behaviour. Such a method would significantly improve the efficiency of the optimisation, potentially

allowing much larger arrays to be considered. The applicability of this type of model in the present situation has not yet been determined, nor has the exact formulation of the optimisation problem to accompany the associated large arrays. These issues will be (at least partly) approached in WG1 WP2 D4, where a verification exercise comparing all modelling approaches will be presented.

7.2.3 Optimisation algorithms

Optimisation of the PTO coefficients relating to each WEC was demonstrated in WG1 WP1 D2 with a local optimisation algorithm. However, using a time-domain formulation, different requirements of the routine are identified. Therefore an examination of the main candidates that may be used for this purpose is contained in Section 7.6. One of the procedures that may be used for PTO optimisation that is used for layout optimisation is a Genetic Algorithm (GA). Details of the implementation of this routine are contained in the WG1 WP1 D2, whilst a summary of the routine itself is given below.

In a GA, a group of solutions 'evolve' in a guided semi-random process towards an optimum. Solutions (also known as 'individuals') are represented by a number of defining variables called 'genes'. A collection of solutions termed a 'population' is initiated, after which there follows sequentially several other populations at stages called 'generations'. After each is created, the value of the objective function is calculated for each individual in the population with the best ones more likely to be selected to proceed. These then form the basis of individuals belonging to the next generation by three reproduction mechanisms: 'crossover', 'mutation' and 'elitism.' Crossover involves creating new individuals combining the features of two 'parent' individuals; Mutation involves a random perturbation to the genetic make-up of a single individual. The highest-rated 'elite' individuals pass into the next generation unchanged. After certain stopping criteria have been met, the final solution is the most highly-rated solution in the final generation. For more details, see Mitchell (1998).

7.3 Time-domain WaveDyn integration

For the Frequency-Domain Implementation Report (WG1 WP1 D2), a link was made between the optimiser and an equation of motion solver that operated purely in the frequency-domain. Since then, the time-domain tool WaveDyn has been integrated into the optimiser module, allowing the optimisation of arrays of WECs with, for example, nonlinear motion constraints and nonlinear external forces (PTO forces and moorings). In this sub-section, the associated implementation is described.

The structure of the entire farm tool ('WaveFarmer') code, which encompasses the function of the optimiser, is shown in Figure 7.4. The WaveFarmer controller file / executable first calls sub-functions (`initialise_workspace.m`) to initialise the workspace directory structure and read in the input data from the user (`get_input_xml.m`) via an .xml input file (`CalculationInputData.xml`). The input is then processed (`process_input.m`) before being sent to one of the optimisation routines for layout or PTO settings, depending on the preference expressed by the user (`optimise_layout.m`, `optimise_PTO.m`). These processes will be described in more detail in the following paragraphs. The output from the optimisation routines is then sent to be processed (`process_output.m`) and delivered back to the user (`user_output.m`).

Note that within the PTO optimisation sub-module, it may be either the MATLAB 'Optimization' or 'Global Optimization' Toolbox that is used, depending on the routine chosen (see Section 7.6). In either case, the functionality of these external packages is provided as part of the farmer tool as a result of compiling the executable. On the other hand, the current implementation of the tool requires users to have a license for the boundary element code WAMIT in order for layout optimisation to function. It should also be noted that the 'WaveDyn' box in the diagram represents the functionality of other modules that feed into it, such as the PTO, moorings and control modules.

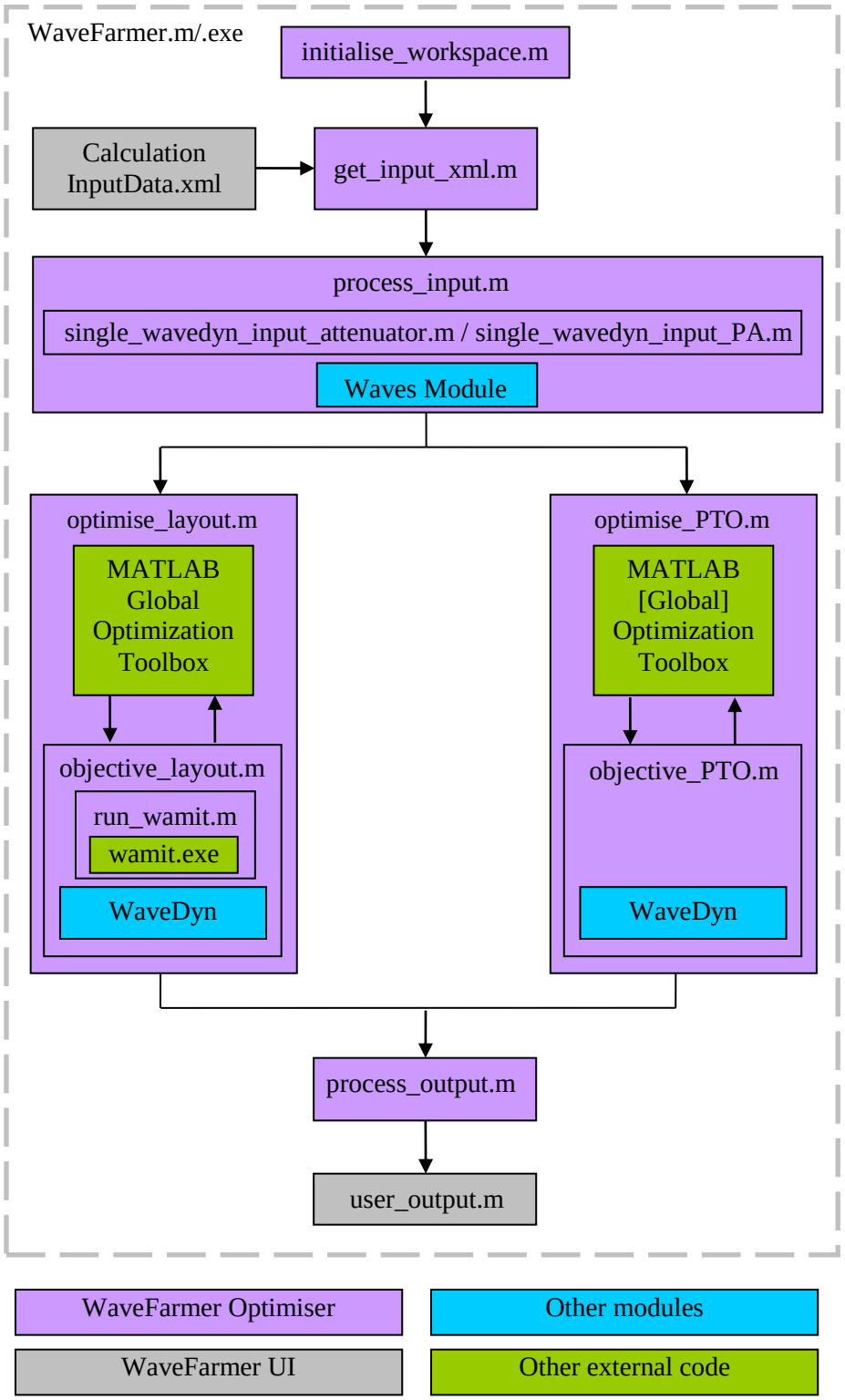

Figure 7.4. Structure of the WaveFarmer code.

The processing of input data (`process_input.m`) serves two principal purposes in the current implementation of the tool:

- Create the wave inputs using the waves module (see also Section 4)
- Define a single WEC in terms of WaveDyn inputs

If standard spectral shapes are used to create a set of wave components to represent an irregular sea in the waves module, the amplitudes may be chosen such that the wave spectrum is exactly recreated in the resulting wave record ('deterministic' amplitudes). However, the phases of the wave components are chosen at random. This does not make a difference to the average power absorption of a system if all relationships are linear, since then the principle of superposition holds in relation to the power absorption from each wave component. However, when nonlinearities are present, different sets of wave components derived from the same spectrum may lead to different performance estimates. Hence in order for the evaluations of the objective function from each array solution to be compared as fairly as is practical, the wave generation process is performed in advance of the evaluations of the objective function.

The definition of the single WEC characteristics is presently performed by one of two functions (`single_wavedyn_input_attenuator.m`, `single_wavedyn_input_PA.m`) relating to the FDCs (attenuator and point-absorber) under consideration. This process involves the setting of certain variables needed for input into WAMIT and WaveDyn. The separation of the single WEC definition from the array definition (required in the evaluation of the objective function) allows different types of converter to be more easily incorporated at a later date, since then the latter does not need to be modified for each WEC type. The two routines used here will eventually be replaced either with one that reads in a WaveDyn input file or with one that collects data directly from the user via the user interface.

The objective functions (`objective_layout.m`, `objective_PTO.m`) which are called by the optimisation functions (`optimise_layout.m`, `optimise_PTO.m`) then perform the following steps:

- Read the single WEC definition and wave inputs
- Generate WAMIT inputs (layout optimisation only)
- Run WAMIT (layout optimisation only)
- Post-process WAMIT output
- Generate array WaveDyn input file
- Run WaveDyn
- Post-process WaveDyn output to produce objective function value

Note that for PTO optimisation, the generation of inputs for and running of WAMIT is not necessary, since the hydrodynamic solution does not change over the optimiser iterations. Instead, in this case, the user points to a directory where WAMIT data exists. With the exception of this difference, the two evaluations of the objective function proceed in a similar fashion, as is described below.

WAMIT inputs are generated and run using the function `run_wamit.m`. The inputs to this function include the number of bodies belonging to each WEC, the number of WECs in the array, the coordinates of all bodies in the array, the mass matrix of each body, the names of the geometric definition files (GDFs) for each body, the water depth, the panel size used to discretise the body geometries and the location of the WAMIT executable. Both WAMIT and WaveDyn require a list of bodies in the system and so the following ordering convention is used: bodies in the first WEC are cycled over first in the order in which they are defined in the single WEC definition, followed by those in the second WEC (as defined by the objective function), and so on. Note that coordinates have to be

converted between WaveDyn and WAMIT coordinate systems that have their origin on the seabed and free-surface, respectively.

The post-processing of the WAMIT output involves extraction of the following WaveDyn input variables from the WAMIT output (see also Section 3):

- Centre of buoyancy information for each body from the WAMIT .out file (`CentreBuoyBodyFix`)
- Mass of displaced water for each body from the .out file (`MeanDispMass`)
- Added mass at infinity for each body from the WAMIT .1 file (`A_infinity`)
- Angular frequencies and wave headings for which data has been calculated (`ExciteFreqs`, `ExciteDirs`). Note that directions required are 180 degrees offset from WAMIT data and Cartesian (rather than nautical) angles are used throughout.
- Amplitude and phase of excitation force at each frequency (`Amp`, `Phase`) from the WAMIT .3 file, the latter calculated in the range $[-\pi, \pi]$.
- Hydrostatic stiffness matrices from the WAMIT .hst file, after removal of non-waterplane moment and buoyancy terms (`HydStaticStiff`).
- Impulse response functions from the added damping matrices in the .1 file, calculated using a superposition of cosine functions (`IRFData`). See WG1 WP1 D1b Equation [3.30] for further details.

The WaveDyn inputs for an array of WECs are formed from by replicating the single WEC inputs for each converter in the array, using the following guidelines:

- Nodes: Each node of the structure in the single WEC definition is replicated *N* times with a new name formed by appending 'W*X*_' to the beginning of the name, where *X* is the WEC number in the array. The 'ground' node of a single WEC then becomes several 'WEC ground' nodes.
- Nodes: One node is formed as the location of a new 'global ground' element.
- Elements: A new 'global ground' element is formed, located at the global WaveDyn origin.
- Elements: The element representing the ground in a single WEC is not copied into the array definition.
- Elements: New rigid links are formed from the 'global ground' node to each 'WEC ground' node. The location of the distal node is set equal to the WEC location within the array. This is constant for PTO optimisation and variable at every function call for layout optimisation.
- Elements: All other elements of the structure in the single WEC definition are replicated *N* times with a new name formed by appending '_W*X*' to the end of the original name, where *X* is the WEC number in the array.
- The following WaveDyn variables are then set in a different way to their equivalents in the single WEC definition:
    - PTO damping settings (`Damping`). These quantities are set to the values specified by the PTO optimisation algorithm or to fixed user-specified values for layout optimisation.
    - `BodyFixedHyOrigin`. This is derived from the coordinates of the WEC within the array since it represents the WAMIT body fixed inertial frame position (and orientation) in relation to the WaveDyn global coordinate frame.

- `BodyInteractOrder`. This needs to correspond with the order that bodies are specified in the WAMIT inputs. The same convention for ordering the bodies within the system is used here as was used to determine the WAMIT inputs.
- `AddMassInf`, `IRFData`, `Amp`, `Phase`. All of these quantities are provided by the post-processing of WAMIT data for the array under consideration.

In the above the term 'elements' is used to refer to those entities that in WaveDyn are referred to as 'bodies,' but may not be physical objects. Figure 7.5 illustrates the formation of a WaveDyn structure of nodes and elements for an array of two WECs using the definition of a single converter. The bodies attached to the nodes are not shown here for clarity.

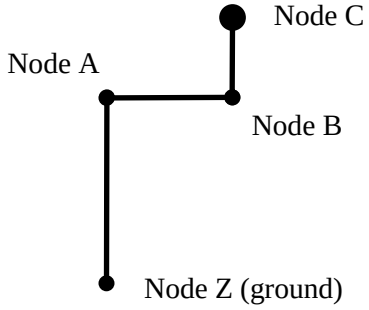

Single WEC WaveDyn structure

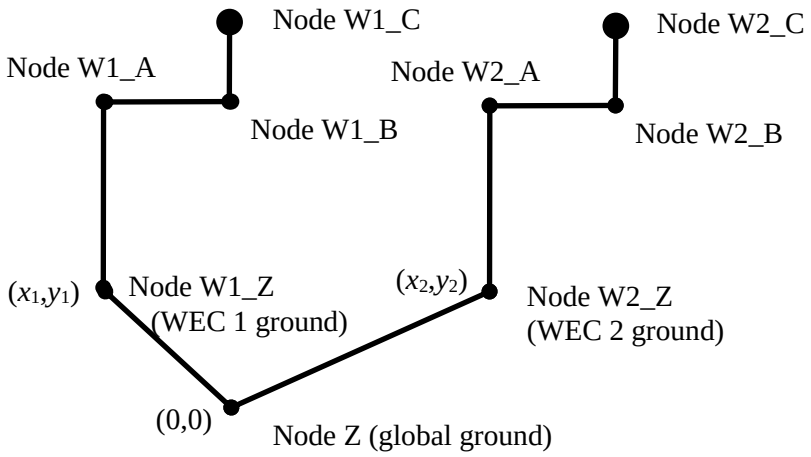

Array WaveDyn structure

Figure 7.5. Single WEC and array WaveDyn structures.

The final stage of the evaluation of the objective function is to post-process the WaveDyn output to form an objective function value. The following points summarise this process:

- An initial period of the simulation is discarded to avoid analysis of the system in a transient state.

- WaveDyn output header files (.%*XX*) whose 'CONTENT' entry ends with '-PTO' are searched for. These correspond to the outputs from the PTO module.
- WaveDyn output data files (.$*XX*) with numbers *XX* matching those found in the previous step are then loaded. The second column of data corresponding to 'Absorbed Power' is saved before being averaged over the period for which calculation has been specified (disregarding the transient period).
- The total power is calculated as the sum of the contributions from all PTO elements. This is then passed on as an objective function value to the optimisation algorithm.

The procedure outlined here has been implemented in the software and applied to arrays of point-absorber and attenuator WECs, leading to the results presented in Section 8.

7.4 Layout optimisation: Genetic Algorithm (GA) parameter setting

The performance of any optimisation routine can depend heavily on the value of certain parameters concerned with its operation. For a local optimisation routine these would include the initial values of the design variables. For a GA, such as the one employed for the layout optimisation, there is a wider range of parameters to consider (including for example, the choice of operators that generate solutions, and parameters governing the length of the optimisation). However, no definitive method exists for determining their value in the general case since the task reduces to a complex optimisation problem in itself.

One methodology for parameter-setting is to run the optimisation with many different combinations of parameters (Child and Venugopal, 2010). Since the GA involves the use of random numbers as part of the routine, a favourable value of the objective function following just one run of the algorithm does not necessarily mean that the settings are advantageous for other runs of the algorithm with different random seeds. Hence a more accurate characterisation of the effectiveness of a certain set of parameters requires the algorithm to be run several times so that an average can be taken. This is extremely computationally intensive and so here only the parameters that have the biggest effect on accuracy are analysed in detail. These consist of the following parameters:

- Generations. This parameter is analogous to the concept of the number of iterations in a standard optimisation routine. From one generation to the next the best current solution may improve so a greater number of generations is likely to lead to a better final solution.
- PopulationSize. Unlike most optimisation routines where there is only one solution per iteration, GAs involve a collection of solutions called a population to exist at any one time. The greater the size of this population, the greater the size of the search space that the algorithm can explore at each iteration, so a larger value of this parameter is likely to lead to a better final solution.

Note that there are (Generations+1)*PopulationSize objective function evaluations that take place in the optimisation, so increasing either of these has considerable impact on the computational burden. As with most optimisation processes, the greatest improvements in function values occur in the first few iterations, after which the improvements become smaller relative to the final solution. Hence there is need to identify a suitable compromise between the effectiveness and efficiency of the algorithm, leading to suitable stopping criteria.

Investigations into the effects of the aforementioned parameters were carried out by repeatedly optimising a test case with different random seeds. For this purpose, the frequency-domain solver was used because of the speed at which it can be executed, although it must be stressed that since it is the properties of the optimiser and not the solution that are under investigation, the results are equally applicable for optimisation with the time-domain solver in the case considered. The test case involved optimising the layout of an array of point-absorbers with the following specification:

- WEC type: point-absorber (truncated vertical cylinder of radius 10m and draft 10m)
- Number of WECs: N=4
- PTO: heave motion of all buoys subject to a linear damping of 640kNs/m
- Minimum separation L=60m (3 WEC diameters)
- Wave climate: unidirectional Bretschneider spectrum with H_{m0}=4m and T_p=10.2s

The PopulationSize parameter was changed set to 10, 20 and 50 in different cases and the best value of the objective function recorded after each generation up to a maximum of 50. This exercise was repeated three times for each case with different random seeds. The progress of the optimisation is shown in Figure 7.6 for three values of population sizes. The horizontal axis shows the number of generations that have occurred, whilst the vertical axis displays the best objective function value of solutions in that generation. Since the optimisation is expressed as a minimisation, the objective function (the negative of total array power in W) falls as the number of generations increase. Solid lines in the graph are mean values over all trials initiated with different random seeds, whilst dashed lines are the maximum and minimum values over the same tests.

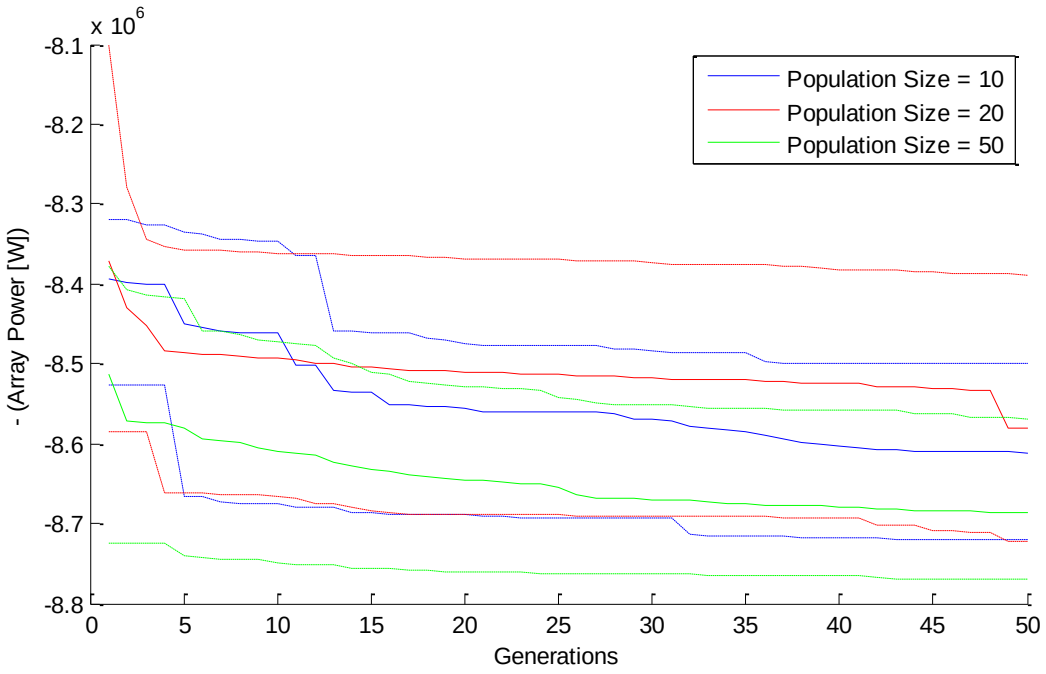

Figure 7.6. Evolution of the solution using a GA optimisation with different population sizes. Solid lines are mean values, dashed lines are minimum and maximum values over the trials.

Figure 7.6 shows that the random search of the first generation achieves an objective function value that is of comparable magnitude to the final solution in each case. Therefore the GA has quickly identified the area of the design space to be exploited in later generations. Using a greater number of generations from this point onwards, the solution never deteriorates, since the best performing "elite" individual is automatically passed from one generation to the next.

A greater population size is likely to give a better final solution in general. However, the mean objective function values for PopulationSize=10 are in fact superior to those for PopulationSize=20 in later generations here. This is due to the random fluctuations in performance of this algorithm. Note

that there is a smaller variation between minimum and maximum values for the case with the largest population size, consistent with expectation that the trial of a greater number of solutions should provide a more accurate solution..

From these results, it is clear that if a value of PopulationSize=10 is taken along with 10 generations, the value of the final objective function is only ~2% worse than with PopulationSize=50 over 50 generations. The former case is also 25 times quicker to run than the latter so may be attractive in situations where calculation of the objective function is very computationally expensive. It should be noted that different characteristics of the optimisation routine may be revealed by using other physical scenarios as the test case. However, since it is not possible to perform this lengthy analysis for all cases, some selection of representative scenarios (as performed here) must be made in order to make progress.

7.5 Computational efficiency of hydrodynamic solution

Optimisation of array layout is particularly computationally expensive due to the fact that a new hydrodynamic solution must be computed for each evaluation of the objective function. Moreover, this issue becomes even more acute as the number of WECs increases. Hence it is vital that computational times are minimised where possible.

Since the boundary element code WAMIT is presently employed to calculate hydrodynamic data, the efficiency of the whole process depends heavily on finding an appropriate set of input parameters to run this software. Such parameters may be set so that the solution is slow and potentially more accurate, fast and potentially inaccurate or a compromise between the two. However, it should be remembered that the goal for the optimiser is not necessarily to evaluate solutions accurately; rather it is to distinguish effectively between less desirable and more desirable solutions. Hence the aim in the investigations contained in this section is to find the parameters that minimise computational times, whilst ensuring that the ability of the optimiser to find maxima or minima is not compromised.

The two parameters that are investigated in this section are:

1. Panel size
2. Frequency resolution

The first of these is an input into the high-order version of WAMIT that controls the size of the mesh used to discretise the geometry of the WEC and on which the hydrodynamic solution is computed. The velocity potential takes the form of a summation of B-splines, whose combined accuracy depends upon the number of sub-divisions (or ‘panels’) in each smooth continuous ‘patch’ of the surface. The panels are automatically generated in such a way as to have maximum length approximately equal to the panel size parameter in dimensional units. Hence smaller values of the panel size parameter correspond to a finer discretisation with a potentially more accurate solution and vice-versa. It should be noted that the setting of this value does not guarantee panels to be of at least that size, more that it is an indicator of the number of subdivisions to be used. This will be analysed in more detail in Section 7.5.1.

The second parameter listed above is the number of incident wave frequencies at which the hydrodynamic solution is to be calculated. Clearly fewer of these mean that computations are quicker, although this also corresponds to a less accurate numerical integration of the power output from an array over an irregular incident wave spectrum. In fact, there also exists the question of how these frequencies or periods should be distributed within a given range. Both of these issues will be examined in Section 0.

Note that the preliminary investigations reported below were performed using the frequency-domain equation of motion solver and so similar investigations will be required in the future in order to determine the similar quantities in relation to integration with the time-domain solver. However these

preliminary results allow generic findings to be obtained, which are directly applicable to the integration of the optimiser module with the spectral-domain solver being developed under WG1 WP2.

7.5.1 Panel size

Since the layout optimisation is governed by a GA which is a stochastic routine, firm conclusions about the quality of the objective function solution cannot be drawn simply by comparing the values obtained by the final solution from a single run. Hence it is in fact more efficient (and more instructive) to test the effects of varying parameters associated with the objective function by performing an exhaustive search of some representative solution space.

In order to further reduce the computational burden, the investigation into the effect of the panel size parameter on power output has been conducted using an array of two point-absorbers. The position of one WEC was fixed at the origin of the defined coordinate system and the total power calculated from the array when the second WEC was placed at grid points surrounding the first. Other variables that were kept constant throughout these tests include:

- WEC geometry: truncated vertical cylinder
- Radius: a=10m
- Draft: d-h=2a=20m
- Mass: neutrally buoyant at rest
- Bathymetry: flat, water depth: d=4a=40m
- PTO: heave motion; all PTO damping coefficients set at 640kNs/m (optimum for individual WEC in wave climate described below)
- Wave direction: β=0 (parallel to the positive x-direction)
- Sea state: Bretschneider (H_{m0}=4m, T_p=10.2s)

With reference to the frequency resolution investigations in the next subsection, it should be noted that 50 angular frequencies equally spaced between ω=0.377rad/s and ω=2.0479rad/s (T=3.1s and 16.7s) were used in these calculations. Four different panel size values were tested: 5m, 10m, 20m, 40m and 80m. Smaller values led to simulations that would not run in a reasonable time frame whilst values much larger than the biggest physical dimension of the WEC (=2πr here) will not lead to different discretisations of the body surfaces.

Figure 7.7 shows the total power from the array for different values of the panel size parameter. The fixed WEC is shown by a green circle whilst the intensity of the grey scale in the surrounding cells represents the total power output in Watts when the second WEC is placed at the centre of that square. The array is viewed from above with the incident waves approaching from the left hand side. Blue circles mark the points that are local minima (that is to say, locations that have a lower power output than neighbouring solutions), whilst red circles denote local maxima.

The first thing to note is that the plots are symmetric about the x- and y-axes due the equivalence of the problem when the entire geometric arrangement is reflected in those lines. There is a pronounced variation in total power output when the position of the second WEC is moved throughout the domain, confirming that the layout of the array has a significant effect on overall performance. This has been shown to be the case for regular wave climates (see, for example, Child and Venugopal, 2010) and to a lesser extent for irregular waves (see Cruz et al., 2010). The variation shown here is strong (with a range of almost 200kW), although the effect may be diminished for alternative input sea states, which may lead to less well defined maxima and minima.

It is clear that the total power output values are similar between values of the panel size parameter. Hence the accuracy of these simulations is not particularly sensitive to changes in this setting. More importantly, however, the locations of the optima are unchanged when the parameter is varied up to a value of 40m inclusively. This indicates that the optimisation routine will still be able to identify the best and worst solutions if the panel size is increased this figure. However, when the panel size is increased further (to 80m), a local maximum appears corresponding to WEC 2 being located at (+/-180,0)m, which was not present in the more accurate simulations. This indicates that such a value of the parameter is not suitable for the purposes of optimisation. Since larger values of the panel size parameter lead to vastly decreased computational times, selection of the largest figure such that the location of the optima is not affected (40m) is justified for the purposes of optimisation.

It should be noted that different conclusions may be reached for other WEC geometries, in particular for more complex shapes. Nevertheless this preliminary investigation indicates that there is considerable potential to explore the use of the panel size parameter to reduce the computational burden of explicit methods to determine the hydrodynamic interactions in for an array of WECs. Furthermore, this may be possible without seriously compromising the conclusion of the optimisation exercise (that is to say, the design associated with the optimisation of the objective function).

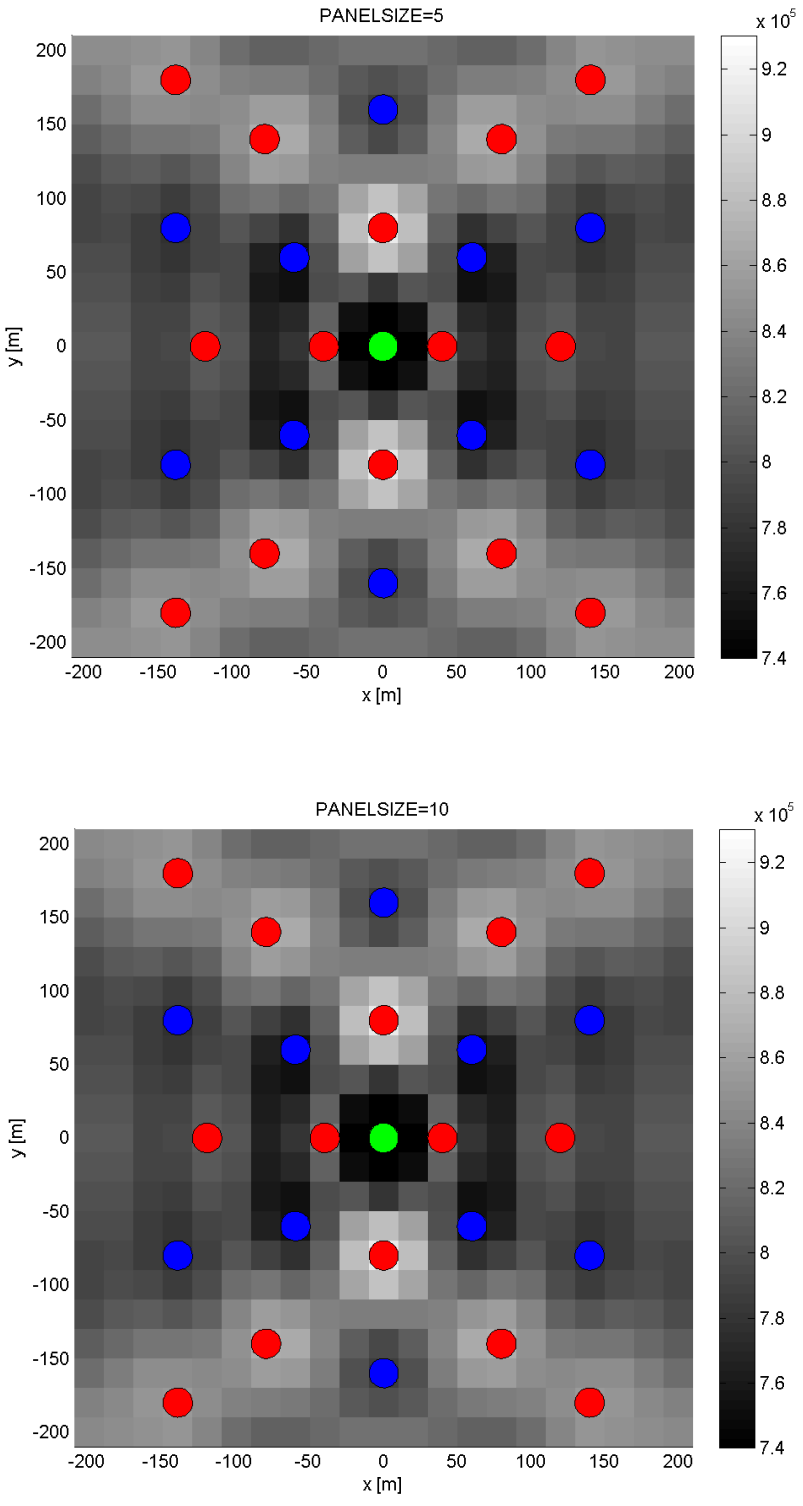

Figure 7.7. Colour intensity map showing power capture in Watt (see legend) from a two-WEC array of point-absorbers with one placed at the origin (green) and the other at surrounding points, viewed from above. Incident waves are travelling in the positive *x*-direction. Red circles - local maxima; Blue circles local minima. Panel size indicated above.

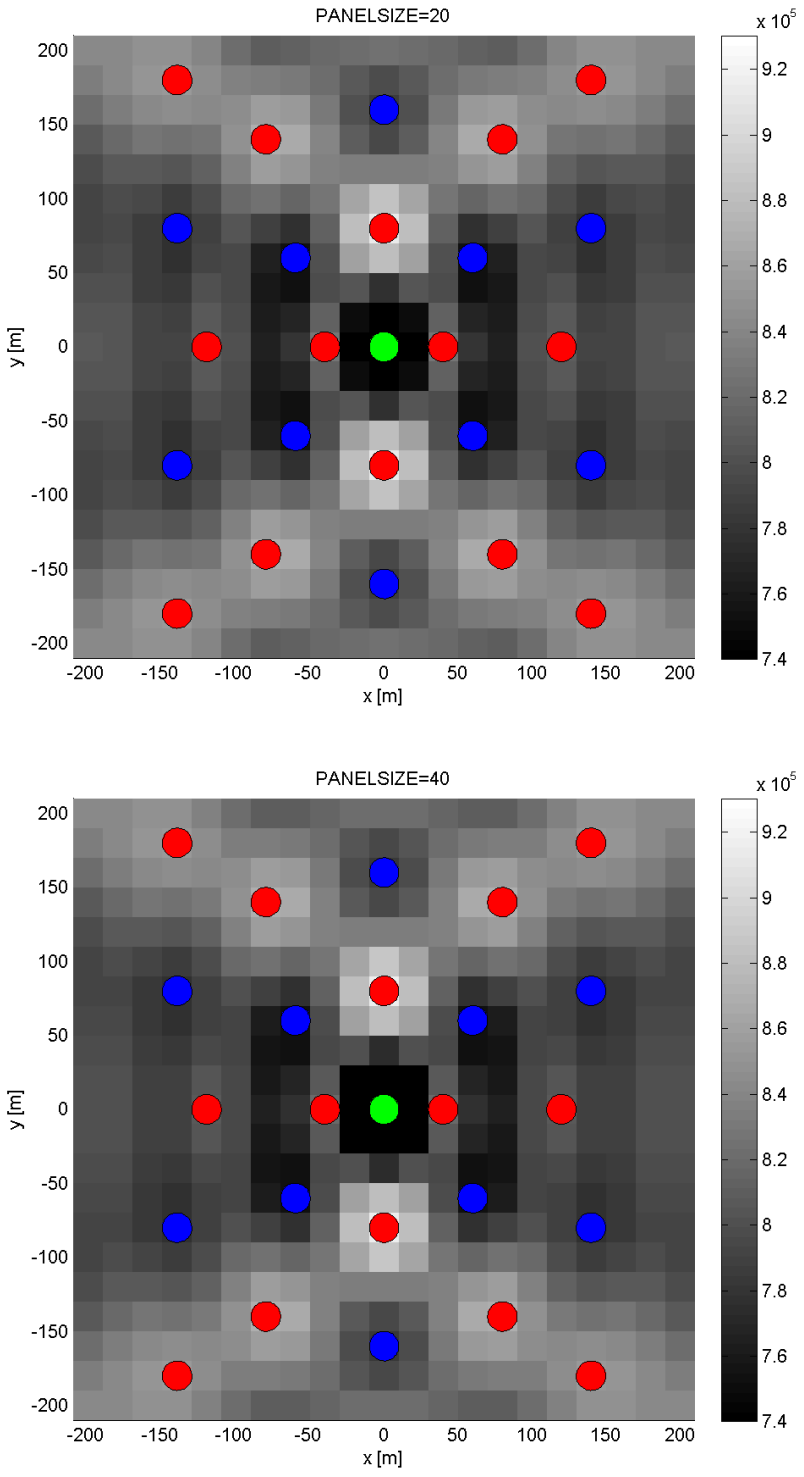

Figure 7.7. (cont) See caption above.

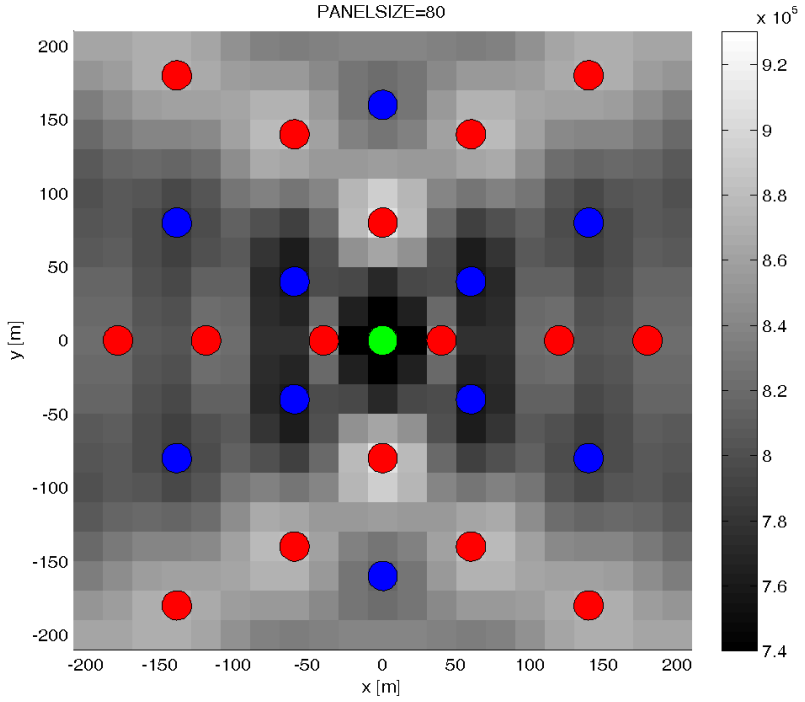

Figure 7.7. (conc.) See caption above.

7.5.2 Frequency resolution

The influence of the frequency resolution in the accuracy of the solution(s) was investigated in the same way as for panel size. The exhaustive optimisation was performed on an array of two point-absorbers (previously described in Section 7.5.1) using different settings for the frequency resolution. A panel size of 40m was chosen for these investigations since it has been deemed appropriate for the layout objective function in the previous section.

The frequency resolution tests were carried out using two ways of distributing the frequencies in a given range:

1. Equal angular frequency spacing
2. Spectral energy-proportional unequal spacing

The first involves the distribution of angular frequencies at equal intervals within a given range (between ω=0.377rad/s and ω=2.0479rad/s or T=3.1s and 16.7s). The second uses an unequal spacing that attempts to calculate the largest contributions to the total power output with greater accuracy than the smaller ones, based on knowledge of the wave spectrum alone.

The calculation of total power output of a WEC in a sea-state involves the numerical integration of the wave energy spectrum multiplied pointwise by the (array-dependent) auxiliary absorber power P_{aux} with respect to frequency:

$$\bar{P}_n = \int 2P_{aux}S(f)df \qquad [7.1]$$

Without knowing the machine response, an indication of where large components of the overall power will come from may be obtained by integrating the contributions from the incident wave spectrum alone. The omnidirectional variance density $S(f)$ is given by $S(f) = \Delta E / \Delta f$, where ΔE is the variance of the free-surface elevation. Hence the aforementioned contributions are equivalent to the

energy contained in each frequency interval used for the numerical integration. One possible method for increasing the accuracy in portions of the frequency range that have a large contribution to overall power is to ensure that the frequencies are distributed such that the spectrum contains an equal amount of energy in each resulting frequency interval.

To ensure that the most important part of the spectrum is captured well, the frequency at the peak of the wave energy spectrum is selected first. The spectrum is then divided up into intervals containing an equal amount of energy, starting at the peak frequency. The end points of the given interval are also selected, as shown by the vertical lines in Figure 7.8. Thus the parts of the spectrum with most energy, that more are likely to contribute most to the total power output (depending on the WEC response), have the densest distribution of frequencies and thus give rise to potentially more accurate results.

Both methods for distributing frequencies were applied with an increasing number of frequencies in the given range to the exhaustive optimisation problem defined in the previous sub-section. Representative results are given in Figure 7.9 and Figure 7.10 for different numbers of equally and unequally spaced frequencies respectively. The grey scales in these plots are aligned with each other for easy comparison between the different cases.

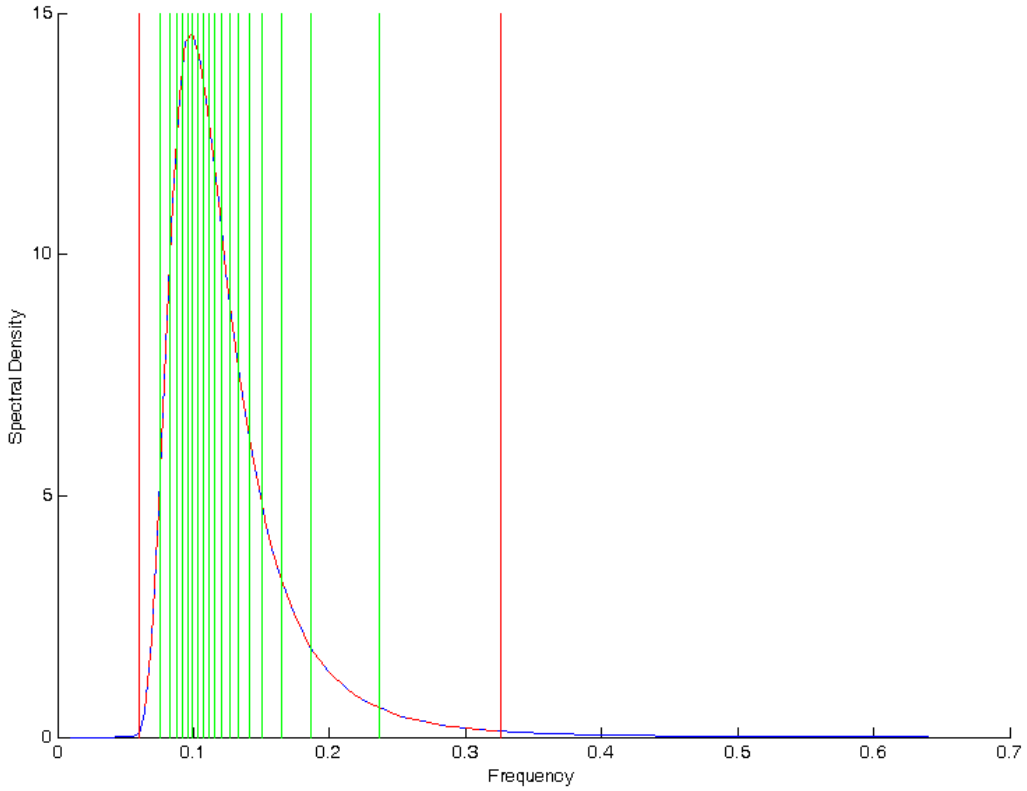

Figure 7.8. Illustration of spectral energy-proportional unequal spacing. Blue curve: Wave energy spectrum, vertical red lines: end points of frequency range for calculations, dashed red curve: wave energy spectrum in the given range, vertical green lines: frequencies selected.

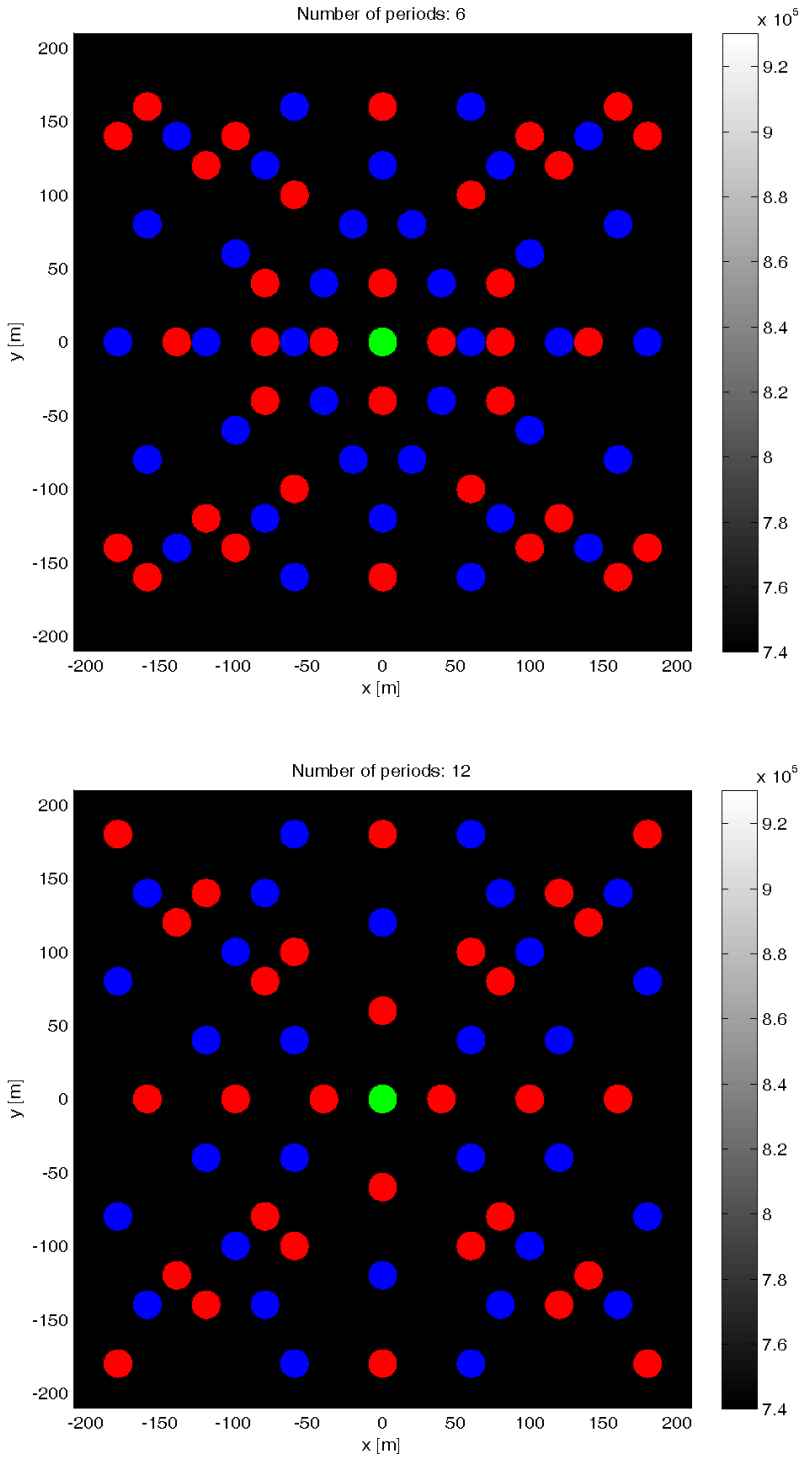

Figure 7.9. Colour intensity map showing power capture in Watt (see legend) from a two-WEC array of point-absorbers with one placed at the origin (green) and the other at surrounding points, viewed from above. Incident waves are travelling in the positive *x*-direction. Red circles - local maxima; Blue circles local minima. Number of equally spaced periods indicated above.

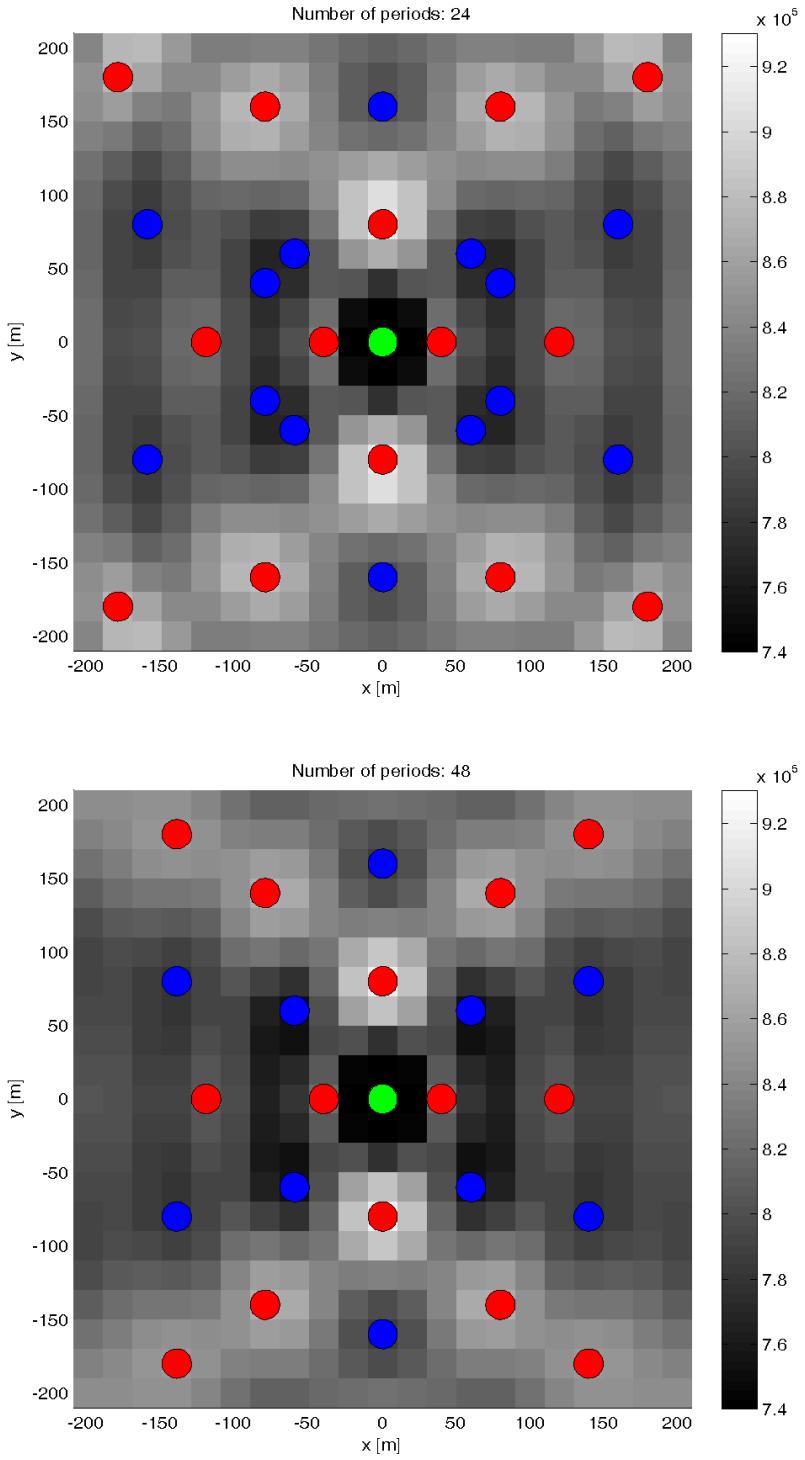

Figure 7.9. (conc.) See caption above.

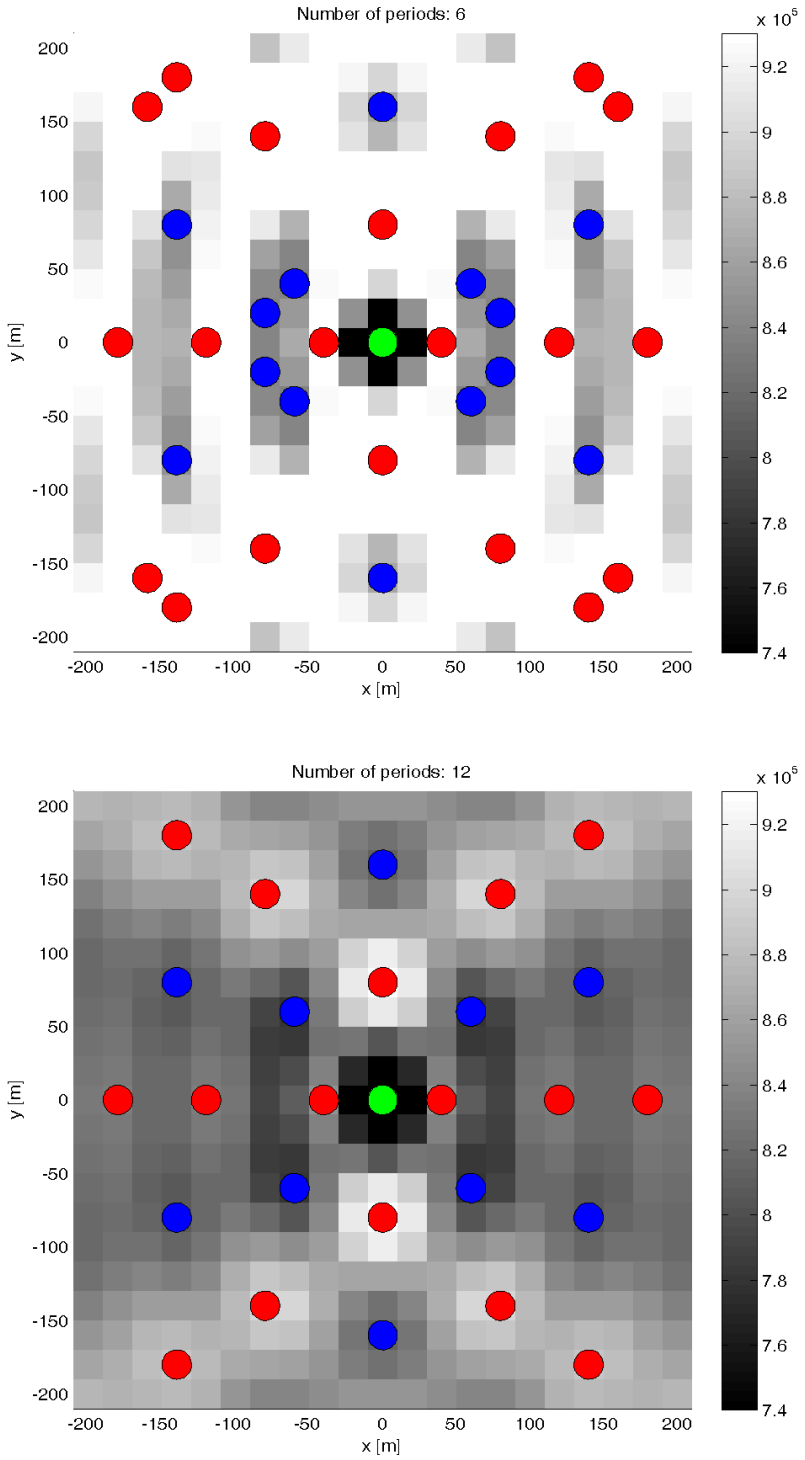

Figure 7.10. Colour intensity map showing power capture in Watt (see legend) from a two-WEC array of point-absorbers with one placed at the origin (green) and the other at surrounding points, viewed from above. Incident waves are travelling in the positive *x*-direction. Red circles - local maxima; Blue circles local minima. Number of <u>unequally</u> spaced periods indicated above.

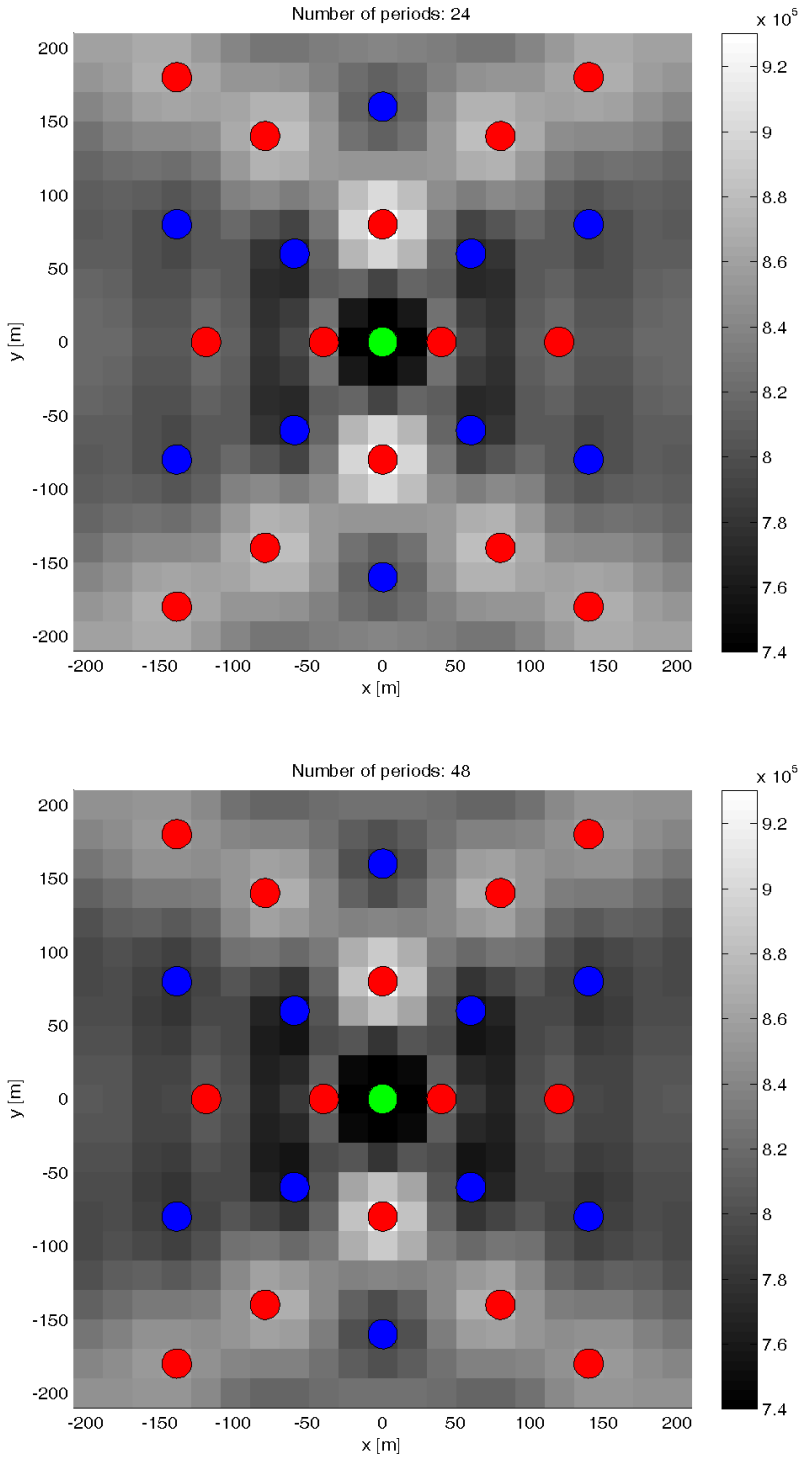

Figure 7.10. (conc.) See caption above.

It can be seen from the previous plots that both the equal and unequal spacing regimes lead to a sufficiently detailed description of the solution space (corresponding to the smaller panel sizes in Figure 7.7) if the number of frequencies is set large enough. Conversely, the nature of the solution is

completely destroyed if the number of frequencies is reduced beyond a minimum threshold (as it is for the six frequency case). However, there are differences between the two methods for an intermediate number of frequencies: whereas reducing the number of frequencies from 48 to 24 in the unequally spaced scheme changes the location of some of the maxima and minima, no such effect is true for unequally spaced frequencies.

The capacity for the unequally spaced scheme to capture the required effects for fewer frequencies is demonstrated further by examining the value of the objective function (maximisation of the total array power) at the largest local maximum in the exhaustive searches (four WEC diameters in the cross-wave direction from the first WEC, having Cartesian coordinates (0,+/-80m)). Figure 7.11 shows the total power for the array plotted against the inverse of the number of periods. The blue line denotes the value of the objective function close to the ideal case of an infinite number of frequencies.

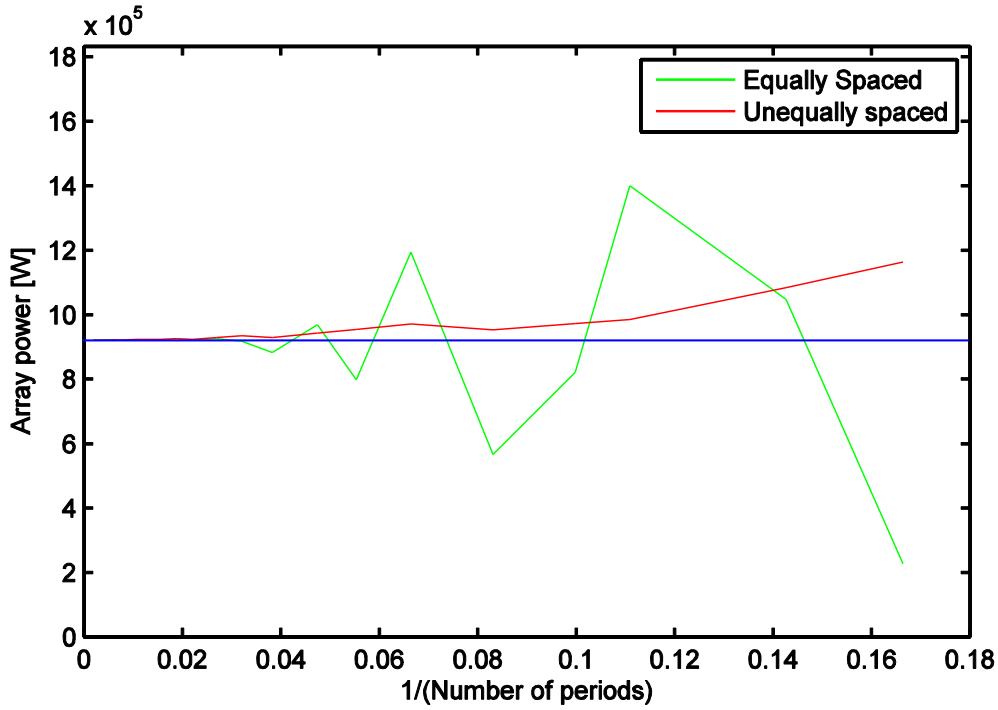

Figure 7.11. Convergence of solution for an increasing number of periods. Array configuration corresponds to local maximum in power output (WEC 1 at origin and WEC 2 at *x* =0m, *y*=80m). Blue line corresponds to an extrapolated value associated with an infinite number of frequencies.

As Figure 7.11 illustrates, and as typical of all such calculations, both regimes of frequency spacing lead to convergence for large numbers of frequencies. However, it is clear that for more moderate values of this parameter, the unequal spacing gets closer to the converged figure and stays closer as the number of frequencies is increased. Hence fewer frequencies are required to reach the same level of accuracy of the objective function using unequal spacing. In addition to the findings in Section 4, the results of this preliminary investigation may be used when devising default settings for the optimiser, although further studies are necessary to understand the influence of WEC specific characteristics on the above conclusions.

7.6 PTO optimisation: algorithm selection

In this section the suitability of a local optimisation routine to the problem of PTO coefficient optimisation is examined. To do this, several procedures were tested on the same problem and the

results compared. The optimisation of the PTO damping coefficients for an array of point-absorbers was considered, for fixed layouts with the following properties:

- WEC geometry: truncated vertical cylinder
- Radius: a=10m
- Draft: d-h=2a=20m
- Mass: neutrally buoyant at rest
- Bathymetry: flat, water depth: d=4a=40m
- Number of WECs: N=4, 10
- Array configuration: square with spacing 4a (N=4) and an extension of this to two rows of five WECs (N=10)
- Wave direction: β=5π/4 (approaching along the diagonal of the square grid)
- Sea state: Bretschneider (H_{m0}=4m, T_p=10.2s)
- Constraints on PTO: min=0, max=1000kNs/m

In order to obtain an indication of whether the number of variables affects the performance of each algorithm differently, two sizes of array were considered, consisting of four and ten WECs. The formation of ten WECs replicated the square formation of four WECs by adding further converters to that configuration at equal spacings to form two lines of five WECs.

The frequency-domain equation of motion solver was used for these tests due to its favourable computational efficiency, although the time-domain counterpart might have been chosen, since the results of the two simulations should match under the linear conditions used here. The optimisations were performed using the Optimization (version 5.1) and Global Optimization (version 3.1) MATLAB Toolboxes. Note that these tools have been upgraded since the Frequency-Domain Implementation Report (WG1 WP1 D2) was written, and hence the algorithms may not be the same as those previously described.

Firstly, local optimisations were conducted for a range of initial points in the PTO coefficients, using the default (‘active-set’) local optimisation algorithm from the toolbox. Three different cases were considered here, with all coefficients within an array being set in an identical fashion with the following values:

- 640kNs/m (equal to the optimum for an individual WEC in the same wave climate)
- 320kNs/m (one half the optimum for a single WEC)
- 940kNs/m (one and one half times the optimum for a single WEC)

The initial point was then set such that all PTOs have a coefficient equal to the optimum for individual WEC in the wave climate (640kNs/m) and the local optimisation algorithm changed to the following routines:

- Active-set
- Interior-point

Finally a genetic algorithm (global optimisation) was applied to the same PTO optimisation problem, using the following parameter settings in addition to the default values provided with the tool:

- Generations=50
- PopulationSize=20

In the case of the GA, three executions of the algorithm were carried out using different random seeds, but otherwise with exactly the same settings as one another.

The results of these optimisations are shown in Table 7.1 and Table 7.2 for arrays of four and ten WECs respectively. For each optimisation, the values of the design variables for the final solution are given, along with the associated objective function value and the number of function evaluations required in total.

Table 7.1. PTO optimisation results for a 4 WEC array using different algorithms.

Algorithm	Initialisation	PTO coefficients [kNs/m]	Array power [kW]	Function evaluations
Active-set	320 kNs/m	744 664 835 743	1570	235
Active-set	640 kNs/m	744 664 835 743	1570	230
Active-set	960 kNs/m	744 664 835 743	1570	241
Interior point	640 kNs/m	744 664 835 743	1570	366
GA	Seed 1	707 605 951 712	1568	1020
GA	Seed 2	924 694 537 602	1555	1020
GA	Seed 3	635 527 718 798	1563	1020

Table 7.2. PTO optimisation results for a 10 WEC array using different algorithms.

Algorithm	Initialisation	PTO coefficients [kNs/m]	Array power [kW]	Function evaluations
Active-set	320 kNs/m	820 880 925 1000 1000 870 1000 724 997	3461	1001
Active-set	640 kNs/m	817 877 924 1000 1000 868 1000 733 1000	3461	1001
Active-set	960 kNs/m	817 878 923 1000 1000 866 1000 733 1000	3461	1008
Interior point	640 kNs/m	816 878 918 1000 1000 866 1000 735 1000	3461	1682
GA	Seed 1	572 441 567 719 400 612 657 627 694 734	3325	1020
GA	Seed 2	965 512 168 586 491 709 694 392 431	3237	1020
GA	Seed 3	674 485 588 560 540 551 434 841 618 561	3317	1020

Many of the final coefficients are significantly different to the isolated WEC optimal values. In particular, for ten WECs, some of the design variables reach the upper bounds of the constraints (1000kNs/m).

The results here confirm previous experience with optimising the PTO coefficients in an array of similar point-absorbers that the choice of initial point does not seem to have a significant effect on the final solution. Furthermore, initial points that are much larger or smaller than the optimised values do not seem to adversely effect the computation time as measured by the number of function evaluations to a great extent. This confirms that the solution space (at least for the examples studied here) is not

multi-modal and so the use of local optimisation is appropriate. However it should be noted that if the solution space is non-smooth (such as may well be the case for more complex PTO arrangements), local derivative-based optimisation algorithms may break down. This limitation does not apply to the GA.

Many more function evaluations are needed for the local optimisation algorithm applied to the larger array than the smaller one. Moreover, this increase is not linear with the number of elements in the array. In fact, the active-set optimisation for simulations with ten WECs terminate prematurely because default maximum number of function evaluations has been exceeded. Hence it is not practical to apply these local optimisation algorithms to medium to large sized arrays. The function evaluations themselves typically also take longer to compute. This is certainly the case where WaveDyn is used as the solver and so local optimisation algorithms should be used with caution here.

For the GA, no well-defined stopping criteria other than the pre-defined number of function evaluations are applied. Hence this number is comparable with the other routines in the results above. However, the analysis in Section 7.4 has indicated that the GA applied here is effective at exploration of the entire solution space, so a smaller number of function evaluations may well produce reasonable results. The disadvantage of the GA is that the 'exploitation' of a particular part of the solution space may be slow, as evidenced in the slight differences in the values of design variables between the local and global routines here.

On balance, it is judged that for the current implementation where the objective function may be very expensive to compute, the GA is the most appropriate optimisation algorithm for PTO optimisation. Therefore the PTO optimisation case studies described in Section 8 are computed with this routine.

7.7 Hydrodynamic interaction estimation: scenario 2A

The implementation of a technique to estimate the hydrodynamic interactions between WECs within the farm tool is planned for the Beta 2 release under Scenario 2A (see Section 7.2.2). Such a technique would eliminate the need for third-party flow solvers to be used whilst the farm tool is in operation, although their use will still be required in advance of farm computations (for explicit characterisation of single WECs). In this section, a review is presented of the literature relating to the principal interaction methods that have been applied in this field, along with some suggested alternative methods. These all relate to linear wave theory and, in that sense, are compatible both with frequency-domain flow solvers and the time-domain tool WaveDyn.

Further investigations will be carried out into the methods detailed here alongside the development of the Beta 2 tool. Note, however, that if the spectral-domain solver being developed in WG1 WP2 proves to be able to adequately represent array behaviour, then the estimation of hydrodynamic interactions between WECs may be performed within that module.

The Point-absorber method

One of the first approximations to the hydrodynamic interaction between WECs was made by Budal (1977), who investigated array effects in the context of a collection of point-absorbers. In this work, an assertion was made that became known as the 'point-absorber approximation;' that the diameter of the WECs is small in comparison to the distance between them. Hence the wave field radiated by the motion of each WEC may be calculated without reference to the diffraction effect of other elements in the array. Evans (1979, 1980) later provided a condition on the body velocity amplitudes that ensures optimal power absorption. This is in fact a natural extension of the equivalent single WEC condition and was arrived at independently by Falnes (1980). A consequence of this, however, is that arbitrary PTO coefficients may not be considered.

Point-absorber theory was recently used as the basis for an optimisation of array layout in regular waves (Fitzgerald, 2006; Fitzgerald and Thomas, 2007). Folley and Whittaker (2009) have also used this approximation to analyse one of the arrays presented by Fitzgerald and Thomas (2007) and, separately, to optimise the position of WECs in irregular waves.

It should be noted that the point-absorber approximation, although faster than most of the other methods described in this section, is not applicable to larger WECs where scattering effects may be important. This limitation means that the technique is unlikely to meet the needs of the generic wave farm tool under development.

The Plane Wave method

The diffraction of an electromagnetic wave field by several cylinders was the focus of research that culminated in the invention of a direct matrix method by Zaviska (1913). This was subsequently used by Spring and Monkmeyer (1974) to deal with diffraction of water waves with multiple bodies. The technique uses the body boundary conditions to simultaneously determine the unknown scattered wave amplitudes.

Simon (1982) adopted a direct matrix approach to analyse wave energy WECs but approximated the diverging wave from one WEC as a plane wave upon reaching other WECs in the array. The resulting 'plane wave' method requires that the spacing between elements (non-dimensionalised using the incident wave number) is large. McIver and Evans (1984) and McIver (1984) later added a 'first correction' term to the expression of the plane wave and derived significantly improved accuracy of results with little extra effort.

In recent years, the Plane Wave method has not been pursued in terms of academic research, perhaps because it has been largely superseded by the Direct Matrix (see further details below) that is capable of accounting for the same phenomena in a more accurate manner.

The Multiple Scattering method

Twersky (1952) discovered an alternative way of solving the multi-body diffraction problem in the field of acoustics by considering the interactions to be a series of consecutive scattering events. Intuitively, contact with each body reduces the amplitude of the resulting wave and so a solution is reached by the convergence of an iterated sequence. This 'multiple scattering' technique was applied to water waves by Ohkusu (1972, 1974) in the study of offshore mobile platforms with multiple supporting bodies.

Work on the multiple scattering method continued with Mavrakos and Koumoutsakos (1987) and Mavrakos (1991), in whose articles the scattering and radiation problems were solved respectively. An application of this theory to wave energy converters was made by Mavrakos and Kalofonos (1997) with several WEC and array geometries being assessed.

A comparison of the multiple scattering, plane wave and point-absorber methods has been carried out by McIver et al. (1996a,b) and Mavrakos and McIver (1997) in the context of wave power. They measured the accuracy of the latter two techniques against that of the former, 'exact' method. In general, the plane wave method was found to break down in long waves but perform well in the high frequency range, whilst for the point-absorber approximation the converse was seen to be true. The multiple scattering technique has, however, itself been criticised. Linton and McIver (2001) state that the multiple scattering method 'rapidly becomes unmanageable as the number of scatterers increases.'

The Direct Matrix method

Kagemoto and Yue (1986) combined the physical concepts associated with the multiple scattering approach and a direct formulation to form what is often referred to as the 'direct matrix' method. This technique is in principle exact within the context of linear wave theory, subject to the truncation of an infinite summation. The scattering characteristics of each individual body under incident progressive and evanescent waves are encapsulated in the diffraction transfer matrix, which allows the unknown wave amplitudes to be solved for simultaneously. The method requires only that the horizontal projections of interacting bodies do not overlap and that a circumscribed vertical cylinder around each body centred on its imaginary origin does not contain the origin of any other body.

Following its formulation, the theory of Kagemoto and Yue (1986) has been widely applied, especially in the field of very large floating structures (VLFSs). These were the subject of a study by the same authors (Kagemoto and Yue, 1993) who incorporated the radiation problem from the motion of the bodies. This theory has been applied in the wave energy field by Child and Venugopal (2007) and by Siddorn and Eatock Taylor (2008). Modifications to the fundamental procedure have also been made in order to efficiently apply the method to a much greater number (~5000) of bodies in the context of a VLFS (Kashiwagi, 2000). Such variations on the method may be of use when calculating interactions in the case of a very large array of WECs.

Employing this method for determining the interactions between WECs instead of using a boundary element method to solve the whole problem may lead to savings in computational time. However, it should be noted that the convergence of the solution series is slower for larger water depths (Child, 2010). The main task in integrating this method with a boundary element solution would be in calculating the diffraction transfer matrix and radiation characteristics using the latter.

Other methods

For periodic arrays of bodies, Linton and Evans (1992, 1993) used the 'multipole' method to solve the hydrodynamic problem. This involves the superposition of singular solutions to the governing equations and choosing their coefficients so as to satisfy the body boundary conditions. The technique was applied to an infinite array of 'Bristol cylinder' wave energy converters by McIver and McIver (1995). Since then, Justino and Falcao (2002) have used the multipole expansion method on small arrays of spherical WECs.

The phenomenon of Bragg resonance was studied by Li and Mei (2007) in the context of a periodic array of circular cylinders. In that work, certain approximations were made based on the assumptions that the incident wavelength is comparable to the spacing between bodies and that the cylinders themselves are much smaller than this length. The same approach has recently been applied to an array of floating wave energy converters by Garnaud and Mei (2010).

Possible new alternative methods

In addition to the more rigorous interaction techniques described above, there may be other more heuristic methods that are capable of discerning good from bad solutions in the optimisation. One such method could involve the calculation of the *q*-factor (power multiplying effect of the farm) from a two-WEC array in an exhaustive search of grid points surrounding one of the WECs. This information could then be used to estimate the enhancement or otherwise in power absorption from every pair of WECs within a larger array.

Alternatively, the radiation and diffraction pattern surrounding a single WEC could be calculated in advance of array computations. Then for each WEC in an array, the wave field incident to it could be approximated by superposing the radiated and scattered wave fields from all other WECs in the array, assuming single WEC behaviour. Finally the single WEC behaviour could be used to determine the

response of that converter, given its modified incident wave field. This is similar to the first iteration in a ‘multiple scattering’ procedure.

8 CASE STUDIES

In this section preliminary results associated with the time-domain functionality of both the loads calculations and the wave farm design tools are presented. The cases described here build on the results presented in WG1 WP1 D2 that were generated using the frequency-domain tools. In Section 8.1, case studies relating to the analysis of a single WEC are presented, using the time-domain solver WaveDyn. Section 8.2 contains details of optimisation scenarios that have been approached with the farm tool (WaveFarmer).

8.1 Time-domain solver (WaveDyn)

To investigate the time-domain response of a generic WEC to different input conditions and external constraints, a WaveDyn model of a heaving point-absorber was created. This consists of truncated vertical cylinder floating in water of finite constant depth. The connection to the seabed is modelled by a rigid link. Between the link and the body is a sliding joint which allows motion only in the heave direction, from which the PTO applies a force. Table 8.1 outlines the geometrical properties of the WEC, along with details regarding the wave input and PTO settings. The numerical mesh used to discretise the WEC wetted profile is illustrated in Figure 8.1 (note that the same mesh was used in the point-absorber array simulations described in Section 8.2). This was used in WAMIT to obtain the hydrodynamic properties of the WEC (excitation force, added-mass at infinity and radiation damping) following a high-order panel method formulation (curved panels used to discretise both the geometry and the velocity potential). A multi-body representation of the FDCs modelled in WaveDyn is given in Figure 8.2.

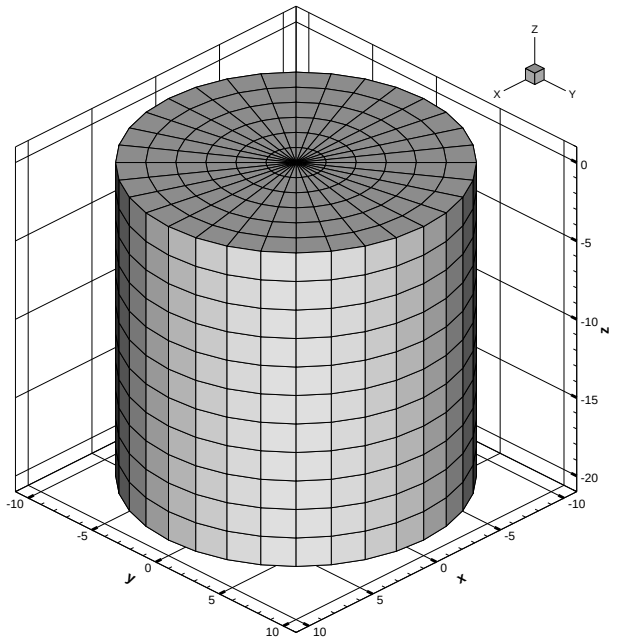

Figure 8.1. Point-absorber geometry.

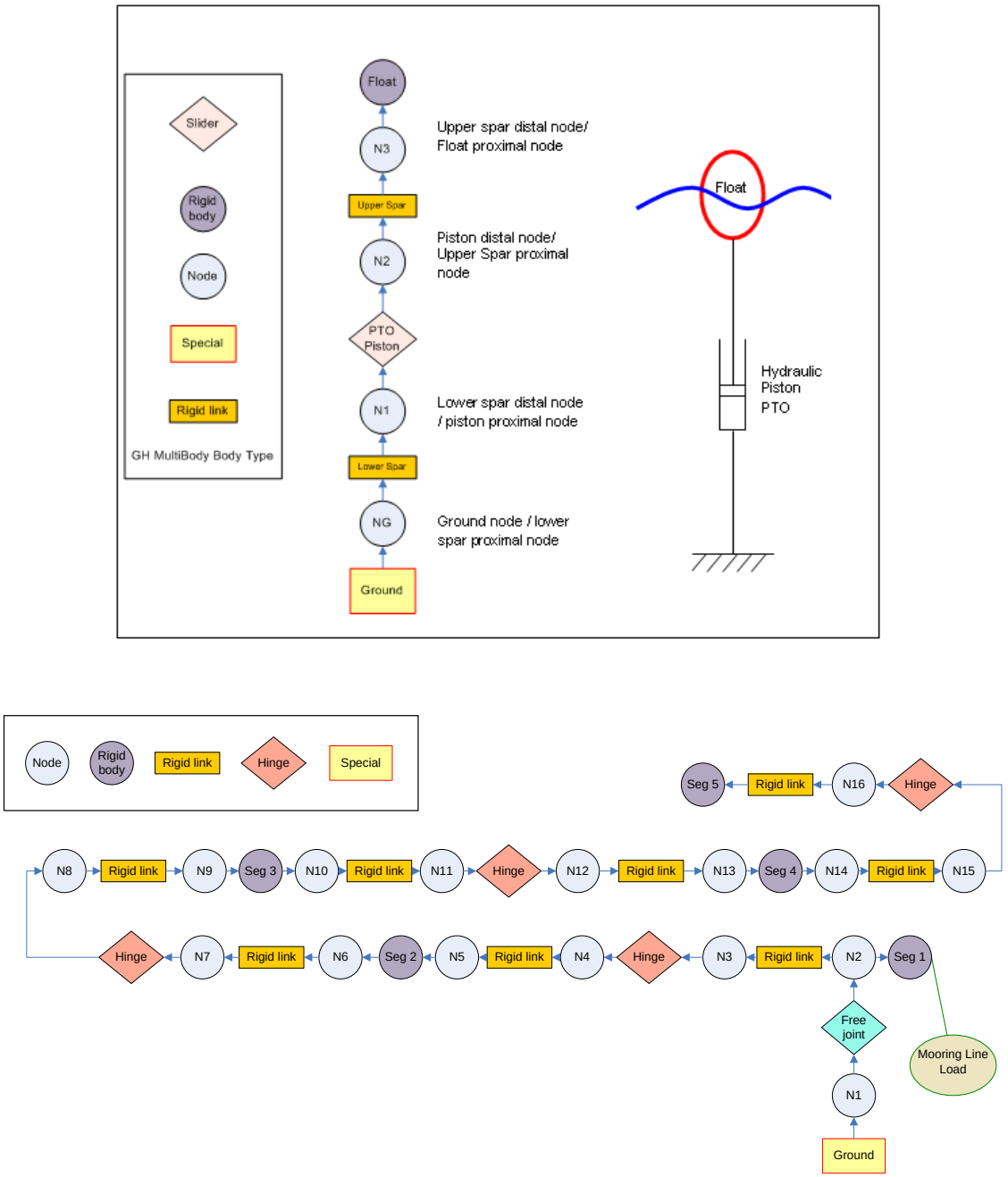

Figure 8.2. A multi-body representation of each FDC:

point-absorber – top; attenuator – bottom.

Property	Value
Wave direction	β=0
Wave climate	Regular waves (A=1m; ω=0.7rad/s)
	Irregular waves (Bretschneider; H_s=4m; T_p=10.2s)
WEC geometry	Point-absorber: Truncated vertical cylinder, radius a=10m, draft d-h=2a=20m
Mass	Neutrally buoyant at rest; mass uniformly distributed
PTO	Absolute heave motion.
	Linear damping with coefficient 2MNs/m; Quadratic damping with quadratic coefficient 6MNs/m.
Control	Passive (constant PTO settings)
Motion	Heave
Bathymetry	Flat, water depth: d=4a=40m

Table 8.1. Single WEC Case Study.

The simulations firstly addressed the response of the WEC to a regular wave while applying two different PTO profiles: a linear and a quadratic characteristic with regard to heave velocity. The PTO damping coefficients were selected to ensure that despite the significant difference in the PTO profiles (see Figure 8.3), the heave response was similar (see Figure 8.4). The results were obtained using a fixed time step of 0.1s for 200s and 1125s simulations (regular and irregular waves, respectively), and used a wave ramp up period of 20s. The use of such ramp up approach allows faster convergence to steady state conditions. In Figure 8.4 only a few wave periods are represented, but it is clear that the heave response is similar irrespective of the PTO profile that is used.

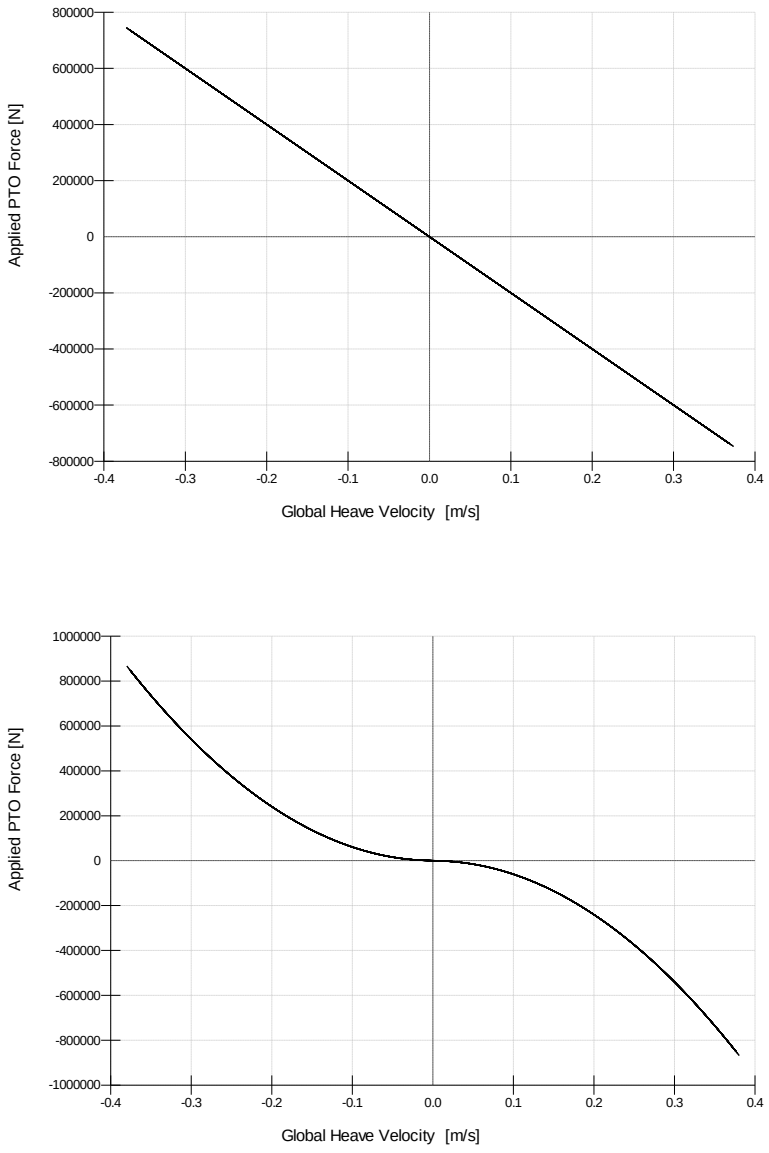

Figure 8.3. Applied PTO profile (in WaveDyn): linear (top) and quadratic (bottom).

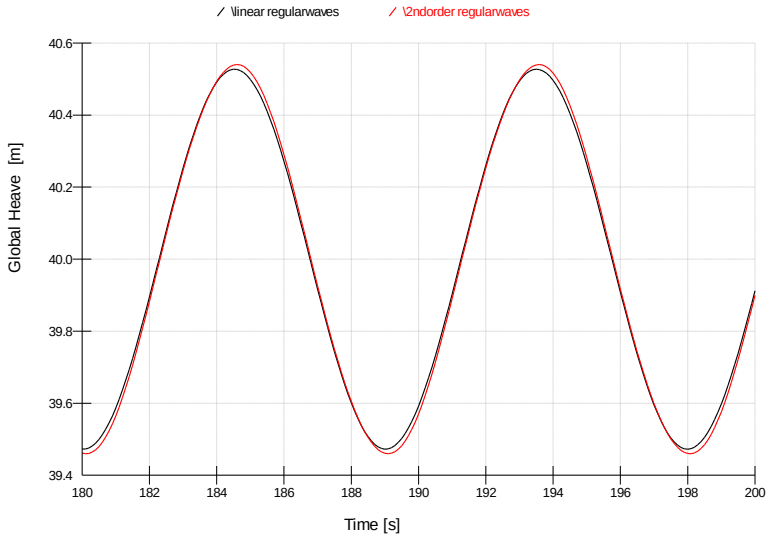

Figure 8.4. WEC motion (heave) when subject to linear and quadratic PTO profiles (regular waves results).

In Figure 8.5 the absorbed power for the regular wave case presented in Figure 8.4 is given. Despite the similarities in the overall heave motion, the influence of the PTO profile is clear in the absorbed power time history, which demonstrates the importance that nonlinearities of the PTO characteristics may have in the power absorption estimates. Furthermore, a time-domain approach is the only formulation that allows nonlinearities in the applied forces to be modelled explicitly, which may prove further important if these have a discontinuous nature. Current developments include addressing the creation of PTO template, which will allow the modelling of specific PTO systems (e.g. hydraulics) in more detail.

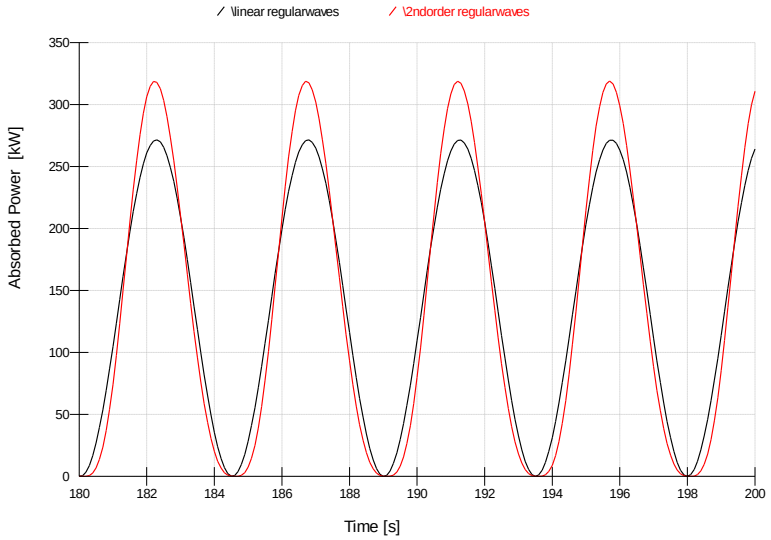

Figure 8.5. Absorbed power when subject to linear and quadratic PTO profiles (regular waves results).

To conclude the loads calculation exercise, the same linear PTO profile was then applied to estimate the WEC response to an irregular wave, as defined in Table 8.1. Figure 8.6 presents the global heave

response and the instantaneously absorbed power as a function of time. As anticipated, in this simple example the peak responses are associated with peaks in the power absorption (note that a passive control approach was selected). Relevant statistics such as averaged absorbed power can be obtained from the corresponding time-histories: for example in this case the average absorbed power is 331kW, and the peak to mean power ratio is 10.4. The statistical processing of the responses will be used to develop additions to WaveDyn core functionalities. These may include specific modules to address aspects of component design, such as fatigue calculation using cycle counting algorithms.

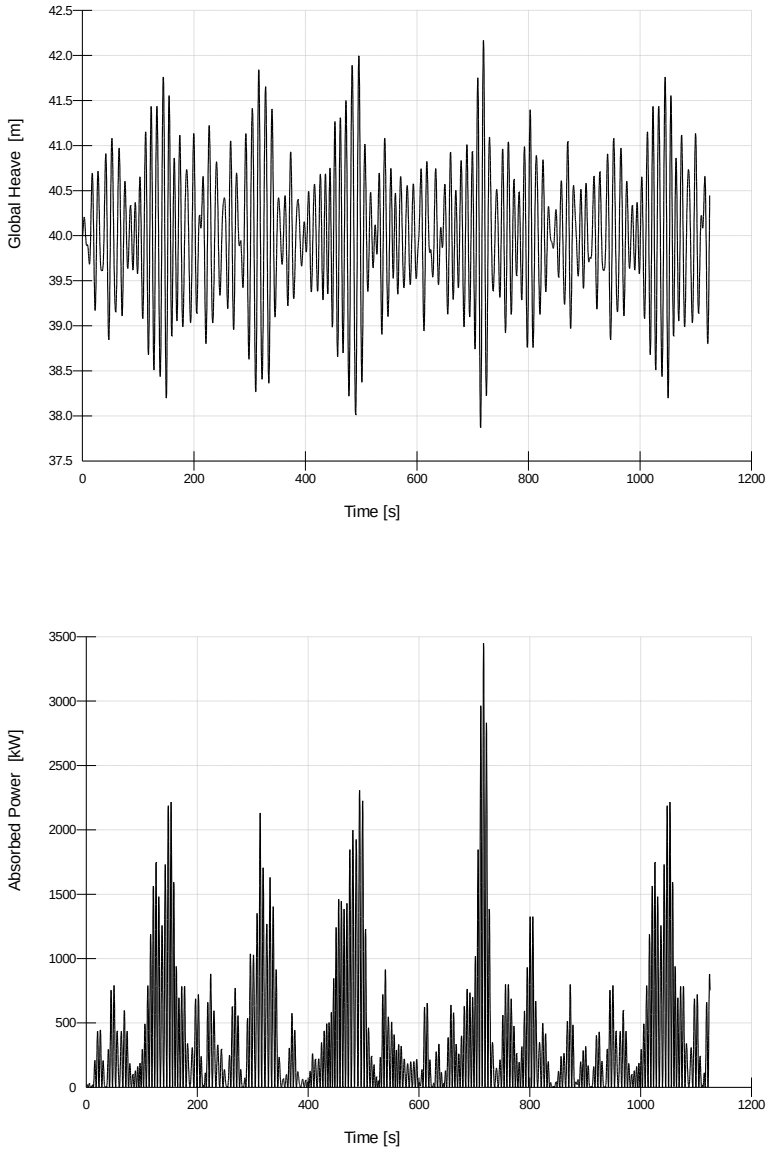

Figure 8.6. Global heave (top) and absorbed power (bottom) for a sample irregular wave input.

8.2 WEC array design tool (WaveFarmer)

Before applying the WaveFarmer tool to a number of case studies involving several converters, the models used to represent the individual WECs used will be briefly described. The first type of WEC to

be examined is the point-absorber analysed in Section 8.1. A PTO force which is a linear function of absolute velocity (with coefficient 640kNs/m) was applied in the layout optimisation cases described below,

The second type of WEC to be considered in this study is a generic attenuator. The model used consists of five articulated horizontal floating cylinders, with two short sections fitted between three long ones (see Figure 8.2 and Figure 8.7). The WEC is aligned head-on to the waves with body 1 able to move in the pitch and yaw directions relative to a fixed point at its front end. The remaining sections of the WEC may only move in the pitch mode relative to neighbouring sections. These four modes are those from which power is converted via PTO forces which are identical linear functions of relative pitch velocity. This arrangement is summarised in Table 8.2.

Property	Value
WEC geometry	5 horizontal cylindrical sections, diameter 3.50m, draft 1.75m. 3 long sections of length 30m, 2 short sections of length 5m between long sections, separated by a clearance of 0.35m.
Mass	Neutrally buoyant at rest. Centre of mass at still water level.
Motion	Relative pitch between adjacent cylinders. Body 1 may pitch and yaw relative to fixed end point.
PTO	Relative pitch motion between each cylindrical section (4 in total). All linear damping with coefficient 1MNms/rad.

Table 8.2. Attenuator definition.

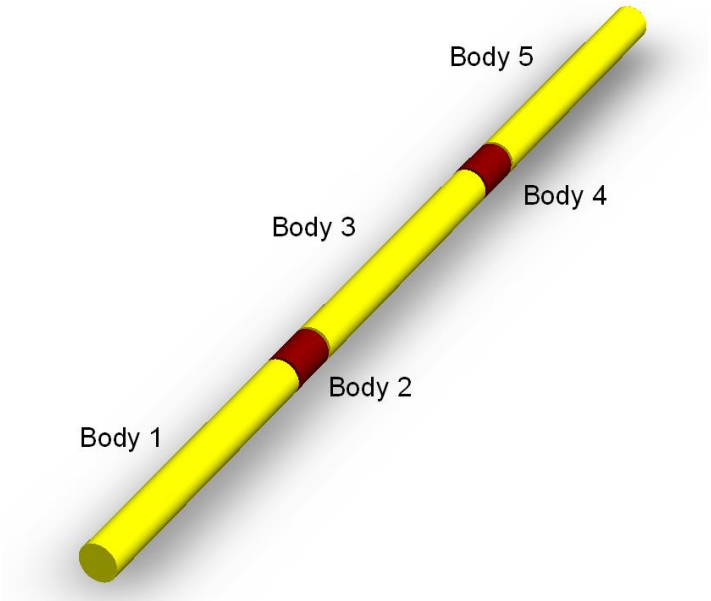

Figure 8.7. Attenuator geometry.

The case studies used to demonstrate the functionality of the wave farm tool are now described. The wave climate for each of the case studies was formed from a Bretschneider spectrum of peak period (T_p) 10.2s and significant wave height (H_s) 4m. For the time-domain calculations a 15 minute wave record was simulated, over which results were computed. The waves module includes an option to

generate the amplitudes of the component waves deterministically rather than randomly. The former option was used here so that the spectrum could be recreated accurately without excessive computation. However, it should be noted that the phases of wave components are still set randomly in the simulation, so that there may be variability in the results using different instances of the wave record generated from the same spectrum. Hence the same record was used in each call to the objective function. WaveDyn computations were initiated with all bodies at rest in their mean positions, after which an initial period of 225s was simulated to cover transient behaviour. Following this, results were derived from 15 minutes of simulated motion, using a fixed time step of 0.1s.

The optimisation of layout using both frequency and time-domain calculations of the objective function requires that the coordinates of WECs are input into both the external hydrodynamics package and the equation of motion solver. This uses a global coordinate system with the seabed forming the *x*-*y* plane and the positive *x*-direction aligned with the wave heading angle β=0. The objective in the all the examples in this section is to maximise power in the given sea-state, unless otherwise stated.

The first case study relates to the optimisation of PTO coefficients in an array of four point-absorbers using the time-domain solver, as summarised in Table 8.3. The configuration used for this purpose is the square arrangement shown in Figure 8.8, where each converter is separated by a centre-to-centre distance of four body radii. In the case of PTO optimisation, the hydrodynamic data only need be calculated once in advance of the optimisation. The PTO damping coefficients are constrained to lie between minimum and maximum values.

Property	**Value**
Wave direction	$\beta=5\pi/4$
Wave climate	Unidirectional Bretschneider spectrum (H_{m0}=4m, T_p=10.2s)
Bathymetry	Flat, water depth: d=40m
WEC type	Point-absorber
Number of WECs	4
Layout	Square, separation: $L=4a$=40m
PTO	Design variables
Constraints	$0 \leq B_{pto} \leq 1000$ kNs/m
Simulation	Time-domain

Table 8.3. Array Case Study 1: PTO optimisation on an array of four point-absorbers.

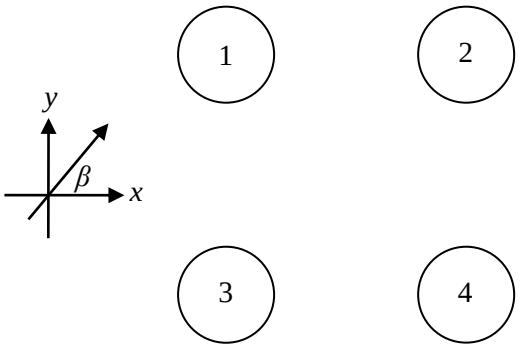

Figure 8.8. Array Case Study 1: Array geometry used for PTO optimisation.

Case study 2 (Table 8.4) involves the layout optimisation of an array of ten point-absorbers using the frequency-domain solver. Here a larger number of WECs is considered, representative of arrays that may be commercially deployed in the medium term. Constraints are applied regarding the minimum and maximum centre-to-centre separation of WECs to avoid collisions / allow access and prevent unfeasibly large arrangements respectively. In addition to this, the number of rows and columns in the regular grid arrangement previously defined (Section 7.2.1) are limited. This constitutes a first representation of a constraint on the maximum dimensions of the array. Two sub-cases are defined for this optimisation problem: maximisation and minimisation of total power output. The latter case is analysed here in order to show the consequences of arranging WECs in the worst configuration.

Property	**Value**
Wave direction	β=0
Wave climate	Unidirectional Bretschneider spectrum (H_{m0}=4m, T_p=10.2s)
Bathymetry	Flat, water depth: d=40m
WEC type	Point-absorber
Number of WECs	10
Layout	Design variables
PTO	All 640kNs/m
Constraints	Regular grid layout, Min (centre-to-centre) separation = 3 diameters = 60m, Max separation = 10 diameters = 200m, Min rows/columns=2, Max rows/columns = N-1
Simulation	Frequency-domain
Objective	a) Maximise array power b) Minimise array power

Table 8.4. Array Case Studies 2a & 2b: Layout optimisation on an array of ten point-absorbers.

The final case study (Table 8.5) considers the layout optimisation of an array of two attenuators. In this case the WECs are all aligned with the incident wave direction but the constraints are designed such that collision would be avoided if two adjacent WECs were to yaw such that their tail ends were facing each other.

Property	Value
Wave direction	$\beta=\pi$
Wave climate	Unidirectional Bretschneider spectrum (H_{m0}=4m, T_p=10.2s)
Bathymetry	40m
WEC type	Attenuator
Number of WECs	2
Layout	Design variables
PTO	All 1MNms/rad
Constraints	Regular grid layout, Min (nose-to-nose) separation = 2 lengths, Max separation = 20 lengths
Simulation	Time-domain

Table 8.5. Array Case Study 3: Layout optimisation on an array of two attenuators.

The values of the objective function (the *Q*-factor, as previously defined) relating to the final solution of each optimisation are contained in Table 8.6. Further analysis is provided in the following sub-sections.

Optimisation	Q
1. PTO, 4 point-absorbers, TD	1.030
2a. Layout max, 10 point-absorbers, FD	1.046
2b. Layout min, 10 point-absorbers, FD	0.723
3. Layout, 2 attenuators, TD	1.023

Table 8.6. Optimisation results for each array case study.

8.2.1 Array Case Study 1

The PTO optimisation case study has produced a set-up that is produces 3.0% more power in the given sea-state than the same number of WECs in isolation. The final PTO coefficients, normalised by the optimal value for a single WEC are 1.0420, 0.9585, 1.2007 and 0.9986 for WECs 1 to 4 respectively. Note that the values for WECs 1 and 4 are similar due to the symmetry of the array at this wave heading. This shows that the optimal coefficients in some cases need to be over 20% different to the value that would be used in isolation.

8.2.2 Array Case Studies 2a and 2b

The configurations produced by layout optimisation using the frequency-domain solver are shown in Figure 8.9 and Figure 8.10 for maximisation and minimisation of total absorbed power respectively.

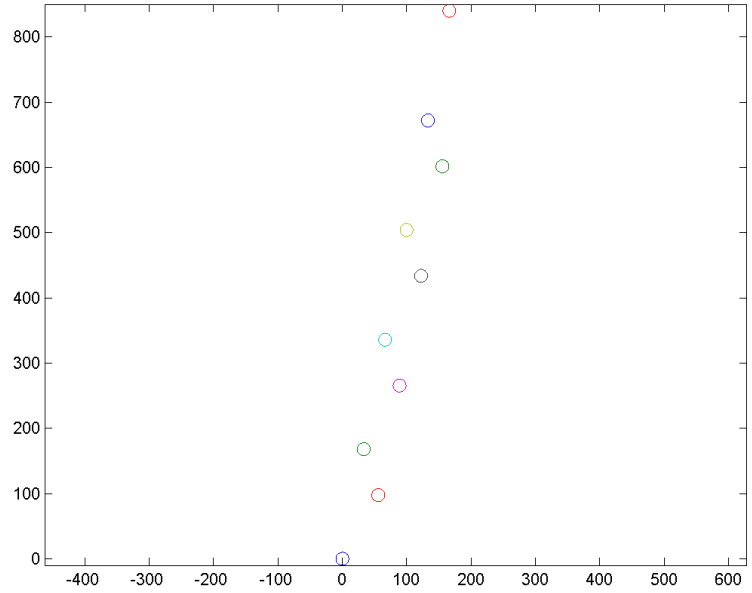

Figure 8.9. Optimal layout for ten point-absorbers where the total power has been maximised (waves approaching from left hand side).

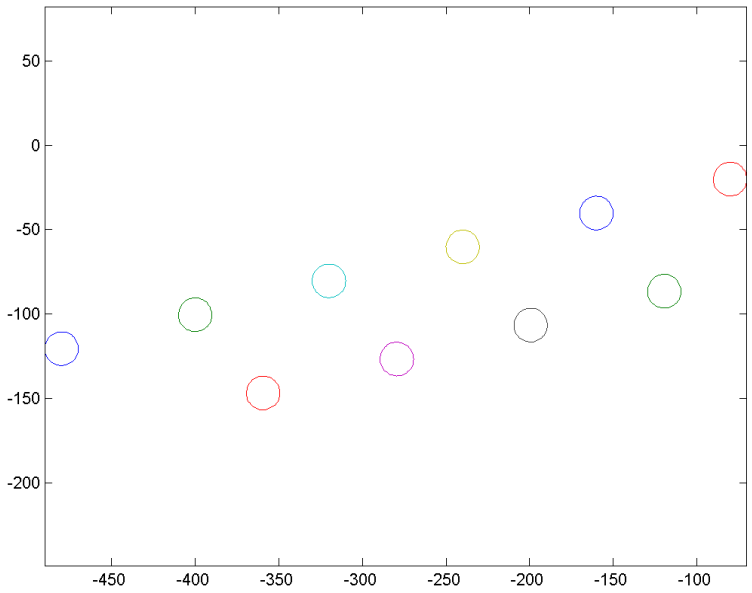

Figure 8.10. Optimal layout for ten point-absorbers where the total power has been minimised (waves approaching from left hand side).

Figure 8.11 and Figure 8.12 show the variation of power output from each WEC in the array with frequency (for the input sea state), divided by the maximum value obtained from an isolated converter.

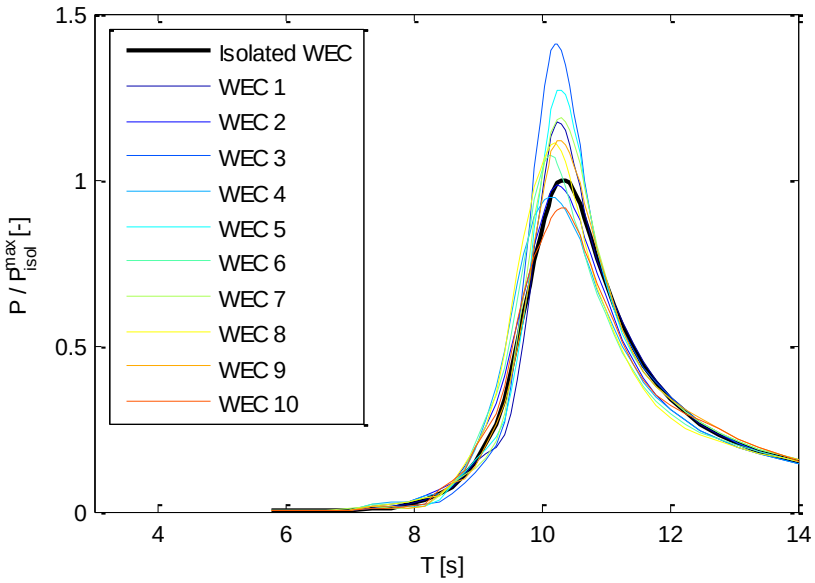

Figure 8.11. Normalised power output as a function of incident wave period from an array of ten point-absorbers whose layout has been optimised for maximum total power production.

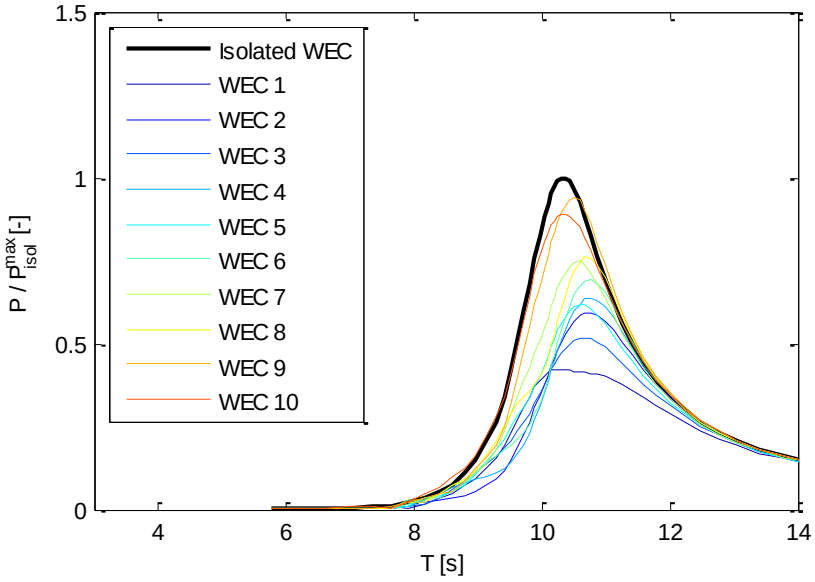

Figure 8.12. Normalised power output as a function of incident wave period from an array of ten point-absorbers whose layout has been optimised for minimum total power production.

The arrangement that maximises the power output can be seen to extend significantly in the cross-wave direction with the down-wave row of WECs slightly offset from the up-wave one. Thus none of the WECs are completely in the lee of another. The lines are not, however, exactly perpendicular to

the incoming wave direction, indicating that either more improvement is possible or that beneficial interactions occur at this angle under the simulation inputs and constraints.

The constraints on the arrangement have ensured that a single very long line of WECs has not been produced. It should be noted, however, that realistic constraints are in fact likely to be even more complicated to express in the given design variables than those shown here.

The most valuable contributions to total power absorption come from the part of the period range where the WEC response and the wave energy spectrum exhibit their peak (at about 10s). Hence, although the curves associated with power from each converter in the array oscillate above and below that of an isolated converter, the optimisation process has ensured that most of the converters exhibit a large gain around the 10s period in Figure 8.11.

The case study associated with the minimisation of the power absorption (Figure 8.10) has led to an arrangement that extends significantly in the down-wave direction without lying parallel to the oncoming wave direction. Similar configurations have been shown in Child and Venugopal (2010) to lead to increased shadowing, where the presence of up-wave WECs prevents their down-wave counterparts from receiving and thus absorbing as much energy.

The variation of power with frequency shows that all converters now behave worse than an isolated WEC around the 10s period. There is, however, a great variation in the performance between converters.

Since the *Q*-factors for the maximal and minimal arrangements are 1.046 and 0.723 (respectively), the possible difference in power absorption by ten WEC arrays as a proportion of the same WECs in isolation is at least 45%. Thus even with constraints on the layout, there is a significant difference between maximum and minimum arrangements. Such strong modifications in power absorption have been shown in regular waves (Child and Venugopal, 2010), however the results presented here extend the findings to irregular waves.

8.2.3 Array Case Study 3

The configuration of attenuators resulting from layout optimisation is shown in Figure 8.13, where waves are incident from the positive *x*-direction.

The arrangement here consists of the two WECs spaced far apart in the down-wave direction. Such a large separation between adjacent converters may not be practical in a realistic setting, showing the need to apply stricter constraints and penalties to the optimisation algorithm in further investigations. The two WECs are also a large distance apart in the cross-wave direction, minimising shadowing.

As for the point-absorber case, the *Q*-factor here (1.023) shows an increase in performance relative to the same number of isolated WECs. Note, however, that it may be that in some situations, the optimal *Q*-factor is less than one. This would indicate that the mitigation of destructive interference might be the most realistic objective in some array optimisation scenarios. The creation of a tool that accurately quantifies the energy yield from an array is equally relevant in such situations (when compared with scenarios of maximisation of constructive effects).

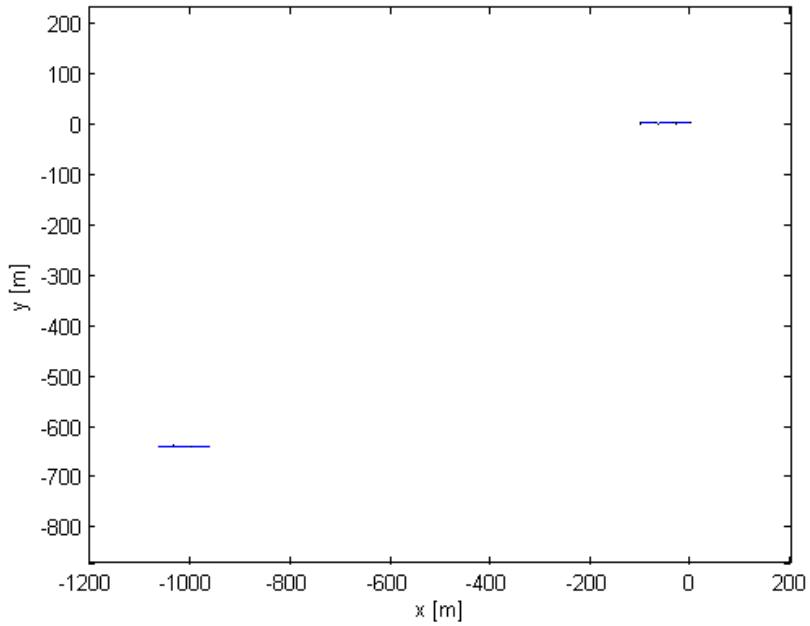

Figure 8.13. Optimised array layout for an array of two attenuators (waves approaching from right hand side).

9 SUMMARY OF KEY FEATURES AND POTENTIAL EXTENSIONS

The final section of this report compiles a list of the key findings which can be derived from the implementation to-date and compared with the original WG1 WP1 D3 targets. It also presents a series of next steps which will be pursued when further expanding the time-domain functionality. However it should be noted that the current time-domain implementation ensures that the core functionalities originally listed in WG0 D1 for the first Beta version are now available.

9.1 Key implemented functionalities: summary to date

The present report describes the current implementation status of the WEC numerical modelling software being developed by GH under the PerAWaT project. The report builds on previous deliverables, namely the methodology report (WG1 WP1 D1B) and the frequency-domain implementation report (WG1 WP1 D2), and details the core aspects and key functionalities of the developed code, with particular emphasis to the performance variables related to time-domain simulations.

In this report the capabilities of the baseline software in a time-domain formulation are presented. These were implemented following the 'Next steps' guidelines presented in previous PerAWaT deliverables. Using the frequency-domain implementation report (WG1 WP1 D2) as a starting point, this report begins by presenting background information regarding the GH multi-body code (Bladed) which is used as the kernel unit to describe the dynamics of the WECs. Under PerAWaT GH has developed a series of software routines that plug into the Bladed code, to allow the definition of a wide range of WECs. This new package (code named WaveDyn) can be considered a loads calculation tool which allows the reduction of the uncertainty in the estimation of the relevant (single WEC) performance variables and the definition of the parameterisation of the WEC behaviour in order to use this in the optimiser module (code named WaveFarmer).

Although the core structure is shared between the frequency- and time-domain formulations, and thus was originally presented in WG1 WP1 D2, it is important to recall the baseline structure. The modules originally envisaged for the WaveFarmer code structure in the Methodology Report (WG1 WP1 D1B, Section 1) are now covered in the WaveDyn multi-body modelling approach, namely the 'FD', 'TD', 'Basic Controller', 'External forces code' and the 'Wave data loader'. The 'Basic Controller' and 'External forces code' blocks operate as the series of parallel multi-body Calculation Modules, whilst the FD and TD blocks are represented in the higher level WVStructure co-ordinating code. The wave data loader is one of the I/O routines in the Hydrodynamics Calculation Module. It is envisaged (although not implemented at this stage) that the Calculation Modules may be developed to give the user the option of replacing the core functionality of each with a DLL interface. WaveFarmer as a software package now refers purely to the array design code (and includes the Optimiser and Mapping blocks shown in WG1 WP1 D1B). WaveFarmer's ability to interact with WaveDyn is described in Section 7.

The multi-body dynamic solver provides a means of mathematically describing the structural forces within the WEC structure. All of the non-structural forces applied to the WEC, resulting from the hydrodynamics, PTO or moorings must be calculated separately in code modules parallel to the core code (MBCore). If the flexible nature of the multi-body structural approach, which allows a range of WECs to be defined and simulated, is to be maintained then a multi-body theme must be propagated throughout these applied force calculations. The hydrodynamic and mooring forces need to be calculated on a body-by-body basis and PTO calculations are associated with a particular joint in the multi-body structure. Furthermore, the separation between the structural and the non-structural code modules facilitates future updates to be developed and implemented on a case-by-case basis.

To summarise the above description, the complete software formulation for the WEC modelling code may be seen as a collection of parallel multi-body Calculation Modules, including MBCore:

- The geometrical/structural definition formulated using the MBCore code.
- A hydrodynamic definition containing the hydrodynamic information and force calculation functions for the wave activated bodies in the system (any wave activated structural body having a parallel hydrodynamic body containing its particular hydrodynamic properties).
- A moorings system built up from multiple mooring line 'bodies', each containing information on the line properties and attachment location on the geometrical structure.
- A PTO system containing information on the PTO properties and force calculation functions for any joint contributing to the energy capture of the device.
- A control system containing the control algorithm used to control / operate the PTO.

Each of these modules (apart from the MB core) was specifically developed (and will continue to be developed) under PerAWaT. The functionalities of each module are discussed in greater detail in the corresponding sections of this report. This includes also the optimiser module and the wave analysis module, which are outside the WaveDyn structure (the former is effectively the core WaveFarmer code and the latter is shared between WaveDyn and WaveFarmer).

The time-domain formulation allows a detailed characterisation of a WEC and / or an array of WECs. The description of the external forces (e.g. mooring force; PTO force), can be highly nonlinear, unlike the frequency-domain approach where these must remain linear (or be linearised) for the model to be valid. This more accurate description of the main subsystems results in a more computationally intensive model, which may lead to limitations regarding the number of WECs if restrictive computational times are applied. Nevertheless it is possible to consider such time-domain formulation as the target in terms of numerical accuracy.

It must be stressed that the current software structure is common to the frequency and time-domain models, and also suitable for coupling with the spectral-domain models developed under WG1 WP2. Synergies with the methodology developed in WG1 WP2 will also allow a spectral-domain representation of the fundamental device concepts (FDCs) via the core modules presented in this report. It is envisaged that such spectral-domain representation will allow the optimisation of large (100+ WECs) arrays of FDCs. The first direct consequence of sharing the core structure is that there are considerable synergies between this report (WG1 WP1 D3) and its frequency-domain equivalent (WG1 WP1 D2 Implementation Report: Frequency-Domain Model).

This has resulted in the use of some sections of WG1 WP1 D2 in this report, with the suitable adaptations and updates. The major differences are associated with the development and implementation of:

- The wave analysis module, namely the method for spectral fitting, accuracy of fitted spectra and the effect of the parameterisation on the energy yield);
- The moorings module, for which the baseline implementation now allows nonlinear applied loads to be considered (results for a case study using one of the FDCs are presented);
- The PTO and control modules, as in the time-domain the description of the external forces can be nonlinear (leading, e.g., to the first PTO template);
- The optimiser module, namely the integration with the time-domain solver (WaveDyn) and detailed investigation regarding aspects that affect the computational efficiency and both the layout and PTO optimisation.

When compared with the formulation presented in WG1 WP1 D2, it is in the above listed modules that most of the time-domain implementation effort is immediately clear, although changes to other

modules (core and structural) were made. Such additional effort should not be neglected as it ultimately ensures that the user of the PerAWaT tools will be able to have a single interface irrespective of the formulation and details that his / her WEC (or array of WECs) model requires.

The initial results presented in this report show the baseline functionality of the code while exploring the potential of a time-domain formulation, namely the ability to apply nonlinear mechanically applied force profiles (e.g. PTO, moorings). In Section 8 the following aspects are covered in the case studies:

- The ability to define different FDCs with different characteristics;
- The influence of different wave input conditions in the response of the WEC;
- The influence of the array layout in the power absorption characteristics;
- The influence of the control of the PTO of each array element in the power absorption characteristics (by treating the array as a power plant).

The detailed description and performance of different FDCs and PTOs presented in Sections 6 and 8 should be analysed carefully. In some cases dimensional results are presented, but it must be recognised that the baseline FDC configurations (WEC geometry, number of bodies, control strategy, etc) have not been optimised, so no conclusion regarding the relative benefits or efficiency of one type of FDC over the other should be made. The results can be considered a mere demonstration that the software developed under PerAWaT can assess such questions a detailed way.

Even though the results in Section 8 are preliminary, such case studies allowed the test of the functionality of each module and an effort was made to align these with the verification scenarios listed in WG0 D1. Furthermore, the core functionality and case studies here presented are also well suited for the configurations to be modelled experimentally under WG2. It is expected that this will ensure that comparisons related to initial results from different project partners (GH, UoOx and QUB) can be more easily made. However, and as listed in WG1 WP1 D1B, these cases should not be confused with a set of representative scenarios for which results will form part of the Beta testing specification and will be presented in WG1 WP1 D4 and D15 (versions A and B). Finally, the report is concluded with the presentation of immediate next steps that constitute further implementation steps to be developed for the Beta releases (Section 9.2).

9.2 Potential extensions

WaveDyn Code Architecture

Much of the initial implementation work has focussed on the WaveDyn code architecture, which has been developed to accommodate time-domain simulation and the frequency-domain results processing. No significant structural changes to the code architecture are envisaged. Further updates to the numerical integrator functionality may be developed, to give the user control over the integrator type used and any related performance parameters.

Hydrodynamics module

Hydrodynamics Calculation Module development work for the time-domain will focus on performance improvements to the baseline implementation described in Section 3. These include:

- Automated analysis and selection of an appropriate impulse response function cut-off time (preventing the user from having to decide how far back in time the radiation force convolution should be completed);

- Development of a system-identification technique to approximate the radiation force impulse response function convolution integral with a finite state-space model (see Methodology Report WG1 WP1 D1b, Section 3.3.4), thereby removing the numerical burden of the convolution process (note the above point on the cut-off time will still be necessary in determining the length of the impulse response function required for the identification process);
- A study on the effect of completing the radiation force convolution integral over increasingly coarse time-steps. A coarse convolution time-step may compare favourably in computational time with the finite state-space model described above.

In addition to this, functionality is required to convert a set of user supplied radiation damping data to impulse response function data, in the event that the latter is not supplied by the user. The conversion process requires the completion of a numerical integration at the start of the simulation, as described in Section 3.4.2.

Further development to incorporate nonlinear hydrodynamic force modelling will be the subject of later deliverables and will be closely linked to the first experimental and numerical verification datasets.

Wave module

The wave module will not require any further major changes. The next steps in the investigation of methods to parameterise the wave climate are:

- Further investigations into the effect of the sea state parameterisation on energy yield prediction (for a representative range of WECs);
- Study the effect of the power matrix resolution on the energy yield prediction;
- Detailed assessment of the influence of directional aspects (including directional spreading).

Moorings module

The moorings module currently uses a look-up table approach, as discussed in Section 5. No information is given to the user (at present) on how to populate such tables. Furthermore, and as originally mentioned in WG1 WP1 D2, this approach may need to be complemented by a more explicit mooring-line model based on a Morison-element approach. The next steps for the moorings module are therefore (with the latter two points being secondary):

- Devise an appropriate procedure to populate the look-up tables (using data available in the literature);
- Develop comparisons with a Morison elements approach (new tests cases);
- Investigate the need for a memory term (via a Convolution integral) for specific mooring arrangements;
- Investigate the possibility of creating a finite-state model of the mooring system with the aim of carrying out convolutions in the time-domain to represent frequency-dependent impedance.
- Adding static-analysis capability to the software so that a realistic equilibrium state to be computed. This equilibrium state is used as the starting-point for time-domain simulations.

PTO and Control modules

It is envisaged that the further development of the PTO and of the control modules will be, as highlighted in Section 6, closely linked. Four generic guidelines for future implementation steps can be summarised by:

- Compare the dynamic response of different FDCs for a range of nonlinear PTO profiles and PTO templates;
- Develop further PTO templates;
- Develop further options for control strategies (e.g. PTO template specific strategies, such as constant pressure (fluctuation in power) and constant power output (fluctuations in pressure) methodologies in the hydraulics PTO template);
- Develop a .dll facility to allow third-parties to provide custom definition files (i.e. their own PTO models and control parameters) to be used in WaveDyn without sharing the details with the WaveDyn user.

The PTO module at present supports both explicit PTO force calculation descriptions and a first PTO template, designed to support much more complex PTO models, with internal system states. This initial template description, for a hydraulic / electrical rectification and smoothing system was provided in Methodology Report WG1 WP1 D1b, Section 5.5.4. The PTO module development work is expected to occupy a significant proportion of the WaveDyn implementation time up until and following the release of the first Beta version of the software.

Optimiser module

Finally, the main optimiser developments that are envisaged at this stage can be summarised in the following points:

- Improve error handling and verification of inputs, so that users better understand the reasons why calculations which are not feasible do not run;
- Carry out further debugging exercises and more extensive functionality testing;
- Investigate the practicalities of incorporating a hydrodynamic array interaction technique into the tool for use by the frequency- or time-domain solver;
- Investigate the coupling of the optimisation algorithm with a spectral solver to determine array behaviour;
- Implement another optimisation algorithm, mostly if justified by issues related to computational effort.

REFERENCES

General

Alves, M (2002). "Incident Wave Identification", MARETEC / AWS Internal Report 2/2002, Lisbon, Portugal

American Petroleum Institute (1997); API RP 2SK, Recommended Practice for Design and Analysis of Stationkeeping Systems for Floating Structures, USA.

Babarit A, Duclos G, Clément A.H, 2004. Comparison of latching control strategies for a heaving wave energy device in random sea. Applied Ocean Research 26, 227-238.

Babarit A, Clément A.H, 2006. "Optimal latching control of a wave energy device in regular and irregular waves"; Published in Applied Ocean Research 28, 77-91.

Brito-Melo, A, Sarmento, A, Clément, A and Delhommeau, G (1998). "Hydrodynamic Analysis of Geometrical Design Parameters of Oscillating Water Columns", Proc. 3rd European Wave Energy Conference, Patras, Greece, Vol. 1, pp.23-30.

Brito-Melo, A, Hofmann, T, Sarmento, A, Clément, A and Delhommeau, G (2000a). "Numerical Modelling of OWC-shoreline Devices Including the Effect of the Surronding Coastline and Non-Flat Bottom", Proc. 10th International Offshore and Polar Eng Conference, Seatle, USA, Vol.1, pp.743-748.

Brito-Melo, A and Sarmento, A (2000b). "Numerical Study of the Performance of a OWC Wave Power Plant in a Semi-Infinite Breakwater", Proc. 4th European Wave Energy Conference, Aalborg, Denmark, pp. 283-289.

Brito Melo, A (2002). "AWS Physics Characterisation", IST Internal Report, Instituto Superior Técnico, Lisbon, Portugal.

Brooke, J (2003). *Wave Energy Conversion*, Elsevier Science.

Budal, K and Falnes, J (1975). "A resonant point absorber of ocean-wave power", *Nature*, Vol. 256, pp. 478-479.

Budal, K (1977). "Theory of absorption of wave power by a system of interacting bodies", *Journal of Ship Research*, Vol. 21, pp. 248-253.

Budal, K and Falnes, J in Count B (Editor), 1980. Power from Sea Waves. Academic Press (London). ISBN: 0-12-193550-7.

Bryden, I (1983). "Long floating cylinders in three-dimensional seas," PhD Thesis, The University of Edinburgh.

Callaghan, J and Bould, R (2006). *Future Marine Energy*, The Carbon Trust.

Centre for Marine and Petroleum Technology (CMPT), 1998. Floating Structures: A guide for design and analysis. Volume 2. Oilfield Publications Limited. ISBN 1 870553 357.

Clare, R, Evans, DV and Shaw, TL (1982). "Harnessing sea wave energy by a submerged cylinder device", *Journal of The Institution of Civil Engineers*, Vol. 73, pp. 356-385.

Clément, A, Babarit, A, Gilloteaux, J, Josset, C and Duclos, G (2005). "The SEAREV Wave Energy Converter, Proc. 6th European Wave & Tidal Energy Conference, Glasgow, United Kingdom.

Count B M, Jefferys E R, Wave power, the primary interface. Proceedings of the 13th Symposium on Naval Hydrodynamics, Paper 8. p1-10. The Shipbuilding Research Association of Japan, Tokyo.

Cruz, J and Salter, S (2006). "Numerical Modelling of a Modified Version of the Edinburgh Duck Wave Energy Converter". *Proc. IMechE Part M: Journal of Engineering for the Maritime Environment*, Vol. 220, pp. 129-147.

Cruz, J and Sarmento, A (2007). "Sea state characterisation of the test site of an offshore wave energy plant", *Ocean Engineering*, Vol. 34 (5-6), pp. 763-775.

Cruz, J, (2008). *Ocean Wave Energy* (Editor), Springer-Verlag.

Cummins W.E, 1962. The impulse response function and ship motions. Schiffstechnik 9, p101–109.

Jefferys in Count B (Editor), 1980. Power from Sea Waves. Academic Press (London). ISBN: 0-12-193550-7.

Dean, R, and Darymple, R (1991). *Water Wave Mechanics for Engineers and Scientists*, World Scientific.

Delauré, Y and Lewis, A (2003). "3D hydrodynamic modelling of fixed oscillating water column by a boundary element methods", *Ocean Engineering*, Vol. 30 (3), pp. 309-330.

Det Norske Veritas (DNV) Software. 'Mimosa' Flyer. Available online, February 2010.

Det Norske Veritas (DNV) Software. 'Riflex – Riser System Analysis Program' Flyer. Available online, February 2010.

Det Norske Veritas (DNV), 2004. DNV-OS-E301, Position Mooring, Norway.

Duclos G, Clément A H, Chatry G, 2001. Absorption of Outgoing Waves in a Numerical Wave Tank using a Self-Adaptive Boundary Condition. Int. Journal of Offshore and Polar Engineering, 11(3), 168–175.

Edinburgh University Wave Power Project, 1987. Solo Duck Linear Analysis. A report to the wave energy steering committee covering work supported by the United Kingdom department of Energy.

Eatock Taylor, R and Jeffreys, E (1985). "Variability of Hydrodynamic Load Predictions for a Tension Leg Platform", *Ocean Engineering*, Vol. 13 (5), pp. 449-490.

Evans, DV (1976). "A theory for wave-power absorption by oscillating bodies", *Journal of Fluid Mechanics*, Vol. 77 (1), pp. 1-25.

Evans, DV (1979). "Some theoretical aspects of three-dimensional wave-energy absorbers", Proc. 1st Symp. Wave Energy Utilization, Gothenburg, Sweden.

Evans , DV, Jeffrey, DC, Salter, SH and Taylor JR (1979). "Submerged cylinder wave energy device: theory and experiment", *Applied Ocean Research*, Vol. 1 (1), pp. 3-12.

Evans, DV (1981a). "Power from Water Waves", *Annual Review of Fluid Mechanics*, Vol. 13, pp. 157-187.

Evans, DV (1981b). "Maximum wave-power absorption under motion constraints", *Applied Ocean Research*, Vol. 3, pp. 200-203.

Evans, DV and Falcão, AF (1986). *Hydrodynamics of Ocean Wave-Energy Utilization* (Editors), Proceedings IUTAM Symposium, Lisbon, Portugal, 8-11 July 1985, Springer-Verlag.

Evans, D., Linton, CM (1993). "Hydrodynamics of wave-energy devices", Annex Report B1: Device Fundamentals/Hydrodynamics, Contract JOU2-0003-DK, Commission of the European Communities.

Falcão, A (2003). "First-generation wave power plants: current status and R&D requirements", Proc. 22nd International Conference on Offshore Mechanics and Arctic Engineering, Cancun, Mexico, Paper No. OMAE2003-37366.

Falnes, J (1980). "Radiation impedance matrix and optimum power absorption for interacting oscillators in surface waves", *Applied Ocean Research*, Vol. 2, pp. 75-80.

Falnes J, 2002. Ocean Waves and Oscillating Systems. Linear Interactions Including Wave Energy Extraction. Cambridge University Press. ISBN 0-521-01749-1.

Faltisen, O (1990). *Sea loads on ships and offshore structures*, Cambridge University Press.

Fitzgerald J, Bergdahl L, 2007. Considering Mooring Cables for Offshore Wave Energy Converters. Proceedings of the 7th European Wave and Tidal Energy Conference, Porto, Portugal

Fitzgerald J, Bergdahl L, 2008. Including moorings in the assessment of a generic offshore wave energy converter: A frequency-domain approach. Marine Structures Volume 21, Issue 1. 23-46

Iserles, A, 1996. A First Course in the Numerical Analysis of Differential Equations. Cambridge University Press. ISBN 0521556554.

Goodman T R, Breslin J P, 1976. Statics and dynamics of anchoring cables in water. Journal of Hydronautics vol. 10, no. 4, 113-120.

Greenhow, M and Ahn, SI (1988). "Added-mass and Damping of Horizontal Circular Cylinder Sections", *Ocean Engineering*, Vol. 15 (5), pp. 495-504.

Haskind, M (1957). "The exciting forces and wetting of ships in waves", *Izv. Akad. Nauk. SSSR, Otd. Tekh. Nauk*, Vol. 7, pp. 65-79.

Havelock, T (1942). "The damping of the heaving and pitching motion of a ship", *Philosophical Magazine*, Vol. 33 (7), pp. 666-673.

Havelock, T (1955). "Waves due to a floating sphere making periodic heaving oscillations", *Proc. Royal Society*, Vol. 231, pp. 1.

Henderson, R, 2006. Design, simulation, and testing of a novel hydraulic power take-off system for the Pelamis wave energy converter. Published in 'Renewable Energy' Vol. 31, 271–283.

Henderson, R (2008). "Case Study: Pelamis", In: Chapter 5, *Ocean Wave Energy* (Ed.: J Cruz), Springer-Verlag.

Hess, J and Smith, A (1964). "Calculation of nonlifting potential flow about arbitrary three-dimensional bodies", *Journal of Ship Research*, Vol. 8, pp. 22-44.

Hess, J (1990). "Panel methods in computational fluid dynamics", *Annual Review of Fluid Mechanics*, Vol. 22, pp. 255-274.

Ho B, Kalman R, 1966. Effective Reconstruction of Linear State-Variable Models from Input/Output Functions. Regelungstechnik 14 (12), 417-441

Jeffrey, DC, Keller, GJ, Mollison, D, Richmond DJ, Salter, SH, Taylor, JM, Young, IA (1978). "Study of mechanisms for extracting power from sea waves", Fourth Year Report of the Edinburgh Wave Power Project, The University of Edinburgh.

John, F (1950). "On the Motion of Floating Bodies", *Communications on Pure and Applied Mathematics*, Vol. 3, pp. 45-101.

Justino, P and Clément A (2003). "Hydrodynamic performance for small arrays of sub-merged spheres", Proc. 5th European Wave Energy Conference, Cork, Ireland, pp. 266-273.

Johanning L, Smith G H, Wolfram J. Towards Design Standards for WEC Moorings. Proceedings of the 6th European Wave and Tidal Conference, Glasgow UK, 223-230

Josset C, Babarit A, Clément A H, 2007. A wave-to-wire model of the SEAREV wave energy converter. Proceedings of the IMechE vol. 221 Part M: J. Engineering for the Maritime Environment.

Katory, M (1976). "On the motion analysis of large asymmetric bodies among sea waves: an application to a wave power generator", *Naval Architecture*, pp. 158-159.

Kinsman, B (1965). *Wind Waves*, Prentice-Hall, pp. 460-471.

Koterayama W, 1978. Motions of a moored floating body and dynamic tension of mooring lines in regular waves. Report of the Research Institute for Applied Mechanics, Kyushu University, Fukuoka, vol. 6 no. 82.

Kristiansen E, Egeland O, 2003. Frequency Dependent Added-mass in Models for Controller Design for Wave Motion Damping. 6th IFAC Conference on Maneuvering and Control of Marine Craft, 17th – 19th September 2003, University of Girona, Spain.

Kung S Y, 1978. A New Identification and Model Reduction Algorithm via Singular Value Decompositions. Proc.Twelth Asilomar Conf. on Circuits, Systems and Computers, November 6-8, 1978, 705-714.

Lamb, H (1932). *Hydrodynamics*, 6th Ed., Cambridge University Press.

Le Méhauté, B (1976). *An Introduction to Hydrodynamics & Water Waves*, Springer-Verlag.

Lee, C-H, Maniar, H, Newman, JN and Zhu, X (1996a). "Computations of Wave Loads Using a B-Spline Panel Method", Proc. 21st Symposium on Naval Hydrodynamics, Trondheim, Norway, pp. 75-92.

Lee, C-H, Newman, JN and Nielsen, F (1996b). "Wave Interactions with Oscillating Water Column", Proc. 6th International Offshore and Polar Engineering Conference, Los Angeles, USA, Vol.1, pp. 82-90.

Lee, C-H, Farina, L and Newman, J (1998). "A Geometry-Independent Higher-Order Panel Method and its Application to Wave-Body Interactions", Proc. 3rd Engineering Mathematics and Applications Conference, Adelaide, Australia, pp. 303-306.

Lin, C-P (1999). "Experimental studies of the hydrodynamic characteristics of a sloped wave energy device", PhD Thesis, The University of Edinburgh.

Linton, CM (1991). "Radiation and diffraction of water waves by a submerged sphere in finite depth, *Ocean Engineering*, Vol. 18 (1/2), pp. 61-74.

Longuet-Higgins M S, 1977. The mean forces exerted by waves on floating or submerged bodies with applications to sand bars and wave power machines. Proceedings of the Royal Society of London A. 352, 463-480.

Maniar, H (1995). "A three-dimensional higher order panel method based on B-splines", PhD Thesis, Massachusetts Institute of Technology.

Martins, E, Ramos, FS, Carrilho, L, Justino, P, Gato, L, Trigo, L and Neumann, F (2005). "CEODOURO: Overall Design of an OWC in the new Oporto Breakwater", Proc. 6th European Wave Energy Conference, Glasgow, UK, pp. 273-280.

Mavrakos, S and McIver, P (1997). "Comparison of methods for computing hydrodynamic characteristics of arrays of wave power devices", *Applied Ocean Research*, Vol. 19, pp. 283-291.

McCabe A P, Aggidisa G A, Stallard T J, 2006. A time-varying parameter model of a body oscillating in pitch. Applied Ocean Research 28, 359-370.

McCormick, M (1981). *Ocean Wave Energy Conversion*, John Wiley & Sons.

McIver, P (1993). "The hydrodynamics of arrays of wave-energy devices", Annex Report B1: Device Fundamentals/Hydrodynamics, Contract JOU2-0003-DK, Commission of the European Communities.

McIver, P and McIver, M (1995). "Wave-power absorption by a line of submerged horizontal cylinders", *Applied Ocean Research*, Vol. 17, pp. 117-126.

Mei, CC (1976). "Power Extraction from Water Waves", *Journal of Ship Research*, Vol. 20, pp. 63-66.

Mei, CC (1989). *The Applied Dynamics of Ocean Surface Waves*, Advanced Series on Ocean Engineering, Vol. 1, World Scientific (revised edition in 2005).

Montgomery, DC (2001). *Design and Analysis of Experiments*, John Wiley & Sons, 5th Edition.

Mynett, AE, Serman, DD and Mei, CC (1979). "Characteristics of Salter's cam for extracting energy from ocean waves", *Applied Ocean Research*, Vol. 1 (1), pp. 13-20.

Nebel, P (1992). "Optimal Control of a Duck", Report of the Edinburgh Wave Power Project, Edinburgh, UK.

Newman, JN (1976). "The interaction of stationary vessels with regular waves", Proc. of the 11th Symposium on Naval Hydrodynamics, London, UK, pp. 491-501.

Newman, JN (1977). *Marine Hydrodynamics*, MIT Press.

Newman, JN (1985). "Algorithms for the free-surface Green's function", *Journal of Engineering Mathematics*, Vol. 19, pp. 57-67.

Newman, JN (1992). "Panel methods in marine hydrodynamics", Proc. 11th Australasian Fluid Mechanics Conference, Hobart, Australia, Keynote Paper K-2.

Newman, JN and Lee, CH (1992). "Sensitivity of Wave Loads to the Discretization of Bodies", Proc. of the 6th Behaviour of Offshore Structures (BOSS) International Conference, London, UK, Vol. 1, pp. 50-63.

Newman, JN and Lee, CH (2002). "Boundary-Element Methods in Offshore Structure Analysis", *Journal of Offshore Mechanics and Artic Engineering*, Vol. 124, pp. 81-89.

Ogilvie, TF (1963). "First and second-order forces on a submerged cylinder submerged under a free-surface", *Journal of Fluid Mechanics*, Vol. 16, pp. 451-472.

O'Leary, M (1985). "Radiation and scattering of surface waves by a group of submerged, horizontal, circular cylinders", *Applied Ocean Research*, Vol. 7 (1), pp. 51-57.

Orcina Ltd. OrcaFlex Manual Version 9.2a.

Payne, G (2002). "Preliminary numerical simulations of the Sloped IPS Buoy", Proc. of the MAREC Conference, Univ. Newcastle upon Tyne, UK.

Payne, G (2006). "Numerical modelling of a sloped wave energy device", PhD Thesis, The University of Edinburgh.

Pinkster, JA (1997). "Computations for Archimedes Wave Swing", Delft University Technology, Delft, The Netherlands, Report No. 1122-O.

Pizer, D (1992). "Numerical Predictions of the Performance of a Solo Duck", Report of the Edinburgh Wave Power Project, Edinburgh, UK.

Pizer, D (1993). "The Numerical Prediction of the Performance of a Solo Duck", Proc. European Wave Energy Symposium, Edinburgh, UK, pp. 129-137.

Pizer, D (1994). "Numerical Models", Report of the Edinburgh Wave Power Project, Edinburgh, UK.

Pizer, D, Retzler, C, Henderson, R, Cowieson, F, Shaw, F, Dickens, B and Hart, R (2005). "PELAMIS WEC - Recent Advances in the Numerical and Experimental Modelling Programme", Proc. 6th European Wave Energy Conference, Glasgow, UK, pp. 373-378.

Prado, M., and Gardner, F (2005). "Theoretical analysis of the AWS dynamics during the submergence operation", Proc. 6th European Wave Energy Conference, Glasgow, UK, pp. 395-400.

Prado, M, Neumann, F, Damen, M and Gardner, F (2005). "AWS Results of Pilot Plant Testing 2004", Proc. 6th European Wave Energy Conference, Glasgow, UK, pp. 401-408.

Prado, M (2008). "Archimedes Wave Swing", In: *Ocean Wave Energy* (Ed.: J Cruz), Springer-Verlag.

Press, W, Teukolsky, S, Vetterling, W and Flannery, B (1992). *Numerical Recipes in FORTRAN*. 2nd Ed., Cambridge University Press.

Rademakers, L, Van Schie, R, Schitema, R, Vriesema, B and Gardner, F (1998). "Physical Model Testing for Characterising the AWS", Proc. 3rd European Wave Energy Conference, Patras, Greece, Vol. 1, pp. 192-199.

Retzler C, Pizer D, Henderson R, Ahlqvist J, Cowieson F and Shaw M (2003). "PELAMIS: Advances in the Numerical and Experimental Modelling Programme", Proc. 5th European Wave Energy Conference, Cork, Ireland, pp. 59-66.

Roache, PJ (1997). "Quantification of Uncertainty in Computational Fluid Dynamics", *Annual Review of Fluid Mechanics*, Vol. 29, pp 123-160.

Roache, PJ (1998). *Verification and Validation of Computational Science and Engineering*, Hermosa Publishers.

Roache, PJ (2003). "Error Bars for CFD", 41th Aerospace Sciences Meeting, Reno, USA.

Romate, JE (1988). "Local Error analysis in 3-D Panel Methods", *Journal of Engineering Mathematics*, Vol. 22, pp. 123-142.

Romate, JE (1989). "The Numerical Simulation of Nonlinear Gravity Waves in Three Dimensions using a Higher Order Panel Method", PhD Thesis, Universiteit Twente.

Ross, D (1995). *Power from the Waves*, Oxford University Press.

Salter, SH (1974). "Wave Power", *Nature*, Vol. 249, pp. 720-724.

Sarmento, A (1992). "Wave flume experiments on two-dimensional oscillating water column wave energy devices", *Experiments in Fluids*, Vol.12, pp. 286-292.

Sarmento, A, Luís, A, Lopes, D (1998). "Frequency-Domain Analysis of the AWS", Proc. 3rd European Wave Energy Conference, Patras, Greece, Vol. 1, pp. 15-22.

Sarpkaya, T and Isaacson, I (1981). *Mechanics of Wave Forces on Offshore Structures*, Von Nostrand Reinhold Company.

Shaw, R (1982). *Wave Energy - A Design Challenge*, Ellis Harwood Ltd, John Wiley & Sons.

Skyner, D (1987). "Solo Duck Linear Analysis", Report of the Edinburgh Wave Power Project, Edinburgh, UK.

Standing, MG (1980). "Use of Potential Flow theory in Evaluating Wave Forces on Offshore Structures", *Power from Sea Waves*, Proc. Conf. Institute of Mathematics and its Applications (Ed. B. count), pp. 175-212, Academic Press, London.

Sumer, BM and Fredsøe, J (1997). *Hydrodynamics around Cylindrical Structures*, Advanced Series on Ocean Engineering, Vol. 12, World Scientific.

Sykes, R, Lewis, A and Thomas, G (2007). "A Physical and Numerical Study of a Fixed Cylindrical OWC of Finite Wall Thickness", Proc. 7th European Wave and Tidal Energy Conference, Porto, Portugal, September 2007.

Taghipour R, Perez T, Moan T, 2008. Hybrid frequency-time-domain models for dynamic response analysis of marine structures. Ocean Engineering 35, 685-705.

Thomas, GP and Evans DV (1981). "Arrays of three-dimensional wave-energy absorbers", *Journal of Fluid Mechanics*, Vol. 108, pp. 67-88.

Thomas in Cruz J (Editor), 2008. Ocean Wave Energy, Current Status and Future Perspectives. Springer-Verlag. ISBN978-3-540-74894-6

Triantafyllou M S, Bliekl A, Shin H, 1986. Static and fatigue analysis of multi-leg mooring system. MIT Sea Grant Program Report, August 1986.

Tucker, MJ and Pitt, EG (2001). *Waves in Ocean* Engineering. Elsevier Science Ltd.

Ursell F, 1964. The decay of the free motion of a floating body. Journal of Fluid Mechanics 19, 305-319

van Daalen, E (1993). "Numerical and Theoretical Studies of Water Waves and Floating Bodies", PhD Thesis, University of Twente, The Netherlands.

van der Pluijm, D and Voors, E (2002). "Power from ocean waves – A study on power conversion with the Archimedes Wave Swing", MSc Thesis, Delft University of Technology.

Vugts, JH (1968). "The Hydrodynamic Coefficients for Swaying, Heaving and Rolling Cylinders in a Free-surface", Netherlands Ship Research Centre TNO, Report No. 112 S.

Walker N S. GMOOR32 Manual v9.2. Global Martime Consultancy Limited.

WAMIT Inc, 2006. WAMIT User Manual Versions 6.3, 6.3PC, 6.3S, 6.3S-PC

Wehausen, J and Laiton, E (1960). "Surface Waves", *Encyclopaedia of Physics*, Vol. 9, pp. 446-778.

Wehausen, J.V., 1971. The motion of floating bodies. Annual Review of Fluid Mechanics 3, 237–268

Yeung, RW (1982). "Numerical methods in free-surface flows", *Annual Review of Fluid Mechanics*, Vol. 14, pp. 395-442.

Yemm, R, Pizer, D and Retzler, C (1998). "The WPT-375 – a near-shore wave energy converter submitted to Scottish Renewables Obligation 3", Proc. 3rd European Wave Energy Conference, Patras, Greece, Vol. 2, pp.243-249.

Yu Z, Falnes J, 1995. State-space modelling of a vertical cylinder in heave. Applied Ocean Research 17, 265-275.

Zentech Inc. ZenMoor by Zentech Flyer. Available online, February 2010.

Section 4

Boukhanovsky AV and Guedes Soares C, (2009). Modelling of multipeaked directional wave spectra. Applied Ocean Research, 31, 132-141.

Bouws E, Gunther H, Rosenthal W, Vincent CL, (1985). Similarity of the wind wave spectrum in finite depth. Part 1: Spectral form. J. Geophysical Res. 90 (C1), 975-986.

Bretschneider CL, (1959). Wave variability and wave spectra for wind generated gravity waves. Tech. Memo. No. 118. Beach Erosion Board, US Army Corps of Eng., Washington DC

Folley M and Whittaker TJT, (2009). The effect of sub-optimal control and the spectral wave climate on the performance of wave energy converter arrays. Applied Ocean Research, 31(4), 260-266.

Guedes Soares C, (1984). Representation of Double-Peaked Sea Wave Spectra. Ocean Eng., 11, 185–207.

Hasselmann K, et al., (1973). Measurements of wind wave growth and swell decay during the Joint North Sea Wave Project (JONSWAP). Deutsch Hydrographishe Zeit, A8:1-95.

Holthuijsen LH, (2007). Waves in Oceanic and Coastal Waters. Cambridge University Press.

Michel WH, (1999). Sea spectra revisited. Marine Technology, 36(4), 211-227.

National Data Buoy Center (NDBC), (1996). Nondirectional and directional wave data analysis procedures. Tech. Doc. 96–01, Stennis Space Center, Miss.

National Data Buoy Center (NDBC), 2003. Handbook of automated data quality control checks and procedures of the National Data Buoy Center. Tech. Doc. 03–02, Stennis Space Center, Miss.

Ochi MK and Hubble EN, (1976). Six-Parameter Wave Spectra. Proc. 15th Coastal Engineering Conference, pp. 301–328.

Pierson WJ and Moskowitz L, 1964. A proposed spectral form for fully developed wind seas based on the similarity theory of S.A. Kitaigorodskii. J. Geophys. Res., 69, 24 5181-5190

Saulnier JB, Clément A, Falcão AF, Pontes T, Prevosto M, Ricci P, (2011). Wave groupiness and spectral bandwidth as relevant parameters for the performance assessment of wave energy converters. Ocean Engineering, 38(1), 2011, 130-147

Torsethaugen K, (1993). A Two Peak Wave Spectrum Model. Proc. 12th Int. Conf. Offshore Mech. Arctic Eng., Vol. 2, pp. 175–180.

Torsethaugen K and Haver S, (2004). Simplified double peak spectral model for ocean waves. Proc. 14th Int. Offshore and Polar Eng. Conf., Toulon, France.

Young IR and Babanin AV, (2006). The form of the asymptotic depth-limited wind wave frequency spectrum. J. Geophys. Res., 111, C06031, doi:10.1029/2005JC003398, 2006.

Young IR and Van Vledder GPh, (1993). A Review of the Central Role of Nonlinear Interactions in Wind-Wave Evolution. Philosophical Transactions: Physical Sciences and Engineering, Vol. 342, No. 1666. (Mar. 15, 1993), pp. 505-524.

Section 5

Aamo O. M., Fossen T. I. (2000), Finite element modelling of mooring lines, Mathematics and Computers in Simulation, vol. 53, Issues 4-6, pp. 415-422.

Isaacson M., Baldwin J. (1996), Moored structures in waves and currents, Canadian Journal of Civil Engineering, vol. 23, pp. 418-430.

Jonkman, J. (2010), Definition of the Floating System for Phase IV of OC3, Technical Report NREL/TP-500-47535, National Renewable Energy Laboratory.

Johanning L. , Smith G. H., Wolfram J. (2007), Measurements of static and dynamic mooring line damping and their importance for floating WEC devices, Ocean Engineering, vol. 34, pp. 1918–1934.

Brown D.T., Mavrakos S. (1999), Comparative study on mooring line dynamic loading, Marine Structures, vol. 12, pp. 131-151.

Faltinsen O. M. (1990), *Sea loads on ships and offshore structures*, Cambridge University Press.

Fitzgerald J., Bergdahl L. (2007), Considering Mooring Cables for Offshore Wave Energy Converters, Proceedings of the 7th European Wave and Tidal Energy Conference, Porto, Portugal, 2007.

Fitzgerald J., Bergdahl L. (2009), Rigid moorings in shallow water: A wave power application. Part I: Experimental verification of methods, Marine Structures, vol. 22, Issue 4, pp. 809-835.

Kreuzer E., Wilke U. (2003), Dynamics of mooring systems in ocean engineering, Archive of Applied Mechanics, vol. 73, pp. 270 – 281.

McCormick M E (2010). *Ocean Engineering Mechanics*. Cambridge University Press.

Orcina Ltd (2008). OrcaFlex Manual, Version 9.2a. www.orcina.com.

Section 6

Falcão A F de O, 2007. Modelling and control of oscillating-body wave energy converters with hydraulic power take-off and gas accumulator. Ocean Engineering, vol. 34, 2021–2032.

Falcão A F de O, 2008. Phase control through load control of oscillating-body wave energy converters with hydraulic PTO system. 'Ocean Engineering' 35, p358–366.

Livingstone M J, 2009. Modelling and Control of a Wave Energy Converter Power Take-Off. Final Year Project Supported by Garrad Hassan and Partners Ltd. Machine Systems Group. University of Bath.

Livingstone M J, Plummer A R, 2010. The design, simulation and control of a wave energy converter power take-off. (submitted for publication in Proceedings of the 7th International Fluid Power Conference, Aachen, Germany).

Section 7

Budal K, (1977). Theory for absorption of wave power by a system of interacting bodies. Journal of Ship Research, 21(4), 248-253.

Child BFM and Venugopal V, (2007). Interaction of waves with an array of floating wave energy devices. In Proceedings of the 7th European Wave and Tidal Energy Conference (EWTEC2007).

Child BFM and Venugopal V, (2010). Optimal configurations of wave energy device arrays. Ocean Engineering, 36(16), 1402-1417.

Child BFM, (2010). On the configuration of arrays of floating wave energy converters. PhD thesis, The University of Edinburgh.

Cruz J, Sykes R, Siddorn P, Taylor, RE, (2010). Estimating the loads and energy yield of arrays of wave energy converters under realistic seas. Renewable Power Generation, IET, 4(6), 488-497.

Evans DV, (1979). Some theoretical aspects of three dimensional wave-energy absorbers. In Proceedings of the 1st Symposium on Ocean Wave Energy Utilization.

Evans DV, (1980). Power from sea waves, chapter: Some analytic results for two and three dimensional wave-energy absorbers, 213-249. Academic Press Inc., London, UK.

Falnes J, (1980). Radiation impedance matrix and optimum power absorption for interacting oscillators in surface waves. Applied Ocean Research, 2(2), 75-80.

Fitzgerald C and Thomas G, (2007). A preliminary study on the optimal formation of an array of wave power devices. In Proceedings of the 7th European Wave and Tidal Energy Conference (EWTEC2007).

Fitzgerald C, (2006). Optimal configurations of arrays of wave-power devices. Master's thesis, National University of Ireland, Cork.

Folley M and Whittaker TJT, (2009). The effect of sub-optimal control and the spectral wave climate on the performance of wave energy converter arrays. Applied Ocean Research, 31(4), 260-266.

Garnaud X and Mei CC, (2010). Bragg scattering and wave-power extraction by an array of small buoys. Proceedings of the Royal Society A, 466(2113), 79-106.

Justino PAP and Falcao A, (2002). Hydrodynamic interactions for small arrays of wave energy devices. In Proceedings of the 21st International Conference on Offshore Mechanics and Arctic Engineering. ASME.

Kagemoto H and Yue DKP, (1986). Interactions among multiple three-dimensional bodies in water waves: an exact algebraic method. Journal of Fluid Mechanics, 166, 189-209.

Kagemoto H and Yue DKP, (1993). Hydrodynamic interaction analyses of very large floating structures. Marine Structures, 6, 295-322.

Kashiwagi M, (2000). Hydrodynamic interactions among a great number of columns supporting a very large flexible structure. Journal of Fluids and Structures, 14, 1013-1034.

Li Yand Mei CC, (2007). Bragg scattering by a line array of small cylinders in a waveguide. Part 1. Linear aspects. Journal of Fluid Mechanics, 583, 161-187.

Linton CM and Evans DV, (1992). The radiation and scattering of surface waves by a vertical circular cylinder in a channel. Philosophical Transactions: Physical Sciences and Engineering, 338(1650), 325-357.

Linton CM and Evans DV, (1993). The interaction of waves with a row of circular cylinders. Journal of Fluid Mechanics, 251, 687-708.

Linton CM and McIver P, (2001). Handbook of mathematical techniques for wave/structure interactions. Chapman & Hall/CRC.

Mavrakos SA and Kalofonos A, (1997). Power absorption by arrays of interacting vertical axisymmetric wave-energy devices. Journal of Offshore Mechanics and Artic Engineering, 119(4), 244-250.

Mavrakos SA and Koumoutsakos P, (1987). Hydrodynamic interaction among vertical axisymmetric bodies restrained in waves. Applied Ocean Research, 9(3), 128-140.

Mavrakos SA and McIver P, (1997). Comparison of methods for computing hydrodynamic characteristics of arrays of wave power devices. Applied Ocean Research, 19, 283-291.

Mavrakos SA, (1991). Hydrodynamic coefficients for groups of interacting vertical axisymmetric bodies. Ocean Engineering, 18, 485-515.

McIver P and Evans DV, (1984). Approximation of wave forces on cylinder arrays. Applied Ocean Research, 6(2), 101-107.

McIver P and McIver M, (1995). Wave-power absorption by a line of submerged horizontal cylinders. Applied Ocean Research, 17, 117-126.

McIver P, Mavrakos S and Singh G, (1996a). Wave-power absorption by arrays of devices. In Proceedings of the Second European Wave Power Conference, 126-133.

McIver P, Mavrakos S and Singh G, (1996b). Wave-power absorption by arrays of devices. Technical report, Commission of the European Communities, Danish Wave Power aps.

Mitchell M, (1998). An introduction to genetic algorithms. MIT Press.

Ohkusu M, (1972). Wave action on groups of vertical circular cylinders. Journal of the Society of Naval Architects in Japan, 131.

Ohkusu M, (1974). Hydrodynamic forces on multiple cylinders in waves. In Proceedings of the International Symposium on Dynamics of Marine Vehicles and Structures in Waves, 107-112.

P. McIver, (1984). Wave forces on arrays of floating bodies. Journal of Engineering Mathematics, 18, 273-285.

Siddorn P and Eatock Taylor R, (2008). Diffraction and independent radiation by an array of floating cylinders. Ocean Engineering, 35, 1289-1303.

Simon MJ, (1982). Multiple scattering in arrays of axisymmetric wave-energy devices. Part 1. A matrix method using a plane-wave approximation. Journal of Fluid Mechanics, 120, 1-25.

Spring BH and Monkmeyer PL, (1974). Interaction of plane waves with vertical cylinders. In Proceedings of 14th International Conference on Coastal Engineering, 1828-1845.

Twersky V, (1952). Multiple scattering and radiation by an arbitrary configuration of parallel cylinders. Journal of the Acoustical Society of America, 24, 42-46.

Zaviska F, (1913). Uber die Beugung elektromagnetischer Wellen an parallelen, unendlich langen Kreiszylindern. Annalen der Physik, Folge.

NOMENCLATURE

Standard Index (S I) Units are used unless stated otherwise

An overdot, $\dot{x}$ indicates differentiation of the quantity x with respect to time.

A X^* indicates the complex conjugate of the complex quantity X

The complex operator, $j = \sqrt{-1}$

A standard glossary of terms can be found in the 2007 Ocean Energy Glossary (IEA-OES), which was followed throughout this document. This document is available at

http://www.wavec.org/client/files/Ocean_Energy_Glossary_Dec_2007.pdf.

Section 3	
A	Wave Amplitude
B_r	Radiation Damping (or Radiation Resistance)
$\underline{d}_{HY}$	General position vector in hydrodynamic coordinates
$\underline{d}_{gHY}$	Position vector of hydrodynamic coordinate system origin in global coordinates
$\underline{d}_{HY\ BF}$	Position vector of body proximal node in hydrodynamic coodinates
$\underline{n}$	Unit vector normal to the surface
f_b	Buoyancy force
f_e	Excitation force
f_{ext}	External forces
f_{hs}	Hydrostatic force
f_r	Radiation force
F_e	Complex excitation force amplitude
g	Acceleration due to gravity

h	Water depth
k	Wave number
$k(t)$	Radiation Impulse Response ('Memory') Function
K_{hs}	Hydrostatic Stiffness
m_m	Physical Body Mass
$m_r(\omega)$	Added Mass at frequency ω
$\underline{n}$	Unit vector normal to a surface
ρ	Density
Γ	Excitation force amplitude coefficient determined by the flow solver
S	Waterplane area
S_j, S_{ij}	Waterplane moments
t	Time
τ	Alternative convolution time ordinate
t_{cutoff}	Convolution cut-off time
θ	Wave direction

$\underline{\theta}_{HY\ BF}$	Vector of roll, pitch and yaw rotations describing the instantaneous position of the body in the hydrodynamic coordinate system
ϕ	Phase
ϕ_e	Complex amplitude phase
ϕ_p	Position related phase
V	Volume
V_0	Mean displaced volume
$[x_B, y_B, z_B]$	Position of the centre of buoyancy for the body, in the hydrodynamic coordinate system
$\omega = 2\pi f$	Angular frequency
Section 4	
a	Wave Amplitude
$D(f, \theta)$	Directional Spreading Function (or Directional Distribution)
$E(f)$	Omnidirectional spectrum or Frequency Spectrum
f	Frequency
f_p	Peak Frequency
f_s	Sampling Frequency
g	Acceleration due to gravity
H_s	Significant Wave Height
$k = 2\pi / \lambda$	Wave Number
L	Duration of simulation
m_n	nth moment of the omnidirectional spectrum
$MDIR$	Mean Direction
r	Generalised JONSWAP spectrum high-frequency tail index

s	Generalised JONSWAP spectrum shape parameter
$S(f, \theta)$	Directional Variance Spectrum
$SDIR$	Mean Spread
T_p	Peak Period
T_e	Energy Period
T_m	Mean Period
T_z	Zero-Crossing Period
α	Generalised JONSWAP spectrum scale parameter
β	Generalised JONSWAP spectrum location parameter
γ	Generalised JONSWAP spectrum peak enhancement factor
Δ	Deviance between measured and fitted spectra
$\delta(\theta)$	Deviance between measured and fitted mean direction
$\delta(\sigma)$	Deviance between measured and fitted spreading function
θ	Direction of wave propagation
θ_m	Mean wave direction (frequency dependent)
λ	Wavelength
η	Sea surface elevation
$\omega = 2\pi f$	Angular frequency
σ_c	Directional Spread (circular moment definition)
σ_l	Directional Spread (line moment definition)
ϕ	Phase
Section 5	
B_{moor}	Damping matrix for the mooring line
K_{moor}	Stiffness matrix for the mooring line

M_{moor}	Inertia matrix for the mooring line
C_a	Added-mass coefficient
C_{curr}	Current force coefficient in ROMEO
C_{wind}	Wind force coefficient in ROMEO
C_s	Shape coefficient for wind/current force calculations in ROMEO
C_h	Height coefficient for wind/current force calculations in ROMEO
X	Complex RAO at a given wave frequency
x_p	Distance from origin of wave system perpendicular to wave direction
χ	$= x \cos\theta + y \sin\theta$ where θ = wave direction
u_f	Fluid velocity component normal to cable element (Orcaflex)
u_s	Velocity of cable element
C_m	Inertia coefficient
ε	Mean axial strain
λ	Expansion factor of cable element
L	Instantaneous length of cable element
L_0	Original (unstretched) length of cable element
E	Young's modulus
D_n	Effective diameter of cable for drag purposes (for flow in normal direction)
D_a	Effective diameter of cable for drag purposes (for flow in axial direction)
$\underline{x}_m$	General position vector in mooring line coordinates
$\underline{p}$	Position vector of mooring attachment point in global coordinates
$\underline{p}_{eq}$	Position vector of mooring attachment when system is at equilibrium
Section 6	See Table 6.3
Section 7	

ψ	Direction of gridline (Set 1)
σ	Direction of gridline (Set 2)
p	Spacing between gridline of Set 2 along gridlines from Set 1
s	Spacing between gridline of Set 1 along gridlines from Set 2
M	Number of gridlines from Set 1 selected to define potential device locations
χ	Device heading
a	Device radius
h	Clearance beneath the device
d	Water depth
B_{pto}	Damping coefficient of PTO
L	Device spacing
N	Number of devices in the array
β	Wave direction
T	Period
T_{-10}	Energy period
T_p	Peak period
H_{m0}	Significant wave height
P_{abs}	Absorbed power

KEY TO ACRONYMS

ADCP	Acoustic Doppler Current Profiler
AIC	Akaike's Information Criterion
BCS	Body-fixed Coordinate System
BDM	Bayesian Directional Method
BEM	Boundary Element Method
DDD	Double Direction Decomposition
DFTM	Direct Fourier Transform Method
DLL	Dynamic-Link Library
DOF	Degree-Of-Freedom
EMEC	European Marine Energy Centre
EMLM	Extended Maximum Likelihood Method
EMEP	Extended Maximum Entropy Principle
EWTEC	European Wave and Tidal Energy Conference
FD	Frequency-Domain
FDC	Fundamental Device Concept
FFT	Fast Fourier Transform
FSP	Full-Scale Prototype
GA	Genetic Algorithm
GH	Garrad Hassan and Partners Ltd
GCS	Global Coordinate System
GUI	Graphical User Interface
IMLM	Iterated Maximum Likelihood Method
JONSWAP	Joint North Sea Wave Project
NURBS	Non-Uniform Rational B-Splines
OWC	Oscillating Water Column

PM	Pierson-Moskowitz
PR	Power Ratio (ratio between measured and expected power)
PTO	Power Take-Off
QUB	Queen's University Belfast
RAO	Response Amplitude Operator
RCW	Relative Capture Width
RMS	Root-Mean-Square
SDD	Single Direction Decomposition
TD	Time-Domain
TFSM	Truncated Fourier Series Decomposition Method
UoOx	University of Oxford
WEC	Wave Energy Converter
WR	Waverider

APPENDIX A IMPLEMENTATION DETAILS (MBCORE)

MBCore: co-ordinate systems

The equation of motion for the system, constructed by MBCore, is expressed in what will here (and throughout the development of WaveDyn) be referred to as the global co-ordinate system; a right-hand inertial frame of reference with its origin defined relative to the position of the Ground body (see the 'location' parameter in Figure A.1) and the *z*-axis being positive upwards. The direction of the positive global *x*-axis is aligned with south for the purpose of defining the incident wave directions. Each rigid body in the system has its own 'body-fixed frame of reference' which is positioned at the body's proximal node and is used to track the body position as it moves in global space. The body-fixed frame of reference of the ground body has the same orientation as the global co-ordinate system and an origin at the ground body proximal node. The orientation of the body-fixed co-ordinate systems for bodies further up the tree-structure are inherited from the bodies below. Bodies with distal nodes allow the user to specify a relative rotation of their distal node to the proximal node; the distal node is the proximal node of the proceeding body in the tree, so specifying a non-zero rotation here rotates the body-fixed co-ordinate system of the proceeding body. This inheritance system is illustrated in Figure A.1 below. The multi-body system may be queried for a position vector describing the global position of a specified body and the instantaneous rotation of its body-fixed frame of reference relative to the global frame at any time.

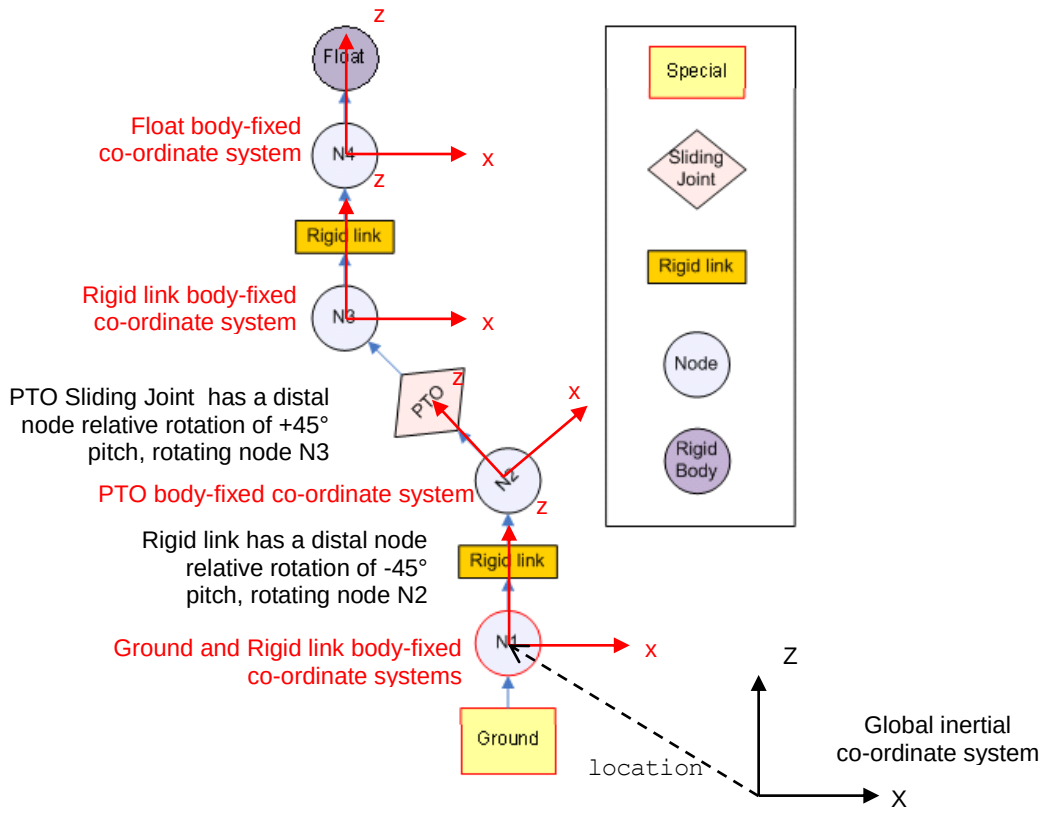

Figure A.1. Global and body-fixed MBCore co-ordinate systems. Note that the body-fixed co-ordinate systems origins are located at the proximal node of each body.

GHTools: vector and matrix Handling support

The mathematical calculations within both MBCore and the other parts of the WaveDyn code are most efficiently and clearly described in a matrix/vector format. GH have developed C++ support for vector and matrix handling in a separate library, GHTools, which is based on the LAPACK/BLAS high performance Fortran mathematical libraries (LAPACK, 2010[2]). GHTools provides matrix and vector type classes designed to handle algebraic operations (typically provided as operator overloadings), as well as an 'EulPar' class designed specifically to cope with the handling of Euler parameter scalar-vector quarterians and conversions to/from three parameter rotation matrices describing successive roll, pitch and yaw rotations about the global axes.

For clarity, the Euler parameter quarterian, $\underline{q}$ used within GHTools is defined for a rotation of angle α about a Cartesian 3x1 unit vector $\underline{n}$ as:

$$\underline{q} = (q_0, q_1, q_2, q_3) \qquad \text{where:} \quad q_0 = \cos(\alpha/2); \quad q_i = n_i \sin(\alpha/2) \qquad \text{[A.1]}$$

$$\text{So that: } q_0^{\,2} + q_1^{\,2} + q_2^{\,2} + q_3^{\,2} = 1$$

The same rotation may alternatively be represented by successive rotations of a roll angle ϕ about the global *x*-axis, a pitch of angle χ about the global *y*-axis and a yaw of angle θ about the global *z*-axis, which may be encapsulated in rotation matrix form as:

$$\underline{R} = R_\theta R_\chi R_\phi = \begin{pmatrix} \cos\theta & -\sin\theta & 0 \\ \sin\theta & \cos\theta & 0 \\ 0 & 0 & 1 \end{pmatrix} \begin{pmatrix} \cos\chi & 0 & \sin\chi \\ 0 & 1 & 0 \\ -\sin\chi & 0 & \cos\chi \end{pmatrix} \begin{pmatrix} 1 & 0 & 0 \\ 0 & \cos\phi & -\sin\phi \\ 0 & \sin\phi & \cos\phi \end{pmatrix}$$

$$= \begin{pmatrix} \cos\theta\cos\chi & \cos\theta\sin\chi\sin\phi - \sin\theta\cos\phi & \cos\theta\sin\chi\cos\phi + \sin\theta\sin\phi \\ \sin\theta\cos\chi & \sin\theta\sin\chi\sin\phi + \cos\theta\cos\phi & \sin\theta\sin\chi\cos\phi - \cos\theta\sin\phi \\ -\sin\chi & \cos\chi\sin\phi & \cos\chi\cos\phi \end{pmatrix}$$

[A.2]

Note the overall rotation matrix, $\underline{R}$, is nonlinear in terms of the roll, pitch and yaw angles and also that the matrix is orthogonal, so that its inverse is simply its transpose.

An introduction to multi-body co-ordinate system transformations

It can be confusing to visualise the correct way to apply a rotation matrix as rotations can be thought of in terms of a rotation of a position vector of a point in space to a new position in the same reference frame, or as a transformation in the co-ordinates of a fixed point, from a rotated frame of reference back to the global frame of reference. This is illustrated by the examples given below.

[2] LAPACK – Linear Algebra PACKage, (2010). Developed since 2004 with the support of the National Science Foundation (USA) under Grant No. NSF-0444486. http://www.netlib.org/lapack/

Consider a rotated relative frame of reference rolled through a 90deg angle, but with its origin located in the same place as the underlying global, inertial frame of reference, as shown in Figure A.2. Point *A* has a position vector d_{gA} = (2,1,1) (*X*,*Y*,*Z*) in global co-ordinates; the $_g$ subscript indicates that the vector values are relative to the global reference frame. Ignoring the local frame for now, in order to rotate point *A* on to another point, *B*, which is has global position vector d_{gB} = (2,-1,1), then it is necessary to multiply the position vector of *A* by the rotation matrix for a 90deg roll:

$$d_{gB} = \underline{R}_{\phi} d_{gA} = \begin{bmatrix} 1 & 0 & 0 \\ 0 & \cos 90 & -\sin 90 \\ 0 & \sin 90 & \cos 90 \end{bmatrix} \begin{bmatrix} 2 \\ 1 \\ 1 \end{bmatrix} = \begin{bmatrix} 1 & 0 & 0 \\ 0 & 0 & -1 \\ 0 & 1 & 0 \end{bmatrix} \begin{bmatrix} 2 \\ 1 \\ 1 \end{bmatrix} = \begin{bmatrix} 2 \\ -1 \\ 1 \end{bmatrix} \qquad [A.3]$$

The same position vector could now be rotated by 90deg about the global y-axis, so that point *A* comes to rest in position *C*, which has global co-ordinates (1,-1,-2) by pre-multiplying the previous result by the pitch rotation matrix:

$$d_{gC} = \underline{R}_{\chi} d_{gB} = \begin{bmatrix} \cos 90 & 0 & \sin 90 \\ 0 & 1 & 0 \\ -\sin 90 & 0 & \cos 90 \end{bmatrix} \begin{bmatrix} 2 \\ -1 \\ 1 \end{bmatrix} = \begin{bmatrix} 0 & 0 & 1 \\ 0 & 1 & 0 \\ -1 & 0 & 0 \end{bmatrix} \begin{bmatrix} 2 \\ -1 \\ 1 \end{bmatrix} = \begin{bmatrix} 1 \\ -1 \\ -2 \end{bmatrix} \qquad [A.4]$$

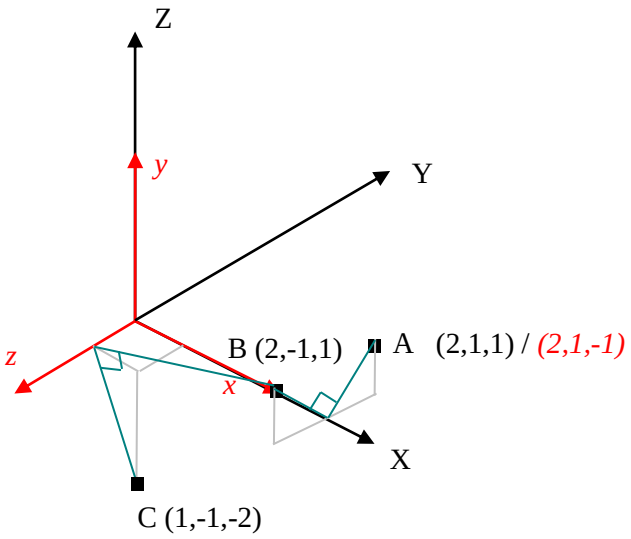

Figure A.2. Rotation of vectors in a fixed reference frame and conversion of vectors between a global (XYZ) and superimposed, rotated, relative frame (*x*,*y*,*z*).

It is possible to complete the two rotations in a single step by multiplying the position vector of A by the combined rotation matrix $\underline{R} = \underline{R}_{\chi} \underline{R}_{\phi}$:

$$d_{gC} = \underline{R}_{\chi} \underline{R}_{\phi} d_{gA} \qquad [2.5]$$

In general, a vector can be rotated within a single reference frame by pre-multiplying by the rotation matrix $\underline{R}$ composed from the required roll, pitch and yaw about the stationary co-ordinate system axes.

Now consider the rotated local reference frame shown in red in Figure A.2. Point *A* has position d_{bA} = (2,1,-1) in this relative co-ordinate system (notice the subscript is now $_b$). If the objective is to convert from global values, d_{gA} to the relative local frame position, then the local reference frame position vector must be multiplied by the *inverse* (the transpose) of the 90deg roll rotation matrix (recalling that the local frame is orientated at a 90deg roll offset from the global frame):

$$d_{bA} = \underline{R}_{\phi}^{-1} d_{gA} = \underline{R}_{\phi}^{T} d_{gA} = \begin{bmatrix} 1 & 0 & 0 \\ 0 & 0 & 1 \\ 0 & -1 & 0 \end{bmatrix} \begin{bmatrix} 2 \\ 1 \\ 1 \end{bmatrix} = \begin{bmatrix} 2 \\ 1 \\ -1 \end{bmatrix} \quad [A.6]$$

In general it is possible to say that, to convert a vector from the global reference frame to a rotated, local relative reference frame with the same origin, it is necessary to pre-multiply the vector by the transpose of the rotation matrix comprised of the rotations that a set of axes starting exactly on top of the global axes would have to go though about the global axes to reach the local, relative frame. Conversely, to convert a vector given in the local, relative frame into global values, it is necessary to pre-multiply by the rotation matrix describing the relative orientation of the local frame:

$$d_b = \underline{R}^{-1} d_g = \underline{R}^T d_g \quad [A.7]$$

$$d_g = \underline{R} d_b \quad [A.8]$$

Typically the local reference frame (most likely a body-fixed reference frame) is unlikely to have its origin on top of the global origin, but will rather have a spatial offset described in global co-ordinates by an additional position vector d_{gBF}, as shown in Figure A.3. This offset can be used to expand the equations A.7 and A.8 to a more general form for any relative (to global) reference frame so that:

$$d_b = \underline{R}^T \left(d_g - d_{gBF} \right) = \underline{R}^T d_g - \underline{R}^T d_{gBF} \quad [A.9]$$

$$d_g = \underline{R} d_b + d_{gBF} \quad [A.10]$$

Note that it is necessary to apply such a spatial offset only in the case of position vectors (denoted here by the letter d), as the difference in position is lost in the differentiation to velocity vectors (it is assumed that the case of a relative reference frame with a *velocity* offset is not of use in the calculations presented in this report). Similarly, force vectors may be transformed from a relative co-ordinate system with a position offset to the global one by simply using the relationships described by Equations A.7 and A.8.

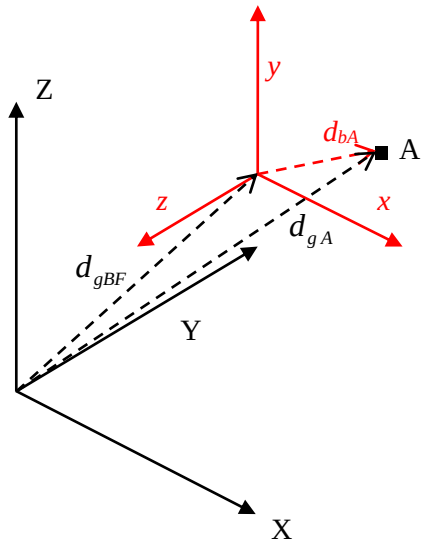

Figure A.3. The position vectors involved in the transformation of the position of a point A from a global (X,Y,Z) to a displaced, rotated relative local reference frame (*x*,*y*,*z*).

APPENDIX B HYDRODYNAMIC COORDINATE SYSTEM TRANSFORMATIONS

It is typical for potential flow solvers to provide hydrodynamic data for a body in a form that refers to the motion about a fixed reference position in global space. This is usually the body's static equilibrium position (in the absence of waves) and is provided in global coordinates as a user input to both the flow solver and to WaveDyn as the `BodyFixedHyOrigin` parameter. Hydrodynamic force calculations are completed for each body by WaveDyn using this local hydrodynamic coordinate system reference plane and forces are converted into the global co-ordinate system before being passed back to the MBCore structural model. MBCore provides body kinematic data for use in the applied force Calculation Modules in the global co-ordinate system only and so it is necessary to apply a set of coordinate system transformations to convert the data to a form relative to the `BodyFixedHyOrigin` before the force calculation may proceed.

The complete set of coordinate system transformations for the Hydrodynamic force calculation module is outlined below. The approach assumes that the reader is familiar with the theory previously provided in Appendix A, however the cases are not identical.

The `BodyFixedHyOrigin` is an inertial reference frame positioned at a stationary point in global space, described by position vector d_{gHY}. The `BodyFixedHyOrigin` is shown in green in the diagrams below, whilst the global frame of reference is shown in black. At a given point in time, a wave activated body may be positioned at any point in global space. Its position and orientation is represented by the instantaneous body-fixed reference frame, which is marked in red.

Conversion of global body X,Y,Z displacements to surge, sway and heave values in the hydrodynamics co-ordinate system:

The task is to determine position vector $d_{HY\ BF}$ from the known global vectors d_{gHY} and d_{gBF}, as shown in Figure B.1. $d_{HY\ BF}$ is a position vector relative to the `BodyFixedHyOrigin` reference plane and so it is necessary to convert the global position vectors to this plane so that the difference between the two will yield the required answer. The conversion requires pre-multiplication by the inverse (transpose) of the rotation matrix describing the orientation of the `BodyFixedHyOrigin` relative to the global origin, R_{HY}, so that the end result takes the form:

$$d_{HY\ BF} = R_{HY}{}^{T} d_{g\ BF} - R_{HY}{}^{T} d_{g\ HY} = R^{T}\left(d_{g\ BF} - d_{g\ HY}\right) \qquad [B.1]$$

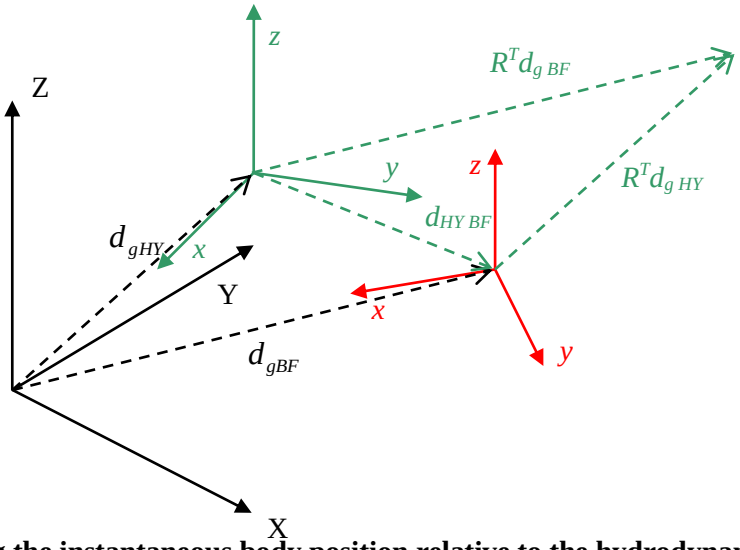

Figure B.1. Determining the instantaneous body position relative to the hydrodynamic reference plane, `BodyFixedHyOrigin`.

Conversion of global body Roll, Pitch and Yaw displacements to the hydrodynamics co-ordinate system:

The procedure described above provides a means of calculating the surge, sway and heave motions of the body only. The roll, pitch and yaw displacements are also required and may be determined as follows:

MBCore can be queried to return the Euler parameter quarternian describing the instantaneous global orientation of the body-fixed (red) reference frame. The Euler parameter can be converted to roll, pitch and yaw angles which may in turn be compiled into a rotation matrix R_{BF} that would rotate the global axes to the orientation of the body-fixed frame. The rotation matrix R_{HY} is also known; this rotates the global axes to the `BodyFixedHyOrigin` orientation.

The objective is to determine the rotation matrix that rotates the `BodyFixedHyOrigin` to the body-fixed reference plane; this is equivalent to the net rotation achieved by rotating the `BodyFixedHyOrigin` to the global orientation and then rotating the result to the body-fixed frame, a process achieved by the combined rotation matrix:

$$R_{HY}{}^{T} R_{BF} \qquad [B.2]$$

A single set of roll, pitch and yaw angles may be extracted from the combined matrix. These angles represent the instantaneous orientation of the body relative to the `BodyFixedHyOrigin` as required.

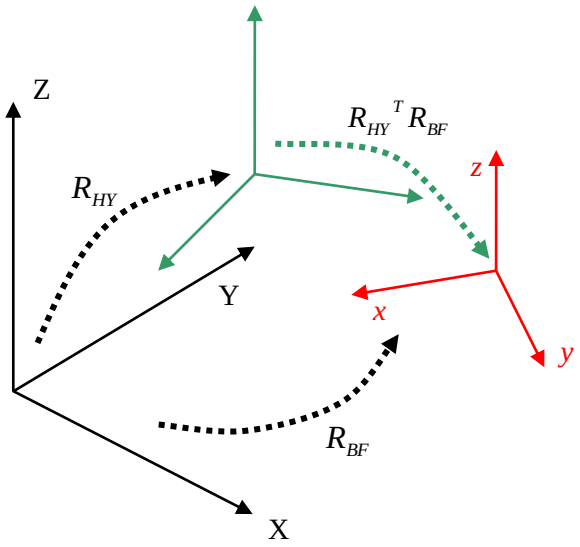

Figure B.2. Rotation matrix combinations for determining the instantaneous body rotation relative to the Hydrodynamic reference frame, `BodyFixedHyOrigin`.

Conversion of global body velocity and force values to the hydrodynamics co-ordinate system:

The velocity transformations are simpler than those for the displacements, as the three different reference frames are not offset from one another in velocity. As a result, the global (*X*,*Y*,*Z*) and (Roll,Pitch,Yaw) velocity vectors describing the body-fixed reference plane, $v_{g\ BF}$ and $\omega_{g\ BF}$ may be rotated directly into the hydrodynamics frame of reference, `BodyFixedHyOrigin` using the R_{HY} rotation matrix alone:

$$v_{HY\ BF} = R_{HY}{}^{T} v_{g\ BF} \qquad \text{[B.3]}$$

$$\omega_{HY\ BF} = R_{HY}{}^{T} \omega_{g\ BF} \qquad \text{[B.4]}$$

The force calculations completed once the body kinematic data from MBCore has been converted are described in Section 3.4. The force vectors must be converted back into the global co-ordinate system to be applied to the structure. The conversion once again involves the hydrodynamics reference frame rotation matrix only:

$$F_{g\ BF}(X,Y,Z) = R_{HY} F_{HY\ BF}(Surge,Sway,Heave) \qquad \text{[B.5]}$$

$$F_{g\ BF}(Roll,Pitch,Yaw) = R_{HY} F_{HY\ BF}(Roll,Pitch,Yaw) \qquad \text{[B.6]}$$